

Penn Center *for*
Musculoskeletal Disorders

UNIVERSITY *of* PENNSYLVANIA

20th Annual Scientific Symposium/Retreat

Wednesday, November 20, 2024
Smilow Rubenstein Auditorium/Commons
8:00am-6:00pm
www.med.upenn.edu/pcmd/

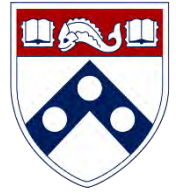
Table of Contents

	Page
Symposium Agenda.....	1
Penn Center for Musculoskeletal Disorders Components.....	2-14
Center Overview.....	2-3
Core I-Biomechanics.....	4
Core II-Histology.....	5
Core III-MicroCT.....	6
Pilot Grant Program.....	7-12
Visiting Professorship Series.....	13-14
Symposium Participants.....	15-19
Speaker Abstracts.....	20-29
Other Abstracts.....	P1-P77
MicroCT	P1-P9
Biomechanics	P10-P29
Histology.....	P30-P49
Other Research (No P30 Core Use)	P50-P77
Symposium Survey.....	

We gratefully acknowledge the financial support provided by the National Institute of Arthritis, Musculoskeletal and Skin Diseases of the National Institutes of Health and the University of Pennsylvania, Perelman School of Medicine for our Center.



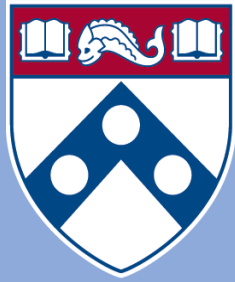
Penn Center for Musculoskeletal Disorders Scientific Symposium Agenda



November 20, 2024

Smilow Rubenstein Auditorium ♦ University of Pennsylvania

- 08:00 – 09:00am **Registration and Poster Set-up**
- 09:00 – 09:15am **Welcome and Overview**
Louis J. Soslowsky, Ph.D.
- 09:15 – 10:15am **Session I: Affiliate Member Session** (Moderator: Xiaowei Sherry Liu, Ph.D.)
- ♦ *Joseph Freeman, Ph.D., Rutgers University, “Methodologies for Regenerating Vascularized Bone”*
 - ♦ *Dirk Hubmacher, Ph.D., Icahn School of Medicine at Mount Sinai, “Leveraging Extracellular Matrix Proteins to Promote Skeletal Muscle Regeneration”*
 - ♦ *Parsaoran Hutapea, Ph.D., Temple University, “Mechanics of Bioinspired Needle Insertion in Soft Tissues”*
- 10:15 – 10:30am **Introduction:** Cartilage Regeneration Advanced Technologies to Enable Motion Center (CReATE)
- ♦ *Overview: Robert Mauck, Ph.D. and Carla Scanzello, M.D., Ph.D.*
- 10:30 – 11:30am **Break and Poster Session (Even Numbered)**
- 11:30 – 12:30pm **Session II: New Member Session** (Moderator: Lachlan Smith, Ph.D.)
- ♦ *Staci Kallish, D.O., “The Penn Medicine Clinic for Inherited Connective Tissue Disorders”*
 - ♦ *Hannah Lee, M.D., Ph.D., “Peripheral Nerve Injuries – Current Techniques and Novel Concepts Using Tissue Engineered Nerve Scaffold”*
 - ♦ *Michael Marks, Ph.D., “Tales from the Dark Side: Cytoskeletal Roles in Melanosome Biogenesis”*
- 12:30 – 01:45pm **Poster viewing and lunch (provided) in Smilow Commons**
- 01:45 – 02:45pm **Session III: Pilot Grantee Session** (Moderator: Maurizio Pacifici, Ph.D.)
- ♦ *Chider Chen, Ph.D., “mTOR-Mediated Ribosome Biogenesis Regulates CD4+ T cell Activation in Osteoporotic Mice”*
 - ♦ *Eiki Koyama, Ph.D., The Molecular Mechanisms Underlying Osteophyte Onset and Growth and Its Pharmacologic Intervention”*
 - ♦ *Carla Scanzello, M.D., Ph.D., “Macrophage Diversity in the Stiffening and Fibrotic Synovial Niche following Joint Injury”*
- 02:45 – 03:30pm **Break and Poster Session (Odd Numbered)**
- 03:30 – 04:30pm **Keynote Speaker** (Moderator: Eileen Shore, Ph.D.)
- Keynote Speaker Title: “Regulation of Post-Natal Growth Plate Maturation.”*
Marie B. Demay, M.D., Professor of Medicine from Harvard Medical School
- 04:30 – 04:40pm **Final Comments Preceding Poster Session and Reception**
- 04:40 – 06:00pm **Poster Session, Presentation of Poster Awards and Reception in Smilow Commons**

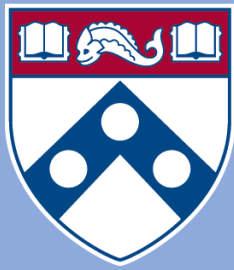


Penn Center *for*
Musculoskeletal Disorders

UNIVERSITY *of* PENNSYLVANIA

Center

Components



Penn Center *for*
Musculoskeletal Disorders

UNIVERSITY *of* PENNSYLVANIA

Center Overview

OVERVIEW OF THE PENN CENTER FOR MUSCULOSKELETAL DISORDERS

Director: Louis J. Soslowsky, PhD (soslowsk@upenn.edu)

Associate Director: Maurizio Pacifici, PhD (PacificiM@email.chop.edu)

Musculoskeletal-related conditions in the United States account for 132 million visits to physicians' offices, 29 million visits to emergency rooms, 15 million hospital outpatient visits, and cost over \$850 billion each year. Further, musculoskeletal injuries in the United States cause workers to miss more than 440 million days of work annually. In fact, more than one in four Americans has a musculoskeletal impairment. With the widespread increase in athletic and recreational activities, and the increase of the elderly population at large, these numbers are expected to rise substantially. Musculoskeletal injuries represent a critical health concern which must be better understood and better treated. To do so, a dedicated and focused strategic effort is required that optimizes research translation from the bench to the bedside in an efficient and effective manner.

The Penn Center for Musculoskeletal Disorders (PCMD) will continue to enhance the research productivity of, and provide critical resources and programs to, investigators to address multidisciplinary research strategies for musculoskeletal problems. The overall goal of this Center is to promote cooperative interactions among investigators, accelerate and enrich the effectiveness and efficiency of ongoing research, foster new collaborations and new research, and ultimately, translate our research efforts into better and new therapies for musculoskeletal disorders. The central theme of the Center will continue to be “Musculoskeletal Tissue Injury and Repair”. This theme is broad (as it includes all musculoskeletal tissue types, such as bone, cartilage, disc, ligament, meniscus, muscle, and tendon), focused (as takes advantage of commonalities in approaches across tissue types), and clinically significant (as it fosters development of assays, procedures and knowledge in preclinical animal and human models of translational relevance). It is important to note that our PCMD is not a “bone center” nor is it a “muscle center”. Rather, it is truly a “musculoskeletal center” and has emerged as the recognized home for musculoskeletal research across the Penn campus and as a technical and intellectual resource for the broader Philadelphia musculoskeletal research community.

One focus of our Center is to translate research themes, approaches, and paradigms that are consistent across different tissues. Musculoskeletal tissues have much in common and their similarities are often overlooked when focus is restricted to a single tissue type. For example, the role of inflammatory cytokines is well studied in several tissue injury and repair scenarios; yet specific findings in one tissue-type are not always known and applied in other tissues. Similarly, the availability of technologies for imaging blood vessel formation in vivo to monitor healing in a given tissue is not always known and available to researchers focusing on other tissues. Given that approaches routinely used to evaluate mechanisms in one tissue could aid researchers in other areas, our Center will work to foster this critical cross-talk.

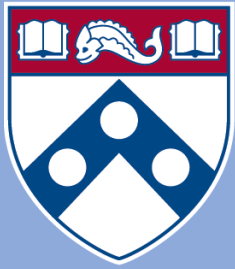
To provide a further focus for our Center, we will continue to develop programs with an emphasis on small animal models utilizing unique and sophisticated methods that can cross length scales to pre-clinical large animal models and human testing. Although large animal models for many human diseases exist and are essential for translational studies, small animals (e.g., mouse and rat) have become more commonly used for fundamental discovery of disease mechanism and initial therapeutic development due to availability of transgenic and knockout approaches and molecular tools, low cost, ease of handling and housing, and other practical issues. However, performing certain assays and experiments in mice and rats can be challenging and these difficulties often cannot be overcome in single investigator laboratories. The PCMD will provide unique expertise and sophisticated analytical tools to investigate musculoskeletal tissues across length scales.

Thus, the primary overall aims of this Center are to enhance and advance the research productivity of investigators in musculoskeletal tissue injury and repair by:

- Aim 1:** Providing innovation within critical resource core facilities in areas that cross disciplines, length scales, and hierarchies. These core facilities are μ CT Imaging, Biomechanics, and Histology.
- Aim 2:** Developing a pilot and feasibility grant program for investigators, with direct mentorship, whereby new approaches, ideas, and collaborations can be developed prior to seeking extramural funding.
- Aim 3:** Developing educational and research enrichment programs spanning tissue types, research approaches, and paradigms, through which members can learn from national leaders and from each other.

High quality musculoskeletal research is currently being conducted by many groups at Penn. While many bring sophisticated approaches to bear on musculoskeletal problems, few groups have the required expertise and facilities to perform high quality and specialized assays in their own labs. Furthermore, most investigators are not aware of approaches utilized, and results obtained, in other tissues that may have direct relevance on their research questions. Ultimately, close cooperation, communication, and collaboration among researchers across musculoskeletal tissue types and from a wide variety of disciplines will significantly enhance the research of our members. The Center will provide opportunities to integrate multi-disciplinary techniques to determine mechanisms for tissue function, injury, degeneration, repair, and regeneration, with the ultimate goal of advancing the diagnosis, treatment, and prevention of diseases and injuries of the musculoskeletal system.

In addition to the specific features described in this proposal, there is an intangible feature of our Center that should not be overlooked. Although our musculoskeletal program is strong nationally, the Penn biomedical research community is large and diverse. As such, the Center serves as an essential mechanism to highlight our successes and the importance and excitement of musculoskeletal research across campus, as well as to institutional leadership. Having a strong voice for musculoskeletal researchers is critical to support our collective and individual research goals. In these ways, the Center - with essential support from the P30 - has become and remains an indispensable resource and advocate for our community.



Penn Center *for*
Musculoskeletal Disorders

UNIVERSITY *of* PENNSYLVANIA

Core I

Biomechanics

Biomechanics Core

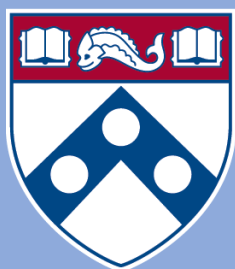
Core Director: Joel Boerckel, Ph.D. (boerckel@penmedicine.upenn.edu)

Technical Director:

The overall objective of the Biomechanics Core is to develop and provide a wide range of innovative biomechanical approaches to evaluate musculoskeletal tissue function in the context of damage, repair, and regeneration, and to provide training and funding for new projects and collaborations utilizing these assays. Over the last decade, our Biomechanics Core at the Penn Center for Musculoskeletal Disorders (PCMD) has grown into a thriving resource for the University of Pennsylvania and Philadelphia area musculoskeletal research community. In this submission, we will further expand our services to meet the increased demand for specialized techniques and develop new and innovative methods that address the multi-scale mechanics of musculoskeletal tissues. These developments will provide customized services that enhance the research productivity of our members. The Specific Aims of the Biomechanics Core are:

- To provide guidance and training on the capabilities, advantages, and disadvantages of the various methodologies to assess musculoskeletal tissue biomechanical function through formal educational enrichment programs and one-on-one interactions.
- To provide expertise and service for biomechanical assays of musculoskeletal tissues
- To develop innovative biomechanical testing techniques that will be applicable to Musculoskeletal research, and in particular those that provide information across tissue length scales.
- To provide funding for the development of new projects and collaborations and to develop preliminary and/or feasibility data for investigators.

Successful completion of these aims will significantly enhance the environment and the capabilities of researchers at the University of Pennsylvania, leading to new approaches to address musculoskeletal disorders and new collaborations between Center faculties who may have not previously included biomechanical function approaches in their musculoskeletal research programs.



Penn Center *for*
Musculoskeletal Disorders

UNIVERSITY *of* PENNSYLVANIA

Core II

Histology

Histology Core

Overview and Mission

The mission of the Penn Center for Musculoskeletal Disorders (PCMD) Histology Core is to provide comprehensive, high quality histology services to musculoskeletal researchers at the University of Pennsylvania and the broader research community.

The Specific Aims of the core are:

- To provide guidance and training on the capabilities, advantages, and disadvantages of the various methodologies to assess musculoskeletal tissue structure and composition through formal educational enrichment programs and one-on-one interactions.
- To provide expertise and service for histological and histomorphometric assays of musculoskeletal tissues.
- To develop new histologically-based techniques that will be applicable to musculoskeletal research.
- To provide funding for development of new projects and collaborations and to develop preliminary and/or feasibility data for investigators.

Services Offered

The core offers a complete spectrum of services from sample preparation and processing, to sectioning, staining and analysis, with capabilities for paraffin, plastic and frozen histology. The core provides state of the art equipment in each of these areas, which can be accessed either on a self-service basis (upon completion of training) or a full-service basis through our full-time histology technician. Service fees are highly competitive, with significant subsidies offered for PCMD members.

- Consultation and protocol development (no charge for first 6 hours)
- Paraffin processing, embedding and sectioning
- Plastic processing and sectioning
- Frozen sectioning, including cryofilm method for undecalcified bone and teeth
- Routine histochemical staining
- Imaging and histoquantitation
- Training in histology techniques

If you are using the core for the first time, we highly recommend scheduling a meeting with one of the core co-directors and the core technician to discuss the scope of your project and specific needs.

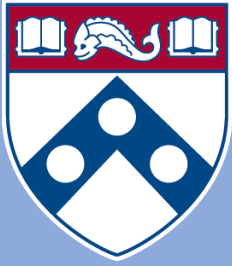
We are very happy to provide letters of support for grant applications. To request a letter, please contact the core co-directors and provide the project title, a brief description of the project and core services you propose to use.

Please visit the core website for more information: www.med.upenn.edu/pcmd/histologymain.html

Co-Directors

Ling Qin, Ph.D. (Plastic and Frozen Histology)
Professor of Orthopaedic Surgery
qinling@pennmedicine.upenn.edu
215 898 6697

Lachlan Smith, Ph.D. (Paraffin Histology)
Associate Professor of Orthopaedic Surgery
lachlans@pennmedicine.upenn.edu
215 746 2169



Penn Center *for*
Musculoskeletal Disorders

UNIVERSITY *of* PENNSYLVANIA

Core III

MicroCT

MicroCT Core

Director: X. Sherry Liu, Ph.D. (xiaoweil@pennmedicine.upenn.edu)

X-ray computed tomography (CT) imaging is an established and powerful tool to successfully analyze and clarify questions in musculoskeletal development, disease, injury and repair. In particular, the development of high-resolution micro-CT (μ CT) over the last two decades has revolutionized the quantitative assessment of calcified and X-ray dense tissue morphology. With the capability of non-destructive, three-dimensional (3D) visualization of tissue structure, μ CT has largely supplanted traditional histomorphometry and has become a gold standard for calcified tissue density and microstructure evaluation.

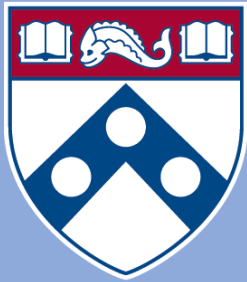
Due to the low intrinsic X-ray contrast of non-mineralized tissues, traditional applications of μ CT in musculoskeletal research have been limited to mineralized tissue. However, the development of contrast-enhanced imaging methods has greatly broadened applications of μ CT to include musculoskeletal soft tissues. This not only enables characterization of soft-tissue morphology, but also yields insight into tissue composition, such as glycosaminoglycan (GAG) density, which is essential for soft-tissue function and mechanics. Another important advance in the past decade is *in vivo* μ CT imaging of living small animals, which enables longitudinal and non-invasive evaluation of changes in the same animal over time. This imaging strategy minimizes the number of animals required while enhancing statistical power. Further, high-resolution peripheral quantitative CT (HR-pQCT), a relatively recent μ CT modality for clinical imaging of calcified tissue microstructure, has inaugurated a new era of non-invasive quantitative skeletal imaging and become a powerful tool for clinical research of musculoskeletal disorders. These new developments in μ CT enable a detailed and quantitative understanding of the genetic influences on the skeleton, as well as modeling and remodeling events in hard and soft tissues during repair, treatment, and altered loading scenarios.

Over the past 4 years, our μ CT Imaging Core (μ CTIC) at the Penn Center for Musculoskeletal Disorders (PCMD) has grown into a thriving resource for the University of Pennsylvania and the region's musculoskeletal research community, serving a vibrant and growing base of 73 active PCMD faculty members and more than 170 trainees from their laboratories. The overall objective of the μ CTIC is to develop and apply a wide range of standard and innovative μ CT imaging approaches to evaluate musculoskeletal tissue development, disease, injury and repair, and to provide training and funding for new projects and collaborations utilizing these approaches.

The Specific Aims for the μ CTIC are:

- To provide guidance and training on the capabilities, advantages, and limitations of using μ CT imaging methods for musculoskeletal research through formal educational enrichment programs, online educational tutorials, and one-on-one interactions.
- To provide a range of μ CT imaging resources, expertise, and services for the study of the structure, function, and physiology of the musculoskeletal system in laboratory animals and humans.
- To develop new μ CT imaging-based techniques that support emerging needs and catalyze innovative musculoskeletal research.
- To provide funding for the development of novel, exploratory projects and collaborations, and to acquire preliminary and/or feasibility data for junior and senior investigators to seek external funding.

By implementing these Aims, the μ CTIC will continue to serve as a unique and indispensable resource for researchers at UPenn, the Philadelphia region, and neighboring states, catalyzing innovative and high impact musculoskeletal research, and stimulating new collaborations between current and new PCMD members who may have not previously included μ CT imaging approaches in their musculoskeletal research programs.



Penn Center *for*
Musculoskeletal Disorders

UNIVERSITY *of* PENNSYLVANIA

Pilot Grant Program

**PENN CENTER FOR MUSCULOSKELETAL DISORDERS
PILOT AND FEASIBILITY GRANT PROGRAM**

The Penn Center for Musculoskeletal Disorders has an ongoing Pilot and Feasibility Grant Program. Submissions should be related to musculoskeletal tissue injury and repair which is the broad focus of the Center and Grants are only eligible for Center members (if you are not a member but would like to become one, please contact pcmd@penntermedicine.upenn.edu). For more information on our Cores and Center in general, please see our web site at www.med.upenn.edu/pcmd. The next Center grant submission deadline is January 29, 2025.

Eligibility

- Only Full Center members are eligible. If you are not currently a member, please go to the link: <http://www.med.upenn.edu/pcmd/memberinfo.shtml>
- Categories of applicants include: 1) Established investigators with a proposal to test the feasibility of a new or innovative idea in musculoskeletal tissue injury and repair representing a clear and distinct departure from their ongoing research, 2) Established investigators with no previous work in musculoskeletal tissue injury and repair interested in testing the applicability of their expertise on a problem in this area, and 3) New investigators without significant extramural grant support as a Principal Investigator to develop a new project.
- Pilot and Feasibility Grants must use at least one of the Center's Research Cores.
- Pilot project awardees are eligible for one year, with a second year to be considered (budgets will be for \$20-50,000 per year and timelines should be for one or two years). The second year of funding, the dollar amount of which would only be for up to half the year one budget, will be considered based on the progress report submitted after the first year of funding and funding availability in the Center. Please note that second year funding will often not be awarded, and when awarded, will be done so primarily to new investigators; second year funding to senior investigators will be quite rare.
- It is expected that these Pilot grants will lead to funding through other independent, extramural mechanisms. Therefore, the likelihood of future extramural funding will enter into the evaluation of these proposals.

Format

- Applications should be formatted loosely in the style of an NIH R03 grant (<http://grants.nih.gov/grants/guide/pa-files/PA-18-488.html>). The main body of the application (Specific Aims through Research Design and Methods-sections 4-7 below) is limited to five pages. The application should be in a single pdf file. The format should be:

- 1) Cover Page (not NIH face page) with grant title, PI name (and co-PI name if applicable), affiliation, contact information
- 2) Budget and brief justification (note that equipment is not allowed) (Please use form PHS398, Page 4)
- 3) NIH Biosketch of PI (and co-PI if applicable) (in the new NIH format)
- 4) Specific Aims
- 5) Significance
- 6) Innovation
- 7) Approach
- 8) Brief Statement of Category of Investigator per guidelines above
- 9) Brief Statement of How this Funding will lead to other Extramural Funding
- 10) Human Subjects and/or Vertebrate Animal Subjects (if applicable)
- 11) Consultants (if applicable)
- 12) Literature Cited
- 13) Certification of Patient Oriented Research (if applicable)

The completed proposal are submitted via the PCMD website by going to the uploaded as a single PDF file.

Please do not hesitate to email pcmd@penntermedicine.upenn.edu with any questions or comments.

Penn Center for Musculoskeletal Disorders Pilot & Feasibility Grants
(all grants awarded since inception of Center)

Awarded 2024-2025

Damaris Lorenzo, Ph.D., Department of Cell, and Developmental Biology: “Contribution of Cytoskeleton Components and Adaptors to Structural and Energetic Adaptations of Skeletal Muscle During Exercise.”

Lachlan Smith, Ph.D., Department of Orthopaedic Surgery: “Extended Release of Therapeutic mRNA to Treat Joint Disease in the Mucopolysaccharidoses.”

Jennifer Kalish, M.D., Ph.D., Department of Pediatrics and Genetics, CHOP: “Mechanisms of Tongue Skeletal Muscle Overgrowth in Beckwith-Wiedemann Syndrome.”

X. Sherry Liu, Ph.D., Department of Orthopaedic Surgery: “Interactions Between Bone and Marrow Adipose Tissue during Lactation and Post Weaning.”

Awarded 2023-2024

Kyle Vining, Ph.D., Department of Preventive and Restorative Sciences, PDM and Materials Science and Engineering, School of Engineering and Applied Science: “Exploring Molecular and Mechanical Mechanisms of Myelofibrosis in Bone Marrow Diseases”

Joel Boerckel, Ph.D., Departments of Bioengineering/Orthopaedic Surgery, Perelman School of Medicine: “Determining the Effects of Maternal Exercise on Fetal Akinesia-Impaired Skeletal Development”

Foteini Mourkioti, Ph.D., Department of Orthopaedic Surgery, Perelman School of Medicine: “Mechanosensing Regulation in Skeletal Muscles”

Awarded 2022-2023

Chider Chen, Ph.D., Department of Oral and Maxillofacial Surgery/Pharmacology, School of Dental Medicine: “mTOR Mediated Ribosome Biogenesis Regulates CD4+ T Cell Activation in Osteoporotic Mice.”

Carla R. Scanzello, M.D., Ph.D., Department of Medicine, Perelman School of Medicine: “Biophysical Regulation of Macrophage Fate and Function in OA”

Eiki Koyama, D.D.S., Ph.D., Translational Research Program in Pediatric Orthopaedics, Division of Orthopaedic Surgery, CHOP: “The Molecular Mechanisms Underlying Osteophyte Onset and Growth and its Pharmacologic Intervention.”

Awarded 2021-2022

Christop Thaiss, Ph.D., Department of Microbiology, Perelman School of Medicine: “Microbiome Control of Musculoskeletal Physiology”

Melike Lakadamyali, Ph.D., Department of Physiology, Children’s Hospital of Philadelphia, and Perelman School of Medicine: “Chromatin Structural Regulation of Chondrocyte Fate in Cell Therapy”

Michael Hast, Ph.D., Department of Orthopaedic Surgery, Perelman School of Medicine: “Development of Load-Bearing Trauma Implants Using Bioresorbable Zinc Alloy Scaffolds”

Awarded 2020-2021

Kyu Sang Joeng, Ph.D., Department of Orthopaedic Surgery, Perelman School of Medicine: “The Function of Mtorc1 Signaling in the Regulation of the Provisional Matrix During Tendon Healing” (*awarded extramural funding from NIH/NIAMS R01AR079486*)

Patrick Seale, Ph.D., Department of Cell and Developmental Biology, Institute for Diabetes, Obesity and Metabolism, Perelman School of Medicine: “Fat and Synovial Tissue Development and Disease Remodeling in Joints” (*awarded extramural funding from NIH/NIAMS R21 AR078650-01A1*)

Josh R. Baxter, Ph.D., Department of Orthopaedic Surgery, Perelman School of Medicine: “Stimulating Muscle-Tendon Healing by Prescribing Mechanical Loading” (awarded extramural funding from R21 AR081497-01)

Awarded 2019-2020

Jaimo Ahn, M.D., Department of Orthopaedic Surgery, Perelman School of Medicine: “The Interplay of Notch Suppression and Hypoxia on Bone Regeneration”

Riccardo Gottardi, Ph.D., Department of Pediatrics, CHOP Pulmonary Medicine: “Impact of Scaffold Microporosity in Guiding Local Stem Cell Differentiation for Osteochondral Repair”

Lachlan Smith, Ph.D., Departments of Neurosurgery/Orthopaedic Surgery: “Emergent Nucleus Pulposus Cell Heterogeneity during Intervertebral Disc Development and Growth” (*awarded extramural funding from NIH/NIAMS R21AR077261*)

Awarded 2018-2019

Miltiadis Zgonis, M.D., Department of Orthopaedic Surgery, Perelman School of Medicine: “Development, Maturation, and Function of Meniscal Radial Elements”

Joel Boerckel, Ph.D., Departments of Bioengineering/Orthopaedic Surgery, Perelman School of Medicine: “Role of Yap/Taz in Osteoprogenitor Cell-Induced Angiogenesis for Vascularized Bone Repair” (*awarded extramural funding from NIH/NIAMS R01AR074948 and R01AR073809*)

Awarded 2017-2018

Nathaniel Dymant, Ph.D., Department of Orthopaedic Surgery, Perelman School of Medicine: “Murine Anterior Cruciate Ligament Reconstruction Model to Understand the Cellular Origins and Mechanisms of Repair” (*awarded extramural funding from NIH/NIAMS R01 AR076381*)

Yangqing Gong, Ph.D., Department of Medicine, Perelman School of Medicine: “Role of Plasminogen in Mesenchymal Stem Cell Function and Post-Injury Bone Regeneration”

Carla Scanzello, M.D., Ph.D., Department of Medicine, Perelman School of Medicine: “Importance of Macrophage Responses in Osteoarthritis” (*awarded extramural funding from NIH/NIAMS R01 AR075737 and T21 RX001757*)

Susan Volk, V.M.D., Ph.D., D.A.C.V.S., Department of Small Animal Surgery, School of Veterinary Medicine: “The Regulatory Roles of Type III Collagen in the Cartilage Collagen Network: Implications for Osteoarthritis Prevention and Treatment” (*awarded extramural funding from NIH/NIGMS R01 GM124091*)

Awarded 2016-2017

Joseph Baur, Ph.D., Department of Physiology Institute for Diabetes, Obesity and Metabolism, Perelman School of Medicine: “Targeting Nad Metabolism in Muscular Dystrophy” (*awarded extramural funding from Elysium Health*)

Yongwon Choi, Ph.D., Department of Pathology and Lab Medicine, Perelman School of Medicine: “Cell Adhesion Regulation of Multiple-Myeloma Induced Bone Destruction”

X. Sherry Liu, Ph.D., Department of Orthopaedic Surgery and Bioengineering, Perelman School of Medicine: “Mechanical Consequences of Modeling- vs. Remodeling-Based Bone Formation” (*awarded extramural funding from the NSF Award #1661858*)

Hongtao Zhang, Ph.D., Department of Pathology and Lab Medicine, Perelman School of Medicine: “Novel Cartilage-Targeting Fc Fusion Proteins as Novel and Effective Treatments For Osteoarthritis”

Awarded 2015-2016

Yeji Zhang, M.D., Ph.D., Department of Physical Medicine and Rehabilitation, Perelman School of Medicine: “Inhibition of Adam-8 to Reduce Intervertebral Disc Degeneration” (*Awarded extramural funding from the VA Merit; VA Competitive Pilot Fund*)

Oren Friedman, M.D., Department of Otorhinolaryngology, Perelman School of Medicine: “Effect Of Injury To Cartilage And Recovery Treatment With Fgf-18”

Harvey Smith, M.D., Department of Orthopaedic Surgery, Perelman School of Medicine: “Impact of Pre-Culture and In Vivo Remobilization on Engineered Disc Replacement” (*Awarded extramural funding from the VA RX002274-01A1*)

Tejvir Khurana, M.D., Ph.D., Department of Physiology, Perelman School of Medicine: “Role of the Il-15 / Il-15ra Axis in Modulating Muscle-Tendon-Bone Adaptation and Repair”

Awarded 2014-2015

Joshua F. Baker, M.D., MSCE, Department of Rheumatology & Epidemiology, Perelman School of Medicine: “Assessment of Intramyocellular Fat Accumulation in Rheumatoid Arthritis Using MR Spectroscopy” (*Awarded extramural funding from American Federation for Aging Research Foundation*)

Russ P. Carstens, M.D., Department of Renal-Electrolyte and Hypertension Division, Perelman School of Medicine: “Roles of Epithelial Splicing Regulatory Proteins in Craniofacial Development” (*awarded extramural funding NIH 1R56DE024749 and awarded R01 NIDCR*)

Foteini Mourkioti, Ph.D., Department of Orthopaedic Surgery, Perelman School of Medicine: “A Novel Molecular Mechanism in Chronic Skeletal Muscle Injury” (*awarded extramural funding R01AR075914 NIH/NIAMS*)

Chamith Rajapakse, Ph.D., Department of Radiology, Perelman School of Medicine: “Biomechanics of Hip Fracture Assessed by MRI” (*Awarded extramural funding from the NIH R01 AR068382*)

Awarded 2013-2014

X. Sherry Liu, Ph.D., Department of Orthopaedic Surgery, Perelman School of Medicine: “Structure and Strength Recovery in Post-Lactation Bone” (*awarded extramural funding from the NIH R03 AR065145 and NSF Career Award #1653216*)

Ling Qin, Ph.D., Department of Orthopaedic Surgery, Perelman School of Medicine: “Novel Anabolic Treatment for Radiation-Induced Osteoporosis” (*awarded extramural funding from the NIH R01AR066098*)

Lachlan Smith, Ph.D., Departments of Neurosurgery/Orthopaedic Surgery, Perelman School of Medicine: “Molecular Mechanisms of Failed Vertebral Bone Formation in Mucopolysaccharidosis VII” (*awarded extramural funding from the NIH R03 AR065142 and the MPS Society*)

Hansell H. Stedman, M.D., Department of Surgery, Perelman School of Medicine: “Molecular Pattern Recognition in Acute and Chronic Injury to Muscle and Myotendinous Junction” (*awarded extramural funding from the NIH R01NS094705*)

Awarded 2012-2013

Jason Burdick, Ph.D., Department of Bioengineering, School of Engineering and Applied Science: “Acellular Fibrous Scaffolds for Stem Cell Recruitment and Cartilage Repair” (*awarded extramural funding from the NIH R01 EB008722*)

James L. Carey, M.D., MPH, Department of Orthopaedic Surgery, Perelman School of Medicine: “Development of a Large Animal Model of Osteochondritis Dissecans” (*awarded extramural funding from the NIH R01 EB008722*)

Andrew Kuntz, M.D., Department of Orthopaedic Surgery, Perelman School of Medicine: “Effects of Intra-Articular Glenohumeral Injection of a Nonsteroidal Anti-Inflammatory Drug on Shoulder Joint Mechanics in a Rat Model”

Arjun Raj, Ph.D., Department of Bioengineering, School of Engineering and Applied Science: “Single Cell Analysis of Molecular and Micromechanical Heterogeneity in Mesenchymal Stem Cells and Engineered Tissues”

Awarded 2011-2012

Struan F.A. Grant, Ph.D., Department of Pediatrics, Children’s Hospital of Philadelphia and Perelman School of Medicine: “Utilization of ChIP-seq to Identify Genes Regulated by Osterix”

Motomi Enomoto-Iwamoto, DDS, Ph.D., Department of Orthopaedic Surgery, Children's Hospital of Philadelphia and Perelman School of Medicine: "Tendon Repair by Retinoic Acid Receptor Agonists" (*awarded extramural funding from the NIH R21 AR062193*)

Ian N. Jacobs, M.D., Department of Otorhinolaryngology: Head and Neck Surgery, Children's Hospital of Philadelphia and Perelman School of Medicine: "A Pilot Study for the Development of a Rabbit In-Vivo Tissue- Engineered Cartilage Graft for Pediatric Laryngotracheal Reconstruction" (*awarded extramural funding from The Triological Society*)

Awarded 2010-2011

Susan W. Volk, VM.D., Ph.D., Dipl ACVC, Department of Small Animal Surgery, School of Veterinary Medicine: "The Role of Type III Collagen in Bone Repair and Regeneration"

Jaimo Ahn, M.D., Ph.D., Department of Orthopaedic Surgery, Perelman School of Medicine: "Toward the Identification of Molecular Pathway Alterations in Aged Fracture Healing: A Pilot Study Utilizing a Genetic Model of Senescence" (*awarded extramural funding from the NIH R03 AG040670*)

Shannon Fisher, M.D., Ph.D., Department of Cell and Developmental Biology, Perelman School of Medicine: "Requirement for Osterix in Skull Formation and Maintenance of Adult Bone in Zebrafish" (*awarded extramural funding from the NIH R21 DE021509*)

Awarded 2010-2011 (Jointly with IOA)

Olena Jacenko, Ph.D., Department of Animal Biology, School of Veterinary Medicine: "Aging of the Hematopoietic Niche" (*awarded extramural funding from the NIH R01 DK088334-01*)

Eileen M. Shore, Ph.D., Departments of Orthopaedic Surgery and Genetics, Perelman School of Medicine: "Modulation of Progenitor Cell Differentiation through BMP Signaling" (*awarded extramural funding from the NIH R01 AR041916-15*)

Kurt D. Hankenson, DVM, Ph.D., Department of Animal Biology, School of Veterinary Medicine: "Notch Signaling in Bone Regeneration" (*awarded extramural funding from the DOD CDMRP*)

Awarded 2009-2010

Ling Qin, Ph.D., Department of Orthopaedic Surgery, Perelman School of Medicine: "Mechanisms of EGFR Action on Bone" (*awarded extramural funding from the NIH R01 DK095803*)

Steven Scherer, M.D., Ph.D., Department of Neurology, Perelman School of Medicine: "Are N-cadherin and L1 Adhesion Molecules Required for Recovery of Muscle Strength after Nerve Injury?"

Nader M. Hebel, M.D., Department of Orthopaedic Surgery, Perelman School of Medicine: "A Pre-Clinical Rodent Model of Intervertebral Disc Autograft Transplant" (*awarded extramural funding from the DOD/CDMRP/PROP OR090090*)

Awarded 2008-2009

Sunday O. Akintoye, BDS, DDS, MS, Department of Oral Medicine, School of Dental Medicine: "Orofacial Bone Marrow Stromal Cells Promote Bisphosphonate-Associated Jaw Osteonecrosis" (*awarded extramural funding from the NIDCR R21 DE022826*)

Margaret M. Chou, Ph.D., Departments of Cell and Developmental Biology, Perelman School of Medicine: "Mechanisms of TRE17/USP6 Function in the Etiology of Aneurysmal Bone Cyst" (*awarded extramural funding from the NIH-NCI R01 CA168452 and R21-CA18601*)

Kenneth W. Leichty, M.D., Department of Surgery, Perelman School of Medicine: "The Role of Inflammation in Regenerative Fetal Tendon Wound Healing" (*awarded extramural funding from the NIH DP2 DK083085*)

Kathleen M. Loomes, M.D., Department of Pediatrics, Children's Hospital of Philadelphia: "The Role of Jag1 in Osteogenesis"

Eileen M. Shore, Ph.D., Departments of Orthopaedic Surgery and Genetics, Perelman School of Medicine: “Analysis of an ACVR1 Knock-in Mouse Model for FOP” (*awarded extramural funding from the NIH R01 AR041916-15S1*)

Awarded 2007-2008

Sherrill L. Adams, Ph.D., Department of Biochemistry, School of Dental Medicine: “Collagen III-deficient Mice as a Model for Musculoskeletal Wound Repair”

Kurt D. Hankenson, DVM, Ph.D., Department of Animal Biology, School of Veterinary Medicine: “Regulation of Bone Formation by Novel Activators of Canonical Wnt Signaling”

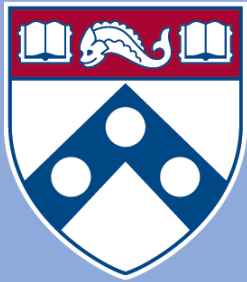
Awarded 2006-2007

Robert J. Pignolo, M.D., Ph.D., Department of Medicine, Perelman School of Medicine: “Stem Cell Rescue of the Osteoporotic Phenotype in a Mouse Model of Accelerated Aging” (*awarded extramural funding from the NIH R01 AG028873*)

Robert L. Mauck, Ph.D., Department of Orthopaedic Surgery, Perelman School of Medicine “Meniscus Repair with a Novel Aligned Nanofiber Scaffold” (*awarded extramural funding from the NIH R01 AR056624 and the VA RR & D*)

Christopher S. Chen, M.D. Ph.D., Department of Bioengineering, School of Engineering and Applied Science: “Mechanotransduction in Mesenchymal Stem Cells” (*awarded partial funding as Co-Investigator on NIH P41 EB001046*)

Pedro K. Beredjiklian, M.D., Department of Orthopaedic Surgery, Perelman School of Medicine: “Role of Hyaluronic Acid Receptors in Tendon Healing” (*awarded extramural funding from the NIH R21 AR052393*)



Penn Center *for*
Musculoskeletal Disorders

UNIVERSITY *of* PENNSYLVANIA

**Visiting Professorship
Series
2024-2025**

Visiting Professorship Series-Academic Year 2024-2025

Tuesday, April 8, 2025, 1:30 pm-2:30 pm / CRB Austrian Auditorium

Title: "Pain Relief through Innovation: Harnessing Biological Pathways to Restore Function and Regenerate Tissue."

Fackson Mwale, M.D., Professor of Surgery, McGill University

Tuesday, March 11, 2025, 1:30 pm-2:30 pm / CRB Austrian Auditorium

Title: "Bone Building and Breakdown from the City of Brotherly Love to the Lone Star State."

Benjamin Levi, M.D., Dr. Lee Hudson-Robert R. Penn Chair and Director, Center for Organogenesis Regeneration & Trauma; Professor in Surgery and Bioengineering, University of Texas Southwestern Medical Center

Tuesday, February 25, 2025, 1:30 pm-2:30 pm / CRB Austrian Auditorium - Joint with IRM

Title: TBD

Matt Greenblatt, M.D., Ph.D., Associate Professor of Pathology and Laboratory Medicine Weill Cornell Medical College

Tuesday, January 14, 2025, 1:30 pm-2:30 pm / CRB Austrian Auditorium

Title: "Building Stronger Bones with Osteoblasts"

Joy Wu, M.D., Ph.D., Professor of Medicine and Vice Chair, Basic Science in the Department of Medicine Stanford University

Tuesday, December 10, 2024, 1:30 pm-2:30 pm / CRB Austrian Auditorium

Title: Intraarticular Microbial Products: a Potential Driver of Osteoarthritis Pathogenesis

Matlock Jefferies, M.D., Clinical Associate Professor of Medicine, University of Oklahoma Health Services

**Wednesday, November 20, 2024, 8:00 am-6:00 pm / Smilow Rubinstein Auditorium & Commons
Annual Scientific Symposium**

Keynote Title: "Regulation of Post-Natal Growth Plate Maturation"

Keynote Speaker: **Marie DeMay, M.D.**, Professor of Medicine, Harvard Medical School

Tuesday, October 22, 2024, 1:30 pm-2:30 pm / CRB Austrian Auditorium - Joint with IRM

Title: "Interrogating Osteoclast Biology by Live Cell Imaging Reveals Novel Insight into their Cellular and Resorption Dynamics"

Sarah L. Dallas, Ph.D., University of Missouri Curator's Distinguished Professor and Lee M. and William Lefkowitz Endowed Professor, University of Missouri-Kansas City

Tuesday, September 10, 2024, 1:30 pm-2:30 pm / CRB Austrian Auditorium

Title: "Bone Microstructure, Mechanics, Mechanobiology, and Beyond"

Xiang-Dong Edward Guo, Ph.D., Professor of Biomedical Engineering, Columbia University

Visiting Professorship Series-Academic Year 2023-2024

Tuesday, June 18, 2024, 1:30 pm-2:30 pm / CRB Austrian Auditorium

Title: "Rotator Cuff Tear and Repair: From Bedside to Bench"

Kathleen Derwin, Ph.D., Department Vice Chair and Associate Staff, Biomedical Engineering Director, Musculoskeletal Research Center, Lerner Research Institute, Cleveland Clinic

Tuesday, May 14, 2024, 1:30pm-2:30pm/CRB Austrian Auditorium/Joint with IRM

Title: "Interrogating Osteoclast Biology by Live Cell Imaging Reveals Novel Insight into their Cellular and Resorption"

Dynamics"

Sarah L. Dallas, Ph.D., University of Missouri Curator's Distinguished Professor, Lee M. and William Lefkowitz Endowed Professor, University of Missouri-Kansas City

Monday, April 15, 2024, 3pm-4pm/CRB Austrian Auditorium/Joint with Pennsylvania Muscle Institute

Title: "Mechanisms of Hippo Pathway Dysregulation in Sarcomas."

Munir Tanas, M.D., Associate Professor of Pathology, Carver College of Medicine, University of Iowa Health Care

Tuesday, March 19, 2024, 130pm-230pm/CRB Austrian Auditorium/Joint with IRM

Title: "Bone Building Molecular Targets: Lessons from Mechanical Signaling in Skeletal Tissues"

Alexander Robling, Ph.D., Chair, Anatomy, Cell Biology & Physiology, Indiana University, School of Medicine

~~**Tuesday, February 20, 2024, 130pm-230pm/CRB Austrian Auditorium**~~ Cancelled

~~*Title: "Perspectives on Tendon Development"*~~

~~**Ronen Schweitzer, Ph.D.**, Interim Director of Research, Shriners Hospital for Children – Portland, Professor in Orthopaedics and Cell, Developmental and Cancer Biology, Oregon Health & Science University~~

Tuesday, January 23, 2024, 130pm-230pm/CRB Austrian Auditorium/Joint with IRM

Title: "Myostatin: A Molecular Rheostat for Muscle Mass"

Se-Jin Lee, M.D., Ph.D., Presidential Distinguished Professor, Genetics and Genome Sciences, Joint Appointment, The Jackson Laboratory for Genomic Medicine, MD/PhD Executive Committee Chair, University of Connecticut

Tuesday, December 12, 2023, 130pm-230pm/CRB Austrian Auditorium

Title: "Understanding Joint Health through Whole Joint Biomechanics and Mechanobiology"

Hai Yao, Ph.D., Professor and Ernest R. Norville Endowed Chair, Associate Chair for CU-MUSC Bioengineering Program, Department of Bioengineering, Clemson University

Wednesday, November 15, 2023, 8am-630pm/Smilow Rubinstein Auditorium & Commons

Annual Scientific Symposium

Title: "Navigating the NIH: The Program Director Perspective"

Keynote Speaker: Charles Washabaugh, Ph.D., Program Director, National Institute of Arthritis and Musculoskeletal and Skin Diseases, National Institute of Health

Tuesday, October 17, 2023, 130pm-2:30pm/CRB Austrian Auditorium

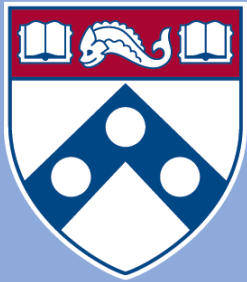
Title: "My Journey to Demystify the Marvelous Misunderstood Meniscus"

Suzanne Maher, Ph.D., Senior Scientist, Research Institute, Co-Director, Orthopedic Soft Tissue Research Program, Research Institute, Associate Director, Department of Biomechanics, Hospital for Special Surgery

Tuesday, September 12, 2023, 130pm-2:30pm/CRB Austrian Auditorium

Title: "Decorin: A Central Player of Cartilage Extracellular Matrix in Health and Disease"

Lin Han, Ph.D., Associate Professor, School of Biomedical Engineering, Science and Health Systems Drexel University



Penn Center *for*
Musculoskeletal Disorders

UNIVERSITY *of* PENNSYLVANIA

Symposium Participants

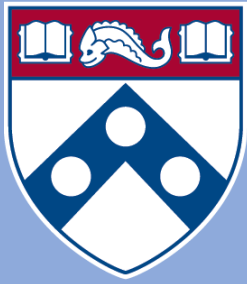
<u>Last Name</u>	<u>First Name</u>	<u>Email</u>	<u>Affiliation</u>
Alavi	Abass	Abass.alavi@pennmedicine.upenn.edu	UPenn
Amin	Silvani	asilvani@seas.upenn.edu	UPenn
Anderson	Jessica	Anderjes@pennmedicine.upenn.edu	UPenn
Angelozzi	Marco	angelozzim@chop.edu	CHOP
Ashford	Anna	aashford@seas.upenn.edu	UPenn
Augustin	Janai	janaiaug@seas.upenn.edu	UPenn
Azar	Reem	razar@seas.upenn.edu	UPenn
Bacchus	Zarah	Zarah0618@gmail.com	Rutgers University-Camden
Baldomero	Genevieve	genevieve.m.baldomero@gmail.com	Jefferson University
Bergstrom	Annika	abergs01@villanova.edu	Villanova University
Berlew	Erin	erin.berlew@pennmedicine.upenn.edu	UPenn
Bernstein	Ellie	elizabeth.bernstein@pennmedicine.upenn.edu	UPenn
Betts	Rebecca	rebecca.betts@pennmedicine.upenn.edu	UPenn
Bhangui	Varad	varadb@seas.upenn.edu	UPenn
Binder-Markey	Ben	bb983@drexel.edu	Drexel University
Blanch	Tyler	tblanch@seas.upenn.edu	UPenn
Blank	Jonathon	jonathon.blank@pennmedicine.upenn.edu	UPenn
Boerckel	Joel	boerckel@pennmedicine.upenn.edu	UPenn
Bonelli	Hannah	bonellih@chop.edu	UPenn/CHOP
Bratten	Alannah	axb988@students.Jefferson University.edu	Jefferson University
Burt	Kevin	kevin.burt@pennmedicine.upenn.edu	UPenn
Calcagno	Mariacristina	mcristina.calcagno7@gmail.com	UPenn
Camacho	Paula	Paula.camachosierra@pennmedicine.upenn.edu	UPenn
Capalbo	Maggs	mhc5270@psu.edu	Penn State University
Carey	Jim	james.carey@pennmedicine.upenn.edu	UPenn
Casila	Joseph Lance	jcasila@seas.upenn.edu	UPenn
Charoensombut	Narintadeach	charoenson@chop.edu	CHOP
Chen	Chider	chenc10@upenn.edu	UPenn
Chen	Jeffrey	jeffcfz@seas.upenn.edu	UPenn
Chen	Mei	meichen40@yahoo.com	UPenn
Chen	Mengcun	chenmc0603@gmail.com	UPenn
Chen	Xiaowen	xwchen@pennmedicine.upenn.edu	UPenn
Cheng	Zhiliang	zcheng@seas.upenn.edu	UPenn
Cheung	Catherine	catwxy@seas.upenn.edu	UPenn
Ching	Stephen	chings@seas.upenn.edu	UPenn
Choi	Eirene	exc125@students.Jefferson University.edu	Jefferson University
Cianci	Justine	ciancij@upenn.edu	UPenn
Ciuciu	Alexandra	axc497@students.Jefferson University.edu	Jefferson University
Collins	John	john.collins2@Jefferson University.edu	Jefferson University
Cone	Stephanie	sgcone@udel.edu	University of Delaware
Cook	Emily	esc6@seas.upenn.edu	UPenn
Das	Suradip	suradip@pennmedicine.upenn.edu	UPenn
Demay	Marie	mdemay@mgh.harvard.edu	Harvard Medical School
Di Pede	Rocco	tuk47720@temple.edu	Temple
Diarra	Fatoumata	fd4820242@gmail.com	UPenn
DiStefano	Michael	micdis@seas.upenn.edu	UPenn
Doro	Miranda	mdoro@sas.upenn.edu	UPenn
Duffy	Michael	michael.duffy@Pennmedicine.upenn.edu	UPenn
Dyer	Olivia	oldyer@udel.edu	University of Delaware

<u>Last Name</u>	<u>First Name</u>	<u>Email</u>	<u>Affiliation</u>
Dyment	Nathaniel	dymen@pennmedicine.upenn.edu	UPenn
Eekhoff	Jeremy	jeremy.eekhoff@pennmedicine.upenn.edu	UPenn
Essaidi	Maha	essmaha@seas.upenn.edu	UPenn
Fainor	Matthew	matthew.fainor@pennmedicine.upenn.edu	UPenn
Fan	Mingyue	mf988@drexel.edu	Drexel University
Farber	Dan	Daniel.Farber@pennmedicine.upenn.edu	UPenn
Flaugh	Rachel	Rachel.flaugh@pennmedicine.upenn.edu	UPenn
Foster	Brad	brf5277@psu.edu	Penn State University
Freeman	Joseph	joseph.freeman@rutgers.edu	Rutgers University
Freeman	Terry	theresa.freeman@Jefferson University.edu	Jefferson University
Friday	Chet	Chet.Friday@Pennmedicine.upenn.edu	UPenn
Fried	Nathan	nathan.fried@rutgers.edu	Rutgers University - Camden
G-H	Sobhan	Sg3833@drexel.edu	Drexel University
Gao	Zichen	gzc@seas.upenn.edu	UPenn
Garduno	Alexis	ag4365@drexel.edu	Drexel University
Gibson	Eve	Eve.Gibson@Pennmedicine.upenn.edu	UPenn
Godshall	Stanton	stanton.godshall@pennmedicine.upenn.edu	UPenn
Gottlieb	Devin	deving26@seas.upenn.edu	UPenn
Graci	Valentina	graciv@chop.edu	CHOP & Drexel
Grant	Struan	grants@chop.edu	UPENN/CHOP
Gullbrand	Sarah	sgullb@pennmedicine.upenn.edu	UPenn
Guo	Hanli	hanliguo1025@gmail.com	UPenn
Halloran	Daniel	hallorand@chop.edu	CHOP
Haseeb	Abdul	haseeba@chop.edu	CHOP
Haughan	Joanne	jhaughan@vet.upenn.edu	UPenn
He	Qi	qi.he@pennmedicine.upenn.edu	UPenn
Heo	Su Chin	heosc@pennmedicine.upenn.edu	UPenn
Heo	Yuna	yunaheo@seas.upenn.edu	UPenn
Hickok	Noreen	Noreen.Hickok@Jefferson University.edu	Jefferson University
Hong	Jenny	hongje@pennmedicine.upenn.edu	UPenn
Hongo	Hiroki	hhhhongo@gmail.com	UPenn
Hosseini	Mahdie	Mahdie.hosseini@pennmedicine.upenn.edu	UPenn
Hsieh	Yi-An	yi-an.hsieh@pennmedicine.upenn.edu	UPenn
Hu	Baofeng	baofeng.hu@pennmedicine.upenn.edu	UPenn
Huang	Darcy	ddhuang@seas.upenn.edu	UPenn
Hubmacher	Dirk	dirk.hubmacher@mssm.edu	Mount Sinai
Hullfish	Todd	todd.hullfish@pennmedicine.upenn.edu	UPenn
Iyer	Keerthana	keerthana.iyer@pennmedicine.upenn.edu	UPenn
Jiang	Xi	jiangxi@pennmedicine.upenn.edu	UPenn
Jin	Vincent	yvjin22@seas.upenn.edu	UPenn
Jo	Sung-Han	josunghan91@gmail.com	UPenn
Joeng	Kyu Sang	joeng@pennmedicine.upenn.edu	UPenn
Johnson	Talayah	talayahj@seas.upenn.edu	UPenn
Jones	Erica	emjones7@pennmedicine.upenn.edu	UPenn
Jung	Jaeun	jaeunj@seas.upenn.edu	UPenn
Kalish	Jennifer	kalishj@chop.edu	CHOP/UPenn
Kallish	Staci	staci.kallish@pennmedicine.upenn.edu	UPenn
Kamalitdinov	Tim	Timur.Kamalitdinov@pennmedicine.upenn.edu	UPenn
Kamona	Nada	nkamona@seas.upenn.edu	UPenn

<u>Last Name</u>	<u>First Name</u>	<u>Email</u>	<u>Affiliation</u>
Karvande	Anirudha	karvande@chop.edu	CHOP
Kaplan	Frederick	Frederick.Kaplan@pennmedicine.upenn.edu	UPenn
Kim	Dong Hwa	kimd1@upenn.edu	UPenn
Kim	Minwook	kimmin@rowan.edu	Rowan University
Kim	Sung	sungyk@seas.upenn.edu	UPenn
King	Grace	gxk218@Jefferson University.edu	Jefferson University
Knudsen-Clark	Amelia	amelia.knudsen-clark@pennmedicine.upenn.edu	UPenn
Koehnken Sawall	Jasmin	koehnkensj@chop.edu	CHOP
Kolasinski	Sharon	sharon.kolasinski@pennmedicine.upenn.edu	UPenn
Koo	Bonhyeock	bonhyeock.koo@pennmedicine.upenn.edu	UPenn
Korte	Scott	skorte@upenn.edu	UPenn
Kotsaris	Georgios	georgios.kotsaris@pennmedicine.upenn.edu	UPenn
Koyama	Eiki	koyamae@chop.edu	CHOP
Kriezis	Antonios	akriezis@seas.upenn.edu	UPenn
Kroll	Emma	krolle@seas.upenn.edu	UPenn
Kupratis	Meghan	meghan.kupratis@pennmedicine.upenn.edu	UPenn
Kwok	Bryan	bk589@drexel.edu	Drexel University
Kwon	Michelle	michelle.kwon@pennmedicine.upenn.edu	UPenn
Largoza	Jonathan	jlargoza@seas.upenn.edu	UPenn
Laslow	Brittany	Brittany.Laslow@Pennmedicine.upenn.edu	UPenn
Le Henaff	Carole	cl1813@cabm.rutgers.edu	Rutgers University
Lee	Hannah	hannah.lee1@pennmedicine.upenn.edu	UPenn
Lee	Ji-Hyung	ji-hyung.lee@pennmedicine.upenn.edu	UPenn
Lee	Wonsae	Wonsae.lee@pennmedicine.upenn.edu	UPenn
Lefebvre	Veronique	lefebrev1@chop.edu	CHOP
Levine	Michael	levinem@chop.edu	UPenn
Li	Anita	anita.li@villanova.edu	Villanova University
Li	Lun	lun.li@pennmedicine.upenn.edu	UPenn
Li	Qiaoli	qiaoli.li@Jefferson University.edu	Jefferson University
Li	Thomas	tl545@drexel.edu	Drexel University
Li	Zizhao	lizizhaomolly@gmail.com	UPenn
Liang	Qiushi	qiushil@seas.upenn.edu	UPenn
Linardi	Renata	rlinardi@upenn.edu	UPenn
Liu	Kiki	liuka@seas.upenn.edu	UPenn
Liu	X. Sherry	xiaoweil@pennmedicine.upenn.edu	UPenn
Liu	Yuchen	yl3358@drexel.edu	Drexel University
Long	Fanxin	longf1@chop.edu	CHOP
Lorenzo	Damaris	damaris.lorenzo@pennmedicine.upenn.edu	UPenn
Lounev	Vitali	vlounev@pennmedicine.upenn.edu	UPenn
Magas	Jenna	magasjenna@gmail.com	Villanova University
Maparu	Auhin	auhin.maparu@pennmedicine.upenn.edu	UPenn
Marcelin	Jonathan	jmarce@seas.upenn.edu	UPenn
Martin	Shaniqua	Shaniqua.martin@students.Jefferson University.edu	Jefferson University
Massie	Anna	amassie@upenn.edu	UPenn
Mauck	Robert	lemauck@pennmedicine.upenn.edu	UPenn
McGinley	Tim	tm3292@drexel.edu	Drexel University
McLaughlin	Eric	eric.mclaughlin@Jefferson University.edu	Jefferson University
Mehta	Samir	samir.mehta@pennmedicine.upenn.edu	UPenn
Mejías Rivera	Loreilys	loreilys.mejias@pennmedicine.upenn.edu	UPenn

<u>Last Name</u>	<u>First Name</u>	<u>Email</u>	<u>Affiliation</u>
Melvage	Autumn	agm107@students.Jefferson University.edu	Jefferson University
Meyers	Michelle	Meyersm9@seas.upenn.edu	UPenn
Moharrer	Yasaman	yasamanm@seas.upenn.edu	UPenn
Moniodes	Arianna	axm584@Jefferson University.edu	Jefferson University
Moreira Perez	Matheus	mym582@Jefferson University.edu	Jefferson University
Mourkioti	Foteini	fmour@pennmedicine.upenn.edu	UPenn
Mundy	Chrissy	matticolac@chop.edu	CHOP
Murphy	Lance	lance.murphy@pennmedicine.upenn.edu	UPenn
Nguyen	Vu	vunguyen@pennmedicine.upenn.edu	UPenn
Nijsure	Madhura	mnijsure@seas.upenn.edu	UPenn
Nixon	Jacob	jacobnix@seas.upenn.edu	UPenn
Nkansah-Andoh	Afua	afuan@seas.upenn.edu	UPenn
Nuss	Courtney	cnuss@pennmedicine.upenn.edu	UPenn
Orozco	Brianna	brianna.orozco@pennmedicine.upenn.edu	UPenn
Pacifici	Maurizio	pacificim@chop.edu	CHOP
Pan	Xuanbei	xuanbeip@seas.upenn.edu	UPenn
Panebianco	Christopher	christopher.panebianco@pennmedicine.upenn.edu	UPenn
Partridge	Nicky	partrinc@cabm.rutgers.edu	Rutgers University
Paschall	Lauren	Ldpaschall23@gmail.com	UPenn
Patel	Neil	nrp46@drexel.edu	Drexel University
Pham	Kenneth	kenneth.pham@pennmedicine.upenn.edu	UPenn
Piasecki	Liz	elizabeth.piasecki@pennmedicine.upenn.edu	UPenn
Pleshko	Nancy	npleshko@temple.edu	Temple University
Potluri	Sriya	Sriya.Potluri@pennmedicine.upenn.edu	UPenn
Potter, MD, FACS	B. Kyle	benjamin.potter@pennmedicine.upenn.edu	UPenn
Rajapakse	Chamith	chamith@pennmedicine.upenn.edu	UPenn
Rajpar	Sam	ibtesam.rajpar@Jefferson University.edu	Jefferson University
Ramesh	Sadhana	rameshs1@chop.edu	CHOP
Rapp	Anna	anna.rapp@pennmedicine.upenn.edu	UPenn
Roberts	Doug	doug.roberts@pennmedicine.upenn.edu	UPenn
Roots	Andre	amoroots@seas.upenn.edu	UPenn
Russo	Devyn	devyn.russo@pennmedicine.upenn.edu	UPenn
Sang	Wen	wen.sang@pennmedicine.upenn.edu	UPenn
Scanzello	Carla	cscanz@pennmedicine.upenn.edu	UPenn/VA Medical Center
Schipani	Ernestina	ernestina.schipani@pennmedicine.upenn.edu	UPenn
Schoenberger	Rayna	Rlschoen@seas.upenn.edu	UPenn
Sedigh	Ashkan	asedigh@villanova.edu	Villanova University
Seidl	Elizabeth	eseidl@seas.upenn.edu	UPenn
Seravello	Donna	donnaser@upenn.edu	UPenn
Sharp	Emily	ees015@seas.upenn.edu	UPenn
Sharp	Kate	katelsharp1@gmail.com	UPenn
Shore	Eileen	shore@pennmedicine.upenn.edu	UPenn
Singh	Sejal	ssingh25@seas.upenn.edu	UPenn
Slaweski	Amber	ays396@Jefferson University.edu	Jefferson University
Smith	Carly	cxs947@students.Jefferson University.edu	Jefferson University
Smith	Gail	smithgk@upenn.edu	Emeritus Prof UPenn
Smith	Harvey	Harvey.Smith@pennmedicine.upenn.edu	UPenn
Smith	Kyra	smithkw@chop.edu	UPenn/CHOP
Smith	Lachlan	lachlans@pennmedicine.upenn.edu	UPenn

<u>Last Name</u>	<u>First Name</u>	<u>Email</u>	<u>Affiliation</u>
Smith	Tarence	tarence.smith@pennmedicine.upenn.edu	UPenn
Song	Ke	ke.song@pennmedicine.upenn.edu	UPenn
Soslowky	Lou	soslowsk@Upenn.edu	UPenn
Spitsin	Sergei	spitsins@upenn.edu	UPenn
Stedman	Hansell	hstedman@pennmedicine.upenn.edu	UPenn
Stewart	Daniel	dancst@vet.upenn.edu	UPenn
Stewart	Holly	hstew@upenn.edu	UPenn
Strand	Kathryn	strandk@seas.upenn.edu	UPenn
Struble	Sarah	shosler@upenn.edu	UPenn
Sudhesh	Reshma	reshma.sudhesh@temple.edu	Temple University
Sun	Tingfang	tingfangsun89@gmail.com	UPenn
Sun	Wei	Wei.Sun@Pennmedicine.upenn.edu	UPenn
Szczesny	Spencer	ses297@psu.edu	Penn State University
Tamariz	Gabriela	gtamariz@alnylam.com	Alnylam Pharmaceuticals
Tamburro	Margaret	margaret.tamburro@pennmedicine.upenn.edu	UPenn
Taylor	CaiAsia	Caiasia.taylor@lions.lincoln.edu	Lincoln University
Thurlow	Nat	nthurlow@seas.upenn.edu	UPenn
Tichy	Elisia	tichye@chop.edu	CHOP
Tomlinson	Ryan	ryan.tomlinson@Jefferson University.edu	Jefferson University
Truong	Huy	huyt@seas.upenn.edu	UPenn
Ural	Ani	ani.ural@villanova.edu	Villanova University
Usher	Helene	usherh1@lasalle.edu	La Salle University
Vining	Kyle	vinink@upenn.edu	UPenn
Wagner	Maggie	magwag@seas.upenn.edu	UPenn
Wang	Bin	bin.wang@Jefferson University.edu	Jefferson University
Wang	Chang	chanwang@seas.upenn.edu	UPenn
Wang	Dian	Dian.Wang@pennmedicine.upenn.edu	UPenn
Watkins	Amanda	watkinsa@upenn.edu	UPenn
Wehrli	Felix	felix.wehrli@pennmedicine.upenn.edu	UPenn
Weiss	Stephanie	weissn@gmail.com	UPenn
Whipple	Sam	whipples1@chop.edu	CHOP
Winslow	Asia	axw784@students.Jefferson University.edu	Jefferson University
Wu	Tiffany	tif5353@seas.upenn.edu	UPenn
Xiang	Jiaqi	Jx338@drexel.edu	Drexel University
Xu	Jimmy	xupei@pennmedicine.upenn.edu	UPenn
Xu	Lin	linxu1@seas.upenn.edu	UPenn
Xu	Xiaoyu	Xiaoyu.Xu@pennmedicine.upenn.edu	UPenn
Xu	Yiyang	xuyiy@pennmedicine.upenn.edu	UPenn
Yang	Shuying	shuyingy@upenn.edu	UPenn
Yang	Yanmei	yanmei.yang@Jefferson University.edu	Jefferson University
Yeoh	Kenji	yeohk@CHOP.edu	UPenn
You	Jianxin	jianyou@pennmedicine.upenn.edu	UPenn
Yu	Ha-Neul	ha-neul.yu@pennmedicine.upenn.edu	UPenn
Zawel	Max	mazawel22@gmail.com	UPenn
Zhang	Deyu	deyuz@pennmedicine.upenn.edu	UPenn
Zhang	Ellen	yzhang98@seas.upenn.edu	UPenn
Zhang	Yeja	yejiazhang07@gmail.com	UPenn
Zhang	Yuqi	yuqz@seas.upenn.edu	UPenn



Penn Center *for*
Musculoskeletal Disorders

UNIVERSITY *of* PENNSYLVANIA

Speaker Abstracts

Bioactive Scaffolds, Free of Exogenous Growth Factors for Vascularized Bone Tissue Engineering

Joseph W. Freeman, PhD
Department of Biomedical Engineering
Rutgers University

Bone loss and skeletal deficiencies from a variety of sources impact the lives of millions of Americans. The bone grafting market in the U.S. has an estimated value at over \$1 billion and is expected to increase due projected increases in the population over age 65. In general, over 3 million orthopedic procedures are performed annually in the U.S.; approximately 500,000 of these are bone grafting procedures. Worldwide, 2.2 million bone grafting procedures are performed each year, making bone second only to blood as the most transplanted material. Bone loss is usually treated using autografts, allografts, metallic implants, or bone cement. Although they have many benefits, each of these materials has drawbacks which limit the extent of their use.

Tissue engineering researchers address this issue by developing regenerative scaffolds designed to work with cells to either create bone in vitro, for later implantation, or in vivo. One prominent issue with regenerative repair options (including allografts) is an inadequate blood supply. This leads to tissue death and eventual implant failure. Our group is developing bone implants designed to create vascularized bone from the patient's cells. This implant uses biochemical cues and physical guidance to simultaneously develop new bone and vasculature. By choosing bioactive materials (natural and synthetic) during implant fabrication, we have demonstrated the ability to control stem cell fate without the large-scale use of exogenous growth factors. In vivo studies show that the implants promote osteogenesis, osteointegration and attract vascularization from surrounding tissue. This combination of bioactivity without exogenous growth factors and load-sharing capability may give physicians a new way to treat a variety of orthopedic injuries without off target growth factor concerns, leading to better long-term outcomes.

Leveraging Extracellular Matrix Proteins to Promote Skeletal Muscle Regeneration

Nandaraj Taye¹, Charlene Redhead¹ & Dirk Hubmacher^{1,2}

¹Orthopedic Research Laboratories, Leni & Peter W. May Department of Orthopedics, Icahn School of Medicine at Mount Sinai, New York, NY, 10029, USA

²Mindich Child Health and Development Institute, Icahn School of Medicine, New York, NY, 10029, USA

Skeletal muscle has a remarkable intrinsic capacity to regenerate minor muscle injuries due to daily activities or exercise. Efficient muscle regeneration requires the coordinated activity of two muscle-resident stem cell populations: Myogenic muscle stem cells (i.e. satellite cells) are the source of regenerating muscle fibers, which ultimately restore muscle contractility, while non-myogenic muscle stem cells (i.e. fibroadipogenic progenitors (FAPs)) regulate satellite cell differentiation and contribute to the restoration of muscle architecture. Importantly, activated FAPs can differentiate into adipocytes, causing fatty degeneration of rotator cuff muscles after rotator cuff tears, or into fibroblasts, causing muscle fibrosis in chronic muscular dystrophies or after volumetric muscle loss due to trauma or surgical resections.

The activation and differentiation of myogenic and non-myogenic muscle stem cell populations is regulated by a network of signaling pathways, including WNT and TGF β signaling. In addition, regulatory extracellular matrix (ECM) proteins, such as decorin, thrombospondins, or latent TGF β -binding proteins fine-tune these signaling pathways in response to muscle injury. We recently showed that the regulatory ECM protein ADAMTSL2 promoted satellite cell-derived myoblast-to-myocyte differentiation, a key step in the regeneration of muscle fibers. Here, ADAMTSL2 augmented WNT signaling by binding to WNT ligands and WNT receptors. After ADAMTSL2 deletion in myogenic progenitor cells, muscle regeneration after injury was delayed and, concordantly, muscle regeneration could be accelerated after injection of the recombinant pro-myogenic ADAMTSL2 domains. In non-myogenic FAPs, however, ADAMTSL2 inhibited their differentiation into fibroblasts by negatively regulating TGF β signaling.

Collectively, our data support a dual role for ADAMTSL2 during muscle regeneration, promoting myogenic muscle stem cell differentiation in a WNT-dependent manner, and attenuating fibrogenic FAP differentiation in a TGF β -dependent manner. Currently, we are testing if scaffold-mediated ADAMTSL2 delivery can promote muscle regeneration after volumetric muscle loss, which represents a significant unmet medical need, in particular for veterans.

Mechanics of Bioinspired Needle Insertion in Soft Tissues

Parsaoran Hutapea, Ph.D.
Department of Mechanical Engineering
Temple University
Philadelphia, PA 19122

Abstract

A conformal semi-automated needling device can benefit a variety of percutaneous medical procedures such as biopsy, deep brain stimulation, gene therapy, in-vivo analysis, local delivery of drugs, etc. This needling device should be flexible enough for geometric conformality to avoid the critical organs and obstacles, or significantly improve distribution of treatment agents or dose. However, steering these needles inside patients' body needs to be highly accurate and safe. Therefore, this type of needles should have provision for sensory feedback and real-time tracking. A robot-assisted smart needling system has the potential for not only improving the quality and accuracy of the surgical procedure. Unfortunately, there is no existing flexible (active) needle that can be used for medical procedures in real-time applications. Although there are some research and developments involving rigid or flexible needle-like structures driven manually or mechanically, but their clinical application is yet to be demonstrated. The answer to this great challenge in surgical needles could be found in advanced materials (smart materials) and nature (insects). Smart materials can be exploited to be used as an actuator to develop an flexible (active) surgical needle for steering control. Additionally, insect stinger structure can be mimicked to create a bioinspired structure that can penetrate tissues with minimal effort. The combination of advanced materials and bioinspired stinger designs can be utilized to develop a smart bioinspired surgical needle for percutaneous intervention in soft tissues with greater flexibility and maneuverability, allowing accurate and easy access to target areas via obstacle avoidance and full conformity with the anatomical structure. Dr. Hutapea will discuss overview of the research activities in the Composites Laboratory at Temple University to develop the smart bioinspired needle device.

Biography

Dr. Hutapea is a Professor in the Department of Mechanical Engineering. He received his BS (1995), MS (1997), and PhD (2000) all in Aerospace Engineering from North Carolina State University, Raleigh, North Carolina. He was a Postdoctoral Fellow in the Department of Mechanical Engineering and Mechanics at Lehigh University, Bethlehem, Pennsylvania. He is a Fellow of the American Society of Mechanical Engineers.

The Penn Medicine Clinic for Inherited Connective Tissue Disorders

Staci M. Kallish, D.O.

Associate Professor of Clinical Medicine (Translational Medicine and Human Genetics)
Medical Geneticist, Hospital of the University of Pennsylvania, Philadelphia, PA, University of
Pennsylvania

Medical Geneticist, Penn Presbyterian Hospital, Philadelphia, Pennsylvania
Medical Geneticist, Children's Hospital of Philadelphia, Philadelphia, Pennsylvania

Inherited connective tissue disorders (ICTDs) represent a heterogeneous group of conditions that may arise from defects in the biosynthesis, assembly, posttranslational modification, secretion, or other processes involved in normal formation of the connective tissues. More than 200 distinct ICTDs have been described, though the most commonly known include Marfan syndrome, Osteogenesis imperfecta, and Ehlers Danlos syndromes. These conditions may present to or require management from a number of different medical specialties due to their multisystemic nature, including cardiology, cardiothoracic, vascular, and neurosurgery, ophthalmology, rheumatology, orthopedics, gastroenterology, dermatology, and others. The Penn Medicine Clinic for Inherited Connective Tissue Disorders within Medical Genetics is the primary home for the diagnosis, genetic testing/counseling, and management of these disorders and for clinical research pertaining to ICTDs.

Peripheral Nerve Injuries – Current Techniques and Novel Concepts Using Tissue Engineered Nerve Scaffold

Hannah Lee, M.D.
Orthopedic Surgery

Abstract

Peripheral nerve injury (PNI) is a common source of disability with a challenging rehabilitation course. Only 50% achieve good to normal outcome despite all the recent advances in surgical techniques. Current gold standard for nerve injuries with a gap is autograft versus distal nerve transfers. However, autografts are associated with donor site morbidity, increased operative time, and most importantly, limited availability. Distal nerve transfers are less anatomic and requires motor and sensory re-education. Therefore, there is a critical need for a potential “off-the-shelf” bioactive scaffold to guide the nerve ends to regenerate in an accelerated yet controlled manner, to achieve a good functional recovery. Specifically temporal and spatial regulation of the neurotrophic growth factor expression is desired. Using tissue engineered nerve grafts (TENGs) and safe and effective adeno-associated viruses (AAVs), we developed novel genetically engineered TENGs expressing neurogenic growth factor with temporal and spatial control (AAV-TENGs). This talk will discuss current surgical techniques and concepts for peripheral nerve surgeries and highlight some of our recent work developing AAV-TENGs.

Bio

Dr. Lee is an Orthopedic Hand Surgeon-Scientist at the CMC-VAMC and Penn, since Fall of 2020. She obtained MD and Bioengineering PhD degrees from University of Pittsburgh and has focused on her research efforts in musculoskeletal regenerative medicine. She had been working closely with Dr. D. Kacy Cullen and Translational Musculoskeletal Research Center and was awarded VA RR&D Career Development Award (CDA-2) for the peripheral nerve regeneration projects.

Tales From the Dark Side: Cytoskeletal Roles in Melanosome Biogenesis

Michael S. Marks

Dept. of Pathology & Laboratory Medicine, Children's Hospital of Philadelphia Research Institute; Dept. of Pathology & Laboratory Medicine and Dept. of Physiology, Perelman School of Medicine, University of Pennsylvania

Melanosomes are membrane bound subcellular organelles within which melanin pigments are synthesized and stored in skin and hair bulb melanocytes and pigment cells of the iris, ciliary body, retina, and choroid of the eye. Melanosomes are members of a family of so-called lysosome-related organelles (LROs) that derive from the endosomal system but are distinct from, and coexist with, classical endolysosomal organelles such as lysosomes within LRO-generating cells. Thus, cells such as melanocytes must sort contents out of the endolysosomal system and into nascent LROs as they are generated and mature. Transmembrane protein contents (such as melanogenic enzymes and transporters) are delivered to LROs by three distinct pathways. The most widely used and interesting of these pathways employs as cargo carriers transient membrane tubules that emerge from endosomes, extend along microtubules for up to 5-10 microns, and transiently fuse with maturing melanosomes. Over the past 20 years, we have learned quite a bit about this pathway from a group of rare genetic disorders, the Hermansky-Pudlak syndromes, in which melanosomes and other LROs are malformed due to a failure of LRO maturation. I will discuss what we know about the generation and targeting of the membrane tubules, the role of microtubules and actin in it, and a reverse process in which missorted cargoes are retrieved from melanosomes by a distinct class of microtubule- and actin-dependent membrane tubules.

mTOR Mediated Ribosome Biogenesis Regulates CD4⁺ T Cell Activation in Osteoporotic Mice

Chider Chen, Ph.D.

Assistant Professor, Department of Oral and Maxillofacial Surgery / Pharmacology

Degenerative diseases, such as postmenopausal related osteoporosis, usually show elevated pro-inflammatory activity, in which T cell activation promotes osteoclastogenesis to reduce bone mineral density. Upon stimulation, naïve T cells leave quiescence state, reprogram metabolic status, initiate cell expansion, and differentiate toward effector T cells. Mammalian target of rapamycin (mTOR) signaling, acts as a metabolic hub to promptly respond to a wide range of environmental cues, functions in two complexes, TORC1 and TORC2. Phosphorylation of 4E-BP1 by mTORC1 to release eIF4E and drive mRNA translation has been shown to control T cell subsets. However, whether translational control can affect metabolism to induce T cell activation in osteoporosis is largely unknown. Thus, it is critical to understand the underlying mechanism of degenerative osteoporosis and develop novel therapeutic strategies accordingly. Using genetic tools and degenerative osteoporotic models, we showed CD4⁺ T cell activation by mTORC1 is required to cause bone loss in osteoporosis, in which activated T cells are able to induce apoptosis of mesenchymal skeletal stromal cells (MSCs). Mechanistically, the translation of pre-accumulated mRNAs encoding key molecules in glycolysis and fatty acid synthesis drives metabolic switch of CD4⁺ T cells in OVX. Stimulation of poised 4E-BP1/eIF4E ribosomal translational machinery regulates T cell activation in OVX. As an anti-inflammation and anti-oxidative phosphorylation (OxPHOS) target, hydrogen sulfide (H₂S) donor treatment significantly alters T cell metabolic status, induces T cell exhaustion and rescues osteoporosis in OVX mice. Collectively, our finding reveals that mTORC1-mediated CD4⁺ T cell activation regulates bone remodeling through metabolic reprogramming of CD4⁺ T cells via regulating ribosome biogenesis. A novel H₂S-based therapy is developed to ameliorate osteoporosis in the postmenopausal mice.

The Molecular Mechanisms Underlying Osteophyte Onset and Growth and Its Pharmacologic Intervention

E. Koyama

Translational Research Program in Pediatric Orthopaedics, Division of Orthopaedic Surgery, The Children's Hospital of Philadelphia, Philadelphia, PA 19104, USA

Introduction/Rationale: Osteophytes, the bony outgrowths characteristic of osteoarthritic joints, emerge at the joint margins where damage occurs. While it is well established that osteophytes initiate at the lateral edge of the articular cartilage and extend outward, the molecular pathways driving their initiation and axial growth remain largely unclear. In this study, we explore the mechanisms regulating osteophyte formation, focusing on key signaling pathways involved in early chondrocyte differentiation and osteophyte expansion. By elucidating these processes, we aim to identify potential therapeutic targets to inhibit osteophyte growth and offer new strategies for managing osteoarthritis.

Materials and Methods: We employed the Destabilization of the Medial Meniscus (DMM) model, a well-established approach for simulating post-traumatic osteoarthritis (OA), to investigate early osteophyte formation. Three-month-old female CD1 mice underwent DMM surgery on their right knees to induce joint destabilization, while sham surgeries were performed on the left knees as controls. Knee joints were collected at 4-, 7-, and 14-days post-surgery to assess osteophyte development in response to mechanical destabilization.

Results: Detailed histological analysis revealed the presence of a fibroblast-like cell population in the lateral margin of the healthy articular cartilage, the region corresponding to the initiation site of osteophyte formation. Following surgical destabilization, these fibroblastic cells underwent rapid proliferation, establishing the cellular foundation for osteophyte development. Over time, these cells differentiated into chondrocytes, ultimately organizing into a growth plate-like structure. This structure exhibited well-defined stages of chondrocyte maturation, including proliferating, prehypertrophic, and hypertrophic chondrocytes, highlighting a tightly regulated process driving osteophyte expansion.

To explore the molecular mechanisms driving early osteophyte formation, we conducted gene expression analysis. Prior to the osteophyte initiation, the fibroblastic cells expressed *Aggrecan*. *Parathyroid Hormone-related Peptide (PTHrP)*-positive cells were detected at the surface of the developing osteophyte. Beneath these cells, actively dividing chondrocytes contributed to further expansion. Deeper within the osteophyte, the expression of *Indian Hedgehog (Ihh)*, a key regulator of chondrocyte proliferation and maturation, became prominent. At the core, *Collagen Type X (ColX)*-positive chondrocytes indicated the onset of hypertrophic differentiation. Bulk RNAseq also revealed increased expression of prochondrogenic signaling molecules during osteophyte development.

This finding suggests that the *Ihh*-PTHrP signaling axis may play a critical role in the initiation and growth of osteophytes. To test this hypothesis, we specifically deleted *Ihh* in aggrecan-expressing cells. In *Ihh^{f/f};Acan-CreER* mice, tamoxifen was administered two days prior to DMM surgery to induce targeted deletion of *Ihh* in aggrecan-expressing cells. Histological analysis two weeks post-surgery revealed striking findings: osteophyte formation was significantly diminished, underscoring the essential role of *Ihh* signaling in osteophyte development. Interestingly, no significant histomorphometric changes were observed in the articular cartilage or subchondral bone at this early stage following DMM surgery. Notably, however, numerous Safranin O-positive cells were observed in the synovial membrane, indicating the activation of prochondrogenic signaling within this tissue, potentially driven by synovial fibroblasts and other cells producing prochondrogenic cytokines. This misdirected differentiation could prompt synovial fibroblasts with chondrogenic potential to migrate to the lateral margin of the articular cartilage, contributing to accelerating osteoarthritis progression. Next, we evaluated the efficacy of PTHrP(7-36)NH₂, an N-terminally truncated PTHrP antagonist, in reducing osteophyte formation. Following DMM surgery, mice received daily subcutaneous injections of PTHrP(7-36)NH₂ at a dosage of 2.0 mg/kg for 2 weeks. Control mice were administered vehicle. Histological analysis conducted two weeks post-surgery revealed continued osteophyte growth in both the PTHrP(7-36)NH₂-treated and control groups, suggesting that the inhibition of PTHrP signaling alone may not be sufficient to prevent osteophyte formation.

Conclusions: Our study elucidates the initiation and progression of osteophytes, demonstrating that fibroblastic, *Aggrecan*-expressing cells at the lateral edge of the articular cartilage provide the cellular foundation for osteophyte formation. As osteophytes grow, they develop a growth plate-like structure with organized cellular architecture. *Ihh* expression was detected in a subset of chondrocytes, whereas *PTHrP* was localized to the surface of the developing osteophyte. Importantly, ablation of *Ihh* significantly inhibited osteophyte development. Therefore, inhibiting *Ihh* signaling may be a promising therapeutic approach. The combined inhibition of both *Hh* and PTHrP signaling may further enhance therapeutic efficacy; however, additional research is necessary. Future research should evaluate osteophyte growth progression over a longer period and systematically assess the sustained efficacy of these signaling inhibitors.

Clinical Significance: These findings provide valuable insights into the molecular mechanisms underlying osteophyte formation and suggest potential therapeutic strategies for mitigating osteophyte growth in affected synovial joints.

Acknowledgements: This work is supported by NIH/NIAMS P30AR069619.

Macrophage Diversity in the Stiffening and Fibrotic Synovial Niche following Joint Injury

Sung Yeon Kim^{1,2}, Easton Farrell^{5,6}, Kevin G. Burt^{2,4}, Bryan Kwok⁷, Alexander Knights⁵, Kate L. Sharp^{2,3}, Vu Nguyen^{2,3}, Lin Han⁷, Tristan Maerz^{5,6}, Robert L. Mauck^{1,2,4}, Carla R. Scanzello^{2,3,4}

1. University of Pennsylvania School of Engineering & Applied Science, Department of Bioengineering, Philadelphia, PA
2. Corporal Michael J. Crescenz VA Medical Center, Translational Musculoskeletal Research Center, Philadelphia, PA
3. University of Pennsylvania Perelman School of Medicine, Division of Rheumatology, Philadelphia, PA
4. University of Pennsylvania Perelman School of Medicine, Department of Orthopaedic Surgery, Philadelphia, PA
5. University of Michigan, Department of Orthopaedic Surgery, Ann Arbor, MI
6. University of Michigan, Department of Biomedical Engineering, Ann Arbor, MI
7. Drexel University, School of Biomedical Engineering, Philadelphia, PA

In joint injury and OA, the synovial membrane undergoes structural and compositional changes characterized by increased matrix deposition, disruption of degradative processes, and abnormal biochemical composition which can stiffen the synovium. This fibrotic remodeling contributes to disease progression, pain, and joint stiffness. Fibroblasts and macrophages, the primary cellular components of the synovial membrane, are key cellular mediators of tissue remodeling. But how evolving fibroblast and macrophage phenotypes and cell-matrix interactions contribute to aberrant tissue remodeling after joint injury is poorly understood. While it is well-established that extracellular matrix mechanical properties can modulate myofibroblast differentiation, recent evidence suggests that macrophages are also mechanosensitive and can tune their phenotype in response to matrix rigidity. However, the functional consequences of altered matrix mechanics on synovial macrophage phenotype and behavior in OA is largely unexplored. Synovial macrophages are highly heterogeneous, with macrophage diversity arising from their polarization and ontogeny. Specifically, tissue-resident macrophages of the intima are derived from a monocyte-independent lineage and form a tight junction-mediated barrier that physically restricts inflammatory cell infiltration into the joint space. By contrast, both resident and peripherally derived macrophages occupy the subintimal layer. Yet, it remains unclear how distinct synovial macrophage populations (resident versus recruited) contribute and respond to synovial tissue fibrosis.

We employed a murine model of experimental OA (the destabilization of the medial meniscus model, DMM) that recapitulates the chronicity of joint inflammation, fibrosis and injury to interrogate immune-stromal cellular dynamics and dissect cell-matrix dialogue in the synovium. We first confirmed that DMM injury leads to synovial matrix stiffening using histology and atomic force microscopy (AFM)-nanoindentation. 4 weeks after DMM surgery there was a 2.1-fold increase in synovial micromodulus compared to sham controls ($p < 0.004$) that persisted at the 8-week timepoint (2.5-fold, $p < 0.013$). Utilizing single cell RNA sequencing (scRNA-seq), we then identified discrete immune and stromal cell types in the healthy and osteoarthritic synovium and compared transcriptional profiles to gain insight into mechanisms responsible for the emergence of pro-fibrotic phenotypes. 5 distinct fibroblast populations were identified by scRNA-Seq, with two transient clusters (Col5a3+ and Prg4^{high}) emerging at 4-weeks post-surgery in both sham and DMM synovium. Lining fibroblasts (Prg4^{high}) were more prevalent in DMM. By 8-weeks, fibroblast proportions in sham and DMM had returned to baseline, but there was a substantial increase in the overall number of fibroblasts in the DMM synovium compared with sham. Global fibroblast transcriptional profiles were more similar between sham and unoperated joints than between sham and DMM at both timepoints, with genes involved in mechanosensing, mechanotransduction, and matrix deposition upregulated in DMM. 14 unique CD45+ leukocyte clusters were also identified, including Trem2+CX3CR1+ lining MΦs. Interestingly, at 4-weeks post-surgery sham- and DMM- operated knees had similar cellular proportions despite differences in synovial stiffness at this timepoint. Despite similar cellular profiles, lining macrophages displayed divergent transcriptomic profiles between sham and DMM. By 8-weeks post-surgery, overall cell numbers decreased in both sham and DMM but increased proportions of Trem2+CX3CR1+ lining MΦs were observed in the DMM synovium.

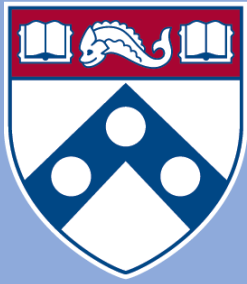
Our analyses revealed that in the DMM synovium, synovial stiffening indicative of fibrotic remodeling is detectable by 4 weeks after DMM injury, and accompanied by increases in transient fibroblast subsets and transcriptional changes suggesting higher mechanoactivity and matrix deposition. Both sham and DMM injury were accompanied by increases in resident and infiltrating macrophage subsets at 4 weeks, but lining macrophages displayed divergent transcriptomic profiles in DMM. Whether these different patterns are driven by divergent cell-matrix interactions or influence the dynamic changes in fibroblast populations in this model remains to be tested. By 8 weeks post DMM, there were sustained elevations in baseline fibroblast and lining macrophage subsets compared with sham operated joints. These findings provide insight into cellular contributions to synovial lining hyperplasia and fibrosis and highlight the importance of evaluating sham-operated controls to deconvolve confounding effects of surgery in this model.

Regulation of Post-natal Growth Plate Maturation by Hormones and Mineral Ions

Marie Demay, M.D.
Professor of Medicine, Harvard Medical School
Physician, Massachusetts General Hospital

A number of developmental and signaling pathways have been shown to regulate the embryonic development and post-natal maturation of the growth plate. Post-natal, hormones and mineral ions play a critical role in growth plate maturation, an effect that is not seen during fetal development due to the highly controlled intrauterine metabolic environment.

The actions of the vitamin D signaling pathway on prevention of rickets have long been recognized. However, rather than exerting its principal effects by direct signaling in chondrocytes, the role of this pathway in growth plate maturation is to maintain normal mineral ion homeostasis. Studies have demonstrated that hypophosphatemia, in the setting of impaired vitamin D signaling or excessive FGF23 action leads to expansion of the hypertrophic chondrocyte layer of the maturing growth plate. This rachitic phenotype can be prevented in the absence of either or both of these hormones, by ensuring normal phosphate signaling. Phosphate decreases mitochondrial membrane potential in hypertrophic chondrocytes, leading to activation of the mitochondrial apoptotic pathway. Small molecule screens have identified the VEGF signaling pathway as a mediator of phosphate signaling in hypertrophic chondrocytes. Chondrocyte-specific depletion of VEGFR2 *in vivo* leads to expansion of the hypertrophic chondrocyte layer, characteristic of rickets, implicating this signaling pathway in the regulation of growth plate maturation by phosphate and vitamin D signaling



Penn Center *for*
Musculoskeletal Disorders

UNIVERSITY *of* PENNSYLVANIA

Micro CT Core Abstracts

High-Speed Treadmill Running Does Not Induce a Tendinopathic Phenotype in Rat Achilles Tendon

Snehal S. Shetye*¹, Margaret K. Tamburro*¹, Ashley K. Fung¹, Thomas P. Leahy¹, Madison N. Magee¹, Harina A. Raja¹, Stephanie N. Weiss¹, Courtney A. Nuss¹, Alexander J. Bein¹, Daniel C. Farber¹, Louis J. Soslowsky¹

¹McKay Orthopaedic Research Laboratory, University of Pennsylvania, Philadelphia, PA, USA

* co-first authors

Margaret.Tamburro@penmedicine.upenn.edu

Disclosures: Snehal S. Shetye (N), Margaret K. Tamburro (N), Ashley K. Fung (N), Thomas P. Leahy (N), Madison N. Magee (N), Harina A. Raja (N), Stephanie N. Weiss (N), Courtney A. Nuss (N), Alexander J. Bein (N), Daniel C. Farber (N), Louis J. Soslowsky (N)

INTRODUCTION: Achilles tendon pathology comprises an increasing and consequential clinical burden,^{1,2} but robust and reproducible preclinical animal models of Achilles tendinopathy are lacking. Overuse is a common etiology of tendon pathology, and exercise-induced overuse has been considered a promising mechanism for creating a clinically relevant tendinopathy model. In rat Achilles tendon, treadmill running at moderate speed (17-20 m/min) results in variable structural and functional outcomes,³⁻⁷ failing to induce a consistent tendinopathy phenotype. Effects of running at higher speeds (> 25 m/min) on Achilles tendon structure and function have not been thoroughly investigated, though early results have shown potential for a tendinopathic phenotype.^{7,8} Therefore, the objective of this study was to rigorously assess the structural and biomechanical impacts of high-speed treadmill running on rat Achilles tendon. We hypothesized that 16 weeks of high-speed treadmill running would induce an overuse tendinopathy phenotype characterized by matrix disorganization, rounded cell morphology, and reduced tensile mechanical properties.

METHODS: Sprague-Dawley rats (~400 g) were randomized into two groups: cage activity (n = 12) and running (n = 9). The running group underwent a 3-week acclimation protocol followed by 16 weeks of high-speed treadmill running (27 m/min, 10° incline, 1 hour/day, 5 days/week); mild electrical shock was used at the back of the treadmill to encourage running. After 16 weeks, Achilles tendons were harvested bilaterally for histological and mechanical assessment. For histology, ankles were prepared for paraffin histology with standard techniques,⁹ sectioned sagittally (7 μm thickness), stained serially with DRAQ5™ (abcam, Waltham, MA, USA) then 0.1 % toluidine blue, and imaged (10X magnification). Midsubstance regions (~1.3 x 0.65 mm) from two sections per tendon were analyzed (CellProfiler™¹⁰) for cell count and nuclear shape. Tendons designated for mechanical testing were first μCT imaged (10 μm resolution, μCT35, Scanco Medical, Brüttisellen, Switzerland) to identify heterotopic ossification (HO). Images were segmented and HO volume was quantified with Amira 6.7 (Thermo Fisher Scientific, Waltham, MA). After scanning, tendons were prepared⁹ and tested with a viscoelastic testing protocol (preconditioning; stress relaxation at 9% strain; sinusoidal frequency sweeps at 0.1, 1, 5, and 10 Hz) followed by a quasi-static ramp (0.3% strain/s) to failure with image capture for optical strain measurement. Digital image correlation software (Vic2D, Correlated Solutions, Irmo, SC) was used to determine strain distributions along the length of the tendon at the transition point, mid-linear region (2 x transition strain), and failure. T-tests were used to compare histological and mechanical properties between cage activity and running groups, and 2-way repeated measures ANOVAs with Šidák's multiple comparison tests were used to assess differences in regional strain and modulus between activity groups. Significance was set at p < 0.05.

RESULTS: All histology samples demonstrated varying amounts of discrete pockets of matrix disorganization, increased staining intensity, and rounded cell morphology, demonstrating an HO phenotype (Fig. 1A). In regions of interest, chosen to exclude regions of suspected HO, cell density and nuclear shape were unaffected by treadmill running (Fig. 1B-D). In contralateral limbs, we consistently detected the presence of HO on μCT, though HO volume (Fig. 2) and mineral density (data not shown) were unaffected by activity level. While running was associated with a decrease in cross-sectional area (CSA, p = 0.04), when normalized to body weight, runners demonstrated increased normalized CSA (p = 0.02). Despite this, no differences were detected between groups in viscoelastic (relaxation at 9% strain, dynamic modulus, phase shift) or elastic (stiffness, modulus) mechanical properties (Fig. 3A-F). Local strain and modulus varied along the tendon length as expected (p < 0.05) but were unaffected by activity group (data not shown).

DISCUSSION: Contrary to our hypothesis, 16 weeks of high-speed treadmill running did not induce an overuse tendinopathy phenotype. While rat Achilles tendon is a well-established model for investigations of HO,¹¹ previous studies of impacts of treadmill running on rat Achilles tendon have not considered potential impacts of HO on tendon structure and biomechanics. We speculate that the high incidence of HO may impact the consistency of both histological and mechanical findings from previous rat Achilles tendon tendinopathy models. Future methods for inducing Achilles tendinopathy should consider alternative approaches to achieve a reproducible phenotype.

SIGNIFICANCE: High-speed treadmill running for 16 weeks did not induce tendinopathic overuse in rat Achilles tendon based on histologic, structural, and mechanical assessments.

REFERENCES: [1] Longo, Sports Med Arthrosc Rev, 2009. [2] Lanto, Scand J Med Sci Sports, 2015. [3] Huang, Ann Biomed Eng, 2004. [4] Glazebrook, JOR, 2008. [5] Abraham, BMC MSK Disord, 2011. [6] Heinemeier, J Appl Physiol, 2012. [7] Xu, Exp Ther Med, 2018. [8] Xu, Med Sci Monit, 2016. [9] Leahy, AJSM, 2022. [10] Stirling, BMC Bioinform, 2021. [11] Pierantoni, FASEB J, 2023.

ACKNOWLEDGEMENTS: Dedicated to the memory of Madison Magee. We thank Miranda Doro for her assistance. Funding support provided by the Penn Center for Musculoskeletal Disorders (NIH/NIAMS, P30 AR069619) and F31AR082282.

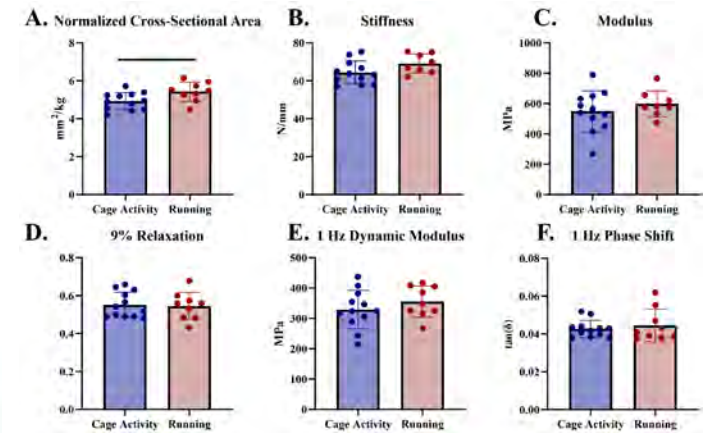
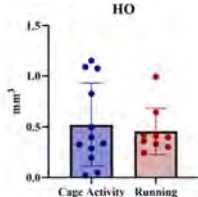
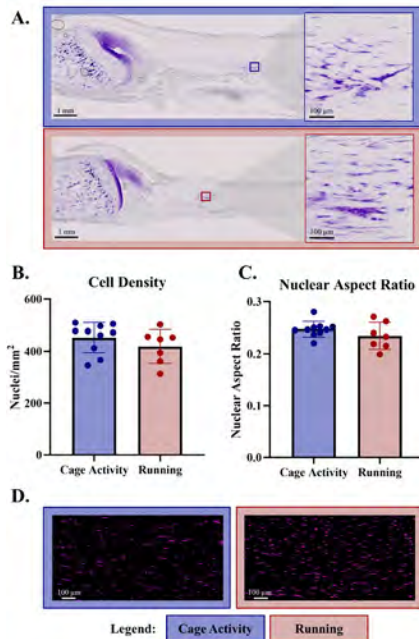


Figure 1: Both cage activity (blue) and running (red) tendons contain discrete regions of disorganization with rounded cells, indicative of HO (A). Running did not impact cell density (B) or nuclear aspect ratio (C) in the midsubstance (representative images shown in D).

Figure 2: Tendons from both activity groups demonstrated HO by μCT. Running did not influence HO volume.

Figure 3: Running increased Achilles tendon CSA normalized to body weight (A). Neither stiffness (B) nor optical modulus (C) were influenced by treadmill running. Similarly, percent relaxation (D), dynamic modulus (E), and phase shift (F) were unaffected by treadmill running (data shown for 1 Hz, consistent across frequencies).

Trabecular Development in Caprine Phalanges and Metacarpal Bones

Maha Essaidi^{1,2}, Christopher J. Panebianco², Karin Vancíková³, Pieter Brama⁴, Niamh C. Nowlan³,
Joel D. Boerckel^{1,2}

¹School of Engineering and Applied Science, University of Pennsylvania, Philadelphia, PA

²Department of Orthopaedic Surgery, University of Pennsylvania, Philadelphia, PA

³School of Mechanical and Materials Engineering, University College Dublin, Dublin, Ireland

⁴School of Veterinary Medicine, University College Dublin, Dublin, Ireland

Introduction:

Trabecular bone only makes up 20% of the human skeleton, yet it is the main t. While bone mineral density (BMD) is commonly used to measure bone strength, it has been identified that combining it with 3D trabecular microstructural indices improves the accuracy of assessing mechanical properties (Ulrich et al. *Bone* 1999). Investigating trabecular osteogenesis, specifically trabecular microarchitecture, is therefore crucial for understanding bone development and improving diagnosis of bone-related diseases. In this study, goats were used as an animal model to study long bone development because they experience similar levels of loading to humans. Unlike humans, goats only have 2 phalanges, and their metacarpus is fused for both phalanges, thus one phalanx can be purposefully overloaded and the other under-loaded. Ruminants have previously been used as large animal models in bone development research, including studies on osteoporosis (Dias et al., *Curr Osteoporos Rep*, 2018). In this experiment, high-resolution micro-computed tomography (μ CT) was used to quantify trabecular bone microarchitecture by calculating morphometric indices and bone volume in goat proximal phalanges 1 (P1) and metacarpus from birth to adulthood. The fusion of the epiphyseal metacarpus in goats occurs during postnatal development and was quantified by measuring the fusion length at the different maturation stages. The aim of this study is to establish a baseline of trabecular bone growth to encourage future research on the underlying mechanobiology and effects of mechanical cues on bone development.

Materials & Methods:

The analysis was performed on 44 goats at different postnatal stages: 3 days (neonate, n=9), 1.5 months (1.5M, n=6), 3 months (3M, n=5), 6 months (6M, n=6), 9 months (9M, n=6), 12 months (12M, n=6), and 3.5 years (adult, n=6).

To prepare for imaging, the bone samples were wrapped in gauze and submerged in PBS (scanning medium). The image acquisition was performed in a Scanco μ CT45 system with an X-ray intensity of 145 μ A, an energy of 55 kVP, an integration time of 400 ms and a resolution of 10.4 μ m (isotropic voxel size). In the reconstructed scans, the trabecular region in each sample was segmented semi-automatically through a combination of manual contouring and range extrapolation across \sim 2,000 slices. The bone volume fraction (BV/TV) was measured from the 2D sections while trabecular number (Tb.N), trabecular thickness (Tb.Th), and trabecular separation (Tb.Sp) were calculated using a sphere-fitting method. To measure the epiphyseal fusion length (FL) in the metacarpi, the voxel size was multiplied by the total number of slices from the first fusion point below the growth plate to the last point of fusion.

For each sample, the data from lateral and medial metacarpal bones were averaged, as were the data from the right and left phalanges. A one-way analysis of variance (ANOVA) with a Tukey's post-hoc test ($\alpha = 0.05$) was conducted to identify significant differences between groups.

Results and Discussion:

An increase in P1 BV/TV was observed (Fig1B), reflecting rapid bone growth relative to total tissue as it matures. The increase in Tb.N and Tb.Th indicates formation of new trabeculae and their increased thickness (Fig.1C-D). The decline in Tb.Sp (Fig1E) highlights reduced spacing between trabeculae, forming a denser network. This implies that the bone is becoming stronger and better able to sustain mechanical loading.

Metacarpi BV/TV and Tb.Th consistently increased (Fig2B-D). However, Tb.N didn't change significantly until 12M, suggesting that postnatal development of the metacarpi is characterized by strengthening existing trabeculae rather than forming new ones (Fig2C), as opposed to P1. No significant changes in Tb.Sp were observed (Fig2E), meaning alteration to trabecular spacing isn't a factor in bone maturation. Between 3M-6M, a decrease in BV/TV, Tb.Th and Tb.N, coupled with an increase in Tb.Sp may represent a period of bone remodeling (Fig1-2).

The metacarpus fused at 3M and rose through 12M, before experiencing a significant drop (Fig.2F). This decline may result from the complete bone fusion at all points, unlike in younger samples.

This study outlines trabecular development in goat phalanges and metacarpi, revealing dynamic growth in P1 and stable growth in metacarpi. Future studies will employ histology to explore changes in cellular architecture during postnatal development. Furthermore, we plan to use goats as a model system to alter the mechanical environment to examine how mechanical loading affects trabecular osteogenesis and metacarpal fusion.

YAP and TAZ mediate mechanical load-induced bone adaptation

Yasaman Moharrer¹, Daniel Horan², Tala Azar¹, Annemarie Lang¹, Alexander Robling², X. Sherry Liu¹, Joel D. Boerckel¹.

¹University of Pennsylvania, ²Indiana University

Bone adapts to mechanical stimuli; however, the mechanotransductive mechanisms are poorly understood. We hypothesized that the transcriptional regulators, YAP and TAZ, mediate bone adaptation to mechanical loads. Osteocyte deletion of YAP and TAZ alters bone architecture and lacunar/canalicular networks.¹ Therefore, we used pharmacologic approaches to acutely inhibit YAP/TAZ signaling in mice with normal developmental history.

We selected two orthogonal inhibitors: verteporfin (VP), which blocks YAP/TAZ co-activation, and MGH-CP1 (CP1), which prevents TEAD binding to YAP and TAZ. We performed i.p. injections of either inhibitor (or DMSO) to 14-wk-old male C57BL/6 mice for 2 weeks. Concurrently, the left tibiae of each mouse underwent in vivo cyclic compressive loading with a 4 Hz sinusoidal waveform, at 1200 cycles per day, for 5 d/wk. over 2 weeks. The peak load induced 1200 $\mu\epsilon$ at the location of maximal strain in the tibial shaft (37%), calibrated by strain gage. Contralateral tibiae served as non-loaded controls. MicroCT and dynamic fluorochrome labeling (calcein and alizarin complexone) were used to quantify cortical bone formation at the site of maximal cortical strain and of trabecular bone in the proximal tibia metaphysis.

Cyclic compressive tibial loading increased tibial cortical thickness in the DMSO group; however, either VP or CP1 treatment abrogated the effect of loading. Neither loading nor YAP/TAZ inhibition significantly altered trabecular bone morphometry (BV/TV, Tb.Th, Tb.N, Tb.Sp). Cyclic loading increased periosteal bone formation, and neither CP1 nor VP treatment significantly blunted periosteal MS/BS, MAR, or BFR/BS. In contrast, at the endocortex, both VP and CP1 treatment abrogated the significant effect of loading on MS/BS, MAR, and BFR/BS.

These data provide the first in vivo evidence that YAP and TAZ mediate mechanotransduction of anabolic loading. In the tibial cortex, both VP and CP1 blocked load-induced cortical bone gains by blunting endosteal rather than periosteal bone formation. Previously, we found that VP alters osteocyte network density and perilacunar dynamics differently in endosteal- compared to periosteal-adjacent osteocytes, suggesting differential drug transport or spatial mechanotransduction. Together, these findings reveal new insights in bone mechanotransduction and identify risks of cancer-treatment-induced osteoporosis by pharmacologic targeting of YAP and TAZ as oncogenes.

1 Kegelman+ JBMR 2019

Assessment of Marrow Adiposity Using Micro-Computed Tomography (μ CT) with Image Registration in Female Mice with Metabolic and Hormonal Challenges

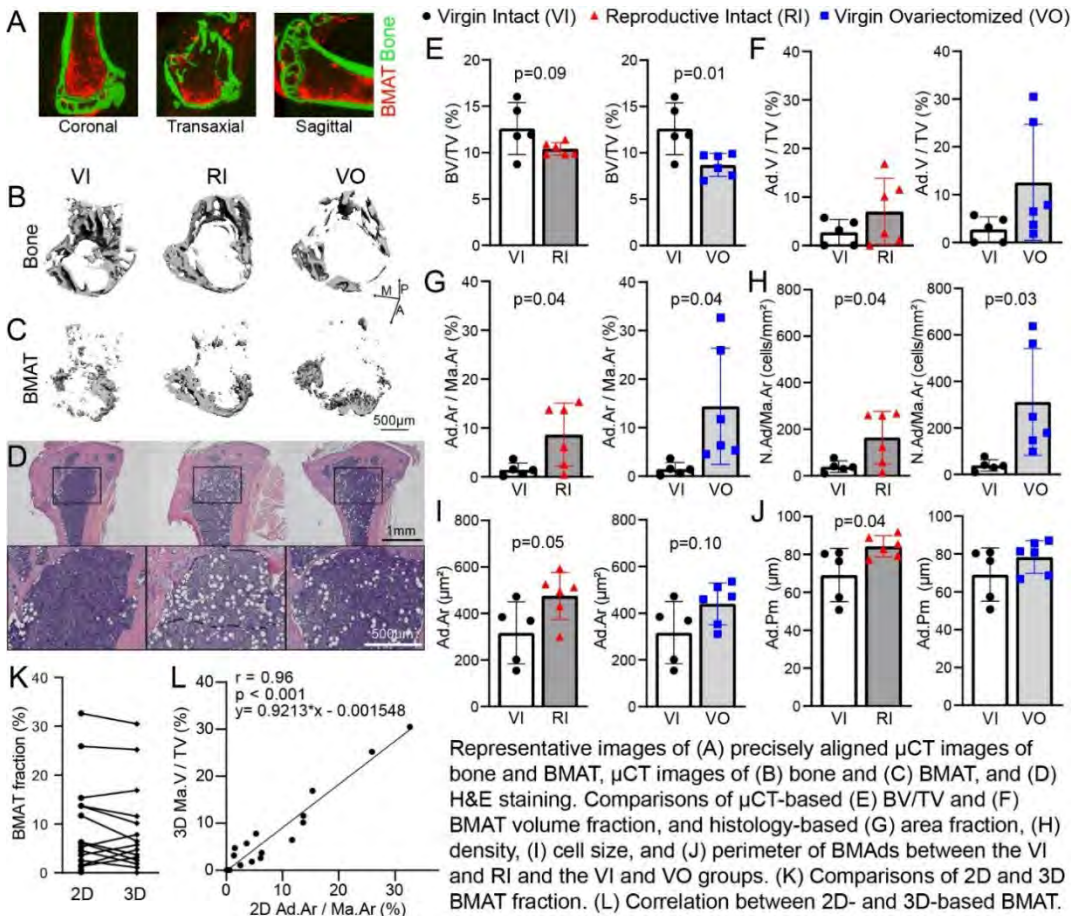
Wonsae Lee¹, Kira Lu¹, Xiaoyu Xu¹, Wen Sang¹, Jesica Jojo¹, Tala Azar¹, Y. Vincent Jin¹, X. Sherry Liu¹

¹ McKay Orthopaedic Research Laboratory, University of Pennsylvania, Philadelphia, PA; wonsae.lee@pennmedicine.upenn.edu

INTRODUCTION: Bone marrow adipocytes (BMAs) are a distinct adipose cell population whose precise function remains elusive, yet their modulation suggests a close interplay with the metabolic milieu. Our previous rodent studies showed a significant reduction in both bone tissue and bone marrow adipose tissue (BMAT) during lactation, followed by recoveries of both tissues postweaning, indicating their active adaptations during metabolic and hormonal challenges. In the current study, we aimed to test whether a history of reproduction and lactation has long-lasting effects on bone and BMAT.

METHODS & RESULTS: Osmium tetroxide-based μ CT and 3D image registration were utilized to achieve precise, 3D measurement of BMAT, which was then compared with the 2D histological measurements of BMAs in 12-month-old virgin intact (VI, n=5) and reproductive intact (RI, n=6) mice. RI mice completed 2 reproductive cycles (pregnancy, 3-week lactation, and 6-week post-weaning recovery). Moreover, virgin ovariectomized mice (VO, n=6, OVX at 6 weeks before euthanasia) were included as a reference group to showcase the effect of estrogen deficiency on bone and BMAT. The left tibiae of all mice were scanned before and after decalcification for osmium tetroxide staining. Custom image registration software (CTPros, Fig.A) facilitated a precise alignment of images of bone tissue and BMAT. The RI group exhibited a trend toward 17% lower BV/TV than the VI group (p=0.09) while the VO group had a 30% lower BV/TV than the VI group (Fig B&E). However, μ CT analysis showed no statistical significance in comparisons of BMAT volume between the RI and VI groups, or the VO and VI groups, despite 1.5-fold and 3.5-fold higher values in the RI and VO groups, respectively (Fig.C,F). Histological analysis of contralateral tibiae with H&E staining revealed a 450%, 323%, 50%, and 22% greater adipose tissue area, density, size, and perimeter of BMAs in the RI vs. VI group (Fig.D,G-J). On the other hand, VO mice had 883% and 703% greater adipose tissue area and density, respectively, with a trend toward 39% greater size of BMAs compared to those of VI mice. Lastly, a high correlation (r=0.96) was found between 2D histology and 3D μ CT measurements of BMAT (Fig.K-L).

DISCUSSION: This study proposes a precise 3D quantification of marrow adiposity in relation to the trabecular compartment through accurate image registration. While 3D and 2D measurements are highly correlated to each other, 3D image enables future analysis of spatial distribution of BMAT in response to metabolic conditions and treatments. It reveals that metabolic and hormonal challenges associated with histories of pregnancy and lactation exert long-lasting effect on both bone tissue and BMAT, to a similar extent when compared with acute estrogen deficiency by OVX. Future research will investigate mechanisms and potential differences in the impact of reproductive history and estrogen deficiency on marrow adiposity.



Maternal exercise rescues fetal akinesia-impaired bone and joint development

Christopher J. Panebianco¹, Yuming Huang², Nidal Khatib^{2,3}, Devin C. Gottlieb¹, Nathaniel Dymant¹, Joel D. Boerckel¹, Niamh C. Nowlan^{2,3}

¹University of Pennsylvania, Philadelphia, PA, USA | ²Imperial College London, London, UK | ³University College Dublin, Dublin, IRL

INTRODUCTION: During development, fetal movements provide the mechanical forces necessary for proper skeletal morphogenesis. Clinical conditions that limit fetal movement (*e.g.*, congenital muscle development defects, low amniotic fluid volume, breech position) can result in limited movement, “fetal akinesia”.¹ Fetal akinesia can cause debilitating skeletal disorders, such as impaired bone development and multi-joint contractures.² Previously, we found that direct mechanical stimulation of explanted fetal limbs taken from muscle-less Pax3^{spd/spd} (Spd) mice rescued effects of fetal akinesia on joint morphogenesis, suggesting that external mechanical stimulation can provide mechanobiological signals lost due to fetal akinesia.³ Here, we tested the hypothesis that maternal exercise could be a non-invasive, *in utero* mechanotherapeutic intervention for fetal akinesia. Since maternal exercise may rescue skeletal deformities by directly restoring missing mechanical signals or by indirectly providing maternally secreted signals, the aims of this study were to determine the effects of maternal exercise on fetal akinesia-impaired skeletal development and evaluate the effects of maternal exercise on physiology-mediated signaling.

METHODS: To determine the effects of maternal exercise on fetal akinesia-impaired skeletal development, we used the muscle-less Pax3^{spd/spd} (Spd) mouse.⁴ Spd heterozygotes, which are phenotypically normal, were crossed to produce litters with wildtype (WT), heterozygous, and homozygous mutant progeny. Pregnant dams were subjected to 1 hr of daily wheel running exercise or sham exercise from E13.5 to E16.5, inclusive. Sham-exercised dams had locked wheels. Embryos were harvested at E16.5, then joint and bone shape were evaluated using whole-mount optical projection tomography. Follow-up analyses were conducted using C57BL/6J mice because it was easier to obtain sufficient sample sizes. C57BL/6J dams were exercised from E13.5 to E16.5, inclusive, with harvest at E17.5. We measured forelimb bone morphogenesis using microcomputed tomography (μ CT, voxel size = 3 μ m, x-ray tube potential = 70 kVp, x-ray intensity = 145 μ A, integration time = 300 ms) and cryohistology. To evaluate the effects of maternal exercise on physiology-mediated signaling, we measured the fetal weight to placental weight ratio (FW:PW) and placental levels of IGF-1 and nutrient transporters. One-way ANOVA with Tukey’s post-hoc test and Student’s t-test were used to find significant differences for Spd and C57BL/6J experiments, respectively ($\alpha = 0.05$). The Kolmogorov-Smirnov test was used for distributions.

RESULTS: Maternal exercise rescued bone mineralization and joint morphometry defects in homozygous Spd mutant embryos. Sham Spd embryos had significantly shorter humerus mineralization length and joint morphogenesis parameters (*e.g.*, lateral condyle height) than Sham WT controls. Exposing Spd embryos to maternal exercise rescued outcomes for bone and joint morphogenesis at E16.5 (Fig 1). Next, we evaluated the effects of maternal exercise in C57BL/6J mice at E17.5. Maternal exercise significantly increased mineralized length of the humeral primary ossification center, confirming the osteogenic effects of maternal exercise on developing WT embryos (Fig 2A). We also found significantly increased F-actin in the humerus primary ossification center, suggesting that maternal exercise enhances mechanoregulated bone development via cytoskeletal tension (Fig 2B). To evaluate the effects of physiology-mediated signaling, we first measured the FW:PW ratio, a measure of placental transport efficiency.⁵ Maternal exercise increased FW:PW, suggesting increased placental transport efficiency (Fig 3A). However, maternal exercise did not significantly enhance placental levels of IGF-1, the major regulator of placental nutrient transporter expression⁵ or amino acid and fatty acid transporter expression (*i.e.*, FATP4 and SNAT4, respectively) (Fig 3B,C).

DISCUSSION: Fetal akinesia affects 1 in 3000 live births. Prenatal screens for clinical conditions that cause fetal akinesia can identify at-risk pregnancies, but current treatments are limited to postnatal intervention (*e.g.*, physical therapy, surgery) and cannot reverse the debilitating skeletal deformities. Herein, we show that maternal exercise can function as a non-invasive, *in utero* therapeutic intervention to prevent fetal akinesia-induced skeletal deformities. Overall, our results show that maternal exercise enhances fetal skeletal development through a mechanism that likely involves both direct mechanical stimulation, consistent with our prior studies,⁶ and maternal-placental transport. While we did not observe effects of exercise on the primary regulators of placental transport *per se*, maternal exercise may impact hormones and growth factors that pass to the fetus and regulate osteogenesis.⁷ Future studies will elucidate the underlying cellular and molecular mechanisms.

SIGNIFICANCE: Maternal exercise may function as a non-invasive, *in utero* therapeutic to treat the effects of fetal akinesia on skeletal development. Additionally, maternal exercise may represent a tractable model for studying developmental mechanobiology *in vivo*.

REFERENCES: [1] Nowlan+ *Eur Cell Mater* 2015; [2] Palacios+ *Teratology* 1990; [3] Ahmed+ *R Soc Open Sci* 2023; [4] Bober+ *Development* 1994; [5] Brett+ *Int J Mol Sci* 2014; [6] Collins+ *Dev Cell* 2023; [7] Babey+ *Nature* 2024

ACKNOWLEDGEMENTS: Work supported by the ERC EU’s Seventh Framework Program [336306], NICHD [R01 HD113596], Penn IRACDA [NIH K12GM081259], Penn Center for Musculoskeletal Disorders [NIH P30-AR069691], and Penn Center for Undergraduate Research and Fellowships.

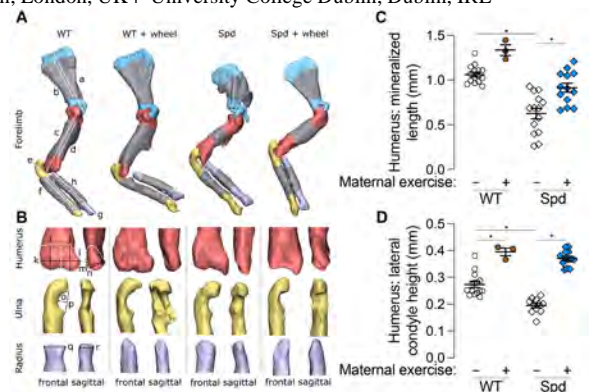


Figure 1. Maternal exercise rescues the effects of fetal akinesia-induced skeletal deformities. (A,B) Optical projection tomography reconstructions showing forelimb morphogenesis. (C,D) Quantifications of humerus mineralized length and lateral condyle height. * = $p < 0.05$.

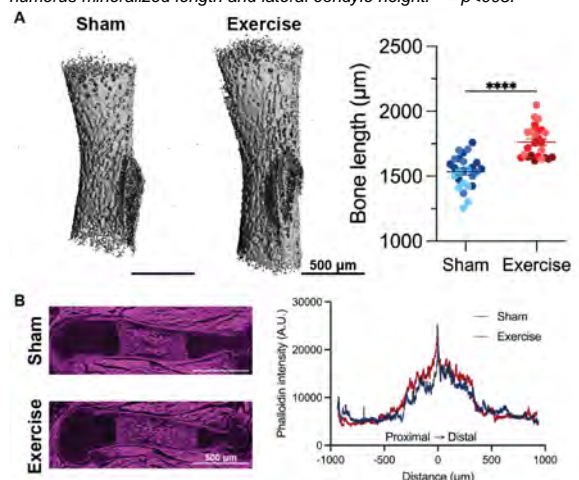


Figure 2. Maternal exercise promotes osteogenesis in WT mice. (A) μ CT reconstructions of the humerus with bone length quantification. **** = $p < 0.0001$. (B) Phalloidin staining with intensity quantification.

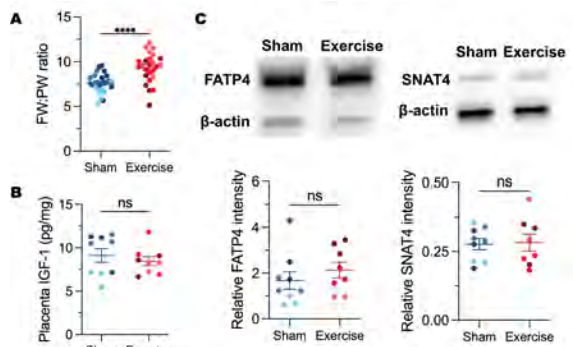


Figure 3. Maternal exercise affects placental transport efficiency, but not nutrient transporter expression. (A) Fetal weight to placental weight (FW:PW) ratio. **** = $p < 0.0001$. (B) Normalized IGF-1 expression. (C) Western blots for FATP4 and SNAT4 with quantifications.

Diabetes Enhances Periodontitis Through Akt1

Lauren Paschall, Xin Huang, Min Liu, John Park and Dana T. Graves, DDS
School of Dental Medicine, University of Pennsylvania

Introduction: Diabetes mellitus is a prevalent metabolic disorder that affects millions of people worldwide. It is well documented that diabetic conditions can exacerbate periodontal diseases through heightened inflammatory responses, leading to alveolar bone loss and eventual tooth loss¹. Dendritic cells, as pivotal modulators of immune responses, are implicated in the pathogenesis of diabetes-induced periodontitis². The serine/threonine kinase AKT plays a critical role in regulating the development and function of various immune cells, including dendritic cells³. This study aims to elucidate the role of dendritic cells in diabetes-associated periodontitis by specifically deleting AKT in these cells under diabetic conditions, thereby investigating the impact on dendritic cell-mediated immune responses.

Methods: Micro CT analysis is an effective technology of nondestructive 3D imaging and material characterization at the tiny level. A good experimental design is essential for getting accurate and dependable results from micro-CT analysis. Sample preparation, scanning conditions, and image processing techniques are all important factors to consider when designing experiments. Choosing the right resolution and contrast levels is critical for capturing the necessary details without sacrificing data quality. Three mouse groups are compared in this study: Normal, Diabetic, and Diabetic AKT1^{-/-}. Diabetes was induced by streptozotocin and compared to control mice that were injected with vehicle alone instead of streptozotocin. The AKT1 gene was deleted in one of the diabetic groups in dendritic cells by CD11c mediated Cre recombinase. Periodontitis was induced by oral inculcation of bacteria, *P. gingivitis* and *F. nucleatum*. Bone loss was measured by microCT.

Results: The results indicate that diabetes had a trend to increase bone loss and significantly reduced bone volume in the bone surrounding teeth ($P < 0.05$). The loss of bone was blocked by Akt1 deletion in dendritic cells ($P < 0.05$). The results suggest that dendritic cells are activated by diabetes and contribute to the reduced periodontal bone associated with diabetes.

References: 1) Taylor, G. W., Burt, B. A., Becker, M. P., Genco, R. J., Shlossman, M., Knowler, W. C., & Pettitt, D. J. (1996). Non-insulin dependent diabetes mellitus and alveolar bone loss progression over 2 years. *Journal of Periodontology*, 67(10), 1085-1093
2) Chen, L., Shen, S., & Mo, J. (2012). The Role of Dendritic Cells in Periodontal Disease. *International Journal of Oral Science*, 4(3), 131-137
3) Zhang Y, Wang X, Yang H, Liu H, Lu Y, Han L, Liu G (2013). Kinase AKT controls innate immune cell development and function. *Immunology*, 140(2),

Acknowledgements: Thank you, Tarence Smith, and Dr. Shuda, to offer me with the opportunity to participate in this internship, which allowed me to form new friends and have a better grasp of career goals and science than I had previously. I would want to thank John Park and Dr. Graves lab throughout my time in the lab, teaching me all the lab skills I know and making this a wonderful and fun experience.

Naproxen may increase bone stress fracture risk and decrease fracture healing

Alexandra Ciuciu, Ryan E. Tomlinson
Thomas Jefferson University, Philadelphia, PA

Highly active individuals commonly take non-steroidal anti-inflammatory drugs (NSAIDs) to relieve musculoskeletal pain and maintain consistent performance. These same individuals are inherently at risk of bone stress fractures due to frequent and repetitive exercise. Growing evidence in humans shows a correlation between frequent NSAID use and a higher stress fracture incidence, so we sought to understand the mechanism behind NSAID effects on bone. We previously reported that adult C57BL/6J females treated with naproxen, the active ingredient in the NSAID Aleve®, for 15 days had diminished bone toughness, load-induced bone formation, and decreased woven bone volume in fatigue fracture calluses. Our current work expands on these findings using the Ptgs2-Y385F, or “mutated”, mouse that features an amino acid substitution in its cyclooxygenase 2 (COX2) protein which mimics a

COX2-specific NSAID’s mechanism of action. To determine COX2-dependent and -independent effects of naproxen on bone, we provide these mutated mice and their wild-type (WT) littermates either vehicle (H₂O) or naproxen (10.9 mg/kg) drinking water for 15 or 30 days. For the 15-day cohort, mice received six bouts of uniaxial forelimb compression using a 2 Hz rest-inserted sinusoidal waveform of 3N for 100 cycles per bout. Calcein and alizarin red were injected on days 5 and 12 respectively. At experimental end, both forelimbs were harvested, fixed, embedded in PMMA, sectioned using a low-speed saw, and imaged using confocal microscopy. Also, right femurs were collected, stored in PBS-soaked gauze at -20°C, scanned using microCT, and mechanical properties were tested using standard three-point bending. Our results demonstrate that WT, but not mutated mice, of both sexes had decreased load-induced bone formation on the periosteal surface (loaded bone formation rate per bone surface was decreased by 28% in treated WT compared to vehicle WT in a two-way ANOVA comparison; two-way ANOVA interaction between genotype and treatment $p=0.029$). This suggests that naproxen decreases strain-adaptive bone remodeling through its known inhibition of COX2, decreasing prostaglandins like prostaglandin E2 (PGE2) that affect load response in bone. Additionally, three-point bending of non-loaded femurs revealed that naproxen treatment for 15 days significantly decreased bone toughness, or resistance to fracture, across sexes and genotypes without significant changes in bone geometry (-25% in Ptgs2-Y385F; -26% in WT; $p<0.0001$ by two-way ANOVA). This suggests a COX2-independent effect of naproxen on bone’s resistance to fracture that is separate from naproxen’s known decrease of strain-adaptive bone remodeling. For the 30-day cohort, mice were pre-treated with vehicle or NSAID in their drinking water for 15 days and were then subjected to a forelimb fatigue injury on day 15. After injury, mice were returned to normal cage activity and continued their drinking water treatment until harvest. Both forelimbs were harvested, stored in PBS-soaked gauze at -20°C, then scanned by microCT. Analysis of the fracture callus revealed that female mice of both genotypes had significantly decreased woven bone volume with naproxen treatment, but males were not affected similarly (-36% in Ptgs2-Y385F; -22% in WT; $p=0.021$ by two-way ANOVA). This result demonstrates that naproxen may have a sex-specific, COX2-independent effect on stress fracture healing. Finally, non-loaded femurs from the 30-day cohort were collected, fixed, decalcified, embedded in OCT, sectioned, and stained with phalloidin for F-actin and DAPI for nuclei. Imaging at 63X using confocal microscopy revealed differences in the dendritic network due to naproxen that were present in females, but not males, of both genotypes (two-way ANOVA interaction between genotype and treatment $p=0.039$). As osteocytes contribute to whole bone changes, these effects on the network could change bone toughness and require further investigation. Together, these results reveal several mechanisms through which naproxen may increase stress fracture risk by decreasing skeletal resistance to fracture and healing.

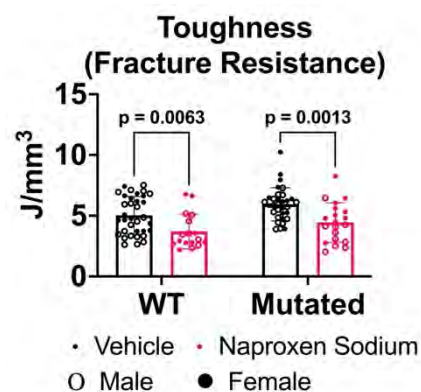


Figure 1: 15 days of naproxen treatment decreases average bone toughness in male and female WT and mutated mice.

Heterotopic Ossification Quantifications in a Pdgfra-FOP (Fibrodysplasia Ossificans Progressiva) Mouse Model

Fatoumata Diarra, Loreilys Mejias Rivera, Eileen M. Shore, Ph.D.

Department of Orthopaedic Surgery and Center for Research in FOP and Related Disorders

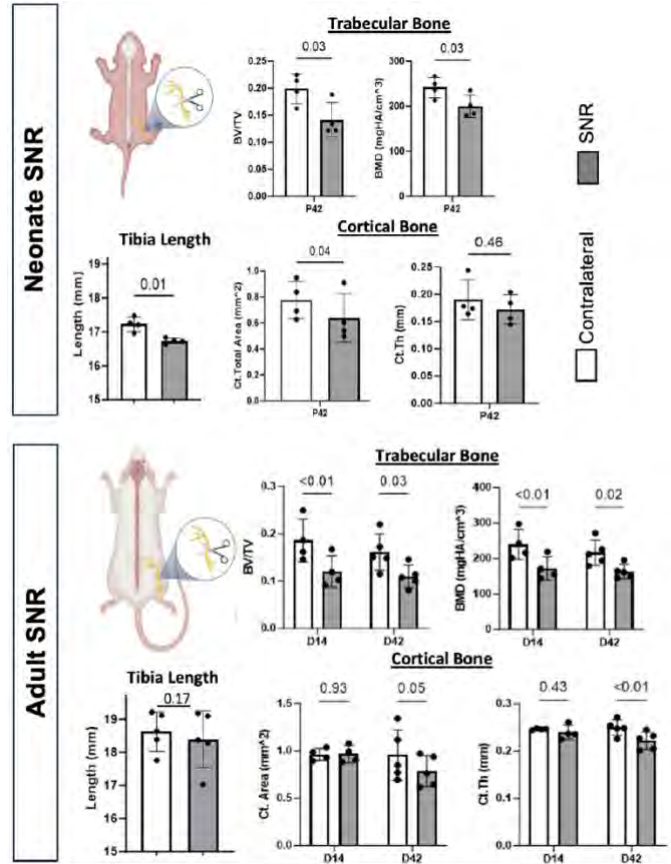
Introduction: Fibrodysplasia Ossificans Progressiva, or FOP, is a rare genetic bone disorder that affects one in a million people worldwide and often hinders one's ability to do normal activities such as movement. This disorder is caused by a missense mutation in the ACVR1 gene (ACVR1^{R206H/+}) that is responsible for the formation of the extra bone structures called heterotopic ossification or HO, due to an injury or spontaneously. HO can be found in places such as tendons, skeletal muscles, and ligaments. The cells that give rise to HO within skeletal muscle are called Fibro-adipogenic progenitors or FAPs.

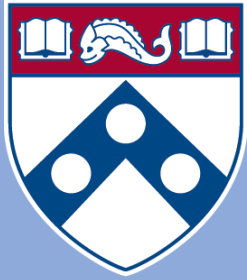
FAPs are multipotent mesenchymal cells that are able to differentiate to multiple lineages. FAPs have a crucial role within the skeletal muscles as they support proper muscle regeneration and send out signals to guide the repair program. As FAPs are a major cell-of-origin of HO in FOP, we developed a FAP-targeting FOP mouse model to further study FAP-specific changes to muscle regeneration and how this leads to HO formation.

Reduced loading after sciatic nerve resection impairs hindlimb growth

Talayah A. Johnson¹, Natalie Fogarty², Alisia Lin¹, Tonia K. Tsinman¹, Xi Jiang¹, Eiki Koyama¹, Lin Han², Josh R. Baxter¹, Joel D. Boerckel¹, Robert L. Mauck¹, Nathaniel A. Dyment¹. ¹University of Pennsylvania, Philadelphia, PA ²Drexel University, Philadelphia

Mechanical forces influence the growth and maintenance of musculoskeletal tissues. By understanding the role of mechanical loading on developmental processes of load bearing tissues, specifically the mechanosignaling events that drive tissue formation and maturation, we can potentially leverage this knowledge to guide new regenerative strategies. We performed unilateral sciatic nerve resection (SNR) in both neonatal (surgery performed on postnatal day 1) and adult (surgery performed at 22 weeks of age) mice to explore how reductions in loading differentially impact the growth and maintenance of hindlimb load bearing tissues. We used video gait analysis to assess limb kinematics, μ CT to assess trabecular and cortical bone parameters, and cryohistology to assess tendon morphology. SNR limbs exhibited sustained gait abnormalities compared to contralateral limbs, including reduced paw print width (a hallmark of sciatic denervation), increased ankle dorsiflexion and reduced hock height ($p < 0.01$). SNR yielded marked alterations in bone parameters at both ages with neonatal limbs having reduced tibial length, trabecular BV/TV, trabecular thickness, and cortical area ($p < 0.05$), and adult limbs having reduced trabecular BV/TV, BMD, trabecular number, and trabecular thickness ($p < 0.05$). As expected, SNR did not alter tibial length in adults. Interestingly, SNR did not alter cortical bone parameters at 14 days post-surgery (D14) but did result in reduced cortical area and cortical thickness by D42 ($p < 0.05$) in the adult group. The differences in the onset of bone loss between trabecular and cortical bone corroborate trabecular bone being more sensitive to altered loading. The differential effects of loading on tissues were also exemplified in tendons where neonatal SNR significantly decreased Achilles tendon cross sectional area (CSA) at postnatal day P14 and P42 ($p < 0.05$, $p < 0.01$), but SNR had much less of an effect on adult tendons. SNR reduced the growth rates of the affected limb in the neonates, resulting in reduce bone and tendon sizes. In contrast, the decrease in bone volume in the adult SNR group appears to be the result of disturbed remodeling processes and increased bone resorption, which is currently being analyzed. Thus, we provide a useful model for understanding the role of mechanical loading in the development of load-bearing tissues, and our data shed light on the mechanisms by which mechanical forces control postnatal hindlimb development and growth.





Penn Center *for*
Musculoskeletal Disorders

UNIVERSITY *of* PENNSYLVANIA

Biomechanics Core Abstracts

Tendon Loads Measured over 2 Weeks of Daily Living are Associated with Achilles Tendinopathy Patient Outcomes

*Ke Song¹, Michelle P. Kwon¹, Andrew K. Smith², Karin Grävare Silbernagel², Josh R. Baxter¹
¹University of Pennsylvania, Philadelphia, PA, ²University of Delaware, Newark, DE
 *Email of Presenting Author: ke.song@pennmedicine.upenn.edu

DISCLOSURES: Ke Song (N), Michelle P. Kwon (N), Andrew K. Smith (N), Karin Grävare Silbernagel (N), Josh R. Baxter (N).

INTRODUCTION: Achilles tendinopathy is a debilitating chronic condition prevalent in physically active adults [1]. Exercise rehabilitation can effectively reduce symptoms in a short term [2], yet long-term outcomes vary greatly among patients [3] as 35–60% still experience pain and up to 50% seek alternative treatments including surgery [4,5]. A major challenge for improving rehabilitation outcomes is to determine the cumulative effects of tendon loading due to exercises and patient-specific daily living. The purpose of our study was to develop a strategy to measure cumulative tendon loads in Achilles tendinopathy patients and determine their associations with patient outcomes and characteristics including age, severity of tendinopathy, and self-reported activity level.

METHODS: We enrolled 8 patients diagnosed with Achilles tendinopathy and 3 pain-free controls after informed consent in this IRB-approved study. We continuously measured loads in each patient’s most painful tendon (random side for controls) over a 2-week span using an instrumented force-sensing insole (Loadsol) and a physics-based algorithm [6]. We computed cumulative tendon loads over the entire monitoring period above 2 pre-defined thresholds: “overall” load as ≥ 0.3 body weight (\times BW) that results from any non-trivial daily living activities [7], and “high” load as $\geq 3.0 \times$ BW which is above walking level and thus primarily due to dynamic exercises [7]. We computed cumulative loading time as the total time when tendon load is over the overall and high thresholds, and cumulative loading impulse as the integral of overall and high load over their cumulative loading time (Figure 1, insets). We defined overall cumulative loading time ($\geq 0.3 \times$ BW) as the “Total Active Hours”, and normalized the overall and high cumulative loading impulse by Total Active Hours to control for the variable total periods that participants wore the instrumented insole. We also normalized high loading time by Total Active Hours to represent the percentage of time when the tendon was loaded above a high level. To determine whether these 3 normalized metrics (overall and high loads per Active Hour; percentage of time over high load) are associated with patient outcomes, we calculated Pearson correlations between these metrics and participant age, self-reported severity of Achilles tendinopathy [8], and a self-reported current Physical Activity Scale (PAS) [2]. We defined a correlation coefficient of $|r| \geq 0.7$ as strong, 0.4 – 0.7 as moderate, and 0.1 – 0.4 as weak [9]. We combined data from the patients and controls for these preliminary analyses (n = 11).

RESULTS: 11 participants (age: 43.5 ± 17.2 y/o, BMI: 30.5 ± 7.0 kg/m²) logged insole data over 10.3 ± 2.3 days (range: 6 – 13), capturing 21.4 ± 9.5 Total Active Hours (11.6 – 46.9) and cumulating $23.5 \pm 11.3 \times$ BW*hours of overall tendon loading impulse (9.8 – 53.5). As a subset of overall load, participants had highly variable high loading time (0.9 ± 0.9 hours, 0 – 2.4) and impulse ($3.2 \pm 3.3 \times$ BW*hours, 0 – 9.3). Per Active Hour, participants cumulated $1.10 \pm 0.17 \times$ BW of overall load (0.82 – 1.28) and $0.14 \pm 0.12 \times$ BW of high load (0 – 0.38). Percentage of time over high load was $3.8 \pm 3.1\%$ (0 – 10.0). Overall load per Active Hour was weakly correlated to age ($r = -0.247$) and severity of tendinopathy ($r = 0.367$), and moderately to self-reported activity level ($r = 0.458$, Figure 1, left). In contrast, reduced high load per Active Hour was strongly correlated to older age ($r = -0.733$) and a lower self-reported activity level ($r = 0.705$, Figure 1, center), while moderately correlated to more severe tendinopathy ($r = 0.548$). Likewise, a lower percentage of time over high load was strongly correlated with older age ($r = -0.744$) and less self-reported activities ($r = 0.707$, Figure 1, right) and moderately with disease severity ($r = 0.558$).

DISCUSSION: Our study is the first we know to experimentally measure Achilles tendon loads during daily living over a weeks-long duration. While the cumulative loading time and impulse are confounded by the inherent variability of data amount available, they also denote the variation of real-world tendon loading profiles due to patient-specific characteristics (age), lifestyles (activity level), and tendon health (severity of tendinopathy). The associations between measured cumulative tendon loads and patient outcomes became more pronounced when loading time and impulse were normalized by Total Active Hours. We found that reduced cumulative high Achilles tendon loads are associated with older age, more severe tendinopathy, and more sedentary lifestyle (Figure 1, center and right). Measured cumulative tendon loads generally matched both self-reported activities and tendon health status. For example, among the 4 individuals who reported the highest current activity level (PAS = 6), the 2 patients had less cumulative high load than the 2 controls. Although preliminary, our data also reveal links between sensor metrics and daily living events, as the patient who cumulated more high load (PAT008, yellow marker) frequently self-reported running via daily text surveys, while the other patient (PAT002, teal marker) did not. Our ongoing research is recruiting a larger homogeneous patient cohort to explicitly define how cumulative tendon loads throughout patient-specific daily living influence the biological health of the Achilles tendon.

CLINICAL RELEVANCE: Tendon loading during daily living is a major contributor to Achilles tendinopathy. Our results confirm the clinical benefits of using self-reported activities and disease severity to guide exercise rehabilitation, while also establishing a rigorous strategy to quantify cumulative Achilles tendon loads throughout daily living. Our wearable sensing paradigm provides clinicians with a powerful tool to identify unique loading profiles that govern patient-specific outcomes, customize rehabilitation exercises, and monitor their impacts out of the clinic to promote the therapeutic effects of tendon loading.

REFERENCES: [1] Shaikh+ *IJSM* 2012. [2] Silbernagel+ *AJSM* 2007. [3] Woodley+ *BJSM* 2007. [4] Silbernagel+ *AJSM* 2011. [5] van der Plas+ *BJSM* 2012. [6] Hullfish+ *Gait Posture* 2020. [7] Baxter+ *MSSE* 2020. [8] Robinson+ *BJSM* 2001. [9] Schober+ *Anesth Analg* 2018.

ACKNOWLEDGEMENTS: Funding for this study was supported by the National Institutes of Health R01AR078898, P50AR080581, and R01AR072034.

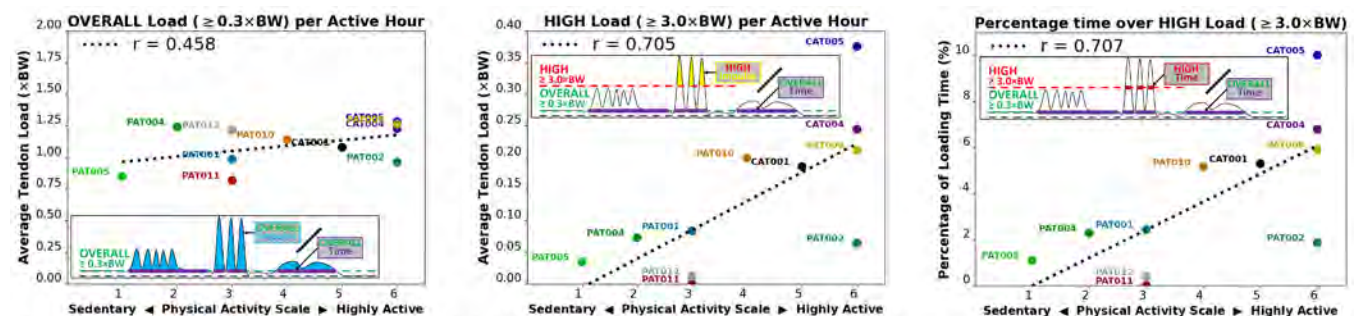


Figure 1. Self-reported activity level vs. normalized Achilles tendon loads measured over 2 weeks of force-sensing insole monitoring: (left) overall tendon load ($\geq 0.3 \times$ BW) per Active Hour, (center) high load ($\geq 3.0 \times$ BW) per Active Hour, and (right) percentage of time over high load. Cumulative high load showed stronger correlations ($r > 0.7$) to self-reported activity level than overall load likely because it varied more substantially among individuals due to occupations and lifestyles. Each marker represents a patient (PAT) or control (CAT). Inset diagrams depict the definitions of each normalized load metric.

Achilles subtendon morphology identified via isolated muscle stimulations is sensitive to ankle angle

Kathryn S. Strand¹, Todd J. Hullfish¹, Maggie M. Wagner¹, Josh R. Baxter¹

¹University of Pennsylvania, Philadelphia, PA
strandk@seas.upenn.edu

Disclosures: None

INTRODUCTION: The Achilles tendon (AT) consists of three distinct fascicle bundles called subtendons, each corresponding to a head of the triceps surae muscles: the lateral gastrocnemius (LG), medial gastrocnemius (MG) and soleus. In a healthy AT, these subtendons deform relatively independently of each other – often described as subtendon ‘sliding’ [1], [2]. In contrast, injured tendons exhibit more uniform displacement, suggesting reduced sliding may impact plantar flexor function [3]. However, current techniques that identify subtendon morphology in vivo are still being refined, and strategies to safely and reliably evaluate subtendon structure throughout tendon healing are lacking. Ultrasound is a widely available and effective modality for imaging the AT, and recent work has applied it in conjunction with neuromuscular electrical stimulation (NMES) to activate individual triceps surae muscles and monitor the corresponding displaced regions within the AT to identify separate subtendons [2], [4]. Using these methodologies, the objective of this study was to evaluate the repeatability of our automated point-tracking tool to identify individual Achilles subtendons and assess the effect of ankle angle on subtendon location. We hypothesized that this tool reliably ($ICC > 0.67$) identifies localized regions of tendon displacement in healthy subjects across separate testing sessions and that subtendon location within the AT would change with ankle angle, which is an important clinical parameter during tendon healing.

METHODS: Eight healthy participants (4M, 4F) provided written informed consent to participate in this IRB approved study. We measured subtendon displacement by stimulating the medial or lateral gastrocnemius muscle in isolation as described by Klaiber [4]. Briefly, participants lay prone with their leg fully extended. We acquired axial ultrasound videos using a 24 MHz linear ultrasound probe (L6-24, GE LOGIQ) positioned 3 cm proximal to the medial malleolus and perpendicular to the AT. Simultaneously, we delivered pulse trains (30 Hz, 400 μ s pulse width, 1 s duration) through hydrogel electrode pairs placed 2 cm apart over the muscle bellies until movement in the AT was visible via the ultrasound video [3]. We performed this testing with the ankle in neutral and 20° plantar flexion at the same stimulation amplitude. This protocol caused negligible plantar flexor torques (mean: 0.662 Nm), demonstrating safety for future use in clinical populations. We repeated this protocol on a separate day to test repeatability. We processed experimental data using custom scripts (MATLAB, R2024a) to determine the displaced regions of the tendon during each muscle stimulation. We manually selected the tendon cross-sectional area from the first ultrasound frame as the tracking region of interest (ROI) and used a Kanade-Lucas-Tomasi point tracking algorithm to identify the displacement of 700 corner point eigenvalues within this ROI. We isolated points with cumulative displacements greater than the third quartile across the ROIs to calculate the area and position of each subtendon (Fig. 1A). Intraclass Correlation (ICC) coefficients were calculated with a two-way random-effects model to establish inter-session measurement reliability. Subtendon location and displacement between ankle positions was compared using paired t-tests or Wilcoxon signed rank tests. We quantified muscle activation by calculating peak root-mean-square (RMS) values from electromyography (EMG) recordings collected from the three plantar flexor muscles during the stimulations and compared them using a Friedman’s test. Significance levels were set to $p < 0.05$.

RESULTS: Subtendon morphology was more reliably measured across sessions with the ankle in neutral under nominal load compared to the ankle in unloaded plantar flexion (Table 1). Ankle positioning also affected LG and MG subtendon location. We found that the LG was more lateral ($p < 0.0001$) and the MG was more medial ($p = 0.0216$) in neutral compared to plantar flexion (Fig. 1B). Both subtendons were located more posterior in neutral ($p < 0.05$) than in plantar flexion (Fig. 1C). Plantar flexion increased subtendon displacements compared to the neutral position ($p < 0.0001$). Stimulating a single gastrocnemius muscle caused detectable EMG measurements at the soleus muscle and the adjacent gastrocnemius (Fig. 2). This muscle cross-talk was greater at the adjacent gastrocnemius than the soleus ($p < 0.0001$), and was also more pronounced when stimulating the MG compared to the LG.

DISCUSSION: This NMES and ultrasound imaging paradigm identifies AT subtendon locations that correspond to the relative anatomical locations of the MG and LG muscles and agree with previous in-vivo and cadaveric studies [3], [5]. The larger displacements detected in plantar flexion agree with prior findings [2] and are likely due to decreased tension within the tendon. This decreased tension as well as the twisted structure of the AT may cause out-of-plane tendon motion not captured via ultrasound, contributing to the weaker ICC values in plantar flexion. These results also support performing this method with nominal tendon strain, which should be carefully considered when evaluating healing tendons that are not mechanically stable (for example, patients <8 weeks post-Achilles rupture). The increased co-activation of the LG during MG stimulations may also explain the weaker ICC values of MG subtendon measurements. This co-activation is likely due to electrical conduction along superficial tissues and may be reduced with targeted nerve stimulation at the innervation site rather than the muscle belly.

SIGNIFICANCE/CLINICAL RELEVANCE: This work provides new guidelines to quantify Achilles subtendon structure and ensure reliable and safe patient evaluations. Future applications of this method can elucidate changes in subtendon structure in different AT pathologies including rupture and tendinopathy. It can also reveal whether certain subtendon morphologies correlate with higher pathology risk, providing valuable insight into the mechanisms behind AT injuries.

REFERENCES: [1] Clark et al. (2018) PeerJ. [2] Lehr et al. (2021) J. Exp. Biol. [3] Khair et al. (2022) J. Appl. Physiol. [4] Klaiber et al. (2023) Clin. Biomech. [5] Pekala et al. (2017) Scand J Med Sci Sports.

ACKNOWLEDGEMENTS: This work was supported by NIH/NIAMS P50AR080581.

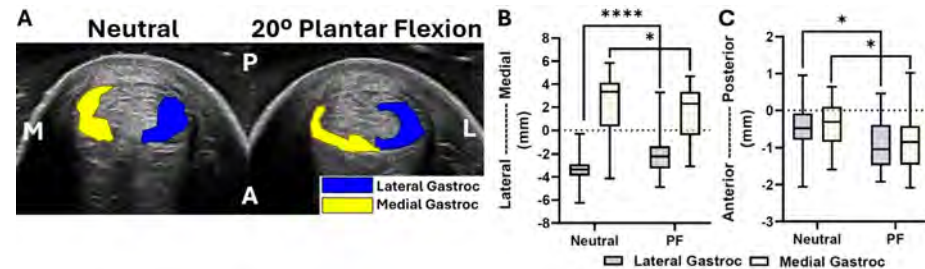


Figure 1. A) Representative subtendon regions identified via point tracking with the ankle in neutral (left) and plantar flexion (right). B) Medial-lateral and C) and anterior-posterior locations of the LG and MG subtendons in neutral and plantar flexion relative to the AT centroid (dotted lines). * $p < 0.05$, **** $p < 0.0001$.

Table 1. ICC values for subtendon measurements.

Measurement	Neutral	Plantar Flexion
AT area	0.826	0.436
LG area	0.616	0.163
MG area	0.722	0.124
LG medial-lateral position	0.889	0.701
LG anterior-posterior position	0.573	0.0849
MG medial-lateral position	0.486	0.0424
MG anterior-posterior position	-0.0345	-0.439

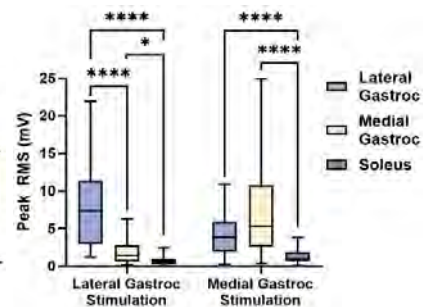


Figure 2. Peak RMS of the triceps surae muscles during stimulations of each gastrocnemius. * $p < 0.05$, **** $p < 0.0001$.

Methodologies for Testing Tendons

Mariacristina Calcagno, Maggie Tamburro, Nat Thurlow, Louis Soslowsky
McKay Orthopaedic Research Laboratory, University of Pennsylvania, Philadelphia, PA

INTRODUCTION: Tendons are fibrous tissues that attach muscle to bone and bear mechanical forces, preventing injury during movement. For example, the patellar tendon (PT) connects the patella to the tibia (for knee extension), and the Achilles tendon (ACH) connects the gastrocnemius to the calcaneus (facilitating plantar flexion of the foot). Tendons are composed of collagen (65-80% of dry mass); collagen fibers align lengthwise. One to two percent of a tendon's dry mass is elastin [1]. This composition yields flexibility and high tensile strength [2]. Tendon properties can be assessed through various methods.

METHODS: The following techniques were executed using mouse tendons.

- 1) **Functional Assessment:** In this assessment, the tendon is stretched vertically (uniaxially) until snapping point using an Instron machine. The first step is to dissect the tendon from a mouse, ensuring it remains moist throughout the dissection process (by spraying it with PBS). After dissection, the tendon is stained with Verhoeff's stain; stain lines are used to analyze strain optically after testing. The PT is stamped to create a "dog bone" shape to reduce stress concentrations and is then potted to prevent slipping while testing in the Instron; the ACH is sandpapered with glue to prevent slipping. The tendon is then loaded into the Instron machines using a custom protocol. As the strain on the tendon increases, images are captured to analyze the tendon's progress until the breaking point.
- 2) **Cross-Sectional Area (CSA):** CSA is valuable in determining relationships between certain tendon qualities, such as Young's modulus. Several techniques exist to measure CSA, such as gravimetric analysis and area micrometer method. However, these techniques are prone to error or cause tendon damage [3]. CSA can be determined using a GiSMO machine, a laser-based device that the tendon passes under while lying flat.
- 3) **Structural Assessment (Histology):** Tendon morphology/cellularity can be determined by staining the tendon with hematoxylin and eosin. The tissues are dehydrated, coated in paraffin, and sectioned before staining. In images, the dark pink tone indicates muscle; the light pink tone indicates tendon; and the purple tone indicates cell nuclei.

RESULTS: The above procedures yielded quantities for properties such as the cross-sectional area, the maximum force sustained, the maximum displacement reached, the stiffness, and the value for Young's modulus of the PT and ACH tendons.

DISCUSSION: Ultimately, techniques like the ones detailed above provide quantitative and qualitative data that can be used to determine the effects of certain variables on tendons (ex., age, variation in collagen makeup, physical exertion, injury, etc.). In recent years, over 30 million people in the United States have experienced tendon injury [4]; knowledge of such properties under various conditions can advance clinical practices in tendon care and orthopedics.

ACKNOWLEDGEMENTS: Thank you to Perelman's Office for Outreach, Education, and Research, especially Mr. Tarence Smith and Dr. Jamie Shuda.

[1] Rajpar, I., & Tomlinson, R. (2022). Function of peripheral nerves in the development and healing of tendon and bone. *Seminars in Cell & Developmental Biology*, 123, 48-56. <https://doi.org/10.1016/j.semdb.2021.05.001>. [2] Thorpe, C. T., & Screen, H. R. (n.d.). Tendon structure and composition. *Advances in Experimental Medicine and Biology*, 920. https://doi.org/10.1007/978-3-319-33943-6_1. [3] Ge, X., Zhang, L., Xiang, G., Hu, Y.-C., & Lun, D.-X. (2020). Cross-Sectional area measurement techniques of soft tissue: A literature review. *Orthopaedic Surgery*. <https://doi.org/10.1111/os.12757>. [4] Ellis, I., Schnabel, L., & Berglund, A. (2022). Defining the profile: Characterizing cytokines in tendon injury to improve clinical therapy. *Journal of Immunology and Regenerative Medicine*, 16. <https://doi.org/10.1016/j.regen.2022.100059>.

A Novel Approach to Annulus Fibrosus Repair via Streptavidin Functionalized Hydrogels

Emily E. Sharp^{1,3}, Lorielle Laforest², Yuqi Zhang^{1,2}, Karen L. Xu^{1,2}, Jason A. Burdick⁴, Robert L. Mauck^{1,3}, and Sarah E. Gullbrand^{2,3}

¹Dept. of Bioengineering, ²Dept. of Orthopaedic Surgery, University of Pennsylvania, Philadelphia, PA, ³Translational Musculoskeletal Research Center, Corporal Michael J. Crescenz VA Medical Center, Philadelphia, PA, ⁴BioFrontiers Institute and Dept. of Chemical and Biological Engineering, University of Colorado, Boulder, CO

Disclosures: RLM (4, 5, 8 – Mechano-Therapeutics, 4Web, and JOR Spine), SEG (6- DiscGenics and Zurimed)

INTRODUCTION: Intervertebral disc (IVD) herniations, where the nucleus pulposus (NP) extrudes beyond the boundaries of the annulus fibrosus (AF), disrupts IVD mechanical function and results in significant pain for patients. The gold standard of care, microdiscectomy, is effective in relieving the immediate symptoms of herniation, however, long-term outcomes can be poor, with patients experiencing as much, if not more, pain at one-year compared to those who did not undergo microdiscectomy.¹ Moreover, microdiscectomy does not restore the mechanical integrity of the AF, allowing for reherniations to occur through the unrepaired defect, and it does not address the inflammatory cascade that accompanies herniation and complicates endogenous healing.² A variety of biomaterial-based strategies for AF repair have been explored in recent years, but generally lack functionality for therapeutic delivery.^{3,4} We developed a norbornene-modified hyaluronic acid (NorHA) hydrogel that satisfies AF repair criteria (biocompatible, injectable, mechanical compatibility)⁵ and is capable of spatiotemporal controlled delivery via secondary reactions between the hydrogel and a desired therapeutic (drug, biologic, nanocarrier, etc.). This delivery system employs biotin-streptavidin chemistry, where the hydrogel is modified with streptavidin and the desired therapeutic is modified with biotin. Here, we evaluated the effect of NorHA functionalization, durability of the biotin-streptavidin reaction with time *in vitro*, and the behavior of the hydrogel *in vivo*.

METHODS: Hydrogel Synthesis and Functionalization: NorHA synthesis and hydrogel fabrication were accomplished using established protocols.⁶ Percent crosslinking was 50% and weight percent was 3% (unless otherwise specified). NorHA functionalization was achieved by incorporating thiol-streptavidin (TS) into the precursor solution. Percent functionalization is referred to in units of TS where 1 unit is roughly equivalent to 3.3% functionalization. Upon UV exposure, hydrogel photocrosslinking and streptavidin functionalization occur simultaneously. **Mechanical Characterization:** 3 and 5 wt% hydrogels with varying degrees of TS functionalization (3, 6, and 9 TS) were tested using a stress relaxation protocol (10% strain at 0.05%/s followed by stress relaxation for 10 min) to determine equilibrium modulus. **Secondary Reaction Validation:** NorHA hydrogels with varying levels of functionalization (0, 3, 6, and 9 TS) were fabricated and allowed to swell overnight prior to being incubated in 30 μ M biotin-modified Cy5 fluorophore for 1 hour at room temperature. Hydrogels were then washed in PBS with 10% fetal bovine serum and 2% penicillin-streptomycin at 37°C overnight before imaging via AxioZoom microscope. Images were taken every 7 days, with media changed every 3-4 days for 4 weeks. Media was collected to measure fluorescence loss with time using a microplate reader. Images were quantified with ImageJ and NorHA fluorescent intensity values were subtracted out to account for non-specific fluorescence attachment at each timepoint. **In vivo Evaluation:** NorHA and NorHA-TS4 hydrogels were implanted subcutaneously into Sprague-Dawley rats for 7 and 28 days, monitoring hydrogel mechanical properties and retention of biotin-modified fluorophore to the hydrogels, as detailed previously. **Statistical Analysis:** All statistics were conducted in GraphPad Prism with a significance threshold of $p < 0.05$. Outliers were removed from each dataset and significant differences were detected using the appropriate ANOVA test.

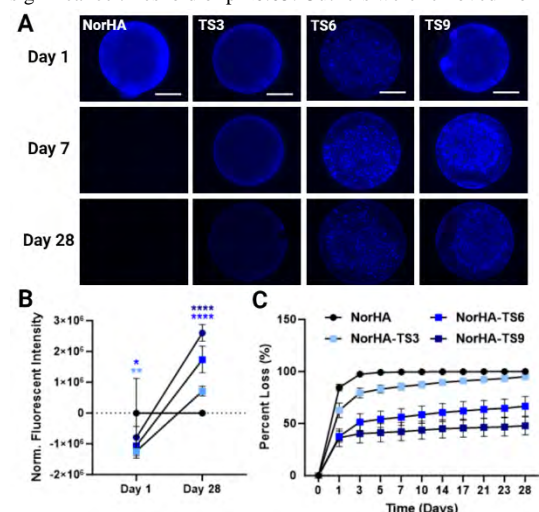


Figure 2: A) Biotin-Cy5 attachment to hydrogels with varying levels of TS functionalization (Scale = 2mm) and their B) normalized fluorescent intensity (with SD) and C) percent loss of fluorescence (with SEM). $n \geq 3$ hydrogels/group.

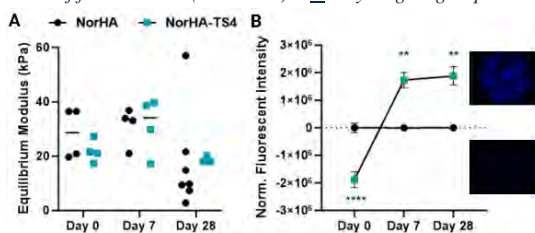


Figure 3: A) Changes in hydrogel mechanics and B) normalized fluorescent intensity with implantation time. $n \geq 3$ hydrogels/group.

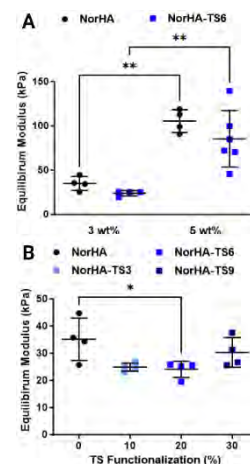


Figure 1: Mechanical characterization of hydrogels when varying A) weight percent and B) TS functionalization in 3 wt% hydrogels. $n \geq 4$ hydrogels/group.

RESULTS: As anticipated, the incorporation of TS did not significantly alter the mechanical properties of the hydrogels while still allowing for mechanical tunability via a change in weight percent (Fig. 1A). Varying the degree of TS functionalization at a constant weight percent did not meaningfully alter the mechanical properties of the hydrogel (Fig. 1B). After incubation in a biotin-modified fluorophore, NorHA hydrogels showed increased fluorescence at Day 1 compared to TS hydrogels but lost all fluorescence by Day 7 (Fig. 2A). Hydrogels with TS functionalization had stable attachment of the biotin-modified fluorophore for at least 28 days (Fig. 2A-B). Importantly, varying the degree of TS functionalization resulted in differential release of the biotin-modified fluorophore, with increased TS functionalization resulting in decreased percent loss at each timepoint (Fig. 2C). TS6 and TS9 hydrogels lost significantly less fluorophore into the washing media compared to non-modified controls across all time points, while fluorescence loss from TS3 hydrogels was not statistically significant from that of non-modified hydrogels at any timepoint. *In vivo* evaluation demonstrated that the mechanical properties of the hydrogels do not significantly change with implantation time, but there was a decreasing trend with time that suggests hydrogel degradation (Fig. 3A). As with *in vitro* examinations, TS hydrogels maintained their fluorophore attachment for 28 days *in vivo* compared to NorHA hydrogels (Fig. 3B).

DISCUSSION: NorHA hydrogels are promising candidates for tissue repair due to their injectability, biocompatibility, and biodegradability; yet are lacking in controlled delivery capacity. Here, we demonstrate that functionalization of NorHA hydrogels with TS does not adversely impact hydrogel mechanics or mechanical tunability. The addition of TS enables a strong, precise secondary reaction between the functionalized hydrogel and a biotin-modified fluorophore that is customizable based on the extent of TS functionalization and is stable both *in vitro* and *in vivo*. This suggests that this secondary reaction could be utilized to localize a therapeutic or delivery carrier to the hydrogel utilizing this same mechanism. Future work will evaluate how effective TS hydrogels are in the repair an AF defect under physiologic load *ex vivo* as well as more exhaustively characterize the attachment and subsequent release of a therapeutic using this delivery system prior to proceeding to additional *in vivo* evaluations.

SIGNIFICANCE: Our TS functionalized hydrogels have the potential to effectively repair the AF or other dense connective tissues through achieving spatiotemporal controlled delivery of a therapeutic to engage endogenous healing capabilities. Ultimately, this could transform clinical practice, creating superior surgical alternatives and outcomes for patients.

REFERENCES: 1. Weinstein, JN *et al.*, Spine (2008) 2. Peredo, AP *et al.* JOR Spine (2021) 3. Sloan, SR *et al.*, Sci. Trans. Med. (2020) 4. Panebianco, CJ *et al.* Euro. Cells & Mat. (2020) 5. Long, RG *et al.*, J Biomech. Eng. (2016) 6. Gramlich, WM, *et al.*, Biomaterials (2013)

Collagens V and XI Jointly Regulate Fibril Assembly and Elastic Mechanical Properties during Tendon Maturation

Nat A. Thurlow, Jeremy D. Eekhoff, Ashley K. Fung, Courtney A. Nuss, Stephanie N. Weiss, Nathaniel A. Dyment, Louis J. Soslowsky
McKay Orthopaedic Research Laboratory, University of Pennsylvania, Philadelphia, PA
nthurlow@seas.upenn.edu

Disclosures: None

INTRODUCTION: Tendon hierarchical structure is established during development through the coordinated assembly of matrix proteins, including minor fibril-forming collagens such as collagens V and XI. Collagen V influences collagen fibrillogenesis through nucleating fibril formation and co-assembling with collagens I and II¹, and lack of *Col5a1* expression leads to larger fibrils, reduced fibril density, and smaller tendon cross-sectional area². Collagen XI has a similar role in fibril regulation during development³ and co-assembles with collagen V to form heterotypic fibrils¹. The expression of genes for collagen V and XI is similar in developing tendons, but the expression of collagen XI encoding genes is decreased in mature tendons compared to collagen V genes. Moreover, in global knockdown mouse models, haploinsufficiency of both *Col5a1* and *Coll1a1* in tandem yielded more irregular fibril shapes and greater heterogeneity of fibril diameters in developing tendons than *Col5a1* haploinsufficiency alone¹. Together, these findings suggest interactive roles between collagens V and XI during development. However, the structural and functional deficits associated with coordinated knockdown of *Col5a1* and *Coll1a1* remain unknown. Since the tendon-specific compound *Col5a1*, *Coll1a1* knockout is postnatally unviable, the objective of this work was to assess the cooperative roles of collagens V and XI during fibril growth and assembly using a tendon-specific (ScxCre) compound *Col5a1* null, *Coll1a1* heterozygous mouse model. Based on prior work in tendons lacking *Col5a1* expression, we hypothesized that ScxCre;*Col5a1*^{flox/flox};*Coll1a1*^{flox/+} (VKO-XIHet) tendons would demonstrate structural changes consistent with aberrant fibril growth.

METHODS: Animals: Male and female postnatal day 30 VKO-XIHet mice (n=10) and ScxCre- littermate controls (Ctrl, n=10) were used (IACUC approved). Transmission Electron Microscopy: Immediately after sacrifice, Achilles tendons (ATs) (n=4/genotype) were isolated, fixed, embedded, sectioned, stained, and imaged as described⁴. Fibril diameters were measured using a custom MATLAB script (n=10 images/sample). Mechanics: AT-calcaneus complexes were harvested, finely dissected, and cross-sectional area was measured using a custom laser device. The free end of the tendon was secured in sandpaper with cyanoacrylate glue, and the calcaneus and sandpaper were gripped in custom fixtures. Tendons were tested in a PBS bath at 37°C using a protocol of preloading to 0.03N, preconditioning for 10 cycles, stress relaxations at 3% and 5% strain, and quasistatic ramp-to-failure at 0.1% strain/sec (Instron 5848). Each stress relaxation was followed by a frequency sweep of 10 cycles at 0.1, 1, 5, and 10 Hz. Statistics: Fibril diameter distributions were compared between genotypes using a Kolmogorov-Smirnov test. Cross-sectional area and mechanical properties were compared across genotypes using a two-sample t-test. Significance was set at p ≤ 0.05, and all data visualization and statistics were conducted in R (v4.3.1).

RESULTS: VKO-XIHet ATs demonstrated substantial changes in fibril structure and mechanical properties. The collagen fibril distribution in VKO-XIHet tendons was different than Ctrl with a distinct population of larger (>175 nm) fibrils (Fig 1A). While fibrils in Ctrl tendons had circular cross-sections, many fibrils in VKO-XIHet tendons had irregularly shaped cross-sections with these irregularities most apparent and severe in the population of larger fibrils (Fig 1B-C). Despite larger fibril diameters, overall tendon cross-sectional area was smaller in VKO-XIHet tendons (Fig 2A). Maximum load, stiffness, and maximum stress were also lower in VKO-XIHet tendons compared to Ctrl (Fig 2B-D). Viscoelastic properties showed minimal differences between genotypes (data not shown).

DISCUSSION: We studied the combined roles of collagens V and XI in establishing structural and mechanical properties of the AT during postnatal growth. Supporting our hypothesis, VKO-XIHet tendons showed fibril-level structural and tissue-level mechanical changes consistent with altered fibril assembly. The shift towards larger diameter fibrils and irregularity of fibril boundaries in VKO-XIHet tendons suggest that these collagen types work in concert to regulate lateral growth of fibrils. This finding is consistent with previous work where the absence of *Col5a1* expression led to larger fibril diameters^{3,5} and irregular fibril boundaries⁵. Additionally, we previously found a 39% decrease in maximum load and a 19% decrease in maximum stress in post-natal day 60 ScxCre;*Col5a1*^{flox/flox} ATs². In comparison, the post-natal day 30 ScxCre;*Col5a1*^{flox/flox};*Coll1a1*^{flox/+} tendons in this study showed 75% and 45% decreases in the same parameters, respectively. These markedly reduced mechanical properties coupled with increased lateral growth in a sizable portion of fibrils demonstrate that ablation of 1 allele of *Coll1a1* in addition to both alleles of *Col5a1* further exacerbates the phenotype during tendon development. Future work will focus on delineating possible compensatory mechanisms between collagens V and XI and understanding interactions at early stages of development.

SIGNIFICANCE: Collagens V and XI have known roles in fibrillogenesis and the acquisition of tendon structure during development. Due to their coordinated roles and structural similarities, defining the interactions between collagens V and XI in tendon is essential to understanding mechanisms underlying collagen fibril formation.

REFERENCES: 1. Wenstrup et al., J Biol Chem, 2011. 2. Connizzo et al., J Orthop Res, 2015. 3. Sun et al., Matrix Biol, 2020. 4. Dunkman et al., Matrix Biol, 2014. 5. Connizzo et al., J Orthop Res, 2016.

ACKNOWLEDGEMENTS: This study was supported by NIH/NIAMS (R01AR073231) and Penn Center for Musculoskeletal Disorders (P30AR069619).

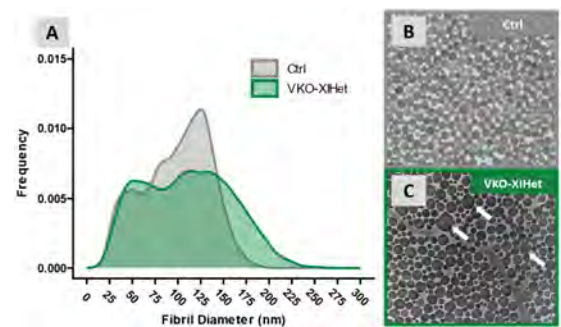


Figure 1: (A) VKO-XIHet fibril distributions demonstrate statistical differences with a population of larger diameter fibrils. Fibril distributions were compared using a Kolmogorov-Smirnov test. (B-C) Fibril boundaries are irregularly shaped in VKO-XIHet tendons (white arrows), especially in larger fibrils.

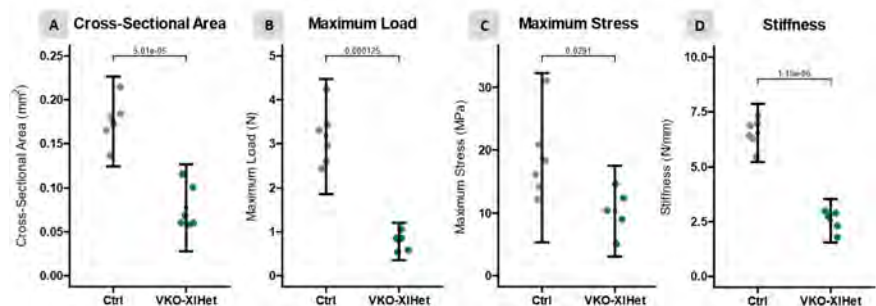


Figure 2: Cross-sectional area (A), maximum load (B), maximum stress (C), and stiffness (D) were significantly decreased in VKO-XIHet tendons. Properties were compared between genotypes using t-tests; p-values are listed above significance bars. Data shown as mean ± SD.

Altered Transcriptional Landscape and Emergent Region-Dependent Mechano-Response in the Developing Porcine Meniscus

Yuqi Zhang¹, Meghan E. Kupratis¹, Giorgos Kotsaris¹, Nathaniel Dymant¹, Lin Han³, Eiki Koyama^{1,2}, Robert L. Mauck¹

¹University of Pennsylvania, Philadelphia, PA, ²Children's Hospital of Philadelphia, Philadelphia, PA, ³Drexel University, Philadelphia, PA.

yuqz@seas.upenn.edu

DISCLOSURES: RL Mauck (4, *Mechano-Therapeutics*; 5, *4Web Medical*; 8, *JOR Spine*), no other disclosures.

INTRODUCTION: The meniscus plays a pivotal role in maintaining joint stability and distributing loads in the knee. However, adult meniscus injuries are challenging due to limited endogenous cell-mediated repair. Despite recent advances, restoration of native tissue structure and biomechanical function after injury has not been realized. Notably, tissue repair is superior in younger tissues and, as such, consideration of how the meniscus initially forms and matures may offer insight into regenerative strategies that could be harnessed for adult repair. To address this, we recently detailed the embryonic formation and postnatal maturation of the murine meniscus. These studies revealed that the cellular and matrix characteristics of the meniscus, including region-specific cartilaginous inner and fibrous outer zones, are established before birth, with further specialization occurring during postnatal growth [1,2]. These studies also showed that mechanical forces, particularly those generated during embryonic development, are essential for proper tissue formation [3,4], but that postnatal weight-bearing had a lesser effect [5]. However, the small size and distinct morphological features (e.g., mice develop ossicles in the meniscus horn) of the mouse model limit its relevance to humans. To bridge this gap, we recently developed a pipeline for the timed acquisition of fetal pig specimens and determined key time points relevant to knee joint formation and meniscus specification [6, 7]. Here, we further this analysis by establishing the transcriptional profile and emergent mechano-responsivity of early meniscus progenitors as a function of gestational state and meniscus region.

METHODS: **Embryo Collection:** Adult Yorkshire pigs were artificially inseminated at the National Swine Research and Resource Center. Pregnancy was confirmed by ultrasound, and sows were euthanized on embryonic (E) day 42 or postnatal (P) day 1. **Cell Isolation:** E42 and P1 menisci from the right hindlimb were isolated using a dissecting microscope. P1 menisci were segmented into an inner and outer region. All tissue was chopped into small fragments and cultured in basal medium (DMEM, 10% FBS, anti/anti) for one passage, after which cells were cryopreserved or used for in vitro studies. **Sequencing:** Frozen cells were submitted to the Center for Applied Genomics at CHOP for RNA extraction, QC, library preparation, and Illumina NovaSeq sequencing. The reads were aligned to the porcine genome (Sscrofa11.1) using STAR within the Galaxy Europe platform, and differential gene expression analysis was carried out using DESeq2. Genes were identified as differentially expressed if the fold change of P1-inner/P1-outer compared to E42 exceeded 1, with a P-adj value below 0.05. Transcripts per million (TPM) values were derived from the mean normalized fragment counts obtained from DESeq2 across all samples. Gene ontology and pathway analyses were conducted using the functional annotation tools Enrichr and g-Profiler. **Mechano-Response Assays:** Isolated cells were cultured on fibronectin-coated polyacrylamide (PA) hydrogels (Soft: 5kPa or Stiff: 55kPa) or glass. Following 1-day in basal media, cells were fixed and stained for YAP, actin, and nuclei. **Imaging:** Confocal microscopy was used to obtain z-stack images at 10X magnification. Images were processed in Cell Profiler to quantify cell area and YAP nuclear to cytoplasmic ratio. **Collagen Contraction Assay:** E42 and P1 cells were encapsulated in 1.5mg/mL Type I collagen gels. Images were taken every other day over 2 weeks. Image J was used to determine the cross-sectional area of each image, and the area was fit to a sigmoidal function to determine time to 1/2 contraction. **Statistics:** 2-way ANOVA using GraphPad Prism was used to make comparisons between groups, with significance set at $p < 0.05$.

RESULTS: To investigate the transcriptional differences in meniscus progenitors during development, we performed bulk RNA sequencing on early passage E42 and P1-inner and -outer cells. Overall, substantial changes in gene expression were observed, with P1-outer cells having a greater number of unique differentially expressed genes (relative to E42 cells) compared to P1-inner cells (Fig. 1b). Interestingly, we found a significant downregulation of COL2A1 in both P1-inner and P1-outer cells compared to E42 (Fig. 1a). Expression related to collagen-containing extracellular matrix and cytoskeleton ontologies during development (Fig. 1c). When placed on PA gels of increasing stiffness (Fig. 2a), meniscus progenitors from E42 (all zones) and P1 inner/outer zone were mechanosensitive. That is, E42, P1-inner, and P1-outer cells all increased in area with increasing stiffness (Fig. 2c). Similarly, for E42 and P1-inner cells, the YAP N:C ratio was higher on 55kPa and glass than on 5 kPa gels (Fig. 2d). Interestingly, outer zone cells (P1-outer) showed a higher YAP N:C ratio than either E42 or P1-inner cells, even on soft (5 kPa) substrates. Given the increasing trends in cell morphological response and YAP nuclear localization in 2D, we next investigated their mechanoresponse in a 3D collagen environment. Similar to the trends observed in 2D, we found increasing contraction of collagen gels seeded with meniscus progenitors from E42 and P1-inner/outer regions. Notably, the P1-inner region cells were slower to contract the collagen gels compared to P1-outer cells (Fig. 3).

DISCUSSION: Our results show a marked shift in the transcriptional program of E42 vs. early postnatal meniscus cells. Remarkably, transcript levels were much higher at E42, suggesting perhaps a greater metabolic activity and phenotypic flexibility in these earlier meniscus progenitors. Interestingly, in P1 cells, a greater number of genes were differentially regulated (up and down) in outer compared to inner cells, suggesting that this region is becoming more clearly specified. This is consistent with other work from our group showing increased mechanics in the outer meniscus compared to the inner meniscus at this stage of development [7]. Differences based on gestational state and region were also evident in 2D and 3D culture. Specifically, P1-outer cells had a higher level of N:C YAP at every stiffness and contracted 3D collagen gels more quickly. This suggests that cells within the outer zone of the meniscus develop a different threshold for mechanical signaling and activation than the inner region. Future work will continue to explore the transcriptional signatures of these progenitor cells and how they change with mechanical perturbation.

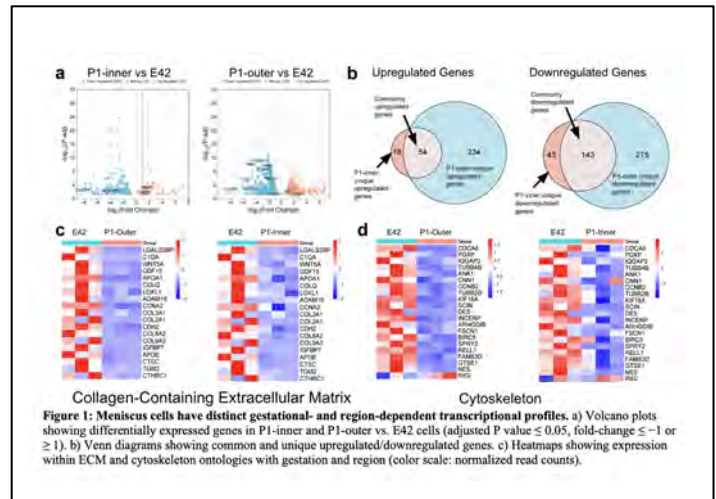
SIGNIFICANCE: This study explored the transcriptional characteristics and mechano-response of porcine meniscus progenitors. Insight into these mechano-regulatory pathways may lead to improved therapeutics to improve meniscus repair.

REFERENCES & ACKNOWLEDGEMENTS: [1] Tsinman+ FASEB J, 2021. [2] Kwok+ Acta Biomater, 2023. [3] Tsinman+ Trans ORS, 2022. [4] Tsinman+ JOR, 2023. [5] Fogarty+ JOR, 2023. [6] Zhang+ ORS, 2024. [7] Kupratis+ SB3C, 2024. Supported by the NIH and the VA.

REFERENCES & ACKNOWLEDGEMENTS: [1] Tsinman+ FASEB J, 2021. [2] Kwok+ Acta Biomater, 2023. [3] Tsinman+ Trans ORS, 2022. [4] Tsinman+ JOR, 2023. [5] Fogarty+ JOR, 2023. [6] Zhang+ ORS, 2024. [7] Kupratis+ SB3C, 2024. Supported by the NIH and the VA.

REFERENCES & ACKNOWLEDGEMENTS: [1] Tsinman+ FASEB J, 2021. [2] Kwok+ Acta Biomater, 2023. [3] Tsinman+ Trans ORS, 2022. [4] Tsinman+ JOR, 2023. [5] Fogarty+ JOR, 2023. [6] Zhang+ ORS, 2024. [7] Kupratis+ SB3C, 2024. Supported by the NIH and the VA.

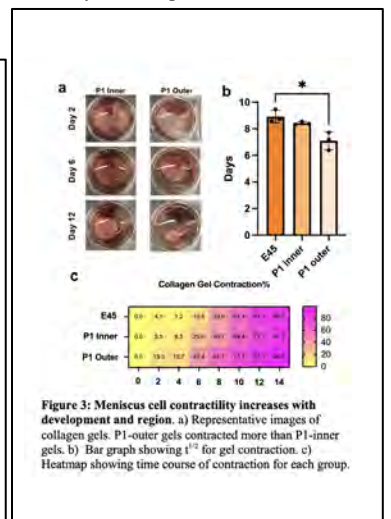
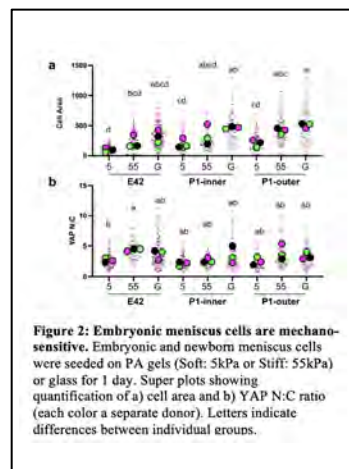
REFERENCES & ACKNOWLEDGEMENTS: [1] Tsinman+ FASEB J, 2021. [2] Kwok+ Acta Biomater, 2023. [3] Tsinman+ Trans ORS, 2022. [4] Tsinman+ JOR, 2023. [5] Fogarty+ JOR, 2023. [6] Zhang+ ORS, 2024. [7] Kupratis+ SB3C, 2024. Supported by the NIH and the VA.



REFERENCES & ACKNOWLEDGEMENTS: [1] Tsinman+ FASEB J, 2021. [2] Kwok+ Acta Biomater, 2023. [3] Tsinman+ Trans ORS, 2022. [4] Tsinman+ JOR, 2023. [5] Fogarty+ JOR, 2023. [6] Zhang+ ORS, 2024. [7] Kupratis+ SB3C, 2024. Supported by the NIH and the VA.

REFERENCES & ACKNOWLEDGEMENTS: [1] Tsinman+ FASEB J, 2021. [2] Kwok+ Acta Biomater, 2023. [3] Tsinman+ Trans ORS, 2022. [4] Tsinman+ JOR, 2023. [5] Fogarty+ JOR, 2023. [6] Zhang+ ORS, 2024. [7] Kupratis+ SB3C, 2024. Supported by the NIH and the VA.

REFERENCES & ACKNOWLEDGEMENTS: [1] Tsinman+ FASEB J, 2021. [2] Kwok+ Acta Biomater, 2023. [3] Tsinman+ Trans ORS, 2022. [4] Tsinman+ JOR, 2023. [5] Fogarty+ JOR, 2023. [6] Zhang+ ORS, 2024. [7] Kupratis+ SB3C, 2024. Supported by the NIH and the VA.



Reduced Type III Collagen Expression During Tendon Healing Impacts Cell Behavior and Mechanical Function Minimally

Margaret K Tamburro, Jaclyn A Carlson, Stephanie N Weiss, William Yen, Susan W Volk, Louis J Soslowsky

After tendon injury, type III collagen (Col3) accumulates in the tendon matrix. Given the structural and functional differences between Col3 and type I collagen (Col1), the primary matrix protein in tendon, Col3 accumulation is believed to contribute to poor tendon function after injury. However, the roles of Col3 in driving cell and functional outcomes after tendon injury are unelucidated. Furthermore, biological sex is known to impact both tendon health and Col3 levels. Therefore, our objective was to define the sex-specific impacts of early Col3 reduction on cell behavior and functional outcomes after tendon injury. We leveraged a mouse model with global, tamoxifen-inducible Col3 knockdown. At postnatal day 90 (p90), wildtype (*Rosa-CreERT2 Col3a1^{+/+}*) and knockdown (*Rosa-CreERT2 Col3a1^{F/F}*) mice received tamoxifen injection (100 mg/kg) and were randomized into uninjured as well as 1-, 3-, and 6-weeks post-injury groups. Animals in injury groups received bilateral patellar tendon injury at p90. At 1-, 3-, or 6-weeks post-injury, mice were sacrificed, and tendons were harvested bilaterally for cell behavior or mechanical assessment. Wildtype and knockdown uninjured controls were collected at the 3-week timepoint, as well. For cell behavior, RNA was isolated, converted to cDNA, and preamplified for qPCR assessment with Fluidigm 96.96 Dynamic Array ($n \geq 4/\text{group}/\text{sex}$). For function, patella-patellar tendon-tibia complexes were tested with a viscoelastic protocol ($n \geq 8/\text{group}/\text{sex}$). Mechanical properties were compared with 2-way ANOVAs (timepoint, genotype; $\alpha = 0.05$). For cell behavior and functional analyses, data from female and male tendons was analyzed separately to probe sex-specific effects. Principal component analysis of gene expression demonstrated separation between injury timepoints but not genotype for female and male tendons. Similarly, functional assessment demonstrated no impact of genotype on stiffness, modulus, and relaxation at 2% and 4% strain and a minimal impact of genotype on dynamic tendon behavior for both sexes. Surprisingly, Col3 reduction at the time of tendon injury had a minor impact on cell behavior and tendon function throughout healing in both female and male tendons. Future investigation into impacts of Col3 reduction on tendon macro-, micro-, and nano-structure will contribute to a more thorough understanding of these findings.

Strain-Induced Collagen Fibril Deformation is Diminished with Advanced Age in Mouse Supraspinatus Tendon

Jeremy D. Eekhoff, Stephanie N. Weiss, Louis J. Soslowsky

McKay Orthopaedic Research Laboratory, University of Pennsylvania, Philadelphia, PA

Disclosures: none

INTRODUCTION: Age-related tendon degeneration increases the risk of rotator cuff injuries which can lead to significant pain and disability.¹ The supraspinatus tendon, as part of the rotator cuff, exhibits region-dependent mechanical properties that change with advanced age which are likely a contributing factor to the increased risk of rupture in the elderly population.^{2,3} While these age-related changes to bulk tissue properties in the supraspinatus tendon have been demonstrated,^{2,4} tendon is a complex hierarchical tissue that dynamically responds to mechanical loading though changes in structural organization at multiple length scales. Despite this, it is unclear how aging affects the relationship between bulk tissue strain and collagen fibril deformation on the nanoscale level.⁵ Therefore, the objective of this study was to determine how collagen fibrils deform with applied strain in different regions of the supraspinatus tendon at two distinct ages. We hypothesized that collagen fibrils would experience deformation earlier in older tendons because of a reduction in early strain attenuation mechanisms such as uncrimping and changes in fiber alignment.

METHODS: Supraspinatus tendon-humerus complexes were harvested from p300 and p570 male wild-type C57BL/6 mice (IACUC approved). Tendon cross-sectional area was measured using a laser displacement sensor. After preparation for mechanical testing, samples were subjected to 10 cycles of preconditioning between 0.02 and 0.04 N followed by a one-minute rest and then a ramp to a randomly assigned strain (1%, 5%, or 9%; $n = 5-6$ /group) at a rate of 0.1% strain per second. The tendon was immediately flash frozen after reaching the target strain, removed from the test fixture, and embedded in optimal cutting temperature compound while keeping the tissue frozen to maintain the applied strain.^{6,7} Cryosections of the tendons were collected at 20 μm thickness and fixed in formalin. Nanoscale topographical images of the sections were acquired using tapping-mode atomic force microscopy (AFM) to visualize collagen fibrils. Five 2x2 μm images were acquired in both the insertion region (within 1 mm of humeral insertion) and midsubstance region (1-2mm away from humeral insertion) across multiple tissue sections for each sample (Fig 1). Collagen fibril d-period was measured using Fourier transform analysis.⁸ The average d-period length, local variance (average variance in d-period length within individual images), and global variance (variance in d-period length across entire sample) were calculated for the insertion and midsubstance regions of each sample. Data for p300 and p570 samples were analyzed independently using two-way ANOVAs including the main effects of region, strain, and their interaction with Tukey-adjusted post-hoc testing within significant main effects.

RESULTS: The applied strains of 1%, 5%, and 9% corresponded to the early toe, early linear, and early yield portions of the stress-strain curves, respectively, in both ages (Fig 2a,b,f,g). Average d-period length increased from 67.8 nm to 68.7 nm with applied strains of 1% to 5% in p300 samples, corresponding to a fibril strain of approximately 1.3% (Fig 2c). However, d-period length was not different between applied strains of 1% and 9%. In contrast with the p300 data, fibrils from p570 samples experienced no strain-induced changes in d-period length (Fig 2h). Moreover, local and global variance in d-period length showed no effect of strain or region in both p300 and p570 ages (Fig 2d,e,i,j).

DISCUSSION: Significant deformation of collagen fibrils was observed in p300 supraspinatus tendons. Unexpectedly, this fibril deformation occurred at the lower applied strain of 5%. Therefore, some of the applied strain is transmitted from the bulk tissue level to the collagen fibrils between the early toe and early linear regions of the loading curve despite the uncrimping and reorganization that would be expected concurrently between these strains.⁹ At the larger applied strain of 9%, the d-period length was no longer different than the 1% strain baseline value. Because the tissue exhibited early yield behavior (i.e., a reduction in modulus) at 9% strain, these data suggest that tissue yielding may result from early damage to the extracellular matrix that causes the collagen fibril d-period to begin to return to its initial length. Similar strain-dependent changes, with larger fibril deformations at intermediate applied strains, were found previously in supraspinatus tendons from younger p150 mice.^{6,7} Contrary to our hypothesis, no fibril deformation was observed in supraspinatus tendons from p570 mice in this study. At this advanced age, the lack of strain transmission from the bulk tissue scale to the fibril scale indicates that smaller-scale mechanisms are likely dominated by structural reorganization such as uncrimping, sliding, and/or realignment rather than deformation of collagen fibrils.^{9,10} Identifying the interplay between, and combination of, these mechanisms which become prominent with advanced age is a promising area for future study. In addition to measuring fibril deformation, this study also investigated the variation in d-period lengths. Even with changing d-period length in p300 samples, the variation remained similar for all strains. Therefore, the increase in d-period length was homogenous across all fibrils in the tissue, rather than the alternative where some fibrils would experience deformation while others would not. However, it should be noted that while fibril deformation was homogeneous in this controlled experiment, more complex mechanical loading of the supraspinatus tendon *in situ* could result in heterogeneous fibril engagement.

SIGNIFICANCE: Results from this study provide insights regarding nanoscale mechanisms that influence age-related degeneration and changes in mechanical properties of supraspinatus tendon.

ACKNOWLEDGEMENT: This study was supported by NIH/NIAMS (AR070750) and the Penn Center for Musculoskeletal Disorders (NIH/NIAMS, P30 AR069619).

REFERENCES: [1] Zhao+ *Orthop J Sports Med* 2021. [2] DiStefano+ *ORS* 2022. [3] Johnson+ *J Orthop Res* 2023. [4] Connizzo+ *J Biomech Eng* 2013. [5] Fang+ *J Orthop Res* 2017. [6] Connizzo+ *J Biomech* 2014. [7] Connizzo+ *Interface Focus* 2016. [8] Rigozzi+ *J Struct Biol* 2011. [9] Miller+ *J Biomech* 2012. [10] Szczesny+ *Acta Biomater* 2014.

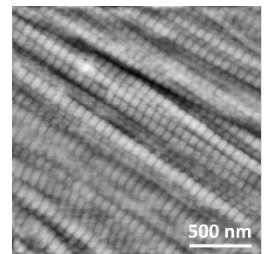


Figure 1. Representative image.

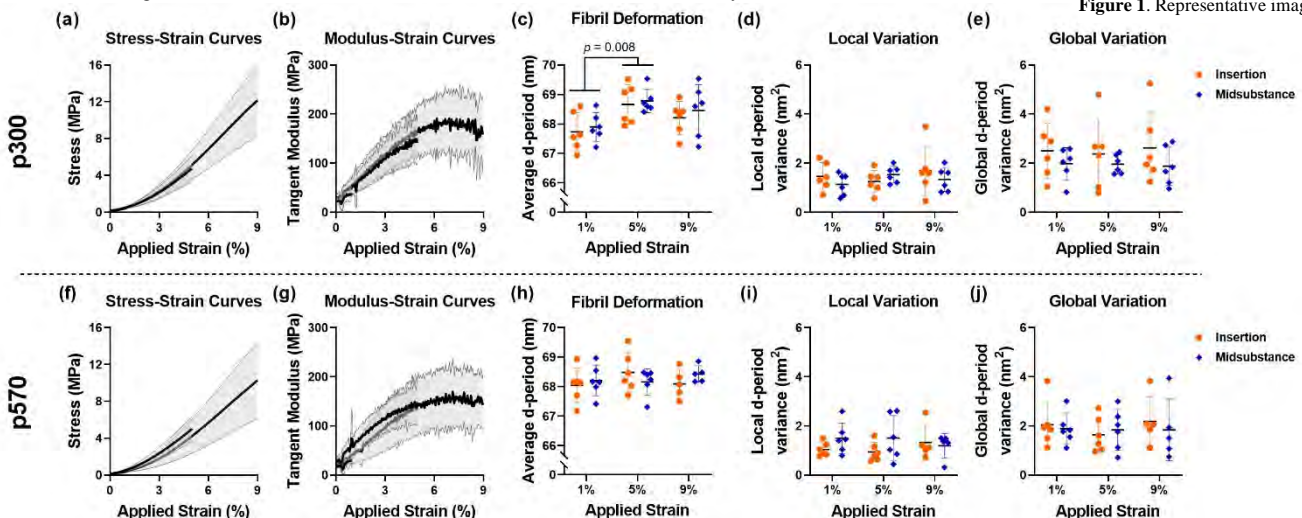


Figure 2. Average stress-strain curves (a,f) and modulus-strain curves (b,g) from p300 and p570 samples. Fibril deformation was significantly increased from 1% to 5% applied strain independently of region in p300 samples (c) but was unaffected by strain and region in p570 samples (h). Local and global variation were unaffected by strain and region in both p300 and p570 samples (d,e,i,j).

Title: Developing In Vitro Hydrogel Models to Study Mechanobiology in Skeletal Muscle Tissue

Authors: Andre Roots, Christopher Madl, Ph.D.

Skeletal muscle tissue repairs itself following physical or chemical injury through the activity of satellite cells, a dedicated population of muscle stem cells (MuSCs). In disease and aging, the regenerative function of MuSCs is diminished, impairing tissue repair. Mechanical signals from the cellular microenvironment are known to influence MuSC behavior, but the role that disrupted mechanical sensing plays in MuSC regenerative function in diseased states remains poorly understood. New 3D in vitro tissue models containing extracellular matrix (ECM) mimicking materials with independent tuning of stiffness, viscoelasticity, degradability, and adhesive cues are required to decouple extracellular factors that impact MuSC mechanical sensing. We are developing novel engineered protein biomaterials and applying them to a culture of human skeletal muscle microtissue models. We are engineering a family of elastin-like proteins (ELPs) with independent primary and secondary crosslinking chemistries, tunable network connectivity, and modular adhesive and degradation motifs to facilitate the formation of the microtissues enabling dynamic crosstalk between cells and their microenvironment. We use these materials to prepare muscle microtissues from human myoblasts containing contractile, aligned muscle fibers and a population of MuSC-like cells. We anticipate that these models will provide new insights into detrimental biochemical signaling caused by abnormal microenvironmental cues present in disease and aging to aid in identifying therapeutic approaches to improve MuSC behavior in adverse conditions.

Understanding the Relationship between Material Distribution, Femur Geometry, and Atypical Femoral Fractures Utilizing MRI-Based Finite Element Modeling

Ashkan Sedigh¹, Christiana Cottrell², Nada Kamona², Brian Vu², Ganen Chinniah², Frank Pham², Jianna Kim², Ryan Shams², Alyssa Rosen², Rahulan Sivakumar², Makayla Clark², Eva Gonzalez-Whitehouse², Chamith S. Rajapakse², Ani Ural¹

¹ Department of Mechanical Engineering, Villanova University, Villanova, PA, USA.

² Departments of Radiology and Orthopaedic Surgery, University of Pennsylvania, Philadelphia, PA

Abstract:

Atypical femoral fracture (AFF) is a rare fracture associated with prolonged bisphosphonate (BP) treatment that occurs in the subtrochanteric and midshaft regions of the femur. Previous studies have shown correlations between femoral geometrical properties and AFF risk. Moreover, several studies showed changes in tissue material properties with BP treatment. Previously, we identified that femoral geometrical properties, most significantly anterior bowing angle (ABA), are highly correlated with AFF fracture load. In this study, we aim to assess the relationship between material property distribution and AFF fracture load using magnetic resonance imaging (MRI)-based finite element (FE) modeling.

MRI of twenty-eight female human cadaveric femora (isotropic resolution=341 μ m) were obtained and segmented to provide the bone volume fraction (BVF) at each voxel. The segmented images were converted to FE models (~700k elements) using Simpleware ScanIP. The models were subjected to stance loading (Fig. 1a). The fracture process was modeled by the cohesive extended finite element method (XFEM) in FE analysis software, Abaqus. Voxel-specific material properties (Fig. 1b) were assigned based on BVF. Elastic modulus varied linearly with BVF¹. Ultimate strength was taken as directly proportional and fracture toughness was taken as inversely proportional to elastic modulus¹⁻³. The stiffness, fracture load, and displacement at fracture load were extracted from the simulations.

The simulation results showed that the fracture load (Fig. 1c,d) at the AFF site has a positive correlation with the entire femur mean BVF ($R=0.50$, $p=0.01$) and mean elastic modulus ($R=0.50$, $p=0.01$) (Fig. 1e). Incorporating our previous femoral geometry data, cluster analysis shows that lower ABA and higher mean BVF increases AFF fracture load (Fig. 1f) decreasing susceptibility to AFF.

This study developed a modeling approach that integrates MRI and fracture mechanics-based FE modeling to assess how femoral material distribution affects the mechanical response at the AFF site. The results underscore the importance of patient-specific AFF risk assessment, as individual variations in geometry and material distribution may have distinct implications. MRI-based FE models provide insight into the multifactorial contributors to AFF risk including material property distribution and geometrical features and may enhance AFF risk stratification and enabling personalized patient interventions.

1. Rajapakse CS, Chang G. Micro Finite-Element Analysis of the Proximal Femur on the Basis of High-Resolution Magnetic Resonance Images. *Curr Osteoporos Rep*. 2018;16(6):657. doi:10.1007/S11914-018-0481-5
2. McCalden RW, McGlough JA, Barker MB, Court-Brown CM. Age-related changes in the tensile properties of cortical bone. The relative importance of changes in porosity, mineralization, and microstructure. *J Bone Joint Surg Am*. 1993;75(8):1193-1205. doi:10.2106/00004623-199308000-00009
3. Zioupos P, Currey JD. Changes in the stiffness, strength, and toughness of human cortical bone with age. *Bone*. 1998;22(1):57-66. doi:10.1016/S8756-3282(97)00228-7

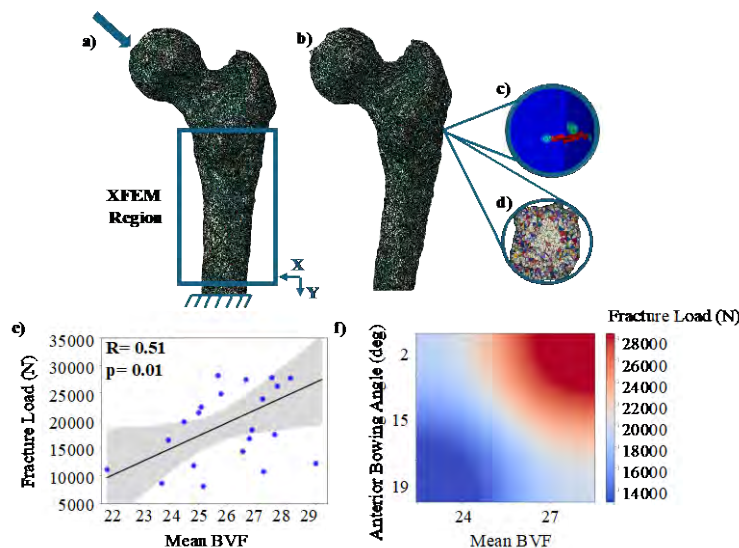


Figure 1. a) Femur FE model with the applied load (blue arrow) and XFEM region (blue box) showing the material property distribution based on bone volume fraction (BVF) measured by MRI b) Deformed femur model post-loading showing (c) the crack formation (red color) and (d) the material distribution at the AFF site. e) Correlation between mean BVF and fracture load f) Influence of anterior bowing angle and mean BVF on fracture load.

Pregnancy Gait Biomechanics using Markerless Motion Capture

Michelle Meyers¹, Afua Nkansah-Andoh¹, Devyn Russo¹, Ke Song, Ph.D.¹, Celeste Durnwald, M.D.², Casey Humbyrd, M.D., M.B.E.¹, Josh Baxter, Ph.D.¹

¹Department of Orthopaedic Surgery and ²Department of Obstetrics and Gynecology, University of Pennsylvania, Philadelphia, PA

Meyersm9@seas.upenn.edu

Disclosures: CH: 7B, 8, and 9; all other authors have no disclosures according to ACCME guidelines.

INTRODUCTION: Musculoskeletal pain is a universal symptom of pregnancy and contributes to increased anxiety and lower quality of life, which can increase perinatal complications [1]. 65% of pregnant individuals report experiencing lower extremity musculoskeletal pain spanning across the hip, knee, and foot/ankle [2]. Individuals undergo significant changes during pregnancy including increased body mass, postural adjustment, and circulating hormones that may affect mobility and contribute to musculoskeletal pain [3,4,5]. However, musculoskeletal biomechanics during pregnancy is chronically understudied, and high-throughput patient testing is critical to identify early predictors of pregnancy related pain and disability. Markerless motion capture is a new technique that allows for participants to wear street clothes and avoid marker placement, therefore, reducing the experimental burden of study participants [6]. This will be specifically beneficial for our third trimester pregnant population who will have stream-lined visits and not be required to change clothes. Our prior work confirmed that markerless motion capture has excellent reliability and correlated strongly with marker-based motion capture [7]. The overall goal of this study was to use markerless motion capture to compare gait kinetics, kinematics, and spatiotemporal parameters of third trimester pregnant individuals and non-pregnant controls to identify compensatory movement strategies during gait. We hypothesized that markerless motion capture can detect differences in gait biomechanics between third trimester pregnant individuals and non-pregnant controls.

METHODS: We recruited a cohort of third trimester pregnant individuals (n = 22, gestational week = 35.3 ± 1.4 weeks, age = 33.4 ± 4.6 years) and a cohort of non-pregnant female control participants (n = 8, age=27.5 ± 2.2 years) with IRB approval and written informed consent. Participants performed six walking trials at their self-selected normal walking speed over a 6-meter distance. We used a high-definition 8-camera markerless motion capture system (Optitrack) to quantify gait biomechanics as we previously described [7]. Specifically, we used commercially available markerless motion capture (Theia 3D) and biomechanical analysis (Visual3D) software to compute lower extremity sagittal inverse kinematics and inverse dynamics for each stance phase of gait. Using a two-sample t-test ($\alpha = 0.05$), we confirmed that normalized step length, normalized step width, and walking speed did not differ between study groups. Confirming consistent walking speed between groups is important because lower extremity biomechanics tend to correlate with walking speed. We used a statistical parameter mapping two-sample t-test (Spm1, $\alpha = 0.05$) to compare joint angles and moments of the control and third trimester participants.

RESULTS: Lower extremity kinematics and kinetics differed between third trimester pregnant individuals and non-pregnant controls (Figure 1). We observed significant increases in the third trimester pregnant individual's hip flexion angle (0-67% of step) and ankle dorsiflexion angle (0-6%, 32-57% of step), and significant decreases in third trimester pregnant individual's knee flexion angle (56-89% of step). Additionally, we found a significant increase in third trimester pregnant individual's hip extension moment (17-51%, 68-100% of step) and early-stance ankle plantarflexion moment (0-38% of step), as well as a significant decrease in knee extension moment (11-45%, 75-93% of step) and late-stance ankle plantarflexion moment (56-89% of step).

DISCUSSION: The observed gait adaptations in third trimester pregnant individuals may be responses to musculoskeletal pain, postural adjustment, and ligament laxity that occur during pregnancy. An increased hip flexion angle in the third trimester cohort suggests a compensatory maneuver to maintain normal walking speed while experiencing restricted movement due to mass increase and redistribution, potentially straining ligaments of the hip (Figure 1, A). Additionally, uterine growth during pregnancy weakens the abdominal muscles thus requiring increased activation of the hip extensors to maintain posture and stability, this is represented by increased moments during the mid- and terminal stance phase of gait (Figure 1, B). Decreased knee flexion during terminal stance corresponds with hyperextension of the knee due to the anterior shift in the center of mass and the ligament laxity that occurs during pregnancy and may contribute to increased knee pain (Figure 1, C). This change in knee angle is coupled with a significant decrease in knee extension moment, supporting a compensatory maneuver to decrease knee loading to avoid painful symptoms (Figure 1, D). Increased ankle dorsiflexion during heel strike and midstance may be a result of increased hip flexion and contribute to changes in the loading biomechanics of the ankle (Figure 1, E). Pregnant individuals experienced a higher ankle plantarflexion moment during heel strike to support an increase and redistribution of mass to prevent falling, however, these patients also experienced a significant decrease in ankle plantarflexion moment during terminal stance to conserve energy while the plantar flexors are heavily engaged (Figure 1, F). The body adapts during pregnancy to not only conserve energy but also protect itself from falling and pain, and the observed phase-specific compensatory strategies to accomplish these aims can lead to loading and extending joints in harmful ways.

SIGNIFICANCE/CLINICAL RELEVANCE: Using markerless motion capture allows us to increase our participant population by lowering the experimental burden imposed on this population, ultimately increasing our knowledge regarding compensatory gait strategies during pregnancy. This opens the door for preventative treatments and specialized musculoskeletal care for pregnant individuals to circumvent pain during everyday actions such as walking.

REFERENCES: [1] Vignato+2021; [2] Vullo+1996; [3] Anselmo+2017; [4] Fitzgerald+2015; [5] Kristiansson+1996; [6] Keller+2022; [7] Song+2023.

ACKNOWLEDGMENTS: We would like to thank the Ruth Jackson Orthopaedic Society (RJOS) and the American Orthopaedic Foot & Ankle Society (AOFAS) for their funding in this project.

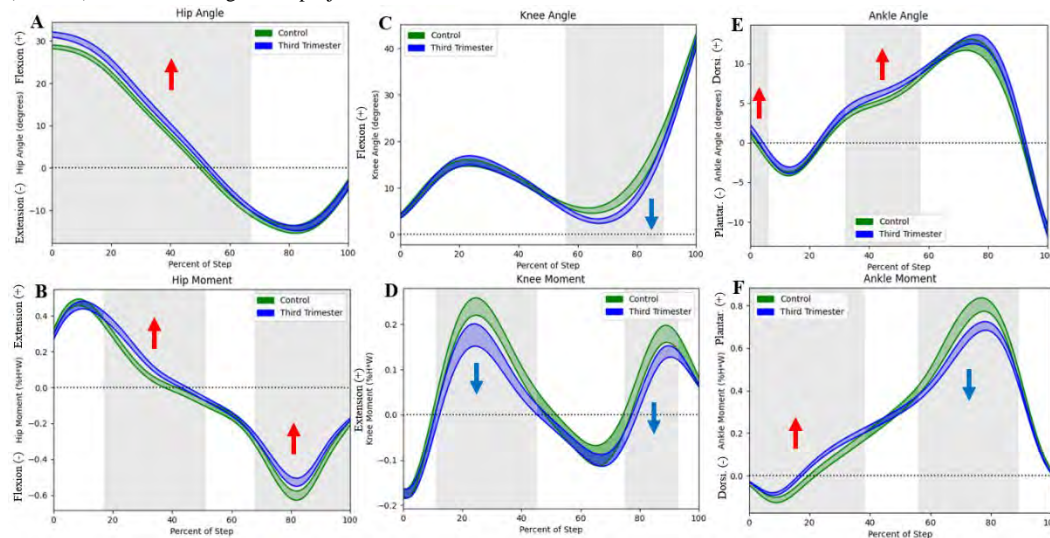


Figure 1. Control and third trimester pregnant cohort hip flexion angle (A), hip extension moment (B), knee flexion angle (C), knee extension moment (D), ankle dorsiflexion angle (E), and ankle plantarflexion moment (F). Shaded areas represent statistically significant differences between cohorts ($p < 0.05$).

Tendon-Targeted Collagen V Deficiency and Knockout Attenuate Mature Supraspinatus Tendon Mechanics

Michael S. DiStefano, Stephanie N. Weiss, Andrew F. Kuntz, Louis J. Soslowsky
 McKay Orthopaedic Research Laboratory, University of Pennsylvania, Philadelphia, PA
 micdis@seas.upenn.edu

Disclosures: AF Kuntz (5, Integra Lifesciences, Orthofix, Inc., FX Shoulder USA, Inc.; 9, American Shoulder and Elbow Surgeons, American Board of Orthopaedic Surgery, Inc.), no other disclosures

INTRODUCTION: Collagen V is a critical tendon matrix protein that regulates fibrillogenesis and is expressed throughout development and in mature tendons [1]. Clinical manifestation of collagen V deficiency is the classic form of Ehlers-Danlos syndrome (EDS), a connective tissue disorder with greater than 50% of patients being haploinsufficient for *COL5A1*, characterized by hyperextensible skin, joint hypermobility and instability, and abnormal wound healing [2]. Recent data from mouse supraspinatus tendon, which experiences a complex, region-dependent (insertion and midsubstance) loading environment within the rotator cuff of the shoulder, demonstrated that deficiency of collagen V during development resulted in severely altered collagen fibril structure, biomechanical properties, and dynamic responses to load [3]. However, the region-specific roles of collagen V tendon-targeted deficiency and knockout on mature supraspinatus tendons remain unknown. The objective of this study is to elucidate the regulatory role of collagen V on supraspinatus tendon whole-tissue and regional mechanics in mature mice using tendon-targeted (Scleraxis-Cre) collagen V heterozygous and knockout mice. Due to the role of collagen V in the regulation of tendon structure during development, we hypothesized that collagen V heterozygous and knockout supraspinatus tendons would have inferior whole-tissue and regional elastic mechanical properties, whole-tissue viscoelastic mechanical properties and reduced regional collagen fiber realignment compared to wild type control tendons.

METHODS: Animals: Supraspinatus tendons (n=10/genotype) from tendon-targeted collagen V heterozygous (TEN-HET) mice (*ScxCre;Col5a1^{fwt}*), knockout (TEN-KO) mice (*ScxCre;Col5a1^{fl/fl}*), and wild-type (WT) control mice (*Cre*-littermates) were used (IACUC approved). Mechanics and Collagen Fiber Realignment: All mice were sacrificed at 150 days old and were subjected to our mechanical testing and collagen fiber realignment protocol [3]: stress relaxations at 3%, 5%, and 7% strain each with subsequent frequency sweeps at 0.1, 1, 5, and 10 Hz, followed by a quasistatic ramp-to-failure. Throughout the ramp-to-failure, dynamic collagen fiber realignment was quantified using cross-polarization imaging, and regional fiber alignment data was interpolated with a polynomial fit as a function of strain from the load-displacement data. Images were acquired during the ramp-to-failure for optical strain tracking of stain lines demarcating the insertion and midsubstance regions of the tendon. Statistics: Comparisons between genotypes were conducted using one-way ANOVAs followed by Bonferroni post-hoc tests. Significance was set at $p \leq 0.05$ and trends at $p \leq 0.1$.

RESULTS: Whole-tendon cross-sectional area was reduced in the TEN-KO group compared to the TEN-HET and WT groups (Fig. 1A). Consistent with our hypothesis, collagen V deficiency and knockout resulted in dose-dependent reductions in elastic mechanical properties (e.g., failure load and linear stiffness (Figs. 1B, C)). Viscoelastic differences were also observed. Percent relaxation was increased in TEN-KO tendons compared with TEN-HET and WT tendons at all strain levels (7% strain shown in Fig. 2A). Additionally, collagen V TEN-HET and TEN-KO resulted in dose-dependent reductions in dynamic modulus, while phase shift was increased in TEN-KO tendons relative to TEN-HET and WT across all strain levels and frequencies (7% strain at 1 Hz shown in Figs. 2B and 2C). As hypothesized, collagen V TEN-HET and TEN-KO resulted in dose-dependent reductions in insertion modulus, while midsubstance modulus was reduced in TEN-KO tendons relative to TEN-HET and WT tendons (Figs. 3A, B). These results are supported by reductions in collagen fiber realignment in TEN-HET and TEN-KO tendons across region, as demonstrated by greater normalized circular variance values for insertion and midsubstance regions from 3-7% strain (Figs. 3C-D), encompassing the toe and linear elastic regions of these tendons.

DISCUSSION: This study investigated the role of collagen V on supraspinatus tendon elastic and viscoelastic mechanics using TEN-HET and TEN-KO mice. Consistent with previous data [3], we demonstrated that tendon-targeted collagen V TEN-HET and TEN-KO resulted in reductions in regional and whole-tissue elastic and viscoelastic mechanical properties. Further, reductions in these properties in our collagen V TEN-HET tendons highlight the allele-dependency of collagen V on tendon elastic and viscoelastic mechanical function and collagen fiber realignment. These functional deficits could be attributed to the improper hierarchical assemblies of TEN-HET and TEN-KO tendons resulting in disorganized tendon matrices with an inferior ability to respond to load [4]. This was evidenced by marked reductions in the TEN-HET and TEN-KO tendons' responses to realign resulting in inferior whole-tissue and regional elastic and viscoelastic mechanical properties. Overall, results demonstrate that decreased collagen V expression detrimentally affects supraspinatus whole-tissue and regional elastic and viscoelastic mechanical properties and collagen fiber realignment.

SIGNIFICANCE/CLINICAL RELEVANCE: This study elucidates the critical role of collagen V in regulating supraspinatus tendon function. Future studies will evaluate the structural and compositional mechanisms that contribute to these mechanical results. Understanding the effects of collagen V in tendon can be used to develop potential treatments modalities for classic Ehlers-Danlos syndrome.

ACKNOWLEDGEMENT: This study was supported by NIH/NIAMS (AR070750) and the Penn Center for Musculoskeletal Disorders (NIH/NIAMS, P30 AR069619).

REFERENCES: [1] Wenstrup et al. *J Biol Chem.* 2011. [2] Steinmann et al. *Conn Tissue, Heritable Disorders.* 2002. [3] Connizzo et al., *Interface Focus.* 2016. [4] Connizzo et al., *J Orthop Res.* 2016.

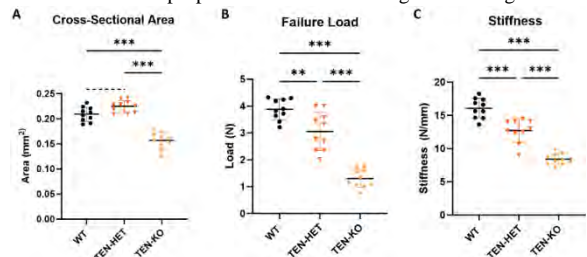


Figure 1. TEN-KO tendons demonstrated reduced cross-sectional area relative to TEN-HET and WT tendons (A). Tendon-targeted deficiency and knockout of collagen V resulted in significant reductions in elastic mechanical properties failure load and stiffness in a dose-dependent manner (B-C). Data as mean \pm standard deviation ($-p \leq 0.1$, $*p \leq 0.05$, $**p \leq 0.01$, $***p \leq 0.001$).

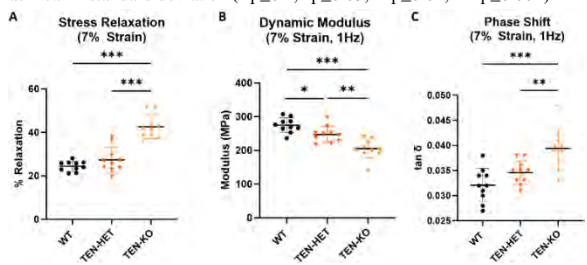


Figure 2. TEN-KO tendons had increased percent relaxation relative to TEN-HET and WT tendons (A). Tendon-targeted collagen V deficiency and knockout resulted in significant reductions in dynamic modulus in a dose-dependent manner (B), while phase shift was significantly increased in TEN-KO tendons relative to TEN-HET and WT tendons (C). Data as mean \pm standard deviation ($*p \leq 0.05$, $**p \leq 0.01$, $***p \leq 0.001$).

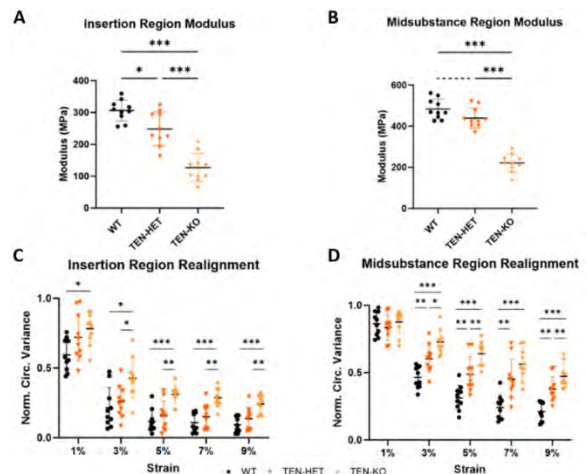


Figure 3. TEN-HET and TEN-KO tendons demonstrated reduced moduli and collagen fiber realignment in the insertion (A, C) and midsubstance (B, D) regions. Decreased normalized circular variance is indicative of increased collagen fiber realignment. Data as mean \pm standard deviation ($-p \leq 0.1$, $*p \leq 0.05$, $**p \leq 0.01$, $***p \leq 0.001$).

Age-related Normative Bone Strength Data for C3 vertebra using Cone Beam Computed Tomography - a retrospective study

Shilpa Shree Kuduva Ramesh Babu¹, Winnie Xu¹, Dan Del Collo¹, Denis Lattanzi¹, Michael Chang¹, Elaina Truong¹, Sally Farhnam¹, Lily Chen¹, Min-Keun (Kevin) Song¹, McKenna Sun¹, Austin Dai¹, Lihini Ranaweera¹, Steven Wang², Anh D Le², David Casper³, Gregory Chang⁴ and Chamith S. Rajapakse¹

- (1) Departments of Radiology and Orthopaedic Surgery, Perelman School of Medicine, University of Pennsylvania,
(2) Department of Oral and Maxillofacial Surgery, University of Pennsylvania School of Dental Medicine,
(3) Department of Clinical Orthopaedic Surgery, Perelman School of Medicine,
(4) Division of Musculoskeletal Imaging, NYU Langone

Abstract:

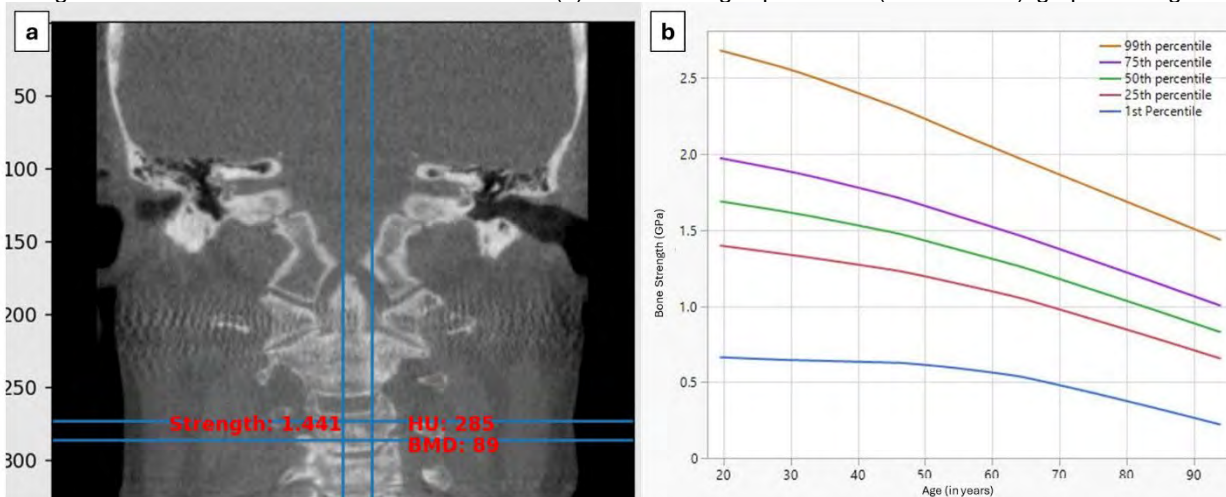
Background: Osteoporosis, a disease characterized by low bone mass and reduced bone strength, leads to an increased risk of fracture. There are numerous studies describing the age-related trends of bone mineral density (BMD). However, how bone strength changes with age has not yet been studied. Using cone beam computed tomography (CBCT) with a reduced radiation dose, we aimed to assess the bone strength of the C3 vertebral body of the cervical spine among a diverse female population.

Methodology: We performed a cross-sectional, retrospective study. Ten female CBCT DICOM files from each decade of the age group of 11–100 years were randomly selected (n = 90). CBCT scans of patients with impaired bone metabolism, vitamin D deficiency, breastfeeding, pregnancy, steroid use, or smoking were excluded. BoneHealth software (Precision Radiomics, University of Pennsylvania, and NYU), a finite element analysis tool, was used to estimate the Hounsfield Unit (HU), BMD, and bone strength of the trabecular part of the C3 vertebral body of the cervical spine. Two standard deviations (SD) above and below the mean bone strength were determined and correlated with age to establish the bone strength percentiles across the population.

Results: There was a highly significant negative correlation between females' C3 cervical spine bone strength and age ($p < 0.001$, $r = -0.62$). The bone strength, BMD, and HU peaked in the 21–30 years age group, with a mean \pm SD of 1.69 ± 0.33 GPa, 97.5 ± 0.31 mg/cm³, and 311.3 ± 0.29 , respectively. There was a significant reduction in bone strength, BMD, and HU by the mean age of 54.6 ± 2.5 years ($p < 0.001$), with a mean \pm SD of 1.26 ± 0.25 GPa, 76 ± 0.22 mg/cm³, and 242.2 ± 0.25 , respectively. Around the age of menopause (~50 years), the bone strength at the 99th, 75th, 50th, 25th, and 1st percentiles were 2.25 GPa, 1.6 GPa, 1.48 GPa, 1.18 GPa, and 0.59 GPa, respectively. (Figure)

Conclusion: This is the first kind of study in the literature to establish bone strength evaluation and its normative data using a low radiation dose, and easily accessible imaging modality, CBCT. These study results further warrant comparison with the standard of care, the DXA modality, for achieving the diagnostic cutoffs for osteopenia and osteoporosis through CBCT.

Figure: (a) Region of interest selection in the trabecula of C3 vertebra in coronal slice of CBCT scan and the simultaneous HU, BMD and Strength assessment in the Bone Health Software (b) Bone Strength percentile (smoothened) graph among females 11-100 years.



Title: Finding Balance: What We Can Learn About Early Post-Operative Recovery from Examining Center of Pressure Data during Y-Balance Testing after Anterior Cruciate Ligament Reconstruction

Authors: Kebeh M, Landrum KM, Greenberg E, VanEenenaam D, Stevens A, England P, Graci V, Ganley TJ, MD

Introduction: Neuromuscular control (NMC) deficits affecting postural control and lower extremity alignment are common after anterior cruciate ligament reconstruction (ACLR), particularly amongst young females, increasing the risk of repeat injury. While Y-Balance Testing (YBT) reliably measures NMC, current evaluative standards do not account for body position or balance control and may lack the granularity required to detect subtle, yet meaningful NMC deficits. We hypothesize that more precise measures of limb positioning and balance will improve identification of post-ACLR NMC deficits. This study aimed to evaluate sex-based and between-leg differences in performance, body position and center of pressure (COP) during the YBT anterior reach (antYBT) after ACLR.

Methods: Patients aged 10-21 years old at the time of injury who had undergone ACLR without complication performed antYBT on a Bertec force plate at three months postoperatively. Maximum reach distance (RD) normalized to patient's height (RDH), time to RD, sagittal plane trunk, knee, and ankle flexion angles, and root mean square (standard deviation) of center of pressure (RMS-COP) were recorded or calculated from video recordings and force plate data. Mixed model 2-way ANOVAs evaluated the effects of sex and ACLR (operative vs non-operative limb) on the outcome measures.

Results: After excluding patients with prior knee surgery or underlying conditions suspected to affect biomechanics, 24 subjects were included. Participants were 62.5% female (N=15) with mean age 14.9±1.9 years. The operative leg demonstrated significantly lower RDH (p=0.002), less knee flexion (p<0.001), less ankle dorsiflexion (p=0.006), longer time to RDH (p=0.010), and greater RMS-COP in the medial-lateral direction (p<0.02) when compared to the nonoperative leg. Female patients demonstrated significantly greater knee (p<0.04) and trunk flexion (p=0.003) overall than male patients. (Table 1)

Conclusion: Greater variability in COP trajectory in the operative leg indicates decreased NMC while maintaining balance, which may lead to increased stress across the ACL if this is not corrected during recovery. There were no statistical differences in reach distance measures based on sex despite the presence of significant differences in trunk and knee angle between the sexes, indicating variability in movement strategies without an impact on RDH, the main YBT outcome measure.

Significance: Assessing body position and COP trajectory, in addition to standardized reach distances, may improve the capacity of clinicians to detect abnormalities in NMC after ACLR. Future research evaluating these characteristics in later phases of recovery is needed to inform rehabilitation planning and reinjury risk factor identification.

Table 1. Performance Measures of Anterior Y-Balance Testing Post-Anterior Cruciate Ligament Reconstruction

	Operative Leg Mean (SD)	Nonoperative Leg Mean (SD)	P value	Male Mean (SD)	Female Mean (SD)	P value
RMS COP Anterior Posterior (mm)	24.3 (6.4)	26.2 (8.7)	0.3	28.3 (7.3)	23.4 (5.7)	0.113
RMS COP Medial Lateral(mm)	19.8 (10.0)	10.7 (8.6)	0.017*	14.3 (6.0)	15.8 (6.4)	0.762
RDH (Maximum Reach Distance/ Height)	0.31 (0.07)	0.34 (0.08)	0.002*	0.32 (0.12)	0.33 (0.03)	0.867
Sagittal Knee Angle (degrees)	68.8 (9.6)	86.1 (9.3)	0.000*	73.6 8.4	80.1 6.5	0.036*
Sagittal Ankle Angle (degrees)	13.5 (5.1)	17.2 (5.3)	0.006*	15.7 4.7	15.1 4.3	0.79
Sagittal Trunk Angle (degrees)	55.5 (21.3)	62.8 (20.2)	0.089	45.7 18.8	68.4 13.1	0.003*
Time to Maximum Reach (s)	6.3 (1.3)	6.9 (1.7)	0.010*	7.0 1.6	6.3 1.2	0.034*
¹ COP: center of pressure						
² RMS: Root mean square						
³ * Denotes statistically significant result						

Impacts of Type V Collage Haploinsufficiency on the Structural Integrity and Immunoresponses of Dermal Wound Healing

Yuchen Liu¹, Daniel C. Stewart², Erin M. O'Brien¹, Chao Wang¹, Bryan Kwok¹, David E. Birk³, Kara L. Spiller¹, Susan W. Volk², Lin Han¹

¹Drexel University, Philadelphia, PA, ²University of Pennsylvania, Philadelphia, PA, ³University of South Florida, Tampa, FL

Introduction: Pathological wounds are a prevalent healthcare problem, affecting more than 40 million Americans [1]. Imbalanced healing often results in fibrotic scar formation, marked by excessive deposition and aberrant assembly of collagen I fibers. Type V collagen, a minor fibril-forming collagen, is a key regulator of the initial fibrillogenesis of collagen I during embryonic development [2], and could be an important player in wound healing [3]. For patients with classic Ehlers-Danlos syndrome (cEDS), a genetic disorder caused by the mutation of human *COL5A1* gene, major symptoms include fragile skin, delayed wound healing and healed scar tissue [4, 5]. Understanding how collagen V contributes to skin tissue integrity and immune response from wound healing will provide new insights for developing effective regenerative strategies and improved care for cEDS patients. This study aims to elucidate how collagen V regulates the tissue structural integrity and immune responses during wound healing by studying the collagen V heterozygous mice, *Col5a1*^{+/-}, an established model of cEDS [6].

Methods: Two 6-mm diameter circular full-thickness dermal punch wounds were created on the lower dorsal skin of *Col5a1*^{+/-} and wild-type (WT) mice at 7 weeks of age and harvested at different post-wound days (PWD) [7]. We applied Picrosirius Red staining and polarized light microscope imaging (PLM) (Olympus BX51-P) to assess the collagen fiber structure of intact skin. CT-Fire was utilized to analyze the fiber length and width of PLM images [8]. Scanning electron microscopy (SEM) was applied at 20k× magnification to image the fibril nanostructure on 10-μm thick cross-sections of intact skin and scar tissue at PWD35. ImageJ was used to measure the fiber diameter of SEM images. PWD35 skin samples were harvested and stamped out into dumbbell-shaped pieces for tensile tests of maximum stress to failure and Young's modulus for both the intact skin and scar tissue (Instron 5542) [9]. Flow cytometry (BD Fortessa or Symphony) was performed to assess PWD14 macrophage activities after re-epithelialization and results were analyzed using FlowJo software [10]. Unpaired two-sample student's *t*-test was applied to determine the effects of genotype at $\alpha = 0.05$.

Results and Discussion: This study highlights the crucial role of collagen V in mediating the integrity of scar tissue and immunoresponses during dermal wound healing. Studying the *Col5a1*^{+/-} mice, we have previously shown that reduction of collagen V led to delayed wound healing and substantially increased scar tissue size using the dermal wound punch model [3]. Here, we further demonstrated that with the reduction of collagen V led to an increase in collagen I fiber size, as marked by wider and longer fibers than their WT counterparts (Fig. 1b,c). At the nanoscale, for both genotypes, the scar tissue showed thinner, densely packed and more aligned collagen fibrils compared to the intact dermis, illustrating the aberrant assembly of collagen during wound healing (Fig. 2a, arrowheads). In comparison to the WT, *Col5a1*^{+/-} mice exhibited thicker collagen fibrils for both intact skin and scar tissue, supporting that reduction of collagen V led to disrupted collagen fibrillogenesis in both normal matrix assembly and aggravated scar formation (Fig. 2b). In alignment with these structural defects, we further demonstrated that *Col5a1*^{+/-} tissues demonstrated lower linear modulus and maximum stress to failure under tensile test compared to the WT counterparts, for both intact skin and scar tissue (Fig. 3b,c). Together, these results illustrated reduction of collagen V impaired the structural integrity and mechanical functions of skin tissue during dermal wound healing. In addition, at PWD14, *Col5a1*^{+/-} mice retained a higher percentage of macrophages in the wound cell population (Fig. 4a), as well as a higher proportion of CD301b and CD206 positive macrophages (Fig. 4b) compared to the WT. These results evidenced elevated activities with dermal dendritic cells and M2 type macrophages [11, 12], which likely results from disrupted matrix remodeling with the reduction of collagen V.

Conclusion: This study highlights that collagen V is a crucial regulator of the structural integrity, mechanical function as well as inflammation-driven macrophage activities during dermal wound healing. Modulating the activities of collagen V could serve as a potential therapeutic target for enhancing wound regeneration and improving the care for cEDS patients.

References: [1] Birk+ 1990. [2] Wenstrup+ 2004. [3] DeNigris+ 2016. [4] Mak+ 2016. [5] Malfait+ 2010. [7] Wenstrup+ 2006. [8] Jorgensen+ 2020. [9] Bermudez+ 2011. [10] O'Brien+ 2022. [11] Kim+ 2018. [12] Xu+ 2020.

Acknowledgements: This work is supported by NSF CAREER CMMI-1751898 as well as the NIH Grant P30AR069619 to the Penn Center for Musculoskeletal Disorders (Biomechanics Core).

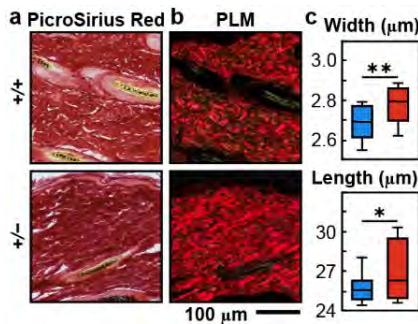


Fig. 1 a) PicroSirius Red histology, b) PLM images of collagen I fibers birefringence and c) comparison of fiber width and length between WT (+/+) and *Col5a1*^{+/-} (+/-) intact skin (Box-and-whisker plot, $n = 5$, *; $p < 0.05$, **; $p < 0.01$).

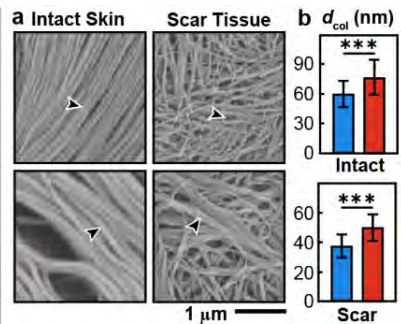


Fig. 2 a) SEM image of intact dermis and scar tissue. b) Comparison of fiber diameter in intact skin and scar tissue between +/+ and +/- mice at PWD35 (mean ± SD, $n = 5$, *; $p < 0.05$, **; $p < 0.01$, ***; $p < 0.001$).

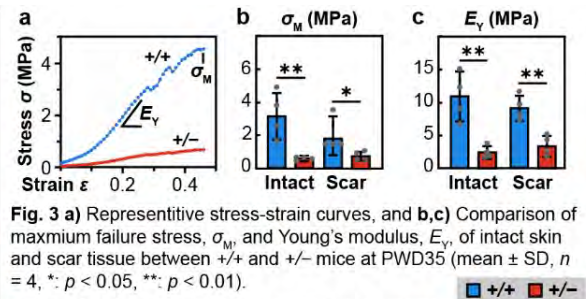


Fig. 3 a) Representative stress-strain curves, and b,c) Comparison of maximum failure stress, σ_M , and Young's modulus, E_Y , of intact skin and scar tissue between +/+ and +/- mice at PWD35 (mean ± SD, $n = 4$, *; $p < 0.05$, **; $p < 0.01$).

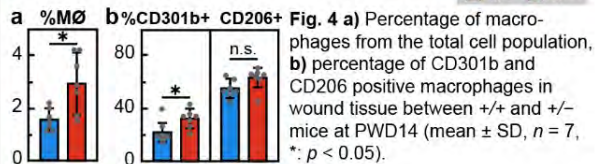


Fig. 4 a) Percentage of macrophages from the total cell population, b) percentage of CD301b and CD206 positive macrophages in wound tissue between +/+ and +/- mice at PWD14 (mean ± SD, $n = 7$, *; $p < 0.05$).

Treadmill Running Does Not Induce Mechanical Changes in the Rat Subscapularis Tendon

Chet S. Friday¹, Courtney A. Nuss¹, Jeremy D. Eekhoff¹, Louis J. Soslowky¹, Andrew F. Kuntz^{1,2}

¹University of Pennsylvania, Philadelphia, PA, ²Corporal Michael J. Crescenz VA Medical Center, Philadelphia, PA

Chet.Friday@Pennmedicine.upenn.edu

DISCLOSURES: CSF (N), CAN (N), JDE (N), LJS (N), AFK (5 – FX Shoulder USA, Integra Life Sciences, Orthofix; 9 – American Board of Orthopaedic Surgery, American Shoulder and Elbow Surgeons)

INTRODUCTION: Rotator cuff tendinopathy, often caused by overuse,^{1,2} results in functional deficits and pain,³ presenting a substantial clinical problem that impacts people of all ages and levels of physical activity.⁴ Previous studies in rat models have shown that exercise-induced overuse results in tendinopathy in the supraspinatus tendon.⁵ However, the impact of increased activity on the remainder of the rotator cuff is unknown. Although previously believed to be an infrequent source of clinical pathology, the subscapularis is now recognized as a common cause of rotator cuff tendinopathy.⁶ Therefore, the objective of this study was to evaluate the impact of treadmill running on inducing tendinopathy in the subscapularis tendon in the rat model. We hypothesized that high levels of treadmill running would lead to tendinopathy and result in decreased mechanical properties in the upper and lower bands of the subscapularis.

METHODS: Treadmill Protocol: Forty-five 16-week-old male Sprague-Dawley rats were subjected to one of three levels of exercise by treadmill running – cage activity (CA), moderate-speed running (MSR, 17 m/min at 10° decline)⁵, or high-speed running (HSR, 22 m/min at 10° decline). Animals subjected to running protocols underwent an acclimation period of two weeks in the MSR group and three weeks in the HSR group, followed by four weeks of treadmill running (1 hour per day, 5 days per week). Animals were sacrificed after completion of the treadmill protocol for mechanical testing. **Sample Preparation:** Subscapularis and supraspinatus tendons were harvested with the left humerus and fine dissected free of non-tendon soft tissue. Subscapularis tendons were separated into upper and lower bands by cutting through the clear delineation point, in order to test the two distinct bands of the subscapularis individually (Fig 1). Tendon cross-sectional areas were measured using a laser-based device⁷ and humeri were potted in polymethyl-methacrylate for testing. **Mechanical Testing and Analysis:** Tendons were secured in custom fixtures at a gauge length of 8mm from the insertion. Testing was performed on an Instron 5542 test frame (Instron, Norwood, MA), and consisted of preconditioning (30 cycles between 0.125% and 0.375% strain at 0.25 Hz), stress relaxation (6% strain for 10 minutes), and quasi-static ramp-to-failure (0.1 mm/s). Tendons were then analyzed for elastic properties (stiffness, modulus), viscoelastic properties (percent relaxation), and failure properties (maximum force, maximum stress) using custom MATLAB scripts. Samples that failed at the grip were excluded from failure property analysis. Data was analyzed using one-way ANOVA followed by a Tukey's post-hoc test ($\alpha = 0.05$).

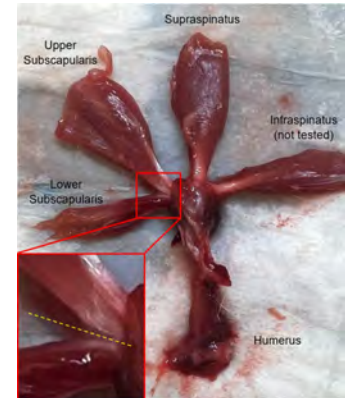


Fig. 1: Photograph of dissected humerus with rotator cuff tendons attached, with delineation point between upper and lower bands of the subscapularis highlighted in yellow.

RESULTS: Upper and lower bands of the subscapularis tendon showed no differences in stiffness (Fig. 2A), grip modulus (Fig. 2B), or percent relaxation (Fig. 2C) between activity levels. Additionally, upper and lower bands showed no differences in maximum force (Fig. 2D) or maximum stress (Fig. 2E) between activity levels. Similarly, supraspinatus tendons showed no differences in any mechanical properties between activity levels (*data not shown*).

DISCUSSION: This study demonstrated that the downhill treadmill running protocols utilized did not induce mechanical changes consistent with overuse in the subscapularis tendon. Although there were no mechanical changes observed, it is possible that treadmill running may have induced biological and/or histopathological changes that have not been evaluated to date. Prior studies using the MSR model focused on the supraspinatus tendon.^{5,8,9} The lack of observed mechanical changes in the subscapularis indicates that the model may not be suitable for this tendon, perhaps due to the unique organization, composition, local loading environment, or relative location of the acromion to the supraspinatus when compared to the subscapularis. Interestingly, this study did not find mechanical changes in the supraspinatus tendon, adding to the mixed results of the treadmill model,^{5,8,9} which may be affected by protocol variables such as treadmill inclination, as well as duration and time of day of running. Taken together, the results of this study in the subscapularis and supraspinatus indicate the described protocol does not induce mechanical changes consistent with tendinopathy that may lead to rotator cuff tears. While recent clinical studies have highlighted the high and previously unrecognized incidence of subscapularis tears,⁶ the relationship of subscapularis tears to preexisting tendon damage, potentially due to overuse, remains unknown and further studies are needed.

CLINICAL SIGNIFICANCE: Increased physical activity did not result in tendinopathy in the subscapularis, suggesting the possibility that exercise-induced overuse does not lead to subscapularis tendon damage and tears in the absence of other contributing factors.

REFERENCES: [1] Gomoll+ Arthritis Rheumatol, 2004. [2] van der Windt+ Ann Rheum Dis, 1995. [3] Millar+ Nat Rev Dis Primers, 2021. [4] Hopkins+ Asia Pac J Sports Med Arthrosc Rehabil Technol, 2016. [5] Soslowky+, JSES, 2000. [6] Bennett+, Arthroscopy, 2001. [7] Favata PhD Thesis, 2006. [8] Parks+ J Orthop Res, 2017. [9] Attia+ J Orthop Res, 2011.

ACKNOWLEDGEMENTS: This study was supported by the Department of Veterans Affairs (RX003652) and the Penn Center for Musculoskeletal Disorders (NIH/NIAMS P30AR069619). We thank Steph Weiss, Maggie Tamburro, Rebecca Betts, Nat Thurlow, and Mitch Hallman for their contributions to rat running.

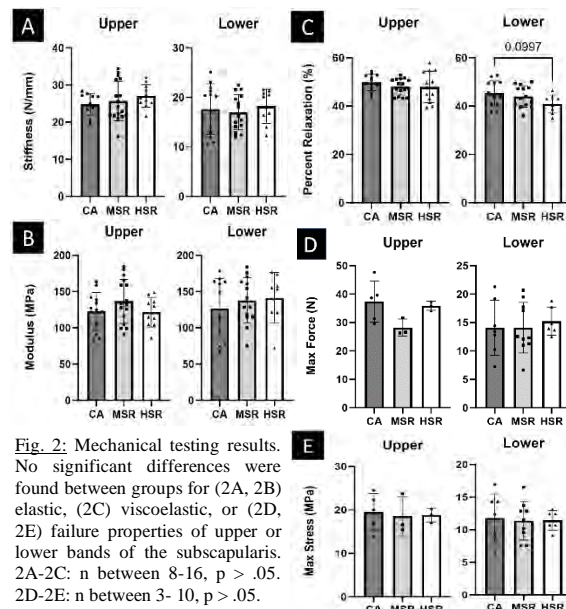


Fig. 2: Mechanical testing results. No significant differences were found between groups for (2A, 2B) elastic, (2C) viscoelastic, or (2D, 2E) failure properties of upper or lower bands of the subscapularis. 2A-2C: n between 8-16, $p > .05$. 2D-2E: n between 3- 10, $p > .05$.

Morphogenesis and Mechano-response of the Developing Porcine Meniscus

Meaghan E. Kupratis¹, Yuqi Zhang¹, Jiaqi Xiang², Bryan Kwok², Nathaniel A. Dymant¹, Lin Han², Eiki Koyama³, Robert L. Mauck¹

¹University of Pennsylvania, Philadelphia, PA, ²Drexel University, Philadelphia, PA ³Children's Hospital of Philadelphia, Philadelphia, PA

Disclosures: RL Mauck (4, *Mechano-Therapeutics*; 5, *4Web Medical*; 8, *JOR Spine*), no other disclosures.

INTRODUCTION: The meniscus is critical for knee joint stability and load distribution. While fetal menisci can undergo robust cell-mediated regeneration, the tissue's regenerative potential declines with maturation.¹⁻² In adults, meniscal tears and subsequent meniscectomy increase early-onset osteoarthritis risk.³ Therefore, understanding initial formation and specification of the meniscus during embryonic development may reveal mechanisms that could be harnessed to promote endogenous tissue repair in the adult. Our group previously examined the embryonic formation and postnatal maturation of the murine meniscus, revealing that its region-specific extracellular matrix (ECM) composition and cellular phenotypes are established prenatally.⁴⁻⁶ While these studies provide critical insight to the mechanoregulation of meniscus morphogenesis, translatability of the murine model is limited by its small size and resultant mechanical and morphological distinctions from humans. To overcome these limitations, the goal of the present study was to establish a more translationally relevant model of knee joint development in the Yorkshire pig. Here, we established the timeline of initial knee formation during early gestation and evaluated the morphology, ECM micromechanics, and emergent mechanoresponsivity of meniscus fibrochondrocytes (MFCs) during perinatal development.

METHODS: Adult Yorkshire sows were artificially inseminated at the National Swine Resource and Research Center (NSRRC, Columbia, MO). Pregnancy was confirmed via ultrasound, and sows were euthanized at embryonic day (E) 28-42 to assess early knee formation and at E45, E63, E84, or postnatal (P) day 0 for subsequent experiments. Adult hindlimb tissues also were collected from the sows at the time of sacrifice. Stifle (knee) joints were fixed in 4% paraformaldehyde, decalcified in formic acid, embedded in paraffin, and sectioned coronally and transversely. Cellularity, proteoglycan distribution, and collagen/fibrous tissue content were assessed via Safranin-O/Fast Green (SO/FG) and Alcian Blue/Picrosirius Red (AB/PSR) staining. Freshly dissected left stifle joints were embedded in OCT and cryosectioned to 10-40µm in the coronal plane. Atomic force microscopy (AFM) nanoindentation was performed in 1X PBS using polystyrene microspherical tips (Ø25µm, $k \sim 0.6\text{N/m}$) at ≥ 10 locations within the inner and outer meniscus per specimen. The effective indentation modulus (E_{ind}) was calculated from the finite thickness-corrected Hertz model (Fig. 2a-b).⁵ Menisci from right hindlimbs were identified and isolated under a dissecting microscope, minced to $\sim 1\text{mm}^3$ and cultured in basal medium (DMEM, 10% FBS, 1% anti/anti) to allow cell egress. Isolated MFCs were seeded on fibronectin-coated polyacrylamide (PA) hydrogels ($E=5$ or 55kPa) or glass for 24h, fixed, and stained for YAP, actin, and nuclei. To assess contractility, bovine collagen-I gels (120,000 cells in 1.5mg/mL collagen) were prepared and gel contraction was measured over 14d in culture. Differences between groups were assessed via two-way ANOVA with Šidák's multiple comparisons test at $\alpha=0.05$.

RESULTS: Histological assessments of the hindlimb during early gestation (E28-42) were used to establish the timing of stifle joint formation in the Yorkshire pig. Cartilaginous condensations at the prospective femur and tibia locations were apparent at E28. Interzone condensation at the future joint line occurred from E32-35 with primitive menisci visible at E35. By E42, the joint was fully cavitated and the menisci were separated from the surrounding articular cartilage (Fig. 1, top row). SO/FG and AB/PSR staining showed regional ECM specification was evident by E63, and the inner and outer zones became increasingly specialized throughout perinatal development and into adulthood (Fig. 1, bottom row). AFM nanoindentation revealed rapid stiffening of the primitive meniscus ECM throughout gestation. The microscale indentation modulus (E_{ind}) of the outer meniscus was significantly greater than the inner zone at all timepoints, indicating the distinct regional microenvironments develop early in prenatal development ($***p < 0.001$, Fig. 2c). E_{ind} within each region were not significantly different through early fetal development but increased 3-fold from E84 to P0 and an additional 5-fold from P0 to adult ($\#p < 0.0001$ vs. fetal, $\wedge p < 0.0001$ vs. P0, Fig. 2c).

Mechanoactivation (e.g., cell area and YAP nuclear localization) of cells from all timepoints increased with increasing substrate stiffnesses, as expected ($*p < 0.05$, $**p < 0.005$, $***p < 0.0001$, Fig. 2d). On substrates of the same stiffness, nuclear YAP increased with maturation ($\#p < 0.001$, Fig. 2e) and in adult tissues, was greater in outer zone MFCs than inner zone MFCs ($\wedge p < 0.001$, Fig. 2e). Similarly, the rate of gel contraction increased with maturation and was greater for outer zone MFCs than age-matched inner zone MFCs. Shorter half-contraction times (time to reach 50% contraction, $t_{1/2}$) were observed with maturation and outer zone specialization ($***p < 0.001$, $****p < 0.0001$, Fig. 2f).

DISCUSSION: This work represents the first study of the morphological and mechanobiological changes that govern meniscus formation and specialization in the Yorkshire pig. In this model, primitive meniscal structures are distinct and separated from surrounding articular cartilage by E42 (comparable to E16.5 in the mouse and \sim E56 in the human). Subsequent histology and AFM nanoindentation revealed the microenvironmental distinctions between the proteoglycan-rich inner meniscus and type-I collagen-rich outer meniscus are apparent early in fetal development. At the cellular level, YAP activation and intrinsic cellular contractility were greater in outer zone MFCs and increased with maturation. Together, these results suggest exposure to a stiffer, more aligned microenvironment *in vivo* may prime MFCs towards enhanced mechanosensitivity. Ongoing work will continue probing the phenotypic and mechanosensitive refinement of the developing meniscus via transmission electron microscopy (TEM), RNAscope, and single cell RNAseq.

SIGNIFICANCE: This work establishes a large animal model of knee joint formation and reveals micromechanical specialization of meniscus ECM and resident cells begins early in fetal development and continues with maturation.

REFERENCES & ACKNOWLEDGEMENTS: [1] Ionescu *Tissue Eng. Part A*, 2011. [2] Qu+ *Sci. Rep.*, 2018. [3] Englund+ *Arthritis Rheum.*, 2009. [4] Tsinman+ *FASEB J*, 2021. [5] Kwok+ *Acta Biomater.*, 2023. [6] Tsinman+ *JOR*, 2023. This work was supported by the NIH (R01AR075418, P30AR069619).

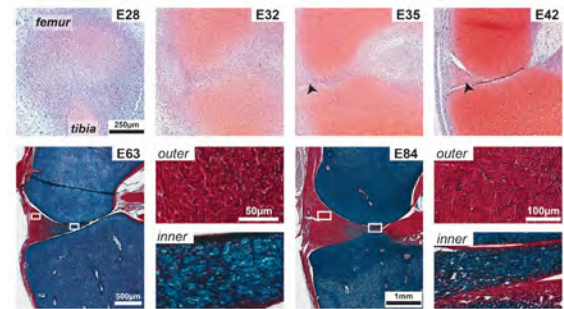


Fig. 1. SO/FG staining of early stifle joint formation (top row). AB/PSR staining shows regional specialization between the proteoglycan-rich inner zone (blue) and collagen-rich outer zone (red) by E63 (bottom row).

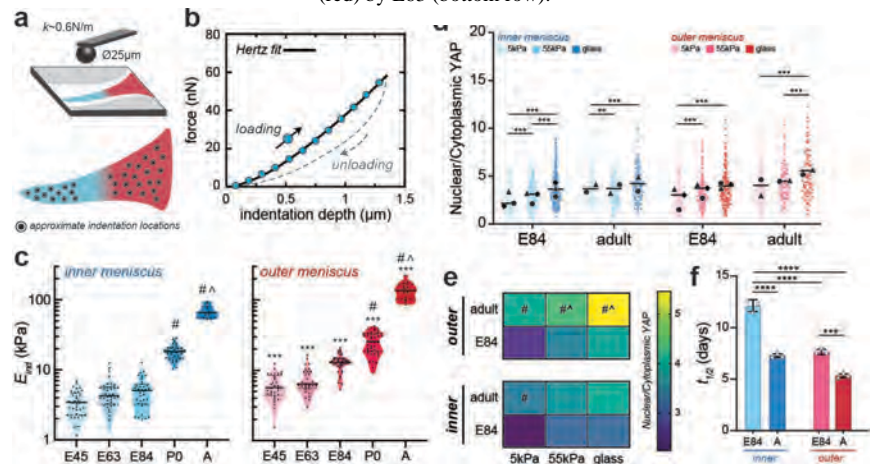


Fig. 2. (a-b) Schematic of AFM nanoindentation methods. (c) E_{ind} of inner and outer meniscus at each timepoint. (d) YAP nuclear localization on substrates of different stiffnesses. (e) Heatmap of YAP nuclear localization changes. (f) $t_{1/2}$ decreases with maturation and outer zone specialization.

Using an instrumented insole to estimate Achilles tendon loading in pregnant women during walking

Afua Nkansah-Andoh¹, Michelle Meyers¹, Devyn Russo¹, Casey Humbyrd, M.D., M.B.E.¹, Josh Baxter, Ph.D.¹

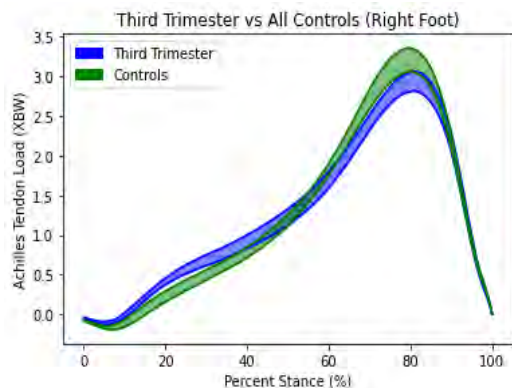
¹Department of Orthopedic Surgery, University of Pennsylvania, Philadelphia, PA

afuan@seas.upenn.edu

Introduction: Over 3 million women per year in the United States alone get pregnant, [1] and nearly 70% of these women experience some type of musculoskeletal pain such as lower back pain, leg pain, or pelvic girdle pain [2]. Despite the large number of pregnant women with musculoskeletal pain and symptoms, biomechanical research has largely avoided studying the effects of pregnancy on musculoskeletal function and symptoms. While most pregnant women experience musculoskeletal pain and symptoms, it is unclear how tendon loading - which is the primary driver of joint loading - changes during pregnancy. The purpose of this study was to quantify Achilles tendon loading in pregnant women while walking and compare it to females who are not pregnant. We hypothesized that pregnant women in their third trimester of pregnancy walk with different Achilles tendon loading profiles compared to women who are not pregnant and have never been pregnant.

Methods: 8 third trimester patients (age: 34.25 ± 3.45 y/o, BMI: 28.83 ± 3.54 kg/m²) and 7 control patients (age: 27.00 ± 1.41 y/o, BMI: 22.34 ± 2.14 kg/m²) performed diagonal walks on flat ground at a medium walking speed after providing informed consent in this IRB-approved study. The BMI for the control and third trimester patients was calculated using their weight at the time of the visit. Patients were provided sneakers (Air Pegasus: Nike, Beaverton, OR) containing an instrumented insole (Loadsol, Novel) to wear during their visit. We used the instrumented insoles to estimate Achilles tendon loading because these sensors increase our ability to collect data faster compared to using embedded force plates that only capture valid data when a patient steps directly on the force plate. Patients were instructed to perform 6 trials at their self-selected medium walking speed for ~6 meters. We estimated the moment about the ankle using our validated algorithm that used foot-ground interaction forces measured by the instrumented insoles [4]. We then divided this ankle moment by 5 cm, which is the Achilles tendon moment arm, to estimate the load experienced by the Achilles tendon. We normalized Achilles tendon loading by body weight to compare between patients. The data for the third trimester and control patients was then averaged using a bootstrap with a confidence interval of 95%.

Results and Discussion: Comparing both the third trimester patients and the control patients, the third trimester patients had an average peak load of 3.06 times body weight while the control patients had a peak load of 3.36 times body weight (Figure 1). Additionally, the third trimester patients had a higher initial load experienced by the Achilles tendon in the first 25% of their step compared to the control group. We hypothesize that the higher initial load experienced by the Achilles tendon in the first 25% of the stance is because of the change in center of mass that pregnant women experience due to the additional weight that they are carrying in the front of their body. Because of this additional weight, their feet must support more weight as they enter heel-strike so they do not fall forward as they walk, causing an increase in the initial load experienced by the Achilles tendon during walking.



Conclusion: Our preliminary findings suggest that pregnant women in their third trimester of pregnancy walk with altered Achilles tendon loading compared to non-pregnant females. Establishing biomechanical differences between pregnant women and non-pregnant women could serve as a predictor for musculoskeletal pain experienced during walking for pregnant women.

Figure 1: Achilles tendon loading during a self-selected medium walking pace estimated by using an instrumented insole placed in lab provided sneakers. Loading was normalized by the patient's body weight in kilograms and was calculated on the right foot.

References:

- [1] M. J.K., B. Hamilton E., J. A., A. Driscoll, and C. Valenzuela. *Births: Final data for 2021*, Jan. 2023. doi:10.15620/cdc:122047
- [2] F. M. Kovaacs, E. Garcia, A. Royuela, L. González, and V. Abraira. "Prevalence and factors associated with low back pain and pelvic girdle pain during pregnancy." *Spine*, vol. 37, no. 17, pp. 1516–1533, Aug. 2012. doi:10.1097/brs.0b013e31824dc674
- [3] F. Dehghan *et al.*, "The effect of relaxin on the musculoskeletal system." *Scandinavian Journal of Medicine & Science in Sports*, vol. 24, no. 4, Nov. 2013. doi:10.1111/sms.12149
- [4] T. J. Hullfish and J. R. Baxter. "A simple instrumented insole algorithm to estimate plantar flexion moments." *Gait & Posture*, vol. 79, pp. 92–95, Jun. 2020. doi:10.1016/j.gaitpost.2020.04.016

3D Collagen Fibril Orientation Mitigates Microscale Fatigue in Bone

Stephen Ching¹, Riti Sharma², Ottman Tertuliano²

¹Department of Bioengineering, University of Pennsylvania

²Department of Mechanical Engineering and Applied Mechanics, University of Pennsylvania

Introduction: Bone is a composite tissue primarily composed of mineral and collagen. Its hierarchical organization gives rise to mechanisms that resist crack growth across all length scales [1,2]. Toughening at the nano- and micro-scale has previously been observed primarily by mineralized collagen fibril pullouts and bridging [3]. However, the fundamental response of mineralized collagen fibrils to dynamic physiological loads remains poorly understood [3]. Our objective is to experimentally answer how nano- and micro-scale mechanisms prevent catastrophic failure during fatigue in bone.

Methods: Bone beams ($50 \times 10 \times 10 \mu\text{m}^3$) were milled from trabecular bone acquired from femoral condyle of human cadaver with no history of bone diseases (Articular Engineering). FIB-SEM was used to mill samples such that the mineralized collagen fibrils were approximately parallel to the length of the beam. A notch was introduced into the beam to create an initial flaw, or “microcrack”. Three-point bending fatigue experiments using an *in-situ* nanoindenter (KLA NanoFlip).

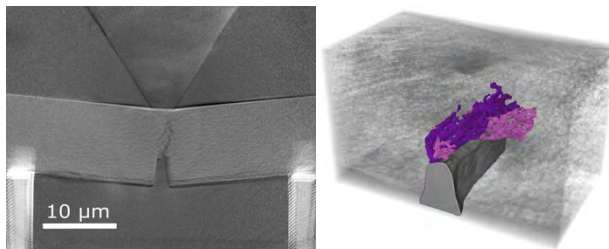


Figure 1. (a) Radiographic imaging of *in situ* nanomechanical experiments resolve nanoscale fibrils (b) Crack and branches can be segmented in 3D from tomography.

we applied 10,000 cycles of constant amplitude loading to initiate and propagate a crack (**Fig 1A**). Load, displacement, and dynamic stiffness were collected throughout the experiment and used to calculate effective crack growth per loading cycle (da/dN) and effective crack length (Δa). The 3D structure of the bone beam was imaged via synchrotron tomography before and after mechanical testing. The resulting volume was imported in 3D Slicer (3DSlicer.org), where post-fatigue cracks were segmented, and their medial surfaces were extracted (**Fig 1B**). Using MATLAB, the volume was divided into subvolumes to quantify the collagen fibril orientation and correlate it to the direction of crack growth.

Results: Tomography data shows the formation of a main crack (primarily mode I) growing vertically from the notch and four crack branches (mixed mode growth) stemming from the main crack. Relative to the surrounding collagen fibrils, the main crack is primarily oriented orthogonal and oblique while the crack branches are highly aligned. A significant difference in alignment between the main crack and the branches was observed ($P < 0.0001$) (**Fig 2A**). Further, when plotted over the effective crack length, the mean crack alignment decrease aligns with the increase in crack growth rate (**Fig 2B**).

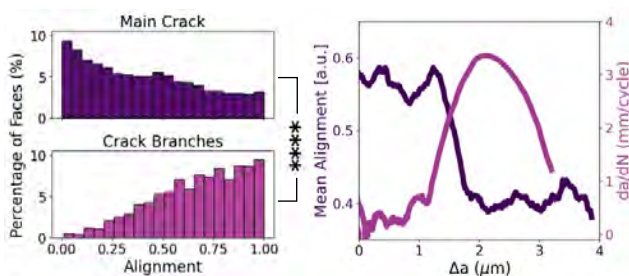


Figure 2. (a) The faces of the main crack are not aligned with surrounding mineralized collagen, but the crack branches are highly aligned. (b) Crack growth is slow when the crack is more aligned but fast when alignment is low.

Discussion: We present a method for performing *in situ* fatigue testing to observe nanoscale behavior in bone. Crack growth rate was slower when Δa was small, and the crack face was better aligned with surrounding collagen fibrils, suggesting that collagen orientation may deflect energy away from the main crack through branching. This dissipative mechanism is a form of toughening that resists the growth of cracks at the micron scale.

References: [1]Ritchie et al., *Physics Today*, 2009. [2]Launey et al., *Annu Rev Mater Res*, 2010. [3]Tertuliano et al., *Bioinspir Biomim*, 2021.

O-PTIR Spectral Imaging of Bone Composition at the Sub-micron Scale

Reshma Sudhesh¹, Michael W. Hast², Chamith S. Rajapakse^{2,3}, Nancy Pleshko¹, William Querido¹

¹Department of Bioengineering, Temple University, Philadelphia, PA

²Department of Orthopedic Surgery, University of Pennsylvania, Philadelphia, PA

³Department of Radiology, University of Pennsylvania, Philadelphia, PA

INTRODUCTION: Osteoporosis is a skeletal disease characterized by decreased bone strength and an increased risk of fractures, disproportionately affecting post-menopausal women. While bone mineral density (BMD) of the femoral neck is the primary metric used for diagnosing osteoporosis, it is recognized that BMD assessment alone is a poor predictor of bone mechanics, failing to identify nearly half of the women at high risk of hip fractures. This is because fracture resistance is influenced by factors beyond BMD, such as bone geometry, turnover rate, porosity, and tissue composition. Furthermore, because bone structure is hierarchical, these properties can vary at different length scales within the tissue. Therefore, elucidating the determinants of osteoporosis requires an understanding of the compositional properties at every level of the bone hierarchy. At the micron and sub-micron levels, mineralized collagen fibers form structures called osteons. Osteons are the basic functional and mechanical units of cortical bone and play key roles in determining bone strength, making them critical subjects for compositional studies. Our research explores the use of a new modality, optical photothermal infrared (O-PTIR) spectroscopy, which enables assessing tissue composition at an unprecedented 500 nm spatial resolution – ideal for studying osteons.

METHODS: Three 1-mm-thick cross-sections of the femoral neck from human cadaveric bones were compositionally assessed using the O-PTIR mIRage microscope in two separate experiments. The first involved collecting spectra from four spatially defined regions: inner, mid, and outer osteonal lamellae, and interstitial space. 5-10 dispersed spectra were collected per region from five osteons per sample. In the second experiment, a line scan collected spectra every 0.5 μm from the center of the osteon, through the lamellae, and into the interstitial space from five different osteons per sample. Post-processing of the spectra included smoothing, baselining, area normalization, and taking the second derivative to better quantify the phosphate (1034 cm^{-1}), carbonate (877 cm^{-1}), and amide I (1660 cm^{-1}) peaks using the Unscrambler software. Peak ratios reflective of mineral content ($1034/1660$) and carbonate content ($877/1034$) were quantified and outliers were eliminated.

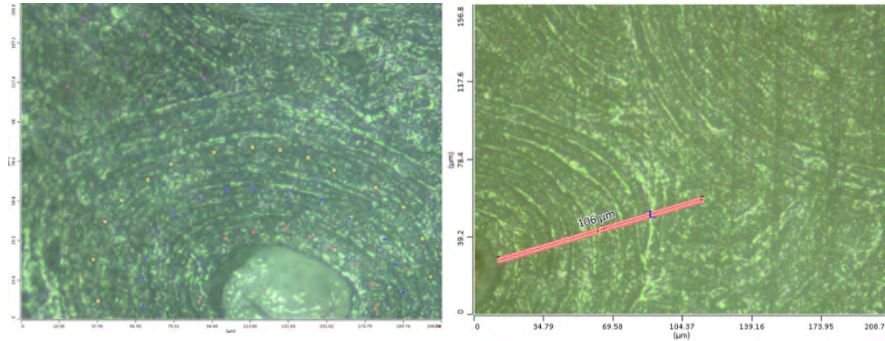
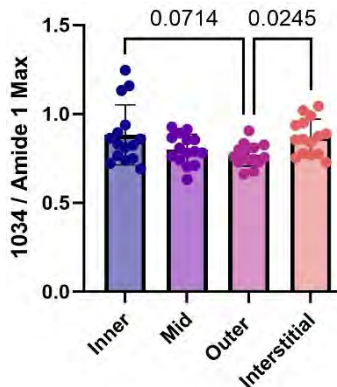


Figure 1: Left – Experiment 1 showing spatially defined regions within osteon.

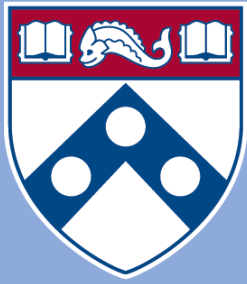
Right – Experiment 2 showing example line scan. Line length pictured is 106 μm .

RESULTS and DISCUSSION: The average peak ratios for mineral content ($1034/1660$) from each region (inner, mid, outer, interstitial) in Experiment 1 revealed significant differences between the inner and outer regions ($p = 0.071$) and between the outer and interstitial regions ($p = 0.024$).



These results indicate that the innermost and interstitial spaces are more mineralized than the center. This was consistent with findings from the line scans in Experiment 2, which showed that mineral content in most osteons followed a concave (U-shaped) trend, indicating that the ends of the osteon are generally more mineralized than the center. Plots for carbonate content ($877/1034$) in the first experiment revealed a significant difference between the inner and interstitial region ($p = 0.0066$), while the second experiment showed an even split between concave and convex trendlines, indicating that carbonate content is much more variable and heterogeneous, consistent with earlier studies. Our research highlights the potential of O-PTIR as a groundbreaking tool for acquiring bone tissue information at an unprecedented resolution.

Figure 2: Experiment 1, Mineral Content Results



Penn Center *for*
Musculoskeletal Disorders

UNIVERSITY *of* PENNSYLVANIA

Histology Core Abstracts

Effects of Maternal Exercise on Embryonic Bone Formation

Devin C. Gottlieb^{1,2}, Christopher J. Panebianco², Niamh C. Nowlan³, Joel D. Boerckel^{1,2}

¹Department of Bioengineering, University of Pennsylvania, Philadelphia, PA,

²Department of Orthopaedic Surgery, University of Pennsylvania, Philadelphia, PA

³University College Dublin, Mechanical and Materials Engineering, Dublin, Ireland

Introduction: Endochondral ossification, essential for fetal long bone development, begins with mesenchymal progenitor aggregation at embryonic day (E) 11.5. By E13.5, chondrocytes form a cartilage template, which matures and leads to the primary ossification center (POC) by E15.5. Increased vascularization at the POC replaces hypertrophic chondrocytes with bone, with remaining chondrocytes localizing to the growth plates.

Mechanical stimulation is known to play a pivotal role in endochondral ossification. Fetuses that lack mechanical stimulation, termed fetal akinesia, have impaired bone growth and skeletal deformities. Postnatal treatments for such conditions are unfavorable due to reduced morphogenic plasticity in the mature skeleton. Even when a musculoskeletal condition relating to reduced movements is identified *in utero*, there is currently no commonly performed treatment that can reduce its severity. Maternal exercise has emerged as a potential *in utero* therapeutic strategy to enhance embryonic skeletal development by providing compensatory mechanical stimuli during critical periods of bone formation. Subjecting pregnant mice to maternal wheel running exercise could serve as a novel system for studying the effects of *in vivo* mechanical loading on skeletal development.

Materials and Methods: Female C57BL/6J mice acclimated to running wheels (minimum 2 weeks), mated, and were caged without wheels until E13.5. Pregnant mice ran for one hour daily from E13.5 to E16.5 (Exercise), while controls (Sham) had locked wheels. Embryos were harvested at E17.5, and forelimb samples were then collected. Isolated forelimbs were embedded in optimal cutting temperature compound for cryosectioning. Serial cryosections (10 μm thickness) of the humerus were then prepared for histological analysis. Sections were stained with collagen 10, phalloidin, and alkaline phosphatase (ALP). Images were captured using the Zeiss Axioscan digital slide scanner, and quantitative analysis was conducted using ImageJ. The Student's t-test and Kolmogorov Smirnov test (significance set at $p < 0.05$) were used to determine significance.

Results, Conclusions, and Discussions: Staining for collagen 10 allowed for the quantification of the distal hypertrophic zone length. A significantly decreased length was seen in the Exercise group, indicating more advanced bone growth. Phalloidin intensity was measured along the humerus to determine the effects of maternal exercise on F-actin distribution within the POC. The Exercise group had a significantly greater intensity throughout much of the POC, indicating a greater level of cytoskeletal tension that is essential for mechanoregulated bone formation. ALP staining for osteoblastic bone formation activity revealed no significant differences in ALP intensity for both the POC and BC regions as a result of maternal exercise, although there seems to be a noticeable increase in the intensity of the BC (which may imply a role in early bone formation). Immunofluorescent staining with endomucin may provide additional insight into the POC, since ALP intensity may be confounded by enhanced blood vessel infiltration, which would indicate POC maturity. These findings imply that the exercise-induced mechanical stimuli during pregnancy can positively influence skeletal development by promoting bone formation processes. Future studies will conduct similar histological analyses on embryos from muscular dysgenesis and Pax3 Spd/Spd mice, which are models of fetal akinesia, to assess the therapeutic capacity of maternal exercise on fetal akinesia.

Tnfaip8 and *Tipe2* Gene Deletion Ameliorates Immediate Inflammatory Responses and Proteoglycan Loss in the Injured Mouse Intervertebral Disc

Zuozhen Tian¹, Jiawei Lu¹, Frances S. Shofer¹, Ling Qin¹, Honghong Sun¹, Yeji Zhang^{1,2}

¹Perelman School of Medicine, University of Pennsylvania; ²Corporal Michael J. Crescenz Veterans Affairs Medical Center, Philadelphia, PA

INTRODUCTION: TNFAIP8 and TIPE2 belong to the TNFa-induced protein 8 (TNFAIP8, also known as TIPE) family. They fine-tune inflammation by controlling apoptosis and directing leukocyte migration. Nucleus pulposus (NP) cell loss is a hallmark of IVD degeneration in response to injury.¹ TIPE2 is required for leukocyte polarization,² and coordinates with TNFAIP8 to direct leukocyte migration.³ *Tnfaip8* and *Tipe2* gene expression changed following mouse tail intervertebral disc (IVD) injury,⁴ suggesting that they play a role in the injury/repair responses. Here, we examined the effects of their function loss on the IVDs in mice with these genes deleted.

METHODS: We studied tail IVDs in TNFAIP8 or TIPE2-deletion and double knockout mice (*Tnfaip8*^{-/-}, *Tipe2*^{-/-}, and *Tnfaip8/Tipe2* dko), and wild type (WT) controls (young adults age 10-11 weeks, mixed males and females). Tail IVDs were injured with the adjacent intact discs as controls. The IVD segments including an intact and an injured IVD were isolated, embedded in paraffin, and sectioned. The sections were stained with Safranin O to reveal proteoglycans, and % red was quantified with the Image J software (NIH Imaging). Macrophages were identified by immunostaining of the F4/80 antigen, a known marker for cells of monocyte-macrophage lineage. Selected inflammatory marker and collagen gene expression was examined by Real Time PCR.

RESULTS: The *Tnfaip8*, *Tipe2*-mutant, and *Tnfaip8/Tipe2* double mutation (*Tnfaip8/Tipe2*-dko) mice all displayed higher levels of Safranin O staining post injury. There were fewer F4/80 positive cells in the injured IVD of *Tipe2*^{-/-} and *Tipe/Tipe2* dko mice than WT controls (n=9-11 mice/group; p<0.05; Fig. 1). *Il6* and *Adam8*, *Col1* gene expression was downregulated, and *Col2* gene expression was upregulated in the injured IVDs of *Tnfaip8/Tipe2* dko mice (n=18-35 mice/group; p<0.01).

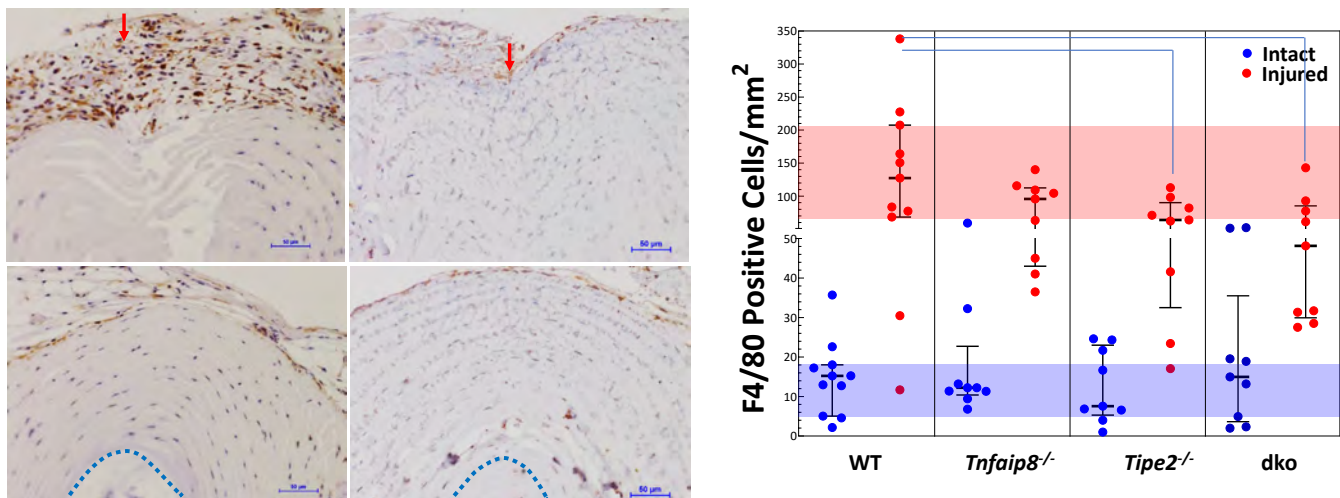


Figure 1. *Tipe2*-mutant (*Tipe2*^{-/-}) and *Tipe/Tipe2* double knock out (dko) mouse shows reduced macrophage (F4/80⁺) recruitment compared with wild type (WT) mouse. A: immunostained intervertebral discs. **Red arrow:** direction of injury to the annulus fibrosus (AF). **Bar: 50 μm.** **Blue dotted line** in intact discs outlines the border of AF and nucleus pulposus (NP). **Brown cells** are F4/80⁺ cells; **scale bars: 50μm.** **B:** F4/80 positive cell count. Each symbol represents data from one mouse; *P<0.05.

DISCUSSION: We found less proteoglycan loss, fewer infiltrating macrophages, lower levels of inflammatory cytokine genes in the IVDs of mice with *Tnfaip8* or *Tipe2*, or both genes deleted. In light of their functions in modulating apoptosis and inflammation, further studies of their distribution and role in disc degeneration and back pain may reveal disease mechanisms and molecular targets for treatments. Preserving proteoglycans and controlling inflammation are goals following an acute IVD injury. TNFAIP8 and TIPE2 may serve as molecular targets to achieve these goals.

Disclosures: This work was supported, in part, by research grants to YZ from the Department of Veterans Affairs Healthcare Network and the NIH (5R21AR078386-02). We gratefully thank Dr. Martin F. Heyworth for critical editing.

REFERENCES:

1. Wei Y, Tian Z, Tower RJ, et al. *Am J Phys Med Rehabil.* 2020.
2. Fayngerts SA, Wang Z, Zamani A, et al. *Nat Immunol.* 2017;18(12):1353-1360.
3. Sun H, Lin M, Zamani A, et al. *Sci Rep.* 2020;10(1):6617-w. 10.1038/s41598-020-63629-w.
4. Tian Z, Shofer FS, Yao L, et al. *JOR Spine.* 2020;3(2):e1093.

Determining the Effect of CD14 Deficiency on Osteoblastogenesis and Subchondral Bone Remodeling In Mice

Kate L. Sharp, Lance A. Murphy, Kevin G. Burt, Anna E. Rapp, Vu Nguyen, Baofeng Hu, Robert L. Mauck, Carla R. Scanzello
University of Pennsylvania, Perelman School of Medicine, Philadelphia, PA

CMC VA Medical Center, Translational Musculoskeletal Research Center, Philadelphia, PA

Disclosures: KLS (N) – katelsharp1@gmail.com, LAM (N), KGB (N), AER (N), VN (N), BH (N), RLM (4, 5, 8), CRS (8).

INTRODUCTION: Osteoarthritis (OA) is a debilitating disease affecting ~54% of US adults at age 75 and over (1). Toll-like receptors (TLRs), in particular TLR4, have been implicated in disease severity and progression in OA (2). The TLR4 co-receptor, CD14, is also associated with OA features including osteophyte formation and pain (2). CD14 sensitizes TLR4, allowing it to respond to low concentrations of its ligand, lipopolysaccharide (LPS), a prevalent inflammatory marker in OA (3). Generally, osteoblasts (OB) from the mesenchymal cell (MSC) lineage are not known to express CD14. However, they do express TLR4, and LPS has been reported to have a dual effect on OB differentiation, being stimulatory at low concentrations and inhibitory at high concentrations (4). Additionally, TLR4KO and CD14KO mice have been reported to have greater bone mineral content than that of wild-type mice (5). With this, we aimed to identify the effect of CD14 deficiency on bone remodeling in a murine model of OA *in vivo* and characterize the effect of low-level OA-relevant LPS stimulation on osteoblastogenesis *in vitro*. **We hypothesized that CD14 deficient mice would show decreased OB activity in response to DMM injury *in vivo* and would exhibit reduced osteoblastogenesis *in vitro* in response to low-level LPS.**

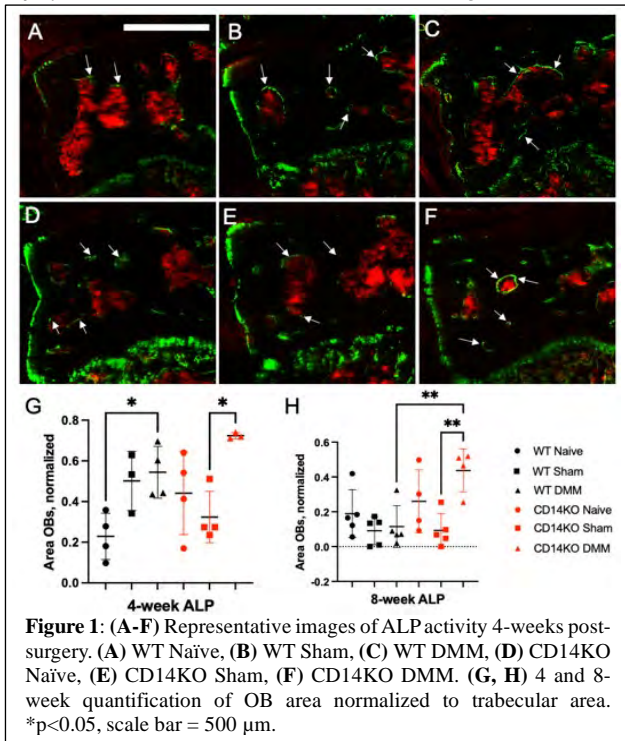


Figure 1: (A-F) Representative images of ALP activity 4-weeks post-surgery. (A) WT Naïve, (B) WT Sham, (C) WT DMM, (D) CD14KO Naïve, (E) CD14KO Sham, (F) CD14KO DMM. (G, H) 4 and 8-week quantification of OB area normalized to trabecular area. *p<0.05, scale bar = 500 μ m.

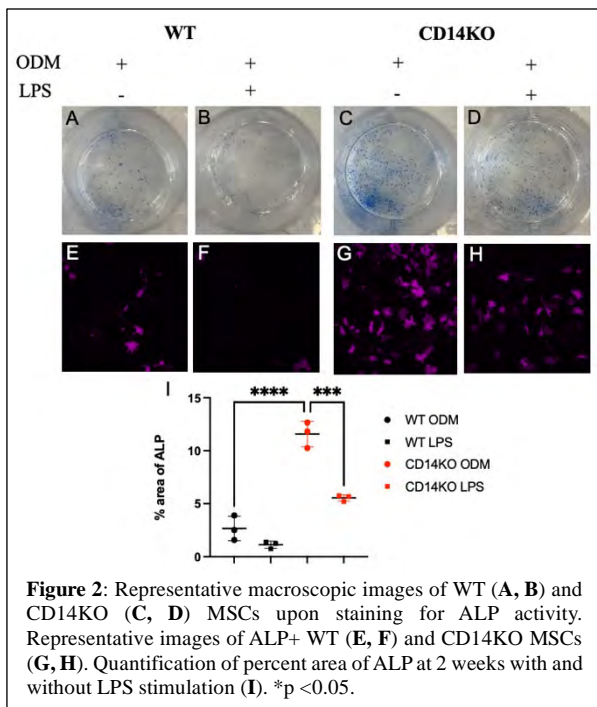


Figure 2: Representative macroscopic images of WT (A, B) and CD14KO (C, D) MSCs upon staining for ALP activity. Representative images of ALP+ WT (E, F) and CD14KO MSCs (G, H). Quantification of percent area of ALP at 2 weeks with and without LPS stimulation (I). *p<0.05.

METHODS: Murine sample processing and cryosectioning: Destabilization of the medial meniscus (DMM) or sham surgery was performed on C57BL/6 (WT) and CD14KO mice at 12 weeks of age. The knees were harvested 4 weeks (n=4) and 8 weeks (n=5) post-surgery, fixed, permeabilized with 20% sucrose/2% polyvinylpyrrolidone (PVP) for 3-4 days before being embedding in optimal cutting temperature compound (OCT) and cryosectioned at 5 μ m. In vivo Alkaline Phosphatase (ALP) staining and analysis: The sections were incubated with the ELF 97 Endogenous Phosphatase Detection substrate (1:20) for 30 seconds and mounted with nucleic acid stain TO-PRO-3 mounting media to detect OBs. The slides were scanned via AxioScan and analyzed using ImageJ to determine the ratio of the area of osteoblasts to the overall trabecular area of the medial subchondral bone region, excluding osteophytes at the margins. MSC isolation and cell culture: Bone marrow was flushed and cultured from the tibiae and femora of 3-6 WT and CD14KO mice at 12 weeks of age. 24 hours after isolation, nonadherent cells were removed from the plate and discarded. The adherent cells were cultured in 10% FBS + 1% penicillin-streptomycin DMEM (complete media - CM) until 80-90% confluency was reached. Upon confluency, the cells were replated and cultured in osteogenic differentiation media (ODM – CM DMEM + 10 μ g/mL ascorbic acid-2-phosphate + 10 mmol β -glycerophosphate) with and without LPS (1ng/mL). ALP staining in vitro and image analysis: After 2 weeks of treatment with LPS, cells were stained for ALP. Cells were imaged at 4x magnification with Cy5 fluorescent filter and percent area of ALP was quantified by mean fluorescent intensity (MFI). **RESULTS:** *In vivo:* Representative ALP staining of WT (Fig. 1A-C) and CD14KO (Fig. 1D-F) sections are shown 4-weeks after surgery at the medial tibial plateau. The area of trabeculae covered by ALP+ cells increased in both the WT and CD14 KO DMM group compared to either naïve or sham controls. (Fig 1G). At 8 weeks there was no difference between WT DMM and WT control groups. However, the CD14KO DMM group was elevated in ALP area compared to both CD14KO sham and WT DMM (Fig. 1H). *In vitro:* After 2 weeks of culture in ODM without LPS, there was more OB differentiation in the CD14KO strain compared with WT (p<0.0001). In LPS treated groups ALP staining decreased in both WT and CD14 strains by roughly 50%, but only significantly in the CD14KO strain (Fig. 2).

DISCUSSION: These findings indicate that OB number increases post OA-inducing DMM injury at 4 weeks in both strains. By 8 weeks, OB number had decreased back to naïve levels in WT mice subjected to DMM but was still increased in the CD14KO strain. This indicates prolonged osteoblastogenesis in response to DMM injury in the CD14KO strain. Consistent with these *in vivo* results, *in vitro* we observed augmented OB differentiation in the CD14KO strain at baseline. Continually, LPS was shown to be inhibitory on osteoblastogenesis, even in the absence of CD14. Future research is needed to explore the mechanisms driving increased osteoblast presence and differentiation in the absence of CD14, including the role of Toll-like receptor signaling in osteoblastogenesis. But overall, these results suggest a complex relationship between LPS, TLR4 and CD14 in osteoblastogenesis that may be relevant to understand TLR effects in disease states characterized by aberrant bone remodeling.

REFERENCES: [1] Elgaddal, N+, *NCHS* 2024; [2] Bartels, Y+, *British Soc. for Rheumatology* 2024; [3] Bandow, K+, *ScienceDirect* 2010; [4] Muthukuru, M+, *Nature* 2014; [5] Johnson, G+, *PubMed* 2004.

Aging Alters Tenocyte Response to Inflammation with Enhanced Sensitivity and Cellular Dysfunction

Tyler Blanch¹, Ellen Y. Zhang¹, Xi Jiang¹, Nathaniel A. Dymant¹, and Su Chin Heo¹

¹University of Pennsylvania, Philadelphia, PA

tblanch@seas.upenn.edu

Disclosures: Blanch (N), Zhang (N), Jiang (N), Dymant (N), Heo (5-4WEB Medical)

INTRODUCTION: Tendon injuries are common due to their critical load-bearing role, often leading to significant debilitation [1]. While the typical tendon injury response involves transient inflammation, aging tissues often fail to resolve these inflammatory signals, resulting in prolonged matrix degradation and altered cell phenotypes [2, 3]. However, the precise mechanisms by which inflammatory conditions affect tendon resident cells (i.e., tenocytes) and how aging influences these responses remain poorly understood. Thus, this study aims to identify the mechanisms of cellular dysfunction following inflammatory stimuli, such as tumor necrosis factor- α (TNF α), with a particular focus on age-related differences. Specifically, by employing super-resolution microscopy (i.e., H2B-STORM) and gene expression analysis, we explore how inflammatory conditions drive age-related phenotypic shift in tenocytes. This investigation probes the underlying mechanisms of tendon aging, with the goal of identifying potential therapeutic strategies to address chronic tendon degeneration.

METHODS: Mouse tenocytes were isolated from young (<5 weeks, male) and mature (>45 weeks, male) tail tendons following established protocols [4]. Tenocytes were cultured in basal media (control) or TNF α -containing media (20 ng/mL TNF α) for 0.5, 1, 3, or 6 hours (H) prior to imaging. To determine chromatin condensation status, fixed cells were immunostained for histone-H2B (Invitrogen) and a custom secondary antibody featuring activator-reporter dye pairs (Alexa Fluor 405-Alexa Fluor 647) for established H2B-STORM imaging [5]. Voronoi tessellation density of STORM images was quantified in MATLAB [5]. Additionally, cells were immunostained for Nuclear Factor Kappa B1 (NF κ B, Invitrogen) and counterstained with phalloidin and DAPI (Invitrogen) for immunofluorescence (IF) imaging. Nuclear localization of NF κ B was analyzed on Image-J. RNA was isolated for RT-PCR and RNA-sequencing (RNA-seq) (n = 3 biological replicates/condition) following established protocols, with downstream analysis conducted in R (DESeq2) [6]. Statistical analyses employed a one-way ANOVA with Tukey's post hoc testing.

RESULTS: H2B-STORM imaging revealed elevated chromatin condensation in mature tenocytes at control conditions compared to young cells (Fig. 1A), and TNF α treatment for 6 hours caused a significant increase in chromatin condensation in the mature cells only (Fig. 1C). Although IF analysis of NF κ B activation revealed consistent nuclear localization rates across both age groups (Fig. 2A), RT-PCR analysis indicated relatively higher expression of degenerative gene expression, such as MMP-13 and Caspase 11, in mature cells (Fig. 2B). Furthermore, the RNA-seq heatmap of tenogenic gene expression demonstrated distinct responses to inflammatory cues in mature cells, marked by reduced expression of tendon extracellular matrix (ECM) genes (Fig. 3A). Gene ontology of RNA-seq results revealed that both age groups exhibited similar upregulated pathways in response to TNF α ; however, young cells tended to downregulate lineage-specific markers, while mature cells showed downregulation in tissue development pathways (Fig. 3C).

DISCUSSION: This study provides crucial insights into the age-dependent responses of tenocytes to inflammatory stimuli, revealing significant differences in cellular behavior and gene expression between young and mature cells. Our findings reveal that mature tenocytes exhibit significant chromatin reorganization and increased chromatin condensation in response to TNF α , leading to altered gene expression and cellular dysfunction. The pronounced increase in chromatin condensation following TNF α treatment in mature cells underscores their heightened sensitivity to inflammatory cues with aging. Moreover, RNA-seq analysis revealed a distinct response to inflammation in mature cells characterized by highly reduced expression of tendon ECM genes and increased production of matrix-degrading enzymes, suggesting a shift towards a catabolic cellular phenotype. This shift, combined with the downregulation of tissue development pathways, points toward a potential mechanism of age-related dedifferentiation under chronic inflammatory conditions. Taken together, these findings underscore the need for targeted therapeutic strategies to address chronic tendon degeneration, particularly in aging populations, by mitigating inflammatory damage and acknowledging that mature tenocytes are more sensitive to inflammation.

SIGNIFICANCE: The study defines tenocyte responses to inflammation across different age groups, elucidating the mechanisms of inflammation-related changes in cell phenotype and guiding future treatment approaches for tendon disorders, including tendinopathy.

REFERENCES: [1] Mafulli+, *Am J Sport Med*, 2000; [2] Ellis+, *J Immunol Regen Med*, 2022; [3] Ireland+, *Mat Bio*, 2001; [4] Lee+, *BMC Musculoskelet Dis*, 2018; [5] Heo+, *Nat BME*, 2023; [6] Anders+, *Mol Biol*, 2010.

ACKNOWLEDGEMENTS: This work was supported by the NIH (P50 AR080581, K01 AR077087) and NSF (CMMI-1548571).

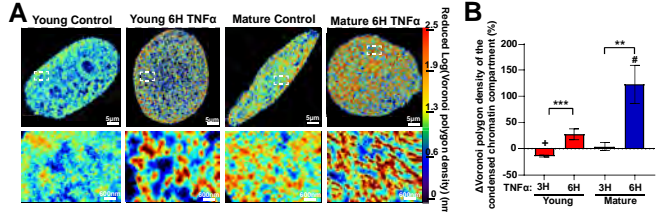


Figure 1. (A) Representative heat map images showing nuclear H2B localization density in young and mature tenocytes under control and TNF (6 hours) conditions. (B) Percentage change in chromatin condensation following TNF α treatment (3 and 6 hours) compared to control groups in young and mature tenocytes. (n=16 cells/group. **: p<0.01, ***: p<0.001).

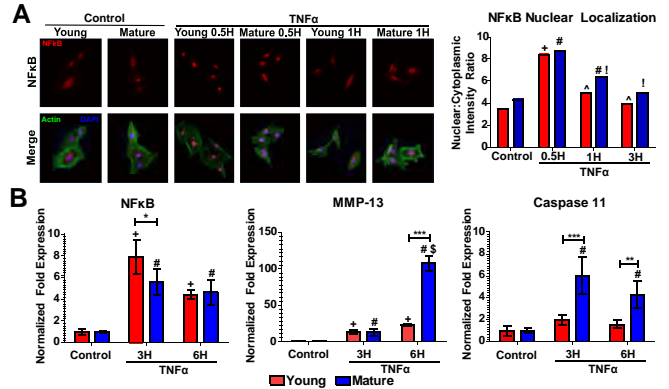


Figure 2. (A) Representative IF images showing NF κ B nuclear localization (red) with actin (green, cytoplasmic) and DAPI (blue, nuclear) counterstains. Quantification of the Nuclear:Cytoplasmic ratio of NF κ B with TNF α treatments (0.5, 1, and 3 hours). (n=60 cells/group). (B) RT-PCR results for NF κ B (left), MMP-13 (middle), and Caspase 11 (right) in control and TNF α -treated cells (3 and 6 hours). (n=3 technical replicates. +: p<0.05 vs young control, #: p<0.05 vs mature control, ^: p<0.05 vs young 0.5H, !: p<0.05 vs mature 0.5H, \$: p<0.05 vs mature 3H, *: p<0.05, **: p<0.01, ***: p<0.001).

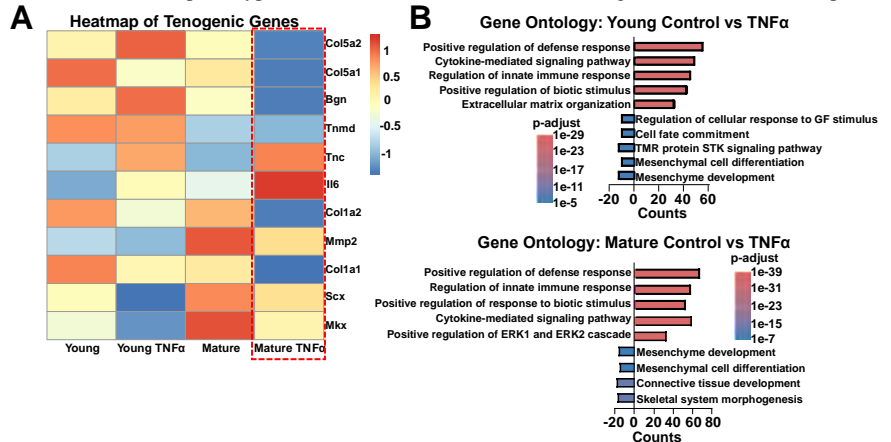


Figure 3. (A) RNA-seq heatmap showing tenogenic gene expression differences between young and mature cells with and without TNF α treatment (6 hours). Color represents calculated z-score. (B) Gene ontology analysis of RNA-seq data indicating significantly upregulated (positive) and downregulated (negative) gene categories between control and TNF α treatment. Bar length represents the number of unique genes per category, and bar color indicates p-adjust value. Results for young cells (top) and mature cells (bottom). (n=3 technical replicates per condition).

sPLA₂ Inhibitor-Loaded Lipid Nanoparticles for Osteoarthritis Treatment

Qiushi Liang (qiushil@seas.upenn.edu)^{1,2}, Tao Gui¹, Lijun Luo², Yulong Wei, Anatoliy V. Popov³, Qi He¹, Kyla Ortved⁴, Andrew Sourkas², Zhiliang Cheng², Ling Qin¹ (¹Department of Orthopaedic Surgery, ²Department of Bioengineering, ³Department of Radiology, ⁴School of Veterinary Medicine, University of Pennsylvania, USA)

Disclosures: Z.C., L.Q., and A.T are inventors on a patent related to this work filed by the University of Pennsylvania (no. 63/043,025., filed 23 June 2020).

INTRODUCTION: Chronic unresolved inflammation plays a critical catabolic role in osteoarthritis (OA) development and progression. Pro-inflammatory cytokines (i.e., IL-1 β and TNF α) up-regulate aggrecanases and collagenases in chondrocytes to degrade cartilage matrix. Secretory phospholipase A₂ (sPLA₂) is a heterogeneous group of enzymes that specifically hydrolyzes the sn-2 ester bond of membrane phospholipids to release free fatty acids, such as arachidonic acid and lysophospholipids, which are upstream mediators of inflammation in many chronic inflammatory diseases, including OA. Varespladib is a potent and clinically tested small molecule sPLA₂ inhibitor (sPLA₂i). In this study, we used lipid nanoparticles (LNPs) to deliver varespladib and evaluated the therapeutic efficacy of sPLA₂i-LNPs in attenuating OA progression in a mouse model.

METHODS: Varespladib-lipid conjugation– sPLA₂-cleavable varespladib-lipid conjugate was synthesized by reacting varespladib with lysophosphatidylcholine. The-COOH from varespladib and -OH from lysophosphatidylcholine form the sn-2 ester bond, which is selectively hydrolyzed by sPLA₂. sPLA₂i-LNP generation– The varespladib-lipid was incorporated into the lipid membrane shell by mixing with DSPE-PEG2000 and DOTAP, a cationic lipid. Horse cartilage explants – Medial femoral condyle cartilage biopsies with a diameter of 6mm and a thickness of 2-3mm from horses were treated with one of the following: PBS, IL-1 β +dimethyl sulfoxide (DMSO), empty LNPs, free sPLA₂i in DMSO, or sPLA₂i-LNPs for 7 days. Animals– All animal work was approved by the Institutional Animal Care and Use Committee at the University of Pennsylvania. 3-month-old male C57Bl/6 mice underwent destabilization of the medial meniscus (DMM) in their right knees and received 10 μ l of PBS, empty LNPs, free sPLA₂i, or sPLA₂i-LNPs via intra-articular (IA) injections starting immediately after surgery at once every 3 weeks for 12 weeks (n=6 mice/time point/group). In the loading model, 2-month-old male C57Bl/6 mice were subjected to a single loading episode composed of 60 cycles of 6 N peak load on their right knees, and IA injected with 10 μ l of PBS or sPLA₂i-LNPs starting immediately after surgery at once every 2 weeks for 4 weeks (n=6 mice/time point/group). Additional groups of mice (n=6/surgery) received sham surgery followed by PBS injections. Histology– Paraffin sections of knee joints were stained with H&E, Safranin O/fast green, or phospho-NF κ B p65 for immunohistochemistry. Pain assessment– Knee joint pain was evaluated weekly using von Frey filaments. Statistics– Data are expressed as means \pm SD and analyzed by one way ANOVA and unpaired, two-tailed Student's t-test.

RESULTS: The sPLA₂i-LNPs had a homogenous diameter around 12 nm (Figure 1A, B). They were stable in PBS over 7 days and in bovine fluid over 4 days, exhibiting satisfactory stability (Figure 1C, D). In vitro sPLA₂ activity assay demonstrated their sensitive response to environmental sPLA₂, with the inhibition effect being strongly correlated with the amount of varespladib (Figure 1E). Treatment of horse cartilage explants with IL-1 β induced OA-like degeneration after 7 days as shown by Safranin O staining (Figure 2). Strikingly, addition of sPLA₂i-LNPs at 60 μ M (sPLA₂i concentration) to culture medium almost completely restored cartilage extracellular matrix (ECM) to a healthy level (Figure 2). Free sPLA₂i showed partial beneficial effects but this effect was minor compared to sPLA₂i-LNPs as the positively charged DOTAP significantly enhanced the penetration of sPLA₂i into the tissue, thereby increasing its local concentration and therapeutic effect. To test the in vivo efficacy of sPLA₂i-LNPs, we utilized two mouse models of OA induced by DMM and loading to mimic chronic OA and post-traumatic OA, respectively. IA injections of sPLA₂i-LNPs into DMM knees greatly improved the morphology and structure of articular cartilage, leading to drastically reduced proteoglycan loss and synovitis at 3 months post-surgery (Figure 3A, B). Compared to free sPLA₂i group, mice receiving sPLA₂i-LNPs displayed 65% and 60% decreases in Mankin score and synovitis score, respectively (Figure 3C, 3D). Loading at 6N caused a lesion with proteoglycan loss in the lateral femoral articular cartilage surface in PBS-treated mice 1 month later (Figure 4A). Remarkably, compared to PBS, sPLA₂i-LNP treatment reduced the length of cartilage injury by 94% and Mankin score by 83% to a level similar to sham group (Figure 4B). Synovitis was partially alleviated (Figure 4C, D), leading to attenuated joint pain (Figure 4E). Mechanistically, sPLA₂i-LNPs significantly reduced levels of phospho-NF κ B p65 in both the cartilage and synovium of loaded knees (Figure 4F, G), thereby inhibiting the pro-inflammatory NF κ B pathway.

DISCUSSION: The delivery of small molecules like varespladib faces challenges such as rapid clearance, uncontrolled release, and low loading efficiency in drug delivery platforms. Our study addresses these issues by conjugating varespladib with lysophosphatidylcholine to create an sPLA₂-responsive LNP for OA therapy. Our results demonstrate that sPLA₂i-LNPs are stable and sPLA₂-sensitive. Additionally, they significantly reduced OA-related inflammation, cartilage degeneration, and synovitis symptoms in mouse OA induced by DMM and loading. Overall, the engineered, sPLA₂-responsive varespladib LNP offers controlled release and enhanced therapeutic efficacy, showing a great promise for OA treatment.

SIGNIFICANCE: This proof-of-principle study demonstrates the release profile and efficacy of LNPs with varespladib-lipid conjugation for OA treatment.

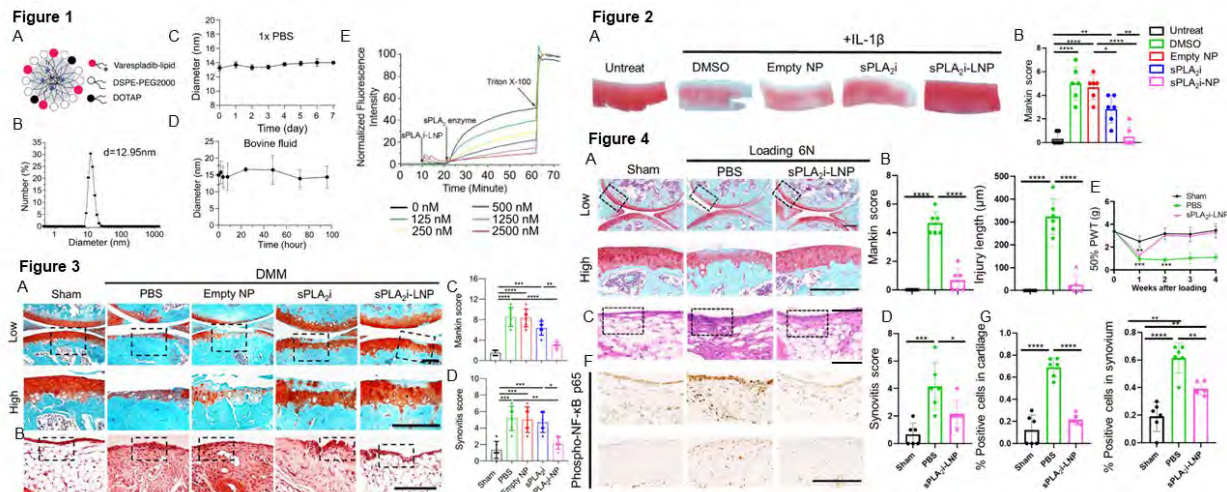


Figure 1. sPLA₂i-LNP synthesis and characterization. A: Schematic diagram of sPLA₂i-LNPs. B: diameter of LNPs by dynamic light scattering. C, D: Stability tests of the sPLA₂i-LNP. E: Inhibitory activities of sPLA₂i-LNPs at different concentrations of varespladib. **Figure 2. sPLA₂i-LNPs protect horse explants from OA degeneration.** A: SO/FG staining of the treated explants. B: Quantification of the Mankin scores across groups. **Figure 3. sPLA₂i-LNPs reduce joint destruction in DMM joints.** A, B: SO/FG results and Mankin scores of the cartilage. C, D: H&E staining of synovium tissue and quantification of synovitis scores. **Figure 4. sPLA₂i-LNPs attenuate joint destruction in loaded joints.** A, B: SO/FG and quantification of cartilage damage, represented by the Mankin scores and injury length. C: Von Frey results until 4 weeks after loading. D, E: H&E staining of synovium tissue and synovitis scores. F, G: Immunohistochemistry staining of phospho-p65 and its quantification. Scale bar, 200 μ m. *P < 0.05, **P < 0.01, ***P < 0.001, ****P < 0.0001.

CD14-deficiency increases osteoclastogenesis via a reduction in Type I Interferon signaling

Lance A. Murphy^{1,2}, Kevin G. Burt^{1,2}, Kate L. Sharp², Baofeng Hu^{1,2}, Vu Nguyen^{1,2}, Robert L. Mauck^{1,2}, Carla R. Scanzello^{1,2}

¹University of Pennsylvania, Perelman School of Medicine, Philadelphia, PA;

²CMC VA Medical Center, Translational Musculoskeletal Research Center, Philadelphia, PA

Disclosures: LAM (N) - Lance.murphy@pennmedicine.upenn.edu, BH (N), KGB (N), MW (N), VN (N), RLM (4, 5, 8), CRS (8)

INTRODUCTION: Osteoarthritis (OA) is also associated with aberrant bone remodeling leading to subchondral sclerosis and osteophyte formation (1). Toll-like receptor (TLR) ligands have been implicated in the severity and progression of OA after joint injury and with degeneration (2). CD14 is a GPI-anchored surface protein that functions as a co-receptor for several TLRs and is highly expressed in myeloid cell lineages, including the precursors of osteoclasts (OCs) (3,4). CD14 and TLR4 levels in the blood are associated with OA and associated osteophytosis (5). Toll-like receptor 4 (TLR4) activation is inhibitory to osteoclastogenesis and can act through multiple pathways, including the sequestration of NF- κ B as well as the production of Type I Interferons (6). Notably, our group previously showed that CD14-deficient mice have less subchondral bone remodeling after joint injury in a DMM (destabilization of the medial meniscus)-model of OA (7). To understand the cellular activities and signaling that underlies the differential bone remodeling observed after joint injury with CD14 deletion, we investigated how CD14-deficient OCs form *in vivo* and *in vitro*. **We hypothesized that depletion of CD14 would protect against TLR4-dependent inhibition of osteoclastogenesis through reduced Type I Interferon signaling.**

METHODS: Destabilization of the medial meniscus (DMM): DMM or sham surgery (n=5 per group) was performed on male C57BL/6 (WT) and CD14^{-/-} mice at 12 weeks of age. **Histology (n=4-5 per group):** Knees were harvested at 4 weeks post-DMM, then fixed, decalcified, and paraffin embedded. Tissue sections from the midpoint of the joint were stained with the Leukocyte Acid Phosphatase kit (Sigma-Aldrich) to identify osteoclasts. Focusing on the medial tibial plateau, OC cell number and trabecular surface area covered by OCs was measured across five 40X fields per mouse and was normalized by total trabecular surface area (ImageJ). **Cell isolation and culture:** For *in vitro* studies, bone marrow (BM) was pooled from the femorae and tibiae of 3 mice from each strain (WT, CD14 knockout, and Type I interferon receptor (IFNAR1) KO). Cells were cultured in complete α MEM + 30 ng/mL M-CSF for 5 days to expand OC precursors. Cells were then replated and cultured with RANKL (100 ng/mL) to induce osteoclastogenesis over 4 days. LPS (1 ng/mL, to activate CD14/TLR4 signaling), a small molecule TLR4 inhibitor (CLI-095), and an anti-IFNAR1 antibody were added alone or in combination to query the effect of specific pathway activation and inhibition. **Tartrate-resistant acid phosphatase (TRAP) staining and image analysis:** Cells were stained for TRAP 3 or 4 days after the addition of RANKL. Cells were imaged under 10X brightfield (5 images/well with 4 wells/timepoint), and OCs were identified by their TRAP staining and multinucleation. Images were quantified for percent area of the field covered by OCs (CellProfiler). **Bulk RNA sequencing:** RNA was harvested from WT and CD14 deficient osteoclasts 4 days after the addition of RANKL. Hallmark pathway analysis was used. Statistics: Unpaired t-tests were used to test differences between groups. Holm-Sidak correction for multiple comparisons was employed when multiple t-tests were used.

RESULTS: Representative TRAP staining in the subchondral bone of the tibial plateau in WT and CD14^{-/-} samples are shown (Fig 1A). Trabecular area covered by OC increased in both strains after sham and DMM surgeries (Fig 1B), but were higher in injured knees from CD14-deficient mice, indicating that OC presence increases with injury, and CD14-deficiency further increases OC presence in response to injury *in vivo*. In *in vitro* experiments, after 3 days of

RANKL treatment, cells from CD14-deficient mice showed more osteoclastic differentiation than WT cells, both in the absence and in the presence of LPS (Fig 2B, left). By day 4, WT and CD14-deficient OCs showed similar area coverage in the absence of LPS. However, when LPS was added, WT osteoclastogenesis was significantly decreased by 67%, whereas CD14-deficient osteoclastogenesis decreased by only 29% and was not significant (Fig 2B, middle). In the presence of the TLR4 inhibitor, CLI-095, osteoclastogenesis was higher for both strains and not impacted by LPS addition (Fig 2B, right), indicating that the impact of LPS on WT cells was mediated by TLR4. Hallmark pathway analysis of bulk RNA seq of OC from WT and CD14-deficient strains showed a decreased Type I interferon signature in CD14-deficient osteoclasts (Fig 3A). CD14-deficient cells again differentiated faster than WT cells at baseline (no LPS), but this difference was mitigated when a neutralizing Type I Interferon receptor antibody was added to the cultures (Fig 3B, left). In the presence of LPS, osteoclastogenesis was diminished in WT cells, and this was not rescued by the Type I Interferon receptor antibody (Fig 3B, middle). The IFNAR1KO cells differentiated faster than the WT cells at baseline, phenocopying the CD14-deficient cells. However, addition of LPS significantly reduced IFNAR1KO osteoclastogenesis, in contrast to the CD14-deficient cells (Fig 3C, right).

DISCUSSION: Our results show that CD14-deficient mice have an increased number of OCs in the medial tibial plateau both at baseline and 4 weeks after DMM or sham injury. Additionally, *in vitro*, CD14-deficient OC precursors differentiate into OCs faster than WT controls in response to RANKL and were less sensitive to the effects of LPS. Using both an IFNAR1 antibody and IFNAR1KO, we confirmed that the increased OC-genesis at baseline is due to Type I Interferon receptor signaling. However, the addition of LPS decreased osteoclastogenesis of the IFNAR1KO cells, but not of the CD14KO cells. This suggests that LPS-induced inhibition of osteoclastogenesis is independent of Type I IFN and is likely mediated through other CD14/TLR4 pathways.

SIGNIFICANCE/CLINICAL RELEVANCE: The protection against subchondral bone thickening observed in CD14 deficient mice in the DMM model (5) may be due to the increased presence of OCs. Understanding the role and specific mechanisms of CD14/TLR signaling in osteoclastogenesis may lead to new therapeutic strategies for diseases characterized by pathologic bone remodeling.

REFERENCES: [1] Donell, S *EFORT* 2019; [2] Miller, R+ 2019 [3] Zanoni, I+ *Front Cell Infect. Microbiol.* 2013; [4] Xue, J+ *Art Res Ther* 2020; [5] Daghestani, H+ *Arthritis Rheumatol* 2015; [6] Ji, J+ *J Immunol* 2009 [7] Sambamurthy, N+ *PLoS ONE* 2018;

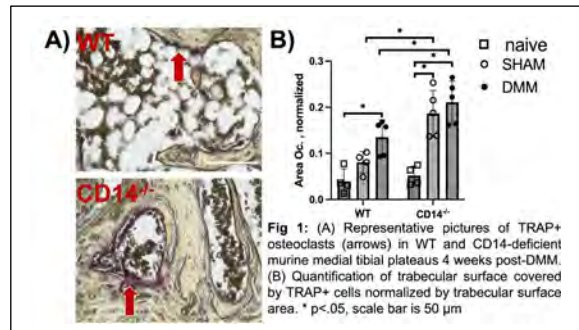


Fig 1: (A) Representative pictures of TRAP+ osteoclasts (arrows) in WT and CD14-deficient murine medial tibial plateaus 4 weeks post-DMM. (B) Quantification of trabecular surface covered by TRAP+ cells normalized by trabecular surface area. * p<.05, scale bar is 50 μ m

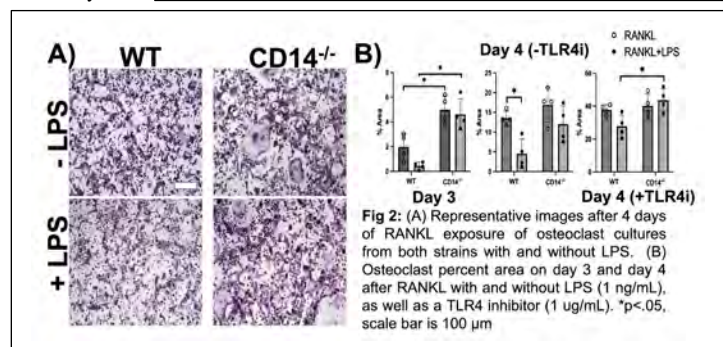


Fig 2: (A) Representative images after 4 days of RANKL exposure of osteoclast cultures from both strains with and without LPS. (B) Osteoclast percent area on day 3 and day 4 after RANKL with and without LPS (1 ng/mL), as well as a TLR4 inhibitor (1 ug/mL). *p<.05, scale bar is 100 μ m

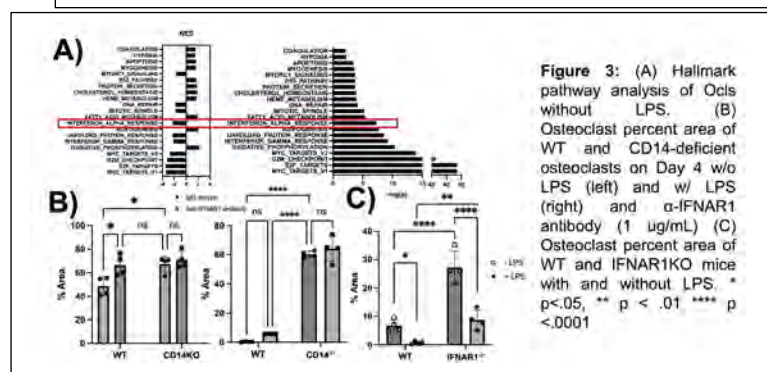


Figure 3: (A) Hallmark pathway analysis of Ocls without LPS. (B) Osteoclast percent area of WT and CD14-deficient osteoclasts on Day 4 w/o LPS (left) and w/ LPS (right) and α -IFNAR1 antibody (1 ug/mL) (C) Osteoclast percent area of WT and IFNAR1KO mice with and without LPS. * p<.05, ** p<.01 **** p<.0001

Promoting an Enhanced Tissue Repair Response with Cold Plasma Stimulation.

Carly J. Smith¹, Amanda Watkins², Abigail Lucas¹, Arianna Moniodes¹, Thomas P. Schaefer², Noreen J. Hickok¹, Theresa A. Freeman¹

¹Department of Orthopedic Surgery, Thomas Jefferson University, Philadelphia, PA

²University of Pennsylvania, School of Veterinary Medicine, Kennett Square, PA

Theresa.Freeman@jefferson.edu

INTRODUCTION: Healing following a surgical procedure is a challenging process that is often compounded in orthopedic medicine when an additional revision surgery is required. Expedited healing following orthopedic surgery would be beneficial to patients and could prevent the need for additional procedures. Cold plasma is an emerging medical technology that generates a cocktail of reactive products including reactive oxygen and nitrogen species (ROS/RNS) that can promote healing in treated tissue [1]. ROS/RNS produced by plasma have been directly implicated in bacterial elimination, increased angiogenesis, and wound healing, and thus may improve patient outcomes when used to treat a surgical incision [2][3]. While the only FDA-approved plasma device, the Renuvion[®] device, is approved for use in elective dermatological procedures, it is not clear what its immediate impact on tissue is or whether it could be repurposed to promote healing in full-depth incisions. The goal of this study is to investigate the ability of a single plasma treatment to enhance the repair of surgically injured muscle.

METHODS: *Device Information:* All experiments were approved by UPenn IACUC committee and were conducted using the Renuvion[®] device (Apyx Medical). Animals were treated with either the Precise Open 44mm Blade or the Apyx 44 Derm Handpiece. All treatments used the settings: 28W, 4L/min helium flow rate. *Chemical Product Analysis:* MilliQ H₂O was treated approximately 2mm from the water surface, and the applicator was moved across the water surface for even treatment. Hydrogen peroxide, using a potassium iodide protocol and nitrites using a Griess reagent protocol were detected colorimetrically on a plate reader at 390 and 548 nm, respectively. *Animals and Surgical Procedure:* 6-hour timepoint: made Sprague-Dawley rats were anesthetized and a craniolateral incision was made between the vastus lateralis and the biceps femoris to access the femur. 1.7 mm titanium screws were placed at the proximal and distal ends, and a mid-diaphyseal empty hole was created to expose the medullary cavity. Animals were treated for 30-seconds with plasma and the incision was closed. 6-hours after index surgery, animals were sacrificed. For 4- and 14-day timepoints: index surgical procedure was as described above without plasma treatment, then followed 7-days later by a revision surgery through the previous incision, then were either untreated or treated for 30-seconds with plasma. A titanium lockplate was secured using 2 proximal and 2 distal 1.7 mm titanium screws and the incision was closed. At 4-days and 14-days post-revision the rats were euthanized and samples collected for the following. *RNA Isolation and Analysis:* Incision site muscle tissue was mechanically disrupted and used for RNA isolation. RNA sequencing and gene expression analysis (NovoGene) was performed on the periprosthetic soft tissue from 6 rats/group. *Histology:* Tissue was fixed in 4% paraformaldehyde (PFA) for >24 hours before being embedded in paraffin blocks. 5 µm sections were used for staining with Toluidine Blue, Masson's Trichrome, Picrosirius Red, and Immunohistochemistry.

RESULTS: Plasma treatment of tissue within the surgical incision led to immediate oxidation of the loose connective tissue and compaction of the collagen fibrils. Treated tissue showed a significant increase in infiltrating innate neutrophils and mast cells. Interestingly, this inflammatory response was highly localized to only the treated tissue areas and does not occur at other areas. RNA sequencing of the treated muscle 6-hours post-treatment revealed upregulation of a tissue-protective response characterized by increased antioxidant signaling, downregulation of apoptosis signaling, and upregulation of tissue-protective genes. In a more challenging revision surgery model, long-term effects of plasma treatment downregulated IL-6 JAK/STAT signaling at 4-days post-treatment, while at 14-days post-treatment plasma downregulates adipogenesis. These molecular changes correspond with a reduction in the amount of inter-fibrotic fat present in the healing muscle 14-days post-treatment. These results indicate that plasma treatment increases stimulation of inflammation followed by rapid resolution and activation of tissue protection, which drives more functional muscle repair.

DISCUSSION: Cold plasma is a candidate therapy to expedite healing following surgery. Our results suggest that the initial spike in the innate immune response to plasma treatment in muscle results in enhanced muscle healing characterized by reduced adipogenesis and enhanced muscle tissue regeneration. This type of therapy can be easily incorporated into standard surgical procedures to promote healing, and as such cold plasma treatment may be a viable addition to the operating room for standard orthopedic procedures.

ACKNOWLEDGEMENTS: This work was supported by NIH grant R01AR076941 (Freeman) from NIAMS. Special thanks to Pietro Ranieri, Autumn Melvage, and Torsten Fras for their help with data analysis and histology.

REFERENCES:

- [1] Braný, D. *et al.* Cold atmospheric plasma: A powerful tool for modern medicine. International Journal of Molecular Sciences vol. 21 (2020).
- [2] Li H. *et al.* Reactive Oxygen Species in Pathogen Clearance: The Killing Mechanisms, the Adaption Response... Front Microbiol. (2021)
- [3] Powers, S. K. *et al.* Reactive Oxygen Species: Impact on Skeletal Muscle. in Comprehensive Physiology 941–969 (Wiley, 2011).

Biomimetic proteoglycan-dexamethasone conjugate for rescue of inflammation-induced cartilage degradation – a novel therapeutic

Elizabeth R. Kahle¹, Annika R. Bergstrom², Hooman Fallahi¹, X. Lucas Lu³, Lin Han¹, Michele S. Marcolongo²
¹Drexel University, Philadelphia, PA; ²Villanova University, Villanova, PA; ³University of Delaware, Newark, DE
 Annika R. Bergstrom: abergs01@villanova.edu

Disclosures: No disclosures.

INTRODUCTION: Articular cartilage chondrocytes are surrounded by a 2-4 μm thick, structurally distinctive pericellular matrix (PCM). In osteoarthritis (OA), degeneration of the PCM is a leading event of disease initiation, contributing to disrupted chondrocyte mechanotransduction and downstream deleterious metabolic changes, resulting in the breakdown of cartilage [1]. Molecularly engineering the PCM holds promising potential for modulating the mechanosensitive activities of chondrocytes to promote regeneration and attenuate disease progression [2]. Our group has synthesized a suite of biomimetic proteoglycans (BPGs), which are composed of natural chondroitin sulfate bristles (CS) and a poly(acrylic acid) (PAA) backbone. These molecules mimic the nano-architecture and water uptake of native proteoglycans [3, 4]. We have demonstrated that BPG10, a ~170 kDa mimic with ~7-8 CS bristles attached onto a 10 kDa PAA core (Fig. 1a), can passively diffuse through all zones of cartilage *in vivo* and *ex vivo*, preferentially localize in the PCM and territorial-ECM (T-ECM). As a result, these BPGs can modulate the local micromechanics of the PCM and in turn, the mechanosensitive activities of residing chondrocytes [5-7]. Building upon this material, our group attached dexamethasone (Dex), a widely used anti-inflammatory glucocorticoid for OA treatment, to BPG via a stable, pH-mediated amide bond to facilitate controlled release of Dex and amelioration of cartilage degradation (Fig. 1a). In this study, we synthesized and characterized BPG-Dex, quantified controlled release *in vitro*, and demonstrated the effect of BPG and BPG-Dex to attenuate the inflammatory response induced by IL-1β using an adult bovine cartilage explant model.

METHODS: Materials preparation. BPG was synthesized as previously described, resulting in a poly(acrylic acid, PAA) core and CS bristles [8]. BPG-Dex was synthesized, purified, and chemically characterized by FTIR and HPLC to determine reaction efficiency, drug release profiles, and drug loading capacity, as well as drug release at pH 6.5 and 7.4 to determine sensitivity of release with pH levels relevant to normal and OA cartilage. **Bovine cartilage sample preparation.** Cylindrical cartilage plugs (4 mm diam) were harvested from *n* = 3 fresh adult bovine knee joints, washed with PBS, and incubated undisturbed in chemically defined chondrogenic DMEM (1% ITS+Premix, 50 μg/mL L-proline, 0.9 mM sodium pyruvate, 50 μg/mL ascorbate 2-phosphate) for 24 hours prior to stimulation with a low dosage of 1 ng/mL recombinant bovine IL-1β for 3 days in 1.5 mL DMEM at 37°C. Fresh IL-1β was administered every 24 hours for the 3-day duration. BPG, BPG-Dex, and Dex were dissolved in complete DMEM at the following concentrations: BPG (10 mg/mL), BPG-Dex (10 mg/mL), and Dex (25 μM). Each treatment well (*n* = 3 plugs) was incubated with 1.5 mL of drug solution for 48 hours and then fresh media was replenished every 48 hours for the remainder of the explant study. **Histology.** Plugs were processed for histology by fixing in 4% PFA in 4°C overnight and then sequentially dehydrated and paraffin embedded [9]. Samples were sectioned at 6-μm thick and stained with Safranin-O/Fast Green (Saf-O/FG) to assess gross-level proteoglycan and collagen changes among groups. **Statistics.** Samples were assessed via measurements of sGAG void (thickness_{sGAG void}) obtained using ImageJ (*n* = 87 measurements from *n* = 9 plugs per condition across *n* = 3 biological repeats). One-way ANOVA with Tukey's post-hoc test for multiple comparisons was performed on sGAG thickness measurements for all groups at a significance level of α = 0.05.

RESULTS: FTIR analysis of the BPG-Dex starting materials and final product showed an addition of aromatic alkene bonds (C-H: 2938 cm⁻¹) from dexamethasone and carbonyl bonds (C=O: 1764 cm⁻¹) and ester bonds (C-O: 1335 cm⁻¹) from the ester linkage between glycine and dexamethasone (Fig. 1b), indicating successful covalent attachment of Dex to BPG. Release of Dex was faster in basic release media (28 days) due to rapid cleavage of the ester bonds compared to acidic conditions (42 days) (Fig. 1c). Cartilage health was maintained during the length of explant culture as demonstrated by live/dead assay (Fig. 2d) as well as sGAG staining between day 1 control (D1C) and day 16 control (D16C), which showed no significant differences (Fig. 2a). IL-1β induced an inflammatory and catabolic response within cartilage, resulting in a salient increase in the thickness of sGAG-depleted regions (Fig. 2c). Free Dex (Dex) had the greatest sGAG loss among treatments administered and was not statistically different to that of the IL-1β treated cartilage (Fig. 2b), indicating no clear signs of rescue from cartilage degradation (Fig. 2a-c). In contrast, BPG demonstrated attenuation of degenerative signs with a significant increase in sGAG retention compared to both IL-1β and Dex conditions (*p* < 0.01, Fig. 2b,c). Furthermore, BPG-Dex (BPG-Dex) had the greatest rescue of inflammatory conditions with sGAG loss statistically comparable to that of both the day 1 and 16 control groups.

DISCUSSION: This study demonstrated that a disease-modifying drug, such as Dex, can be coupled to BPG using an environment-susceptible linker to provide long-term controlled release *in vitro* up to 42 days. Further, under an inflammatory environment *ex vivo*, cartilage degeneration as measured by GAG staining, can be significantly attenuated via BPG alone. This effect was further amplified by the use of BPG-Dex, surpassing the efficacy of free Dex administration. BPG alone has demonstrated the addition of GAGs or reduction in GAG depleted thickness, likely due to mechanobiological effects previously documented by BPG alone [5]. Early treatment regimens with BPG suggest that BPG was able to attenuate IL-1β-induced degeneration (e.g. increased cytokines, increased enzyme production, decreased proteoglycan production) as measured by sGAG depleted thickness measurements. The addition of BPG-Dex, further attenuated sGAG, hallmarking nearly a complete rescue. BPG-Dex delivers Dex at a 200-2000 times lower dose than those used for intra-articular injections, which may reduce unintended adverse effects of free Dex on the joint clinically. These findings provide direct molecular evidence that the BPG-Dex conjugate can molecularly engineer cartilage in early stages of IL-1β induced inflammation and thus, has the potential to serve as a multi-functional, minimally invasive therapeutic to reverse OA progression by protecting chondrocyte PCM microenvironments. **SIGNIFICANCE/CLINICAL RELEVANCE:** This study demonstrates that BPG-Dex conjugate can be used to rescue cartilage GAG depletion by mitigating the inflammatory response, and thus, could potentially be used as a therapeutic for OA.

REFERENCES: [1] Chery+ 2020. [2] Guilak+ 2018. [3] Kim+ 2015. [4] Prudnikova+ 2019. [5] Kahle+ 2022. [6] Phillips+ 2019a. [7] Phillips+ 2019b. [8] Prudnikova+ 2018. [9] Han+ 2019.

ACKNOWLEDGEMENTS: This work is supported by NIH R01AR080139.

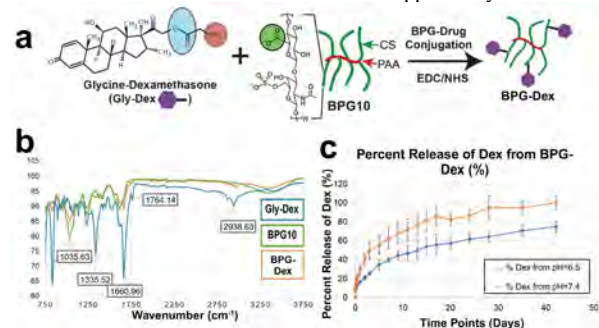


Fig. 1 a) Scheme for BPG-Dex synthesis. Glycine-Dex (Gly-Dex) reacts with BPG through standard EDC/NHS chemistries to yield the desired BPG-Dex drug construct. **b)** FTIR spectra of glycine-dexamethasone (GD), BPG, and BPG-glycine-dexamethasone (BPG-Dex). **c)** Percent of Dex released from BPG-Dex in pH = 7.4 and 6.5 PBS. Cumulative release percentage was tracked over the course of 42 days from *n* = 3 repeats per condition. Half of the total Dex is released in 3 days in basic release conditions and 50% of the total Dex is released in 13 days from acidic release conditions.

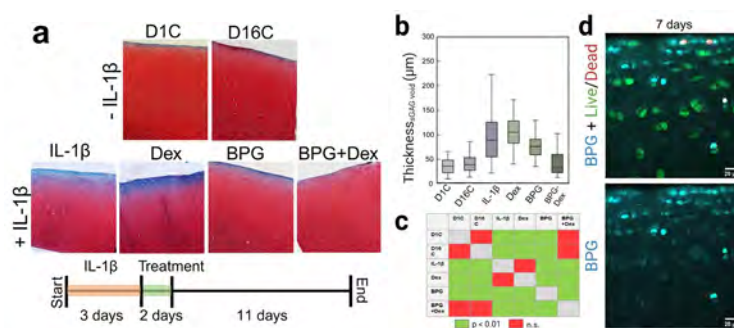


Fig. 2 a) Histological staining of Safranin-O (sGAG) and Fast Green (collagen) of controls and treatment groups. Top row: controls from 24 hours after explantation (D1C) and age-matched (D16C). Bottom row: All groups that received IL-1β including the control condition (IL-1β) and three treatment groups (Dex, BPG, and BPG-Dex). **b)** sGAG void thickness assessment of controls and treatment groups with **c)** table of statistical significance between groups. **d)** Retention of BPG within cartilage explants for 7 days. Top image: live cell (calcein AM, green) and dead cell (ethidium homodimer-1, red), and BPG (cyan). Bottom row: isolation of the BPG channel.

TGFβ1-dependent mTORC1-STAT3 signaling pathway is indispensable for tenocyte maturation in vitro Three-Dimensional (3D) tendon construct.

Bon-hyeock Koo^{1#}, Aiden Smith¹, Kyu Sang Joeng^{1*}

¹ McKay Orthopaedic Research Laboratory, Department of Orthopaedic Surgery, Perelman School of Medicine, University of Pennsylvania, Philadelphia, PA 19104-6081, USA

ABSTRACT

The Transforming Growth Factor-β 1 (TGFβ1) is well-known growth factor involved in tenocytes differentiation, ECM production, and regulating cell fate. We previously demonstrated that TGFβ1 has a critical role in the formation of *in vitro* 3D tendon constructs using mouse primary tendon cells. In this study, we investigated the function of Mammalian target of rapamycin complex 1 (mTORC1) and Signal transducer and activator of transcription 3 (STAT3) signaling in the formation of TGFβ1-induced *in vitro* 3D tendon constructs using specific inhibitors, rapamycin (mTORC1 inhibitor) and stat3 inhibitor. TGFβ1 treatment activated both mTORC1 and STAT3 in 3D tendon constructs. The treatment of rapamycin or stat3 partly attenuated TGFβ1-dependent cellular, molecular, and matrix changes in the 3D tendon constructs. Overall, this study asserts that mTORC1-STAT3 signaling axis is a downstream mediator of TGFβ1 signaling in the formation of 3D tendon constructs.

Type III Collagen Expression Decreases During Neonatal Tendon Development and is Unchanged in Early Neonatal Tendon Healing

Margaret K. Tamburro¹, Jaclyn A. Carlson,^{1,2} Miranda K. Doro,¹ Stephanie N. Weiss,¹ Susan W. Volk,² Louis J. Soslowsky¹

¹McKay Orthopaedic Research Laboratory, University of Pennsylvania, Philadelphia, PA

²School of Veterinary Medicine, University of Pennsylvania, Philadelphia, PA

Margaret.Tamburro@penmedicine.upenn.edu

Disclosures: Margaret K. Tamburro (N), Jaclyn A. Carlson (N), Miranda K. Doro (N), Stephanie N. Weiss (N), Susan W. Volk (N), Louis J. Soslowsky (N)

INTRODUCTION: After tendon injury, fibrovascular scarring leads to inferior tendon function and high re-injury risk. Specifically, poor and insufficient remodeling of the provisional, type III collagen (Col3)-rich matrix to a highly aligned, type I collagen (Col1)-rich matrix results in a disorganized and weak matrix throughout healing. Much like the early healing matrix in adult tendon, developing embryonic tendon contains high levels of Col3 [1]. However, the magnitude and timing of *Col3a1* gene expression in the developing and healing neonatal tendon have not been elucidated; this information may provide crucial foundation for investigations of neonatal development and healing as potential mechanisms of superior tendon remodeling from a Col3- to Col1-rich matrix. Therefore, the objective of this study was to define the expression profile of the *Col3a1* gene throughout early neonatal development and healing. We hypothesized that *Col3a1* expression would be highest immediately post-partum and decrease throughout neonatal development. Additionally, we expected healing neonatal tendons to mount a quick and robust Col3 response with increased *Col3a1* expression during early healing timepoints.

METHODS: For investigations of neonatal development, thirty-five right knees from C57/B6 wild-type (WT) mice were harvested at postnatal days 0, 3, 7, 10, and 14 (p0, p3, p7, p10, p14; n ≥ 6/group mixed sex). For investigations of neonatal healing, twelve WT mice received right patellar tendon biopsy punch injury (0.3 mm diameter, performed under 10X magnification; Fig 1A-B) at 7 days of age. Right knees were harvested at 3- and 7-days post-injury, corresponding to p10 and p14 of the mice, respectively (n = 6/group mixed sex). All studies were IACUC approved. For all groups, patella-patellar tendon-tibia complexes were fixed for 4 hours in 4% paraformaldehyde, dissected, and cryo-embedded. Tendons were sectioned coronally (40 μm) and micro-dissected with a 25G needle to ensure proper isolation of the neonatal tendon for developmental ages (p0, p3, p7, p10, p14) or injured matrix for healing timepoints (3 days post-injury/p10, 7 days post-injury/p14). Dissected tendon tissue was digested, and RNA was isolated as described [2]. qPCR for *Col3a1* and *Abl1* (housekeeper) was performed. ΔCt values were calculated with reference to *Abl1* expression (ΔCt = Ct_{*Abl1*} - Ct_{*Col3a1*}). A one-way ANOVA was used to assess differences in *Col3a1* expression between developmental ages and healing timepoints. Significance was set at p < 0.05.

RESULTS: Supporting our hypothesis in the developing neonatal tendon, *Col3a1* expression was highest at p0 and decreased through p14, representing a 76% decrease in average *Col3a1* expression throughout this period (Fig 2A). Interestingly, *Col3a1* expression was not increased with neonatal injury throughout early healing timepoints. *Col3a1* expression 3 and 7 days after injury was not different from the uninjured baseline at p7 (Fig 2B) or from *Col3a1* expression at corresponding, uninjured developmental timepoints (p10 and p14; Fig 2B).

DISCUSSION: In this study, we defined the expression profile of the *Col3a1* gene throughout early neonatal development and healing to provide crucial foundation for investigations of neonatal development and healing as potential mechanisms of superior tendon remodeling.

Development is regarded as the ideal physiologic process for tendon matrix formation. Many regenerative approaches seek to recapitulate development, making the study of a key component of the developing tendon matrix, Col3, an important foundational step. *Col3a1* expression was previously known to be high *in utero* [1], and the current study is the first to measure the decrease in *Col3a1* expression in early neonatal development. Given the importance of temporally coordinated *Col3a1* expression in other developing, fibroblast-rich tissues [3], this *Col3a1* expression decrease may implicate Col3 in regulation of neonatal tendon development. Moreover, the temporal profile of *Col3a1* expression during neonatal development follows the same temporal profile of *Col3a1* expression during mature tendon healing [4] where expression is high after injury and decreases as healing progresses. Encouragingly, this highlights commonalities between neonatal development and mature healing which may be leverageable in approaches that seek to improve mature healing through biomimicry of neonatal development. Further research is evaluating additional developmental timepoints to identify when homeostatic *Col3a1* expression is achieved.

Neonatal tendon healing is another model of improved tendon matrix formation as neonatal healing is superior in speed and quality [5, 6] to mature healing. Given the similarities between healing in neonatal and mature contexts, neonatal tendon healing has become a favorable model for investigations of improved healing. Interestingly in the current study, neonatal injury did not affect overall *Col3a1* expression during early healing. This indicates a significant deviation from mechanisms of mature tendon healing where dramatically increased *Col3a1* expression is considered a hallmark of the healing response. Our previous investigations of mature mice (same C57/B6 strain) demonstrate increased *Col3a1* expression in early healing (Fig 3) [7, unpublished]. Given the improved healing observed in neonatal tendon, this finding may reveal potential for *Col3a1* modulation as a therapeutic method for improved tendon healing. Additional earlier and later healing timepoints are being explored to understand the complete temporal profile of *Col3a1* expression after neonatal tendon injury. Furthermore, immunostaining for Col3 will be completed for all developmental and healing timepoints to evaluate protein translation to add to the gene expression findings from the current study.

SIGNIFICANCE/CLINICAL RELEVANCE: Understanding temporal and mechanistic dynamics of neonatal tendon development and healing may highlight novel targets for improving tendon healing through regenerative approaches.

REFERENCES: [1] Birk et al, Eur J Cell Biol, 1997. [2] Leiphart et al, ORS, 2022. [3] Niederreither et al, Matrix Biol, 1995. [4] Dyment et al, PLoS ONE, 2013. [5] Ansorge et al, JOR, 2012. [6] Howell et al, Sci Rep, 2017. [7] Leahy et al, JOR, 2023.

ACKNOWLEDGEMENTS: This study was funded by NIH R01GM124091, R01AR080029, F31AR082282 and the Penn Center for Musculoskeletal Disorders (P30AR069619). The authors thank Nat Thurlow and Ashley Fung for their assistance with this work.

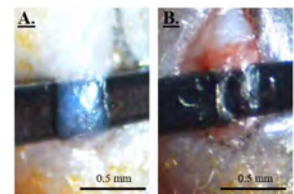


Figure 1: (A) Uninjured p7 patellar tendon. (B) p7 patellar tendon after biopsy punch (0.3 mm diameter) injury.

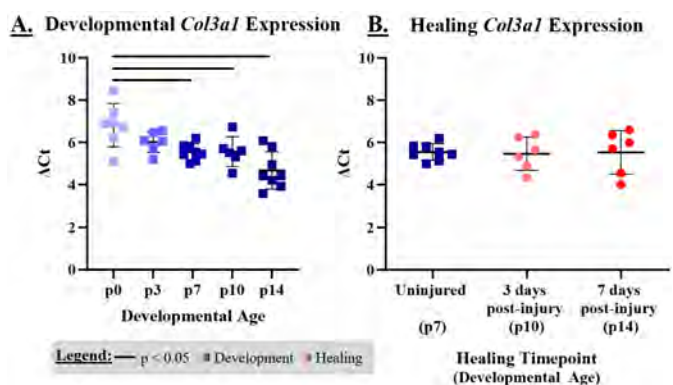


Figure 2: (A) Throughout postnatal development, *Col3a1* expression decreases. (B) After injury induced at p7, *Col3a1* expression is not increased 3 or 7 days after injury.

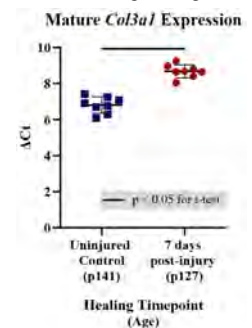


Figure 3: *Col3a1* expression during early tendon healing increases in mature mice [7, unpublished].

Imaging Mass Cytometry Reveals Distinct Synovial Cell Immunophenotypes in Overloading and Surgical OA Models

Kevin Burt^{1,2}, Vu Nguyen², Yasaman Moharrer¹, Joel Boerckel¹, Narine Hakobyan³, Rachel E. Miller³, Robert Mauck^{1,2}, Carla Scanzello^{1,2,4}

¹Department of Orthopaedic Surgery, Perelman School of Medicine, University of Pennsylvania, Philadelphia, PA; ²Translational Musculoskeletal Research Center, Crescenz VA Medical Center, Philadelphia, PA; ³Rush Medical College, Chicago, IL; ⁴Division of Rheumatology, Perelman School of Medicine, University of Pennsylvania, Philadelphia, PA.

Disclosures: KGB (N) - kevin.burt@penmedicine.upenn.edu, VN (N), YM (N), JB(N), NH (N), REM(N), RLM (4,5,8), CRS (8)

INTRODUCTION: Contrary to initial characterization of OA as a non-inflammatory arthritis, joint inflammation is a now a widely accepted feature of disease. Macrophages have been identified as a key player in joint inflammation, playing vital roles in the defense of pathogenic and tissue damage associated insult¹. Thus, evaluating macrophage and other immune cells responses during the onset of OA is fundamental. Surgical destabilization models have been widely utilized for their ability to reproducibly progress to end-stage-OA. However, the effect of the traumatic surgical approach on surrounding soft tissues (i.e., synovium), complicates evaluation of disease propagating inflammation. Utilizing methods in spatial proteomics and transcriptome sequencing, we hypothesize that the innate immune response following non traumatic mechanical overloading will be distinct from those of surgical destabilization.

METHODS: Surgical OA model: Destabilization of the medial meniscus (DMM) surgery was performed to induce OA in skeletally mature (12-wk old) male C57BL/6 (WT) mice². Sham surgery with incision but no resection of the meniscotibial ligament was used as a control for DMM. **Bulk RNA-sequencing (n=4):** Bulk RNA sequencing was performed on naive (non-operated), sham, and DMM mice at 2-, 4-, and 8-wks post injury. Synovial and fat pad tissue was pooled from 8 mice for each biological replicate. Genes with a p-adj.<0.05 and a fold change>1.5 or <-1.5 were identified as differentially expressed (DE). **Non-surgical loading OA model:** Mechanical overloading was performed on skeletally mature male WT mice via an acute loading event (40 cycles, 9N max load, 0.1 Hz)³. Contralateral non-loaded knees were used as controls. **Histopathology (n=5-6):** Evaluation of cartilage damage⁴ and synovitis⁵ was performed 2-wks post-surgery or loading on Toluidine Blue and HE stained sections, respectively. **IMC (n=5-6):** Paraffin embedded sagittal knee sections underwent heat-mediated antigen retrieval and overnight incubation with a 24-marker multiplex panel of metal-conjugated antibodies, followed by incubation with Intercalator-Ir nuclear stain, and imaging using a Hyperion Imaging System (Standard Biotoools). **Spatial protein expression and cellular phenotype analysis:** Single cell masks were created using the nuclear stain (deepcell.org). IMACyE software was used to create t-distributed stochastic neighbor embedding (t-SNE) dimensionality reduction analysis with arcsin transformation to produce data normalization and cluster analysis⁶. **Statistical analysis:** Student's t-test or two-way ANOVA (indicated in figure legends), with p<0.05 considered significant.

RESULTS: Bulk RNA sequencing of synovial tissue revealed substantial early (5,249 DE genes) and lasting (3,332 DE genes) transcriptional changes between sham and control mice. Notably, many fewer (only 45) DE genes were identified between sham and DMM synovial tissue 8-weeks post-surgery (Fig. 1A,B). Histopathologic analysis at 2-wks post injury revealed a similar extent of robust early (2-wks) synovial inflammation (increased cellularity, lining hyperplasia, and fibrosis) in both sham and DMM groups, while the synovium of loaded and unloaded control knees where similar with little to no histological evidence of inflammation (data not shown). Spatial phenotyping via IMC revealed a highly distinct cellular landscape across sham, DMM, and acutely loaded synovium (Fig. 2A-C). Marked increases in a F4/80+ myeloid, perivascular (CD31+) myeloid, and monocyte/macrophage population were observed in both sham and DMM synovium, compared to unloaded and loaded conditions (Fig. 2C,D). Alternatively, unloaded and loaded synovium maintained a population of adipocytes (Perilipin+), which were significantly diminished within both sham and DMM groups (Fig. 2C,D). Comparing between unloaded and acutely loaded synovium, immunophenotyping revealed a lining macrophage population (CD45+,F4/80+,CD64+,MHCII+) that was increased 2-wks following the singular loading event compared to the unloaded knee (Fig. 3).

DISCUSSION: Bulk sequencing revealed substantial transcriptional changes (3,332 DE genes) between sham surgery and naïve synovial tissue 8-wks post-surgery. In contrast, only 45 DE genes were identified between sham and DMM at 8-wks, suggesting the surgical insult alone can initiate lasting substantial transcriptional changes within the synovium. To isolate loading-driven synovial inflammation in the absence of surgical insult we utilized high dimensional spatial proteomics (IMC) to immunophenotype synovial tissue in surgical (DMM) and non-surgical loading models of OA. We identified robust synovial inflammation in both surgical sham and DMM synovium, characterized by the increased presence of many myeloid lineage cells, monocytes, and mature macrophages, as well as neural and perivascular cell clusters. Interestingly, both sham and DMM surgical groups revealed a loss of adipocytes, compared to the unloaded and loaded groups. Given the importance of adipose-cartilage crosstalk during OA progression, these findings reveal another important distinction between disease pathology across models⁷. Lastly, while histologically similar and healthy appearing, loaded synovium developed a lining macrophage cell cluster (F4/80+, MHCII+, CD64+) two weeks following the singular loading event that was absent in the unloaded condition. Future work is focused on isolating how these load-responsive immune cells contribute to disease.

SIGNIFICANCE: These results reveal the robust early inflammatory response and lasting transcriptional changes following surgical insult to the knee joint, findings that should be considered in future evaluations utilizing surgical destabilization models. Additionally, novel methods in spatial proteomics provided insights into the localization of a lasting loading responsive macrophages within the synovium, which may serve as a potential therapeutic target for OA initiated by non-traumatic overloading.

REFERENCES: ¹Sanchez-Lopez, Nat Rev Rheumatol (2022), ²Glasson, OAC (2007), ³Cho, NBM (2015), ⁴Glasson, OAC (2010), ⁵Obeidat, OAC (2024), ⁶Somarakis, IEEE Trans Vis (2020), and ⁷Collins, PNAS (2020).

ACKNOWLEDGEMENTS: Funding - I01 RX002274-06S1 (VA RR&D), I01 BX004912 (VA BLR&D), R01 AR075737 (NIAMS), IK6 RX003416 (VA RR&D), and the CReATE Motion Center (I50 RX004845).

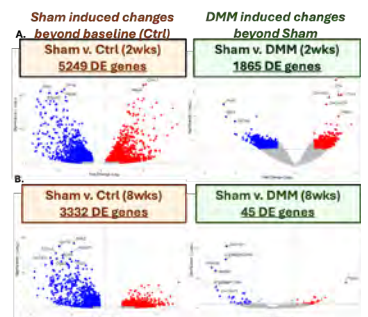


Figure 1: Bulk RNA sequencing. Volcano plots indicating sham induced changes beyond baseline (Ctrl) and DMM induced changes beyond Sham.

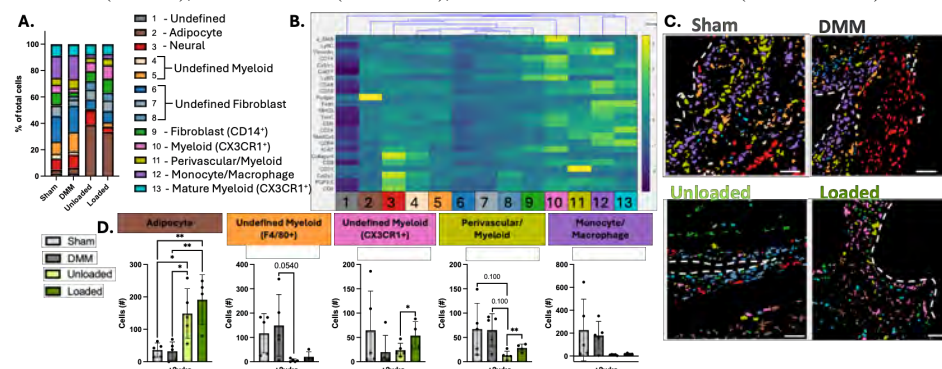


Figure 2: IMC analysis of synovial cell phenotypes. (A) Cell cluster analysis. (B) Marker expression heatmap within clusters. (C) Cell number analysis within clusters. (D) Cell cluster assignment within synovium. Synovial lining = white-dashed line. Scale bar = 50µm. *p<0.05, **p<0.01 by Paired T-test (unloaded vs. loaded) or one-way ANOVA with Tukey post-hoc (all other comparisons).

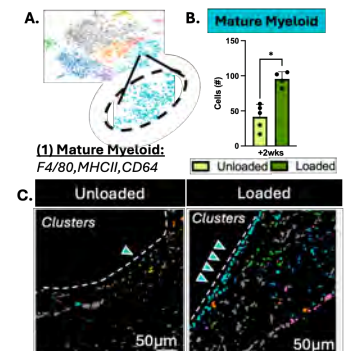


Figure 3: Load-induced synovial cell phenotypes. (A,B) Unique cell cluster analysis. (C) Cluster assignment within synovial ROIs. Synovial lining = white-dashed line. *p<0.05 by Paired T-test.

Assessing Cell Therapy Retention and Survival Across a Spectrum of Intervertebral Disc Degeneration in Rabbits

Matthew Fainor^{1,2}, Aira Bazaz¹, Harvey E. Smith^{1,2}, Sarah E. Gullbrand^{1,2}

¹University of Pennsylvania, Philadelphia, PA; ²Corporal Michael J. Crescenz VA Medical Center, Philadelphia, PA

INTRODUCTION: Cell therapy is a minimally invasive strategy for the potential treatment of intervertebral disc degeneration (IVDD). Although numerous studies have transplanted cells into the nucleus pulposus (NP) of degenerative intervertebral discs (IVDs), none of these interventions were able to homogeneously restore full disc function,^{1,2} and most human clinical trials remain unreported.³ Techniques for tracking cell retention and survival post-injection often use lentiviral transfections to image a living cell population over time,⁴ but these in situ live cell tracking methods have not been used to assess transplanted cell survival across a spectrum of IVDD in non-rodents. Understanding how a disc's degenerative state affects the viability of transplanted cells will be key to understanding the limitations of cell-based therapies and crucial for identifying candidates suitable for these treatments. Using an established rabbit puncture model of IVDD in which a progressive decrease in small molecule diffusion across the endplate occurs,^{5,6} we characterized the survival of transplanted mesenchymal stromal cells transfected with a firefly luciferase lentiviral vector across a spectrum of degenerative microenvironments by varying injury severity and time post-puncture.⁵⁻⁶ We hypothesized that cells would survive more robustly in discs with less severe degeneration.

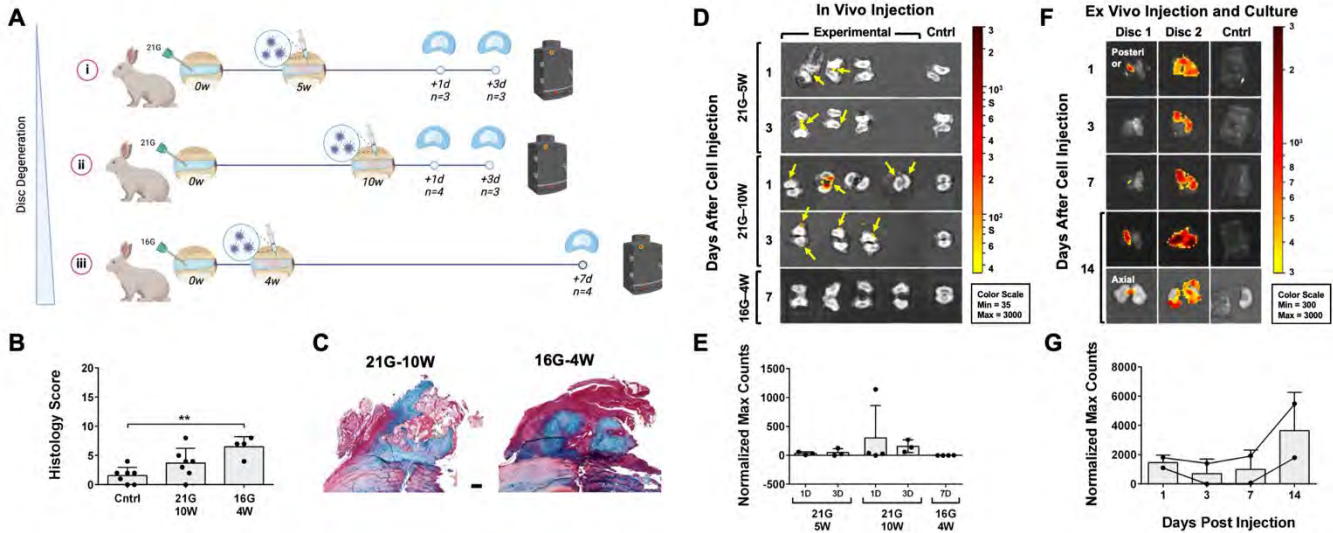


Figure 1: (A) Experimental groups and their respective endpoints. (B) Disc histology scores and (C) axial Alcian Blue/Picrosirius Red-stained cross-sections of anterior disc osteophytes (scale = 500 μ m). (D) IVIS images of luminescence emitted by live bMSCs 1, 3, and 7 days following in vivo cell injection in discs split axially (positive signal indicated by yellow arrows), and (E) quantification of in vivo max luminescent counts measured axially and normalized to controls. (F) IVIS images of luminescence emitted by live bMSCs transplanted ex vivo into 16G-4W degenerative IVDs maintained in organ culture for 14 days (n = 2), and (G) quantification of max luminescent counts anteriorly/posteriorly over the 14 day culture period normalized to control.

METHODS: P1 bone marrow-derived bovine mesenchymal stromal cells (bMSCs) were transfected at an MOI of 500 using 12 μ g/ml polybrene and a lentivirus encoding for green fluorescent protein (GFP) and firefly luciferase (AMSBio LVP1060-PBS). Transfected GFP+ cells were sorted from GFP- cells at P3 or P4 via flow cytometry. Six male New Zealand White rabbits underwent intervertebral disc puncture to induce IVDD as previously described.^{5,6} In each rabbit, a combination of L23, L34, L45, L56, and L67 discs were punctured using either a 16G or 21G needle and allowed to degenerate for 4 and 5/10 weeks, respectively, after which 500,000 - 1 million sorted P5 or P6 GFP+ bMSCs were delivered to each disc via 25 μ l DMEM injection using a 27G needle. Animals were euthanized and their discs isolated 1, 3, or 7 days after cell delivery, incubated in 300 μ g/ml D-Luciferin for 10 minutes, and imaged on IVIS to detect luminescence produced by living cells (Figure 1A). Organ culture was used as a positive control to validate the survival of transplanted cells in a culture environment. Five weeks after injury, the L56 discs of two 16G-punctured rabbits were isolated and transferred to culture. Twenty four hours later, 1 million cells in 25 μ l DMEM were injected into each disc using a 27G needle. Discs were returned to culture and imaged at days 1, 3, 7, and 14 following cell injection. **RESULTS:** Cells were injected into degenerative rabbit discs occupying a range of degenerative states (Figure 1B). Many of the discs in the mid (21G-10W) and most (16G-4W) degenerative groups developed anterior osteophytes (Figure 1C). In the least degenerative group (21G-5W), detectable cells were found in the surrounding soft tissue 1 day post-injection and remained in the soft tissue when assessed 3 days post-injection. Only one disc in this study, a 21G-punctured, 10-week degenerated disc, retained live transplanted cells inside the disc 24 hours after injection, and by 3 days post-injection all detectable cells were localized to anterior osteophytes. No luminescent signal was measured in any 16G-punctured discs 7 days after cell transplantation. Overall, retention of living cells for more than 24 hours was poor across all groups (Figure 1E). Ex vivo, transplanted cells survived for 14 days when injected into 16G-4W discs removed for organ culture (Figure 1F). Transplanted cells were more well retained in the nucleus pulposus of explant 2 than in explant 1 (Figure 1G).

DISCUSSION: In this work, we successfully delivered a bioluminescent bMSC cell therapy to rabbit discs along a spectrum of degeneration and were able to detect those live cell populations at early timepoints after delivery. Increases in luminescent signal over the 14 day ex vivo culture period indicated that bMSCs could survive in the most degenerative discs when maintained in an ideal nutrient environment. In vivo, cell survival was significantly ablated, and no cells survived in the most degenerative discs after 1 week. Viable cells were detected within the disc space in only one sample across all states of degeneration. At acute timepoints, IVIS imaging indicated that live cells were predominantly displaced from the disc space to the surrounding soft tissue in the least degenerative discs and to the anterior osteophytes in the mid-degenerative discs. The formation of anterior osteophytes is a well-reported phenomenon in this rabbit puncture model, and, in agreement with our findings here, previous work also suggests that extruded cell therapies localize to these osteophytes.⁷ Similarly, MSCs progressively migrated out of the disc space and into the vertebral bone when delivered to rat caudal discs.⁸ Staining for intracellular GFP is ongoing in order to determine whether the delivered cells were completely extruded from the disc space in all groups or if many perished in situ. Future work will deliver the cell therapy in a viscous radiopaque carrier to prevent rapid cell extrusion from the disc, minimize osteophyte formation,¹⁰ and confirm injection into the NP in order to more comprehensively understand the relationship between disc health and transplanted cell survival.

SIGNIFICANCE: Understanding how a disc's degenerative state affects the survival of transplanted cells is key to understanding the limitations and possibilities of cell-based therapies for IVDD and, in turn, identifying patients suitable for these treatments.

REFERENCES: [1] Tong+ *Transl. Res.*, 2017. [2] Li+ *Stem Cells Int.*, 2022. [3] Ambrosio+ *JOR Spine*, 2024. [4] Leo+ *Spine*, 2004. [5] Ashinsky+ *OA&C*, 2019. [6] Fainor & Orozco+ *JOR Spine* 2023. [7] Vadalà+ *Tissue Eng. Regen. Med.*, 2012. [8] Maidhof+ *J. Orthop. Res.*, 2017. [9] Feng+ *J. Neurosurg. Spine*, 2011. [10] Li+ 2014 *Tissue Eng.*, 2014.

ACKNOWLEDGEMENTS: This work was supported by the University of Pennsylvania's University Research Foundation.

A Multiphasic ECM Scaffold System for Rotator Cuff Repair with Tailored Stiffness and Structure for Enhanced Regeneration

Zizhao Li¹, Se-Hwan Lee¹, Ellen Y. Zhang¹, Marina Santos¹, Lin Xu¹, Ruqiang Lu², Dong Hwa Kim¹, Jaecun Jung¹, Jayden Shin¹, Richard Tran², Nathaniel Dymant¹, Thomas Schaefer¹, and Su Chin Heo¹

¹University of Pennsylvania, Philadelphia, PA; ²Acuitive Technologies Inc., Allendale, NJ

DISCLOSURES: Li (N), Lee (N), Zhang (N), Santos (N), Xu (N), Lu (N), Kim (N), Jung (N), Shin (N) Tran (N), Dymant (N), Schaefer (1, 3B, 3C, 5, and 6), and Heo (5)

INTRODUCTION: Rotator cuff tears are prevalent and often result in significant pain and functional impairments (Fig. 1A) [1-2]. While tissue engineering holds promise for advancing rotator cuff entheses repair, current methods fall short in providing the essential bioactive and biophysical cues, as well as the structural complexity required for effective tissue regeneration [3-4]. To address these limitations, we have developed a novel tunable biomimetic matrix-based multiphasic scaffold (BMS) specifically designed for rotator cuff entheses repair [5]. The BMS features three distinct phases that replicate the native tissue environment to promote zone-specific regeneration: 1) Phase I includes an aligned-nanofibrous decellularized tendon extracellular matrix (dECM) combined with 'stiff' methacrylated hyaluronic acid (MeHA) for the tendon zone interface; 2) Phase II incorporates nonaligned-nanofibrous dECM with 'soft' MeHA for the tendon-calcified zone interface; and 3) Phase III utilizes a porous citrate-based Citrepore™ composite scaffold for the calcified zone-bone interface (Fig. 1B). In a previous study, we confirmed that each phase of the scaffold induces zone-dependent cell differentiation and phenotype akin to the rotator cuff entheses [5]. Here, this study aims to further evaluate how each scaffold phase influences cell transcriptional profiles and to assess the in vivo efficacy of the BMS using a preclinical rabbit model.

METHODS: Four types of tunable decellularized tendon ECM (dtECM) nanofiber scaffolds were produced: 'Soft' Align (AL), 'Soft' Non-Align (NAL), 'Stiff' Align (AL), and 'Stiff' Non-Align (NAL), following established protocols [5]. Bovine mesenchymal stem cells (bMSCs, from 3 different donors) were cultured on these scaffolds, and mRNA was extracted for RNA sequencing (Azenta). Differential gene expression was analyzed using DESeq2 with a significance threshold of $p < 0.001$. The expression profiles of tenogenic and chondrogenic genes were evaluated for each condition. Porous citrate-based Citrepore™ composite scaffolds, fabricated using solvent casting particulate leaching (provided by Acuitive Technologies Inc.), were examined by scanning electron microscopy (Hitachi S-4800 SEM) after immersion in simulated body fluid (SBF) to evaluate mineralization capacity of the scaffold surface. Citrepore™ composite scaffold degradation rates were assessed in vitro in phosphate-buffered saline (PBS, pH 7.4) over 56 days. Rotator cuff implantation surgeries were performed on rabbits following the IACUC guidelines. Four weeks post-surgery, ex vivo micro-computed tomography (μ CT, Scanco μ CT45) was used to quantify bone volume fraction and trabecular number in a 2-mm-thick region of interest in the humerus. Shoulder samples were embedded in paraffin, sectioned into 8 μ m slices, and analyzed histologically with hematoxylin and eosin (H&E) staining.

RESULTS: RNA-seq analysis demonstrates that Phase I ('Stiff' AL) scaffolds markedly enhance tenogenic gene expression, confirming their effectiveness for tendon zone regeneration in rotator cuff entheses repair (Fig. 1C). Phase II ('Soft' NAL) scaffolds significantly boost both chondrogenic and tenogenic gene expression, making them ideal for the tendon-calcified zone interface (Fig. 1C). Visual and qualitative assessment revealed notable mineralization on Citrepore™ composite scaffolds immersed in SBF (Fig. 2A), with around 80% mass retention after 56 days in PBS, indicating excellent degradation performance compared to Citrepore™ only scaffolds (Fig. 2B). In vivo studies showed strong integration of BMS scaffolds with fibrocartilaginous tissue at the entheses site (Fig. 3A). Four weeks post-surgery, μ CT scans indicated comparable trabecular numbers between BMS-implanted and non-implanted groups, with the BMS-implanted group exhibiting a significantly higher bone volume fraction (Fig. 3B-C). Histological analysis at week 4 revealed well-defined tendon, fibrocartilage, and bone layers at the surgical site in the BMS-implanted group (Fig. 3D).

DISCUSSION: In this study, our development of a bioactive, stiffness and structure-tunable extracellular matrix-based multiphasic scaffold system marks a notable advance in tissue engineering for rotator cuff entheses repair. RNA sequencing and in vivo animal tests demonstrated that the Phase I 'stiff' align (AL) and Phase II 'soft' non-align (NAL) nanofibers effectively enhance tenogenic and fibrochondrogenic differentiation of MSCs, enabling zone-specific tissue formation and improved integration within the rotator cuff entheses. This targeted differentiation supports the development of distinct tissue types and promotes better tissue integration, emphasizing the scaffold's potential for tailored regeneration and repair.

Additionally, the Phase III Citrepore™ composite scaffolds facilitated mineralization, which is crucial for effective bone regeneration and tissue integration. The scaffold system showed significant efficacy in repairing the tendon-bone interface in a rabbit model, replicating the biomechanical and chemical properties of native tissue. Future research will aim to integrate additional bioactive components to further enhance the scaffold's regenerative capacity, with insights from this study guiding larger animal trials.

SIGNIFICANCE: This study introduces a novel multiphasic scaffold system that significantly enhances rotator cuff entheses repair by replicating the native biomechanical and biochemical properties, offering a promising approach to improve clinical outcomes and restore functional integrity in rotator cuff injuries.

REFERENCES: [1] Sambandam+, *World J Orthop* 2015; [2] Kuroda+, *Clin Orthop Relat Res* 2013; [3] Newsham-West+, *J Anat* 2007; [4] Chainani+, *Tech Orthop* 2016; [5] Li+, *ORS* 2023; [6] Tran+, *Soft Matter* 2010.

ACKNOWLEDGEMENTS: This work was supported by the Penn Health-Tech, NIH R21AR07770, NIH P50 AR080581, and NSF CMMI 1548571.

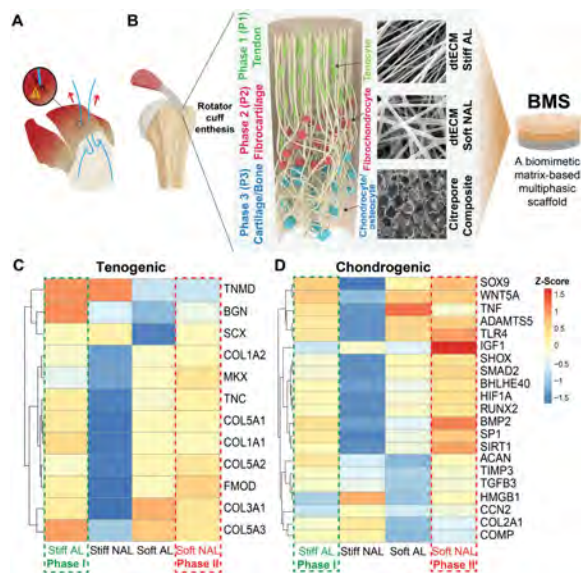


Fig. 1: (A) Schematic showing the rotator cuff post-suture repair, highlighting high-risk tear zones and illustrating the scaffold's role in reinforcing these critical areas. (B) Schematic of the biomimetic multiphasic scaffold (BMS), showing its zonal structure that replicates the biological features of the native rotator cuff fibrocartilaginous entheses. (C) Heatmap of tenogenic gene expression in bovine MSCs (bMSCs) cultured on four distinct substrate types. (D) Heatmap of chondrogenic gene expression in bMSCs cultured on the same substrates [Stiff AL = Stiff aligned dECM nanofibers, Stiff NAL = Stiff non-aligned dECM nanofibers, Soft AL = Soft aligned dECM nanofibers, Soft NAL = Soft non-aligned dECM nanofibers, n = 3 from 3 different donors].

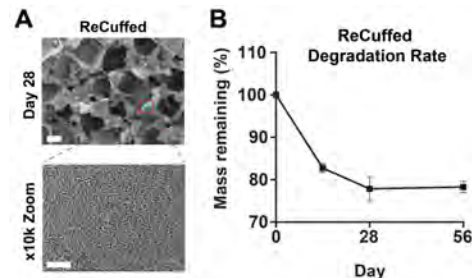


Fig. 2: (A) Scanning electron microscopy (SEM) images of the Citrepore™ and Citrepore™ composite scaffolds showing surface morphology at Day 28. Scale bar = 200 μ m (overview) and 2 μ m ($\times 10k$ zoom). (B) Degradation rate of the Citrepore™ and Citrepore™ composite scaffolds in phosphate-buffered saline (PBS) over time, with data presented as mean \pm SD [n = 4 per group].

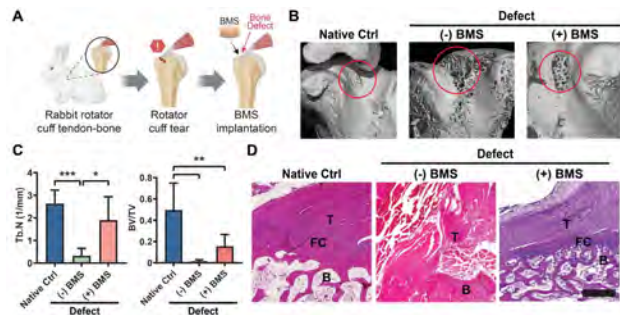


Fig. 3: (A) Schematic of BMS implantation in a rabbit rotator cuff tear model. (B) Micro-CT images comparing native rotator cuff, non-BMS-implanted, and BMS-implanted sites at 4 weeks post-operation, with the surgical site highlighted. (C) Quantitative analysis of trabecular bone number (Tb.N) and bone volume/total volume (BV/TV) in the region of interest (ROI) (n = 5). (D) H&E staining showing the tendon-bone interface at native and implanted sites (scale bar = 1 mm).

Inhibition of Fibroblast Activation Protein Restores the Homeostatic Phenotype of Mechano-activated Synovial Fibroblasts

Elizabeth R. Bernstein^{1,2,3}, Brendan Stoeckl^{1,2,3}, Rachel Flaugh^{2,3}, Robert L. Mauck^{1,2,3}, Liane Miller^{2,3}

Depts. of ¹Bioengineering and ²Orthopaedic Surgery, University of Pennsylvania; ³CMC VA Medical Center, Philadelphia, PA

Introduction: Osteoarthritis (OA) is a major source of pain and disability and current treatments are limited to symptom management. Recently, synovial fibrosis has been identified as a potential driver of disease. Pro-inflammatory cytokines and extracellular matrix (ECM) stiffening in the synovium activate fibroblast-like synoviocytes (FLS), priming them to differentiate into myofibroblasts. These activated cells secrete additional ECM and inflammatory mediators, creating a vicious cycle of stiffening, inflammation, and degeneration. Fibroblast activation protein (FAP) is expressed in the synovium of patients with OA and contributes to disease progression, but the mechanisms by which it does so are undefined. This study sought to determine whether FAP inhibition can reverse the activation of FLS seen in OA.

Methods: Minipigs underwent destabilization of the medial meniscus (DMM). Synovium was harvested at 6 weeks and 6 months and scored or analyzed for FAP and α SMA expression. An *in vitro* model of FLS activation was established by culturing bovine FLS on glass with TGF β -1. FAP inhibitor (FAPi) and Fasudil, a Rho/ROCK inhibitor that inhibits cell contractility, were added to activated FLS. After 6 days, cells were stained for actin, α SMA, paxillin, and FAP. Cell area, actin: α SMA colocalization, and focal adhesions were quantified, as was the expression of FAP, ACTA2, FN1, and CCN2. To assess contractility, FLS were seeded in collagen gels and percent initial area was quantified over time. Correlations between IF and synovitis scores were determined by linear regression. Other outcomes were compared by two-way ANOVA.

Results: FAP expression correlates with α SMA, inflammation, and hyperplasia in OA synovium. FAP and α SMA staining intensity increased in DMM synovium at both 6 weeks ($p < 0.01$, $p = 0.0004$) and 6 months ($p < 0.05$, $p < 0.0001$) (Fig 1A), with a positive correlation between FAP and α SMA staining intensity for individual donors ($R^2 = 0.4294$, $p < 0.001$). FAP intensity was also correlated with synovial inflammation ($R^2 = 0.33$, $p < 0.01$) and hyperplasia ($R^2 = 0.22$, $p < 0.05$) (Fig 1B). FAP inhibition rescues mechano-activated FLS. Activation of FLS on glass with TGF β increased cell spreading, actin: α SMA colocalization ($p < 0.0001$), and expression of FAP, α SMA ($p < 0.0001$), CTGF ($p < 0.0001$), and FN ($p < 0.001$) (Fig 2A,C,D). Treatment with FAPi significantly reduced actin: α SMA colocalization ($p < 0.01$) and α SMA expression ($p < 0.001$) and decreased cell area and expression of FAP, CTGF, and FN (Fig 2A,C,D). FAP inhibition also reduced focal adhesion number ($p < 0.0001$) and area ($p < 0.0001$) (Fig 2B,E) and contraction of FLS-embedded collagen gels ($p < 0.05$) (Fig 3).

Discussion: Our findings show that FAP inhibition can rescue the transcriptional and functional profile of activated FLS. Our *in vivo* porcine data indicate that the upregulation of FAP seen in human OA synovium is replicated in our large animal model and is correlated with progression of synovial pathology. The correlation of FAP and α SMA suggests that more mechano-activated cells express higher levels of FAP. *In vitro*, FAPi reversed the activated FLS phenotype, and did so to an equivalent or greater extent than Fasudil. FAPi's reduction of focal adhesion quantity and size implies that FAP may contribute to FLS activation by promoting focal adhesion initiation and maturation.

Significance/Clinical Relevance: These data reveal a role for FAP in FLS mechanobiology, offering a potential mechanism by which this protein contributes to OA. The finding that FAPi effectively rescued the homeostatic phenotype of activated FLS indicates that it is a promising therapeutic for treating OA.

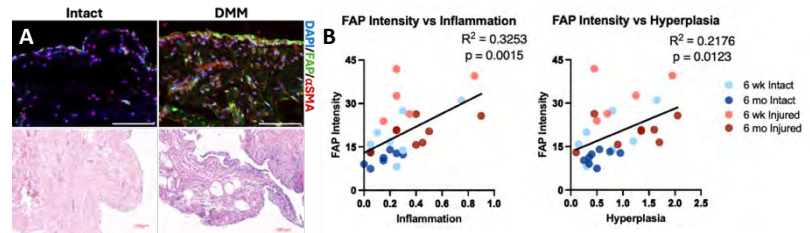


Figure 1. (A) Images of porcine synovium. Scale = 100 μ m. (B) Correlation of FAP staining intensity and synovial scoring.

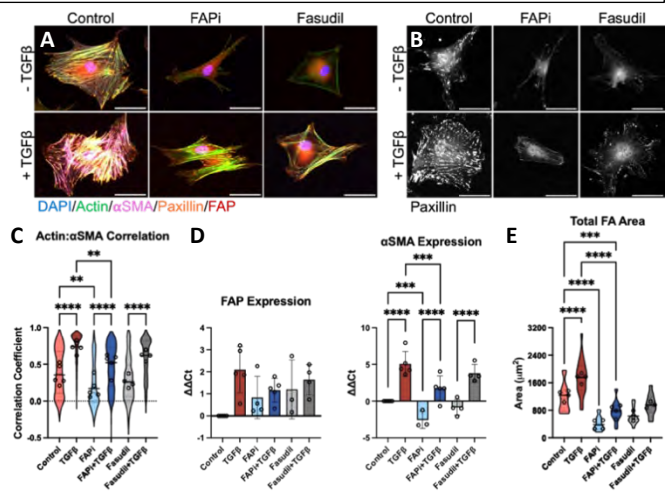


Figure 2. Images of (A) bovine synoviocytes (B) focal adhesions. Scale = 50 μ m. (D) Actin: α SMA colocalization. (E) RT-qPCR. (E) Total focal adhesion area per cell. ** $p < 0.01$. *** $p < 0.001$. **** $p < 0.0001$.

Figure 3. Quantification of collagen gel contraction. * $p < 0.05$. *** $p < 0.001$.

Analysis of Accessible Stem Cell Sources for Chondrogenic Repair of Temporomandibular Joint Osteoarthritis

Hannah M. Bonelli^{1,2}, Cristina Barbella^{2,3}, Hagar M. Kenawy^{2,4}, Riccardo Gottardi^{1,2}

¹University of Pennsylvania, Philadelphia, PA, ²Children's Hospital of Philadelphia, Philadelphia, PA, ³Brown University, Providence, RI, ⁴Center for Innovation & Precision Dentistry, Penn Dental Medicine, Philadelphia, PA
bonellih@chop.edu

DISCLOSURES: RG is co-inventor of a non-provisional patent application for MEND technology.

INTRODUCTION: Juvenile idiopathic arthritis is the most common chronic arthritis in children, of which, up to 96% experience temporomandibular joint osteoarthritis (TMJOA) [1]. TMJOA is characterized by the degradation of the articular cartilage on the surface of the mandibular condyle, leading to pain, joint clicking, and stiffness [1]. Pediatric TMJOA may also impair communication skills because of pain during talking [1]. Current treatments for TMJOA focus on palliative care, such as pain medication and physical therapy; however, these strategies ease the symptoms but do not achieve repair [1, 2]. In severe cases, adults can undergo total joint replacement, but children whose TMJ is not yet fully developed are often excluded from this treatment option [2]. Hence, tissue engineering repair of the TMJ is an active area of research that is exploring biomaterials combined with the use of mesenchymal stem cells (MSCs), typically sourced from bone marrow of the iliac crest [2]. Notably, however, bone marrow derived MSCs are not the highest performing chondrogenic cell-source and are hardly obtained in a minimally invasive manner especially for pediatric patients [3]. Furthermore, mandibular condyle cartilage presents a unique engineering design challenge, consisting of a layer of hyaline cartilage covered by a layer of fibrocartilage [2]. For these reasons, we aim to (1) test minimally invasively accessible autologous stem cell sources derived from auricular and gingival tissues of the same animal donor and (2) layer these cells within an extracellular matrix biomaterial developed in the Gottardi lab which is based on porcine meniscus decellularization (MEND) for TMJ condyle cartilage repair [4].

METHODS: *Stem cell extraction and expansion:* Ear cartilage progenitor cells (eCPCs) and chondrocytes (CC, positive control) were extracted from 10 mm ear biopsy punches of Yorkshire porcine tissue. Cartilage was minced and digested in pronase for 20 min at 37C and in collagenase II for 4 h at 37C. After filtering through a 70 µm strainer, cells were plated on a fibronectin coated 6-well plate for eCPC selection. After 20 min, the non-adherent CCs were moved to non-coated wells. Porcine gingival MSCs (GMSCs) were extracted from attached gingiva of the same animal after mincing and incubating in a 4% dispase solution for 2 h, followed by 2 h in collagenase I. After filtering through a 70 µm strainer, cells were plated. *Proliferation Assay:* After initial expansion, all cell types were plated in a 6-well plate at a density of 50K cells per well. At each timepoint, cells were lifted and counted (n=3 wells per timepoint).

Chondrogenic Pellet Culture: Cells were pelleted at a concentration of 300k cells/pellet. After 24 h, pellets were switched to chondrogenic medium containing DMEM, 10µg/mL Insulin-Transferrin-Selenium, 40µg/mL L-proline, 2% PSF, 50 µg/mL ascorbic acid, and 10ng/mL TGF-β3. After 21 days of differentiation pellets were analyzed via Alcian Blue staining for glycosaminoglycans (GAGs) and collagen I and collagen II immunostaining (IF), as well as RT-qPCR for expression of chondrogenic genes (*ACAN*, *SOX9*, *COL1A1*, *COL2A1*) and biochemical analysis (total GAG/DNA content), normalized to Day 0 of differentiation. *MEND fabrication and seeding:* Adult porcine menisci were sectioned radially to a thickness of 1 mm and subjected to freeze/thaw cycles followed by pepsin and elastase digestion. Sections were biopsy punched to 6 mm diameter and seeded with 100K cells per MEND using a transwell plate and serum gradient to drive chemotactic migration for 5 days. Re-seeding uniformity through the 3D scaffold was assessed by Calcein-AM and DAPI.

RESULTS SECTION: *Proliferation Assay:* eCPCs grew faster than GMSCs and CCs, reaching confluency by day 5, with the most growth between days 3 and 5 (data not shown). GMSCs and CCs follow a slower but relatively linear growth rate. *Chondrogenesis:* Alcian Blue revealed strong sulfated GAG secretion in eCPC pellets, meeting or even surpassing that of the positive control, CCs (Fig. 1). We used immunostaining for collagen I and collagen II to establish the propensity of each cell type to produce a more fibrocartilaginous (collagen I) or hyaline-like cartilage (collagen II). Compared to GMSCs, eCPCs secreted more collagen II than collagen I (Fig. 1) By RT-qPCR, eCPCs have similar expression of *SOX9*, *ACAN*, and *COL1A1*, but higher expression of *COL2A1* compared to GMSCs, although it did not reach statistical significance (Fig. 2). *MEND cell seeding:* All cell types easily migrated through the scaffold as seen in the Calcein-AM live staining of the top and bottom views of the scaffold (Fig. 3). DAPI staining of cross sections showed a uniform distribution of cell nuclei throughout the scaffold for all cell types (Fig. 3).

DISCUSSION: Our initial data suggests that eCPCs differentiate towards a more hyaline phenotype based on the higher expression of collagen II than collagen I, whereas GMSCs assume a more fibrocartilaginous phenotype, with a higher proportion of collagen I. These findings suggest that eCPCs might be more suitable for regenerating the hyaline layer of the TMJ cartilage and the GMSCs for the covering fibrous layer. As expected, when seeding MEND with each cell type, the signal expressed in different planes of the scaffold and the positively stained cells present on the bottom suggest robust migration throughout the porous scaffold. Given this uniform seeding for all cell types, our future studies will include the precise assessment of the scaffold remodeling which we expect to develop into a more fibrocartilaginous and hyaline-like phenotype for the GMSC-seeded and eCPC-seeded MEND, respectively. In addition to being porcine derived instead of human, these results are representative of one biological donor in technical triplicate and we are currently testing two more matched biological replicates (all cell types sourced from the same animal). We expect to use superimposed layers of GMSC-seeded MEND and eCPC-seeded MEND to mimic the spatial patterning of TMJ cartilage with a bilayered scaffold. Notably, both eCPCs and GMSCs are an attractive autologous stem cell source for chondrogenic repair of TMJOA that can be accessed with minimally invasive approaches and with the capacity of specific differentiation to regenerate each layer of the TMJ cartilage.

SIGNIFICANCE/CLINICAL RELEVANCE: Combining eCPCs and GMSCs is a promising approach for TMJ repair, as they are both accessible in a minimally invasive manner and can specify towards a hyaline and fibrocartilaginous phenotype, respectively. MEND demonstrates promise with easy recellularization and composition close to that of TMJ cartilage, matching key requirements for clinically relevant articular cartilage engineering.

REFERENCES: [1] Stoll + Ped. Rheum. (2018) [2] Mélou + Medicina (2022) [3] Caldwell + OA Cart. (2015) [4] Gehret + BioRxiv (2022)

ACKNOWLEDGEMENTS: Support from the Children's Hospital of Philadelphia Research Institute, Fontaine Fellowship, and T32-AR007132. Thanks to Dr. Quanzhou Zhang for help with GMSC extractions.

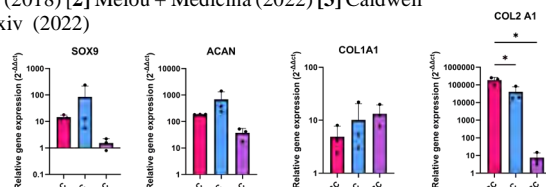


Fig 2. RT-qPCR for key chondrogenic genes after 21 days of pellet culture. One-way ANOVA, *p < 0.05

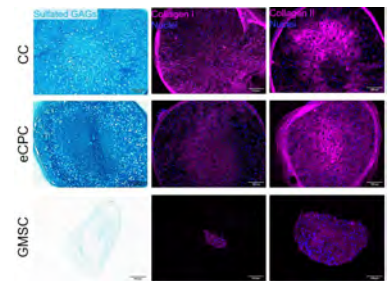


Fig 1. (left to right) Alcian Blue and IF for Collagen I and Collagen II for CCs, eCPCs, and GMSCs.

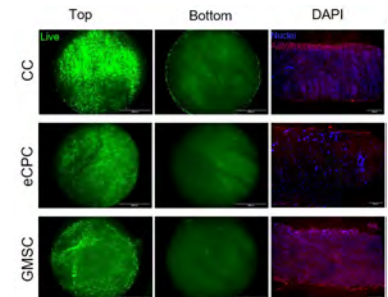


Fig 3. Top and bottom views of MEND seeded with the various cell sources. DAPI staining of the seeded scaffold cross-section (red, autofluorescence).

Title: Periosteal $Pdgfr\alpha$ -lineage cells contribute to heterotopic ossification in
Fibrodysplasia Ossificans Progressiva

AUTHORS: Loreilys Mejías Rivera^{1,2,4}, Brian Herman², Diego Ocaranza Nuñez², Alexandra Goodwin², Fatoumata Diarra², Foteini Mourkioti^{2, 5, 6} and Eileen M. Shore^{2,3,4,6}

AFFILIATIONS: ¹Cell and Molecular Biology, Genetics and Epigenetics Graduate Program, University of Pennsylvania, Philadelphia, PA 19104, USA.

Departments of ²Orthopaedic Surgery, ³Genetics, ⁴Center for Research in FOP and Related Disorders, ⁵Cell and Developmental Biology, Perelman School of Medicine, University of Pennsylvania, PA 19104, USA

⁶Penn Institute for Regenerative Medicine, Musculoskeletal Program, Perelman School of Medicine, University of Pennsylvania, PA 19104, USA

Abstract

In the rare genetic disorder Fibrodysplasia Ossificans Progressiva (FOP), bone forms in soft connective tissues such as skeletal muscle, due to mutations in the BMP type I receptor *ACVR1/ALK2* (*ACVR1^{R206H/+}*). In FOP, instead of regenerating functional muscle after injury, damaged tissue transitions to heterotopic ossification (HO). We and others have shown that the cellular source of HO in FOP can be largely attributed to fibro/adipogenic progenitors (FAPs), a $Pdgfr\alpha$ + mesenchymal population residing within skeletal muscle. Previously we showed that mutant FAPs do not return to quiescence post-injury, instead serving as HO progenitors, while miscommunicating with muscle stem cells to impair muscle regeneration. Interestingly, recent studies identified that interstitial muscle FAPs are not the only cells that express *Pdgfr\alpha* in musculoskeletal tissue. *Pdgfr\alpha* is also expressed by a cell population in the periosteum, a thin connective tissue with $Pdgfr\alpha$ + skeletal progenitors that surrounds bones. Although the periosteum has been suggested as a potential source of HO progenitors, this has never been investigated in the context of FOP. To examine how *Acvr1^{R206H/+}* $Pdgfr\alpha$ -lineage cells affect the regenerating muscle microenvironment and lead to ectopic bone formation, we generated an inducible *Pdgfr\alpha*-Cre;*Acvr1^{R206H/+}* mouse model and used micro-computed tomography and histology to evaluate HO progression with and without muscle injury. We found induction of *Acvr1^{R206H}* mutation alone induces periosteal expansion by 5 days post tamoxifen (dp TAM), although with variable penetrance in the hindlimb bones examined (tibia, fibula and femur), and periosteal osteogenesis is detected by 10 and 14dp TAM. In response to skeletal muscle injury, mutant mice showed impaired muscle regeneration with significantly smaller cross-sectional area of centrally nucleated myofibers, and HO robustly formed within skeletal muscle at sites of injury. We further found that the thickness of mutant tibia periosteum expanded significantly compared to controls at sites proximal to the injured muscle by 5 dpi. This periosteal expansion is driven by a significant increase in cambium layer thickness, where $Pdgfr\alpha$ + skeletal progenitors reside. Over time (10 dpi), this periosteum transitioned to endochondral ossification that infiltrated the surrounding skeletal muscle. Periosteal expansion appears to be systemic after muscle injury as the femur (distal to injury) also had significant increases in thickness. Altogether, our data offer new cellular perspectives and provide the foundation to understand skeletal muscle and periosteal cell interactions and responses that will be important in future therapeutic approaches to improve muscle repair and reduce bone formation in FOP.

YAP and TAZ regulate fetal growth plate chondrocyte hypertrophy and maturation

Christopher J. Panebianco¹, Joel D. Boerckel¹

¹Department of Orthopaedic Surgery, University of Pennsylvania, Philadelphia, PA

Long bone growth occurs through continued expansion and remodeling of growth plate cartilage, via chondrocyte proliferating and hypertrophy; however, the transcriptional mechanisms are poorly understood. The transcriptional regulators yes-associated protein (YAP) and transcriptional co-activator with PDZ-binding motif (TAZ) control the development of many organs, including bone. Deleting YAP/TAZ from Col2a1-lineage chondrocytes impaired bone growth, but surprisingly did not alter proliferating chondrocytes.¹ Recently, our group showed that deleting YAP and TAZ from Osterix-expressing (Osx) osteoprogenitors and hypertrophic chondrocytes (HCs) also impaired bone development.² Together, these findings suggest HC-intrinsic roles of YAP/TAZ signaling, but how they regulate hypertrophy and bone growth is unknown.

In wildtype (WT^{f/f}) growth plates, YAP and TAZ immunostaining was minimal in proliferating chondrocytes, but abundant in HCs (Fig 1A). We therefore deleted YAP and TAZ from HCs using a Col10a1-Cre mouse (YAP/TAZ cKO^{Col10}), and analyzed hypertrophic cartilage at E17.5. Cre-mediated recombination reduced the percentage of YAP+ and TAZ+ HCs in the distal femur hypertrophic zone (HZ) by 60% and 50%, respectively, and did not alter YAP/TAZ expression in the proliferating zone (Fig 1A). YAP/TAZ deletion elongated the HZ and caused precocious hypertrophy initiation (Fig 1B). HZ elongation was characterized by expansion of pre-hypertrophic and calcified hypertrophic regions, but did not alter the morphology of the transverse cartilage septum (Fig 1C).

Together, these findings demonstrate that HC-intrinsic YAP/TAZ signaling regulates both hypertrophy initiation and maturation. Previously, we showed that YAP/TAZ deletion from Osx+ HCs and osteoprogenitors caused both growth plate expansion and disordered remodeling of the cartilage septum.² Here we show that YAP/TAZ cKO^{Col10} phenocopied Col2a1-cKO mice,¹ with hypertrophic expansion, but normal transverse cartilage septum. Thus, YAP and TAZ act intrinsically in HCs to control hypertrophy without altering recruitment of remodeling capillaries and septoclasts to the chondro-osseous junction. Future studies will mechanistically explore how HC-intrinsic YAP/TAZ signaling controls endochondral ossification, but our data shows that HC-intrinsic YAP/TAZ signaling is necessary for proper endochondral ossification.

Refs: [1] Vanyai+ *Development* 2020; [2] Collins+ *Dev Cell* 2024

Innovative Scaffold Delivery for Localized Hh Pathway Activation in Tendon-to-Bone Repair

Jonathan Marcelin¹, Rashad Madi¹, Timur Kamaliddinov¹, Sereen Assi¹, Xi Jiang¹, Dong-Hwa Kim¹, Elizabeth Bernstein¹, Takanori Kokubun^{1,2}, Robert L. Mauck¹, Andrew F. Kuntz¹, Nathaniel A. Dymant¹

¹University of Pennsylvania, Philadelphia, PA, ²Saitama Prefectural University, Koshigaya, Japan
jmarce@seas.upenn.edu

Disclosures: AF Kuntz (5 - Integra Lifesciences, Orthofix, Inc., FX Shoulder; 9 - American Shoulder and Elbow Surgeons, American Board of Orthopaedic Surgery), RL Mauck (4 - Mechano-Therapeutics, LLC; 6 - 4Web Medical; 9 - JOR Spine).

INTRODUCTION: Anterior cruciate ligament (ACL) injuries are a leading cause of training and sports-related injuries. Even with improved surgeries and rehabilitation, fewer than half of patients recover fully due to post-op complications such as graft failure, knee instability, and bone tunnel widening [1]. Integration between the tendon graft and adjacent bone is critical for restoring function following ACL reconstruction (ACLR). We previously demonstrated that the hedgehog (Hh) signaling pathway, a critical mediator of enthesis maturation [2], promotes the zonal, fibrocartilaginous tendon-to-bone attachments in the bone tunnels after ACLR [3]. Given the importance of Hh in various tissues and organs, there is an unmet need to localize delivery of Hh signaling drugs to promote tunnel integration while not eliciting off-target effects. Hence, we devised two scaffold delivery systems to localize release of smoothened agonist (SAG), a small molecule Hh signaling agonist, in different concentrations to support tendon-to-bone integration. SAG was infused into polycaprolactone (PCL) electrospun nanofibers in the first scaffold, whereas it was infused into poly(lactic-co-glycolic acid) (PLGA) microspheres that were sintered between PCL fibers in the second scaffold, known as the Bilayer Delivery System (BiLDS). The advantage of the BiLDS is that the SAG microspheres can be positioned directly in the bone tunnels, avoiding potential off-target effects from SAG release into the joint space [4]. The primary objectives of this study are to incorporate SAG into these scaffolds and analyze the release pattern *in vitro* to determine if SAG release can locally trigger the Hh pathway to ultimately promote tunnel integration.

METHODS: All animals and procedures were IACUC approved. **PCL Scaffold Fabrication:** PCL solution (35 wt%) was prepared in DMF/THF with SAG at different concentrations (0, 0.001, 0.01, 0.1 mg/ml) and electrospun on a rotating mandrel. **SAG In Vitro Release Study:** Blank and SAG-infused scaffolds were placed in culture media in tubes on a shaker at 37°C (Fig. 1A) and conditioned media (CM) was collected over 28 days. CM samples from days 2, 8, 16, or 26 were applied to bone marrow stromal cell (bMSC) cultures for 4 days. Gli1 gene expression was assessed by qPCR. **BiLDS Fabrication:** The microspheres (MS) were loaded with SAG (0.1mg/ml) and created as previously described [5]. They were resuspended in PBS, and the BiLDS were created by heat sintering 20 µL (0.17 mg/µL) of the solution between two aligned PCL electrospun nanofibrous sheets in a region that is 20mm long (average length of the rabbit bone tunnel). Our pocket design featured several diamond-shaped pockets (Fig. 2A) instead of a single pocket to increase durability during surgical transplantation. **Rabbit ACLR Reconstruction Implant Feasibility Study:** Flexor digitorum longus (FDL) tendons were harvested from two cadaveric rabbits. The tunnels were drilled, and the graft was inserted such that the microspheres were only in the bone tunnels and not the joint space (Fig. 3). We then fixed and sectioned the tissue immediately after implantation.

RESULTS: Delivery of conditioned media from the PCL scaffold to bMSCs increased Gli1 expression in a dose- and time-dependent manner: As expected, there was a marked increase in Gli1 expression with the direct addition of 3nM (2-fold) and 300nM (70-fold) of SAG directly to the media ($p < 0.05$, Fig. 1B). Furthermore, there was a dose- and time-dependent effect of scaffold SAG release on Gli1 expression ($p < 0.05$, Fig. 1C). Time did not alter Gli1 expression in the empty scaffolds, maintaining levels comparable to the control media (C in Fig. 1B). Notably, all SAG concentrations (0.001, 0.01, and 0.1 mg/ml) showed significantly higher Gli1 expression compared to empty scaffolds in CM collected on day 2, with levels akin to the 300nM media for the 0.01 and 0.1 mg/ml scaffolds. Intriguingly, while Gli1 expression remained high in the 0.1 mg/ml SAG scaffold for CM collected up to day 26 ($p < 0.05$), both the 0.01 and 0.001 mg/ml groups exhibited reduced Gli1 expression over time in CM (Fig. 1C). These findings suggest that the 0.1mg/ml group released enough SAG over 26 days to sustain activated Gli1 expression in bMSCs. **Delivery of conditioned media from the BiLDS to bMSCs increased Gli1 expression in time-dependent manner:** We conducted a similar study where we delivered conditioned media collected on days 1 and 14 to murine bMSC cultures for 3 days. There was a 6.9-fold and 4.9-fold increase in Gli1 expression in the bMSCs, respectively, which compared to a 3.4-fold increase from SAG (3nM) added to the media (normalized to control media) (Fig. 2B). **SAG infused BiLDS/graft construct remained intact during ACLR:** In a surgical feasibility study, we implanted the BiLDS into cadaveric rabbit bone tunnels. We found that the SAG microspheres (dyed with red Alexa Fluor 555 in Fig. 3) sintered between PCL sheets could be positioned within the bone tunnels between the tendon graft as visualized by sagittal and axial micrographs (Fig. 3).

DISCUSSION: This study offers crucial insights into the release of SAG from different scaffold systems and its effect on downstream Gli1 expression. The *in vitro* release profile was dose dependent with CM from the 0.1 mg/ml concentration inducing sustained, elevated Gli1 expression over 26 days. Moreover, to localize the delivery to the bone tunnel and avoid release in the joint space, BiLDS with SAG infused MS were fabricated and implanted in a rabbit femur as a proof of concept for a future localized therapy.

SIGNIFICANCE/CLINICAL RELEVANCE: This study demonstrates promising drug delivery systems to leverage the therapeutic potential of the Hh pathway to promote tendon-to-bone integration.

REFERENCES: 1. Rizer et al., *Skeletal Radiol.*, 2017; 2. Dymant et al., *Dev Biol*, 2015; 3. Kamaliddinov et al., *Osteoarthritis Cartilage*. 2023; 4. Lin et al., *Nat Med.*, 2009; 5. Kim et al., *Acta Biomater.*, 2020

ACKNOWLEDGEMENTS: Work supported by NIH R21AR078429, P30AR069619, F31AR079840 (TBK), T32-AR007132 and, R01AR076381.

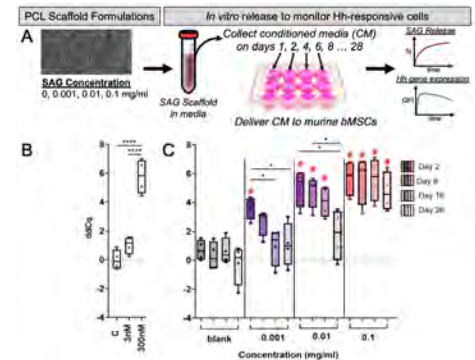


Figure 1. SAG release study experimental design (A). CM released from SAG PCL scaffolds was collected every other day for 28 days. Murine bMSCs were given either SAG directly to the media (B) or CM from the scaffolds at different time points (C) and Gli1 expression was measured via qPCR. * $p < 0.05$; # $p < 0.05$ vs. blank

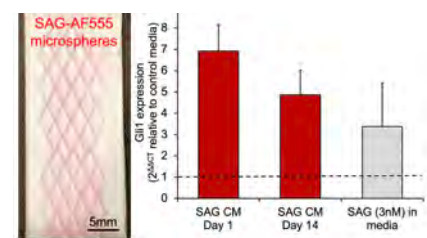


Figure 2. BiLDS Scaffold (A). Gli1 expression of bMSCs treated with conditioned media (CM) from SAG loaded BiLDS on day 1 and day 14 compared to SAG (3nM) given directly to media, normalized to fresh media (C, n=2)

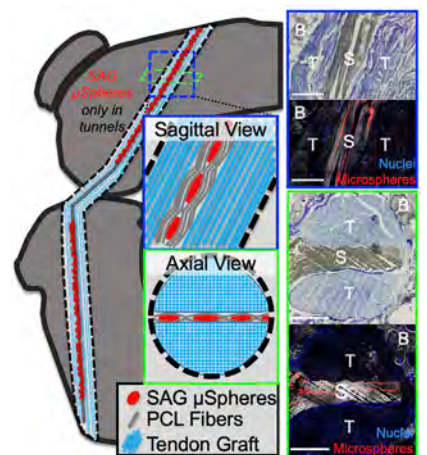


Figure 3. BiLDS scaffold sutured between tendon graft such that SAG microspheres are only in bone tunnels (left). Histology images of rabbit femur showing BiLDS containing AF-555 (red) SAG microspheres (right). B: bone, T: FDL tendon, S: BiLDS scaffold.

SIRT6 Activation and Axitinib Restricts Endochondral Ossification *In Vivo*

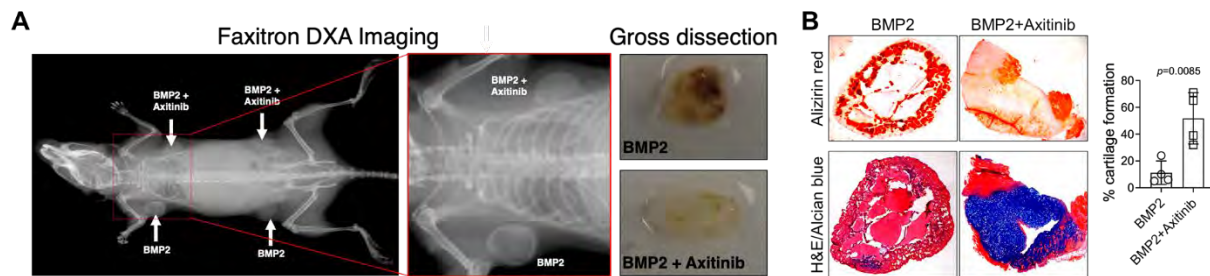
¹Matheus Moreira Perez, ¹Abu Mansalay, ¹Autumn Melvage, ¹Amber Slaweski, ¹Theresa Freeman, ¹John A. Collins, ¹Thomas Jefferson University, Philadelphia, PA, USA

INTRODUCTION: Precise stem cell signaling cues are needed to induce chondrocyte differentiation and the formation of articular cartilage. Current techniques to form stable articular cartilage are suboptimal and form fibrocartilage or bone through endochondral ossification. As such, new strategies that induce stem cells to inhibit endochondral ossification and promote stable articular cartilage are needed. Our prior data, and that of others, demonstrates that activation of the pro-longevity sirtuin, SIRT6, can regulate stem cell function and differentiation in a variety of models. In this study, we adopted an *in vivo* endochondral ossification model (using exogenous BMP2) and tested the effect of a small molecule activator of SIRT6, MDL-800, or a VEGF receptor 1, 2, and 3 inhibitor, Axitinib, to skew stem cell differentiation towards cartilage in mice.

METHODS: Animal studies were approved by the Thomas Jefferson University Institutional Animal Care and Use Committees following guidelines from the National Institutes of Health Guide for the Care and Use of Laboratory Animals. Twelve-week-old C57BL/6 mice (n=4/group) were subcutaneously injected with 300 μ l of Corning Matrigel Matrix Basement Membrane containing recombinant BMP2 (6 μ g/ml) with or without axitinib (3mM), or MDL-800 (25 μ M) (2 technical replicates/mouse). After 14 days, mice were euthanized, and Matrigel constructs were visualized *in vivo* using a DXA Analysis System (Faxitron) prior to microCT analysis of bone, and histological analysis of bone and cartilage formation by alizarin red and H&E/Alcian blue staining.

RESULTS: 14 days after injection, matrigel constructs were clearly visible in the abdomen of mice as assessed by DXA scanning (**Fig 1A**). Matrigel constructs containing BMP2 presented with a brown/red coloration indicative of blood vessel penetration into the masses, whereas BMP2 plus axitinib (**Fig 1A**) or MDL-800 constructs presented as white and opaque. Matrigel constructs containing BMP2 formed bone, indicating that resident and migrating stem cells that invaded the matrigel constructs underwent endochondral ossification *in vivo*. Bone formation was evidenced by positive staining for alizarin red (calcium deposition) and negative staining for alcian blue (proteoglycans). Supplementation of BMP2 containing matrigel constructs with axitinib inhibited bone formation and skewed stem cell differentiation towards forming cartilage, characterized by significantly lower levels of alizarin red staining and significantly higher levels of staining with alcian blue ($p=0.085$) (**Fig 1B**). Supplementation of MDL-800 into matrigels containing BMP2 significantly decreased bone formation by 80% ($p<0.0001$).

DISCUSSION: The use of axitinib to inhibit VEGF mediated bone formation is a simple and non-invasive way to assess chondrogenic stem cell differentiation and cartilage formation *in vivo*. This study demonstrates that axitinib, in the presence of BMP2, skewed migrating resident stem cells towards chondrogenic differentiation and cartilage formation rather than bone via endochondral ossification, as was observed with BMP2 alone. Additionally, activating SIRT6 with MDL-800 profoundly inhibited BMP2-mediated bone formation through yet unidentified mechanisms. Our prior work has demonstrated the effects of SIRT6 to critically regulate chondrocyte and cartilage integrity *in vitro* and *in vivo*. Therefore, identifying the SIRT6-mediated mechanisms that regulate stem cell differentiation *in vivo* represents the next step in our investigations.



Matrigels subcutaneously injected into four sites of mice could be visualized as masses 14 days after administration (A). Matrigels containing BMP2 were macroscopically brownish in color whereas Matrigels containing BMP2 and axitinib were whitish and opaque (A). Histological analysis demonstrated that BMP2 containing Matrigels formed bone (positive for alizarin red) and Matrigels containing BMP2 and axitinib formed cartilage (positive for alcian blue) (B).

Determining the Microbicidal Efficacy and Tissue Toxicity of Liposomal Vancomycin with and without Cold Thermal Plasma Treatment to Combat Orthopedic Infection

Alannah Bratten¹, Carly Smith¹, Amanda Watkins², Ross Duncan³, Autumn Melvage¹, Thomas P. Schaer²,
Brendan Gilmore³, Noreen Hickok¹, Theresa A. Freeman¹

¹Department of Orthopedic Surgery, Thomas Jefferson University, Philadelphia, PA

² University of Pennsylvania, School of Veterinary Medicine Department of Clinical Studies New Bolton Center,
Kennett Square, PA

³Queens University Belfast, School of Pharmacy, Belfast, Northern Ireland

Theresa.Freeman@jefferson.edu

INTRODUCTION: This goal of this study was to compare the microbicidal efficacy and tissue toxicity of liposomal vancomycin with and without cold thermal plasma treatment versus traditional-unencapsulated vancomycin to combat a *Staphylococcus aureus* (*S. aureus*) infection in an *in vivo* rat model.

METHODS: At the index surgery, screws were placed in the rat femur with a *S. aureus*-soaked collagen sponge placed on top before the incision was closed. Seven days later a revision surgery was performed the screws were removed and four new screws and a lock plate installed. The wounds were treated with 10mg of either 1) unencapsulated vancomycin 2) liposomal vancomycin, 3) liposomal vancomycin with cold J-plasma treatment, or 4) betadine control. After 4 days, the hardware and muscle tissue (vastus lateralis) were collected and analyzed for CFU to determine infection level, qPCR to determine cytokine expression and histology staining with toluidine blue (mast cells for immune cell activation) and picosirius red (collagen for fibrosis). Changes in CFU between the Day 0 and Day 4 were calculated to determine response to treatment compared to untreated infection. The number of mast cells within the 4-5 tissue sections/rat were analyzed by microscopic image analysis. The picosirius red stain was used to determine percent fibrosis in each muscle section. The biceps femoris was homogenized in Trizol for RNA extraction (Macherey-Nagel) and qPCR analysis to measure the levels of expression for interleukin-1 β (IL-1 β) and interleukin-6 (IL-6). Statistical significance was determined using one-way ANOVA on Prism (GraphPad) with a significance level $p \leq 0.05$.

RESULTS: The bacterial CFU count from hardware and muscle show a significant decrease with traditional vancomycin (TDV) or liposomal vancomycin (LPV) treatment, as compared to the infection alone control group. However, no significant difference between the two vancomycin treatment groups was observed. When cold plasma was added to the LPV (LPV-CP) a significant decrease was observed in the muscle tissue, but not on the hardware. The transcript levels of IL-1 β and IL-6 by qPCR were slightly, but not significantly lower in the vancomycin groups compared to the untreated infected rats. IL-1 β expression was further reduced in LPV-CP group, but was still not significantly different. Histology also showed no significant differences between fibrotic tissue area or mast cell number between the groups by image analysis quantitation. In this analysis, the LPV group had the highest amount of fibrotic tissue and cold plasma treatment decreased this. Interestingly, LPV and LPV-CP both exhibited an increased trend in mast cells.

CONCLUSION: Liposomal vancomycin, with or without cold plasma treatment, does not significantly change the bactericidal efficacy or tissue inflammation and fibrosis when compared to traditional vancomycin, in the *in vivo* rat model. These results differ from to the *in vitro* data, potentially due to differences in environmental factors such as serum or diffusion effects.

TNFAIP8/TIPE2 Inactivation Modulates Extracellular Matrix Organization Gene Expression and Preserves Intervertebral Disc Structure in the Mouse

Ken Chen, Zuozhen Tian, MS, Frances S. Shofer, PhD, Srish S. Chenna, Daniel Z. Sandroni, Ling Qin, PhD, Yejia Zhang, MD, PhD

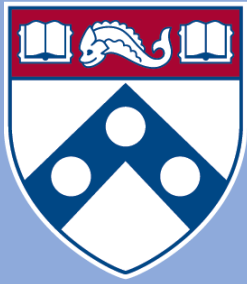
Hospital of the University of Pennsylvania, and Corporal Michael J. Crescenz Veterans Affairs Medical Center, Philadelphia, PA.

Background. Back pain related to intervertebral disc (IVD) degeneration is a common clinical problem. Inflammatory cytokines and chemokines have been found in painful/degenerative human IVDs,¹ and may account for some of the painful symptoms. The TNFAIP8 (tumor necrosis factor- α -induced protein 8) family comprises four highly homologous mammalian proteins, designated TNFAIP8 and TIPE1-3 (TNFAIP8-like 1-3, or TIPE1-3). *Tnfaip8* and *Tipe2* gene expression is perturbed by injury to the mouse IVDs, and TNFAIP8 and TIPE2 loss of function ameliorated immediate proteoglycan loss and inflammation in the injured IVDs.

Methods. The effects of their function loss on the IVDs in mice (male, 3-months old) with both genes deleted were compared with whole RNA transcriptome sequencing (RNASeq). Morphological features of IVDs in the young adult *Tnfaip8/Tipe2* double knockout (dKO) mice were compared with wild type (WT) mice on the same genetic background with Safranin'O and Hematoxylin & eosin staining. Histological scores were assessed by 2 independent readers.

Results. A total of 349 genes differed in the IVDs of dKO and WT (*P.adj* <0.01) mice. Gene ontology (GO) analysis for biological processes was performed, to give meaning to the 349 differentially expressed genes. Extracellular matrix organization and Cell-substrate adhesion were the two most represented biological pathways. Protein-protein interaction network analysis revealed that fibronectin 1 (FN1) and thrombospondin 1 (THBS1) had the highest number of protein-protein interactions. The dKO mouse IVDs displayed higher levels of Safranin'O staining compared with WT [Δ =10.4; 95% confidence interval (CI): 6.8, 14.0; *p*=0.0001]. Furthermore, the histological scores of WT mouse IVDs were significantly higher than those of dKO mice (Δ =1.6; 95% CI: 0.7, 2.4; *p*=0.0007).

Discussions. In summary, an unbiased bulk RNASeq approach was used to compare the transcriptomes of *Tnfaip8/Tipe2*-dKO and WT control mouse IVDs. Profound differences in the gene expression profiles were detected between the mutant and WT mouse IVDs. Importantly, *Tnfaip8/Tipe2*-dKO mouse discs retained more proteoglycan than the WT mice. Although the TNFAIP8 family play important roles in regulating immune function and are likely required for survival, reduced expression locally in the disc may be beneficial in preventing tissue degeneration.



Penn Center *for*
Musculoskeletal Disorders

UNIVERSITY *of* PENNSYLVANIA

**Other Research
(No P30 Core Use)**

Biomarker Signature Discovered by SomaScan in Patients with Severe Low Back Pain-a Pilot Study

Quinn Tate¹, Dessislava Z. Markova², Frances S. Shofer¹, Ken Chen¹, Christopher C. Kepler², Jose A. Canseco², Joshua F. Baker¹, Timothy Dillingham¹, Yejia Zhang^{1,3}

¹University of Pennsylvania; Philadelphia, PA;

²Thomas Jefferson University; Philadelphia, PA;

³Corporal Michael J. Crescenz Veterans Affairs Medical Center, Philadelphia, PA.

Introduction. Low back pain related to intervertebral disc (IVD) degeneration is a common clinical problem. Biomarkers for pain have been examined with a candidate marker approach in the past (1). In this study, we examined 1500 serum proteins using a proteomic approach.

Methods. Whole blood samples were obtained from 29 patients with severe low back pain before surgery and 11 healthy controls. Patient-reported outcomes were collected preoperatively and the degree of IVD degeneration was classified using Pfirrmann grade on preoperative imaging. Serum was separated from the whole blood, and 55 µl of serum was used to quantify protein levels by SomaScan (SomaLogic, Denver, CO).

Results. Levels of 370 proteins from patients with chronic low back pain varied significantly from healthy controls ($p < 0.05$). Among these, 247 proteins were found at higher levels in the participants with low back pain than in the control group, and 123 proteins were lower. Biomarker signatures discovered clearly distinguish patients with low back pain from normal controls (Figure 1). Further, a comparison of back pain patients < 40 years of age and similarly aged healthy controls showed that inflammation-related pathways were upregulated in the patients, with leukocyte proliferation pathway the most enriched, and STAT3 (signal transducer and activator of transcription 3) showing the largest number of protein-protein interactions. Among the downregulated biomarkers comparing these 2 cohorts, SMAD protein phosphorylation pathway was the most enriched, and IL6 (interleukin 6) the most connected. Older back pain patients ≥ 40 years of age differed from younger patients in immune-related pathways, while CD36 (cluster of differentiation 36) has the most interactions with other proteins. The biomarkers identified in the serum shared similar pathways as those identified in the IVD tissues, which bears a chemokine signature.

Discussion. This is a preliminary study of the serum of 40 subjects including participants with severe low back pain prior to undergoing low back surgery, and normal controls. Of the 1500 proteins studied, 370 proteins were identified as significantly different between the two groups. Further study with a larger sample number is needed. However, this profile may provide valuable information in the diagnosis of low back pain. Further study of changes of these biomarkers throughout various treatments of low back pain may help identify outcome predictors. Overrepresented pathways and proteins with the largest network connections may be effective treatment targets.

References

1. Zhang Y, Yao L, Robinson KM, Dillingham TR. Biomarkers in the Degenerative Human Intervertebral Disc Tissue and Blood. *Am J Phys Med Rehabil.* 2022 Oct 1;101(10):983-987. doi: 10.1097/PHM.0000000000001943. Epub 2021 Dec 27. PubMed PMID: 34954738; PubMed Central PMCID: PMC9209568.
2. Zhang Y, Chee A, Shi P, Adams SL, Markova DZ, Anderson DG, Smith HE, Deng Y, Plastaras CT, An HS. Intervertebral Disc Cells Produce Interleukins Found in Patients with Back Pain. *Am J Phys Med Rehabil.* 2016 Jun;95(6):407-15. doi: 10.1097/PHM.0000000000000399. PubMed PMID: 26495812; PubMed Central PMCID: PMC4841745.
3. Kepler CK, Markova DZ, Dibra F, Yadla S, Vaccaro AR, Risbud MV, Albert TJ, Anderson DG. Expression and Relationship of Proinflammatory Chemokine RANTES/CCL5 and Cytokine IL-1 β in Painful Human Intervertebral Discs. *Spine (Phila Pa 1976).* 2013 May 15; 38(11):873-80. PMID: 23660804.

Colla1 Expression Decreases while *Col3a1* Expression Increases after Neonatal Tendon Injury

Miranda K Doro¹, Margaret K Tamburro¹, Jaelyn A Carlson^{1,2}, Susan W Volk², Louis J Soslowsky¹

¹McKay Orthopaedic Laboratory, University of Pennsylvania, ²School of Veterinary Medicine, University of Pennsylvania

INTRODUCTION: Injured tendons in adult mammals heal with collagen III (Col3)-rich fibrovascular scarring. Col3 fibrils organize as a meshwork to resist low levels of multiaxial tensile strain.¹ In contrast, type I collagen (Col1) fibrils, the primary component of healthy tendon, align in parallel in uninjured tendons to resist high levels of uniaxial tensile strain. Consequently, healed tendons have compromised function and higher re-injury risk. Unlike injured adult tendons, neonatal tendons heal quickly with full recovery of functional properties.² Contributions of Col3 to the enhanced neonatal healing response are beginning to be explored; given the recently demonstrated dynamic nature of *Col3a1* expression throughout development,³ *Col3a1* expression during neonatal healing must be assessed relative to appropriately matched developmental controls. Furthermore, given the significance of coordinated *Colla1* and *Col3a1* expression in matrix development,⁴ *Col3a1* expression dynamics should be contextualized in terms of *Colla1* expression dynamics to better understand regulation of matrix formation during neonatal development and healing. Therefore, the objective of this study was to define the dynamics of *Colla1* and *Col3a1* expression following neonatal tendon injury. We hypothesized that, compared to physiologic developmental baseline, both *Colla1* and *Col3a1* expression would increase in early neonatal tendon healing and return to developmental baseline by 21 days post-injury (dpi), reflecting a healing response that is more efficient and complete than adult healing.

METHODS: C57/B6 wild-type mice (n = 9, mixed sex) received left patellar tendon biopsy punch injury (0.3mm diameter, performed under 10X magnification) at postnatal day 7 (p7). Right patellar tendons served as uninjured developmental controls. Mice were sacrificed at 7-dpi (p14, n = 5) and 21-dpi (p28, n = 4). At the time of sacrifice, left and right patellar tendons were isolated and homogenized in TRIzolTM (Invitrogen, Thermo, Waltham, MA). RNA was extracted, converted to cDNA, and pre-amplified (14 cycles) with TaqMan assays for *Col3a1* and *Abl1* as described.⁵ qPCR was performed for *Colla1*, *Col3a1*, and *Abl1* (housekeeper). Δ Ct values were calculated with reference to *Abl1* expression, and fold change (FC) was calculated relative to uninjured developmental controls ($2^{\Delta\Delta Ct}$). Repeated measures two-way ANOVAs (injury status, timepoint) with multiple comparisons were used to assess differences in gene expression ($\alpha = 0.05$).

RESULTS: *Colla1* expression increased while *Col3a1* expression was unchanged throughout physiologic development from p14 to p28 (Fig. 1A-B). Early after neonatal injury, at 7-dpi, *Colla1* expression was decreased while *Col3a1* expression was increased compared to physiologic baseline (Fig. 1A-C). As healing progressed through 21-dpi, *Colla1* expression increased but remained below physiologic baseline while *Col3a1* expression decreased but remained above physiologic baseline (Fig. 1A-C).

DISCUSSION: We defined *Colla1* and *Col3a1* expression dynamics during early and late healing to better understand matrix regulation during neonatal healing. In development, from p14 to p28, we observed an increase in *Colla1* expression while *Col3a1* expression remained consistent. This complements previous work showing *Col3a1* expression decreases from p0 to p14³ and suggests that expression may plateau at p14, remaining consistent through p28.³ Dynamic *Colla1* expression in the context of stable *Col3a1* expression from p14 to p28 may implicate a changing Col3:Col1 ratio as important in physiologic tendon development. Injury disrupts physiologic *Colla1* and *Col3a1* expression in the healing neonatal tendon, with no return to baseline in late healing; *Colla1* expression decreases while *Col3a1* expression increases. This *Col3a1* expression increase parallels mature tendon healing, implying that neonatal injury may serve as a model of superior healing which is translatable to the adult condition.⁶ Moreover, these expression dynamics may indicate that the neonatal healing process is ongoing at 21-dpi. Notably, in healing neonatal Achilles tendons, mechanical properties are recovered by 21-dpi.² As such, neonatal healing may restore mechanical properties despite persistent gene expression changes, or alternatively, this study may highlight differences in patellar and Achilles tendon healing. Mechanical assessment of healing neonatal patellar tendons should be pursued to further understand these possibilities. Results from this study should be interpreted with consideration of the limitations of comparing injured and uninjured contralateral limbs. Systemic effects of injury on the contralateral limb have the capacity to influence tendon gene expression.⁷ Additionally, as this investigation focused gene expression, future work will assess Col1 and Col3 protein amounts, offering a more comprehensive understanding of tissue healing. Nevertheless, this investigation demonstrates similarities in the *Col3a1* expression response in neonatal and adult tendon healing, highlighting the importance of continued study of mechanisms of improved healing in neonates and contributions of Col3 to superior neonatal healing to ultimately identify translatable targets for improving mature healing.

REFERENCES: [1] Williams IF, McCullagh KG, Silver IA, et al, *Connect Tissue Res* 1984. [2] Ansgore HL, Hsu JE, Edelman L, et al., *J Orthop Res* 2012. [3] Tamburro MK, Carlson JA, Doro MK, et al., *ORS* 2023. [4] Niederreither K, D'Souza R, Metsäranta M, et al., *Matrix Biol* 1995. [5] Leiphart RJ, Weiss SN, Soslowsky LJ, et al., *ORS* 2022. [6] Dymont NA, Liu CF, Kazemi N, et al., *PLoS One* 2013. [7] Moran TE, Ignozzi AJ, Burnett Z, et al, *Arthrosc Sports Med Rehabil* 2022. This study was funded by NIH R01GM124091, R01AR080029, F31AR082282 and the Penn Center for Musculoskeletal Disorders (P30AR069619).

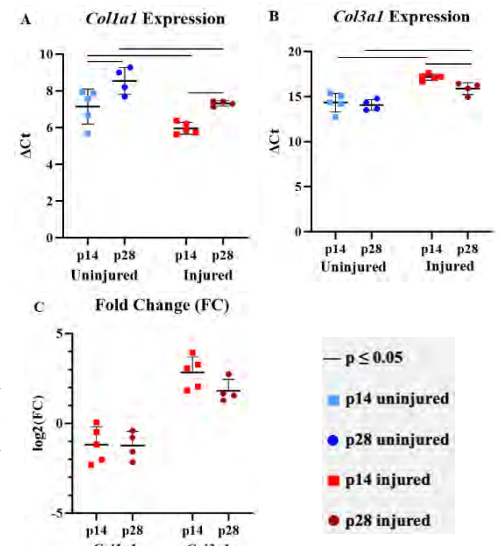


Figure 1. (A) *Colla1* increases from p14 to p28 in uninjured development and decreases at 7- and 14-dpi; (B) *Col3a1* is unchanged from p14 to p28 in uninjured development and is increased at 7- and 14-dpi; (C) Compared to baseline, injured tendons have a reduced *Colla1* FC and increased *Col3a1* FC at early and late healing timepoints.

Super-Resolution Tracking and Machine Learning of HDAC1 Predicts Dynamic Chromatin Remodeling

Tyler Blanch¹, Dong-gi Lee¹, Felicia Pinto¹, Dokyoon Kim¹, and Su Chin Heo¹

¹University of Pennsylvania, Philadelphia, PA

tblanch@seas.upenn.edu

DISCLOSURES: Blanch (N), Lee (N), Pinto (N), Kim (N), Heo (5-4WEB Medical)

INTRODUCTION: DNA conformation within the nucleus plays a crucial role in regulating gene expression, and its dysregulation is implicated in various pathologies [1]. The steady-state conformation of the genome is influenced by multiple epigenetic remodeling enzymes, including histone deacetylase 1 (HDAC) [2]. Traditional methods for characterizing these enzymes have been limited by cell-free systems or diffraction-limited techniques, leading to inaccuracies in *in-vivo* predictions. To overcome these limitations, this study employs single particle tracking (SPT) of HDAC in live cell nuclei, combined with machine learning (ML) approaches, to achieve high-precision quantification and prediction of epigenetic status. For this, HDAC or histone protein H2B (H2B) is fluorescently labeled, and their molecular trajectories are analyzed with kinetic modeling to classify them into diffusive regimes: chromatin-bound (Bound) or freely-diffusing (Free) (Fig. 1A). Trichostatin A (TSA), a chemical that promotes chromatin relaxation, is used to validate our new algorithms by increasing chromatin polymer diffusion, thereby increasing the measured Bound diffusion coefficient (DC) value [3]. Furthermore, ML, specifically a decision tree (DT) method, is applied to classify HDAC and H2B trajectories based on TSA treatment durations. Using our new approaches, we predicted how mechanical perturbations in cells regulate chromatin organization.

METHODS: HeLa cell lines were established via lentiviral transduction to express fusion proteins containing a HaloTag (i.e., HDAC-HaloTag or H2B-HaloTag). The cell lines were cultured on coverglass slides and labeled with JF-549 HaloTag ligand (Promega). Chemical inhibitor treatments included TSA (histone deacetylase inhibitor, 200 ng/mL for 6 or 24 hours) and Y-27632 (Y27) (ROCK inhibitor, 20 μ M for 1 hour). Imaging was performed using the Nanoimager (ONi). Spot detection and tracking were performed with TrackMate (ImageJ), and kinetic modeling of experimental data was achieved on SpotOn [4, 5]. Trajectories were classified using ML algorithms in Python, with 5-fold cross validation and 100 repetitions. Additionally, super-resolution imaging of H2B (H2B-STORM) was performed on fixed HeLa cells immunostained for H2B (Invitrogen) and analyzed following established protocols to validate chromatin condensation status [6].

RESULTS: HeLa cell lines were confirmed to express functional HDAC and H2B fusion constructs. SPT and H2B-STORM imaging was conducted according to the workflow schematic (Fig. 1A). Kinetic modeling of H2B trajectories revealed a significant increase in the DC of the Bound fraction following TSA treatment, without notable changes in the Bound:Free enzyme ratio (Fig. 1B). H2B-STORM of fixed cells treated with TSA revealed a decrease in chromatin condensation as expected (Fig. 1C), indicating the observed increase in Bound DC was due to the decreased chromatin condensation state. This observation is consistent with previous research on chromatin diffusion, validating that SPT accurately captured nanoscale chromatin dynamics. ML analysis of H2B trajectories identified 6 key trajectory features with the highest predictive potential for classification (Fig. 2A). Using these features, decision tree modeling achieved 98.3% classification accuracy for H2B trajectories from control and TSA-treated cells (6 and 24 hours) (Fig. 2B). To further validate these findings, we then measured HDAC diffusion using SPT. Here, TSA was used to corroborate HDAC observations with H2B data, while Y27 was applied as an inhibitor of mechanical stimuli to mimic the epigenetic changes observed with mechanical dysregulation in cells. Representative images of HDAC trajectories for each treatment are shown in Fig. 3A. Bound HDAC trajectories with TSA treatment revealed trends similar to those observed with H2B, confirming successful measurement of enzyme diffusion (Fig. 3B). Y27 treatment similarly showed a significant increase in DC and a notable decrease in the proportion of Bound HDAC enzymes within the nucleus (Fig. 3B-C), indicating reduced enzyme activity. Consistent with the increased Bound DC, Y27 treatment also led to a significant decrease in chromatin condensation state measured with H2B-STORM imaging (Fig. 3D).

DISCUSSION: This study innovatively combines super-resolution imaging techniques, SPT and H2B-STORM, with ML to explore epigenetic enzyme dynamics within intact nuclei. Our H2B-STORM results, which demonstrate chromatin relaxation following TSA treatment, align with existing literature on chromatin physics, validating our approach. The integration of ML enhances our analysis by enabling precise classification and prediction of chromatin dynamics based on enzyme trajectory data. This novel application demonstrates how individual epigenetic enzymes can influence genome organization, with DT methods achieving high predictive accuracy. SPT of HDAC, combined with Y27 treatment, reveals that mechanical cues induce significant genome reorganization and reduce HDAC binding activity in cells. These findings underscore the complex interplay between mechanical forces and epigenetic regulation, offering new insights into maintaining cell phenotype and gene expression. Our study establishes a new benchmark by integrating advanced imaging techniques with sophisticated computational methods, thereby deepening our understanding of chromatin dynamics.

SIGNIFICANCE: This study provides critical insights into the molecular mechanisms underlying chromatin dynamics and epigenetic regulation, offering potential therapeutic targets for diseases related to chromatin dysfunction and mechanical stress, such as epigenetic and age-related disorders, and tendinopathies.

REFERENCES: [1] Wang+, *Nature*, 2022; [2] Magaril+, *Cell Dev Biol*, 2023; [3] Good+, *Epigen*, 2017; [4] Tineves+, *Sci Dir Method*, 2017; [5] Hansen+, *eLife*, 2018; [6] Heo+, *Sci Adv*, 2022. **ACKNOWLEDGEMENTS:** This work is supported by the NIH (P50 AR080581) and NSF (CMMI-1548571).

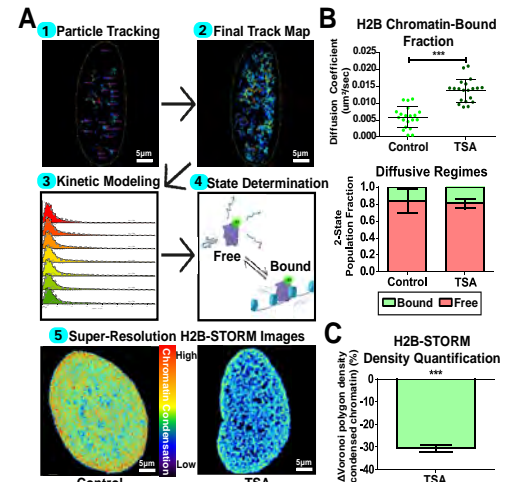


Figure 1: (A) Schematic illustrating the workflow for single particle tracking (SPT) analysis (steps 1-4) and H2B-STORM imaging for assessing genome density (step 5). (B) Diffusion coefficient values for H2B proteins under control and TSA (6 hours) conditions (top) and the proportion of diffusive populations identified (bottom). (C) Percentage change in H2B-STORM density following TSA (6 hours) treatment. (n=20 cells/group for SPT and n=10 cells/group for H2B-STORM. ***: p<0.001).

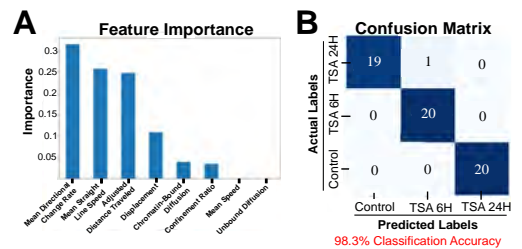


Figure 2: (A) Predicted importance of enzyme trajectory parameters for SPT data analysis with machine learning. (B) Confusion matrix showing classification accuracy of H2B SPT data with TSA treatments (6 and 24 hours) and controls. (n=20 cells/group). 98.3% Classification Accuracy

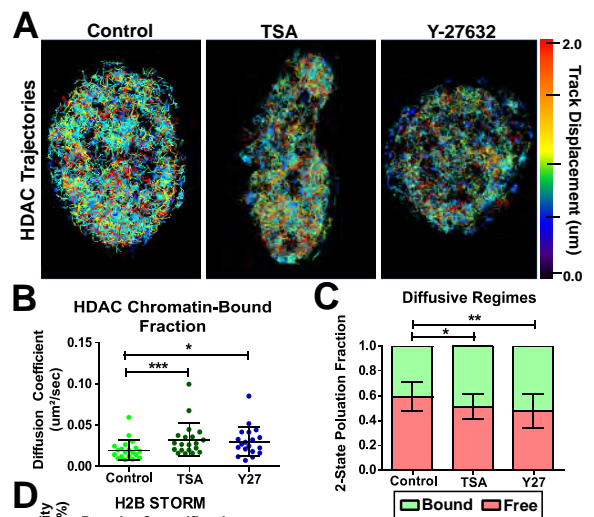


Figure 3: (A) Representative images of HDAC SPT data, showing track displacement under TSA or Y27 treatment. (B) Diffusion coefficients of Bound HDAC following TSA or Y27 treatment. (C) Proportions of diffusive HDAC populations with TSA or Y27 treatment. (D) Percentage change in H2B-STORM density with Y27 treatment. (n=20 cells per group for SPT and n=10 cells per group for H2B-STORM. TSA treatment for 6 hours. *: p<0.05, **: p<0.01, ***: p<0.001).

A distinctive non-telomeric function of TRF2 essential for stem cell identity and muscle repair

Ji-Hyung Lee¹ and Foteini Mourkioti^{1,2,3}

¹Department of Orthopaedic Surgery, Perelman School of Medicine, University of Pennsylvania, Philadelphia, PA 19104, USA.

²Department of Cell and Developmental Biology, Perelman School of Medicine, University of Pennsylvania, Philadelphia, PA 19104, USA.

³Penn Institute for Regenerative Medicine, Musculoskeletal Program, Perelman School of Medicine, University of Pennsylvania, Philadelphia, PA 19104, USA.

Telomeric proteins are present in all mammalian cells protecting chromosomal ends and ensuring organismal homeostasis. While their primary role is to safeguard telomeric ends, they have been suggested to have additional roles in certain tissues. Muscle stem cells (MuSCs), expressing the universal transcription factor Pax7, are fundamental to preserving the high regenerative capacity of muscle. Yet, the cell-autonomous mechanism that regulates Pax7 to maintain MuSC identity is unclear. Here, we uncover that the telomeric protein TRF2 is critical to sustaining stem cell identity in adult muscles and is dynamically regulated upon injury. MuSC-specific TRF2 ablation in mice aggravates muscular dystrophy, mimicking closely the severity of the human disease. Mechanistically, TRF2 binds G-quadruplex DNA structures within regulatory regions of the Pax7 gene to facilitate its expression. These findings identify a unique non-telomeric TRF2 function essential for transcribing Pax7, the master stem cell regulator of the myogenic lineage, to modulate cellular properties critical for stem cell maintenance.

Emergent Mechano-Activated Synovial Fibroblasts Drive Fibrotic Remodeling in a Murine Model of OA

Sung Yeon Kim^{1,2}, Easton Farrell³, Kevin G. Burt^{1,2}, Alexander Knights³, Vu Nguyen^{1,2}, Tristan Maerz³, Carla R. Scanzello^{1,2}, Robert L. Mauck^{1,2}
¹University of Pennsylvania, ²Corp. Crescenzo VA Medical Center, Philadelphia, PA, ³University of Michigan, Ann Arbor, MI
 Sung Yeon Kim: sungyk@seas.upenn.edu

Disclosures: (RLM): JOR Spine, Mechano Therapeutics, 4Web Medical; (CRS): A&R, OA&C

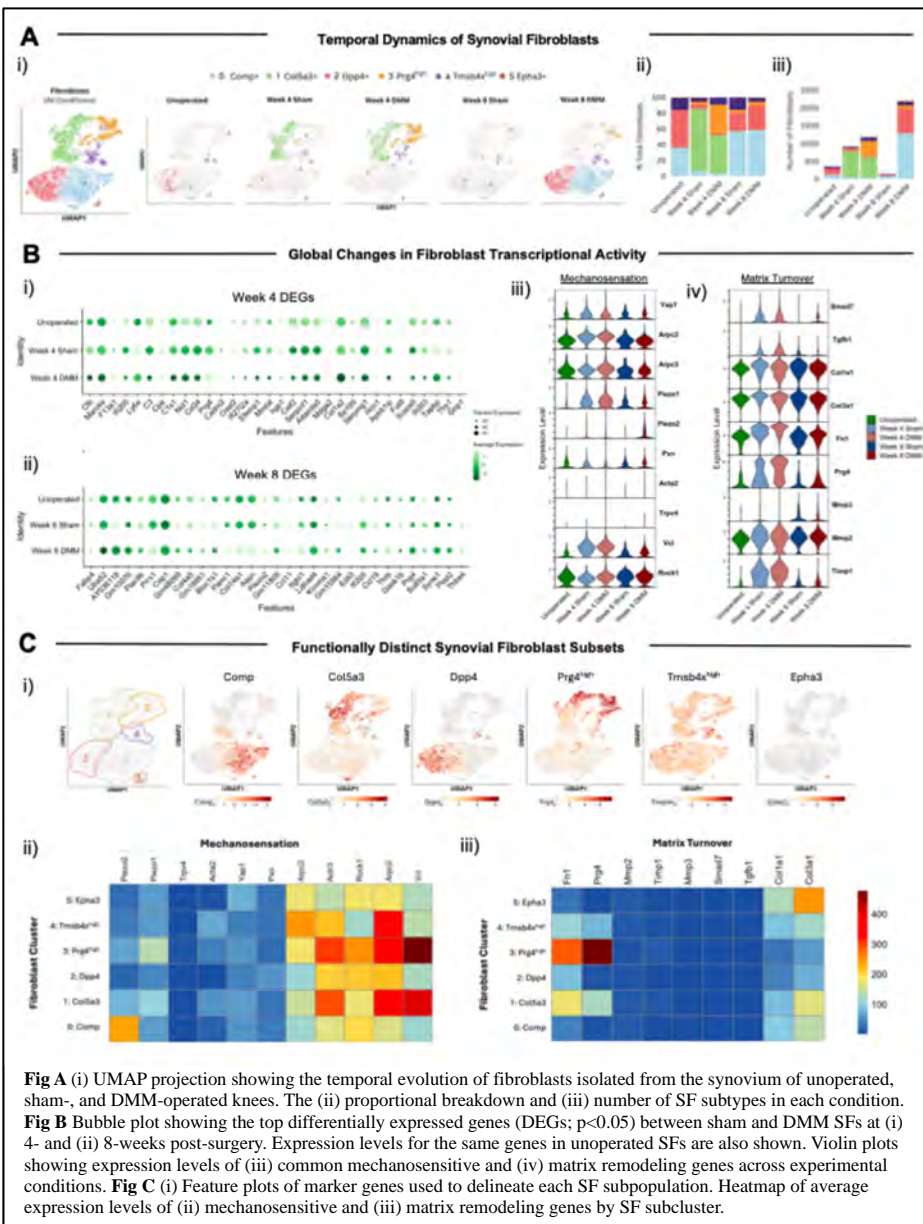
INTRODUCTION: In osteoarthritis (OA), the synovium undergoes marked structural and compositional changes, including fibrotic remodeling [1]. Previously, we probed the microenvironmental mechanics of synovium across different species and disease models and found that fibrotic remodeling of the synovial extracellular matrix (ECM) leads to increased tissue stiffness. Specifically, in both murine destabilization of the medial meniscus (DMM) and naturally occurring canine knee injury models, we found that the synovium stiffens by a factor of 2- to 4-fold within 4 weeks of injury [1,2]. Given that higher stiffness promotes aberrant behaviors in synovial fibroblasts (i.e., an increased myofibroblastic phenotype and decreased lubrication) [3], *the goal of this study was to interrogate how the dynamic physical microenvironment in the fibrotic synovium after injury modulates their in vivo transcriptional behavior and function.*

METHODS: **scRNA-seq:** All animal procedures were IACUC approved. At 12-weeks of age, male C57BL/6J mice underwent surgical DMM on the right knee to induce OA while sham surgery was performed on contralateral knees. Separate mice were utilized as unoperated controls. At 4- and 8- weeks post-DMM, the synovial tissues from each group (n=15/group) were isolated and digested in Liberase (1U/mL) and DNase I (200 µg/mL) before they were further processed for single-cell RNA sequencing (scRNA-seq) (10X Genomics), with synovial fibroblast populations identified and was explored here.

RESULTS: Single-cell transcriptomic profiling of the synovium revealed 5 distinct synovial fibroblast (SF) subsets and their temporal dynamics in the murine DMM model. Notably, at 4-weeks post-surgery, transient SF clusters expressing Col5a3+ and Prg4^{high} emerged in both sham and DMM synovium (**Fig Ai**). By 8-weeks, both the sham and DMM synovium had returned to baseline proportions of SF subsets (**Fig Aii**). However, the DMM synovium at this timepoint saw a substantial increase in the overall number of SFs (**Fig Aiii**), with a large pool of Comp+ and Dpp4+ SFs present. Across all clusters, SFs in the sham group at both 4- and 8- weeks were transcriptionally more similar to SFs in unoperated controls than those in the DMM synovium (**Fig Bi; Fig Bii**). Across all SF clusters, mechanosensitive cell machinery and transcription factors were generally upregulated in the DMM synovium compared to unoperated and sham controls (**Fig Biii**). Genes involved in matrix turnover/remodeling were likewise increased in DMM synovium compared to unoperated and sham at each timepoint (**Fig Biv**). Interestingly, the transient Col5a3+ and Prg4^{high} subpopulations had the highest expression of mechanosensing machinery (**Fig Cii**) and slightly higher matrix remodeling activity (**Fig Ciii**) compared to the other SF clusters, with the Prg4^{high} cluster expressing abundant fibronectin (FN).

DISCUSSION: Synovial fibrosis is a hallmark of OA and is characterized by excessive ECM deposition which is likely to disrupt cellular function [3,4]. Here, we interrogated the phenotype and function of SF subpopulations in the stiffening ECM using in a murine model of OA. Our results show that the sham surgery in this DMM model elicits alterations to the stromal population, but that these changes ultimately resolve by 8-weeks. In contrast, DMM caused sustained changes in the stromal population, including a dramatic increase in the number of SFs. We identified 2 highly mechanoactive subtypes, namely Col5a3+ and Prg4^{high} SFs, that emerged as a consequence of surgery in both sham and DMM joints. However, the Prg4^{high} population, which showed the highest expression of mechanosensitive (e.g., vinculin - involved in focal adhesion maturation) and matrix (e.g., fibronectin - involved in nascent matrix assembly) genes, were most highly expanded in DMM synovium. This SF subset may thus play a central role in driving fibrotic progression. Our data also suggest a bi-directional interaction between cells and the ECM, wherein the stiffened synovial matrix in DMM leads to increased mechano-signaling and expansion of other SF subsets, instigating a feed-forward cascade of disease.

SIGNIFICANCE: These findings implicate mechanotransductive processes in distinct cell subpopulations during the progression of synovial fibrosis in OA. Understanding the mechanisms of cell-ECM crosstalk may identify novel targets to slow disease.



REFERENCES: 1: Kim+ ORS, 2023, 2: Lemmon+ OAC, 2024, 3: Bonnevie+ OAC, 2024, 4: Knights+ eLife, 2022.

ACKNOWLEDGEMENTS: Supported by the VA (I21 RX003854, I50 RX004845, IK6 RX003416), NIH (P30 AR069619), and NSF (CMMI-1548571).

Repetitive Mechanical Stress Triggers Epigenetic Reprogramming and Transcriptional Alterations in Tendon Cells

Yuna Heo¹, Ellen Y. Zhang¹, Yongho Bae², Su Chin Heo¹

¹University of Pennsylvania, Philadelphia, PA, ²University at Buffalo, Buffalo, NY
yunaheo@seas.upenn.edu

Disclosures: Y. Heo (N), E. Zhang (N), Y. Bae (N), S. Heo (5-4WEB Medical Inc.)

Introduction: Mechanical overloading affects tendon properties by altering extracellular matrix (ECM) organization and composition, as well as gene expression, which in turn impacts tenocyte phenotype and contributes to pathological changes [1-3]. While mechanical stress is essential for maintaining tendon integrity, excessive loading can lead to tissue degeneration (i.e., tendinopathy, a common musculoskeletal disorder that poses a significant clinical challenge), especially in the Achilles tendon [4]. Epigenetic mechanisms, including DNA methylation and histone modification, play a crucial role in regulating gene expression in response to mechanical forces [5]. Despite increasing recognition of how altered biophysical environments influence tenocyte epigenetics in tendon degeneration, the cellular and molecular mechanisms driving tendinopathy progression remain unclear. Therefore, this study aims to elucidate how repetitive tensile loading, simulating an overuse tendon degeneration model *in vitro*, impacts transcriptomic and epigenetic alterations in bovine Achilles tenocytes. By enhancing our understanding of these molecular mechanisms, this research supports the development of targeted therapeutic strategies.

Methods: Tenocytes were isolated from juvenile bovine Achilles tendons and expanded to passage 1 (P1) on tissue culture plastic. P1 tenocytes were seeded onto aligned poly(ϵ -caprolactone) (PCL) nanofibrous scaffolds (2×10^6 cells per scaffold) and cultured for 2 days in basal media. A custom tensile loading bioreactor applied cyclic uniaxial force at 3% or 8% strain amplitudes (at 1 Hz) to the tenocyte-seeded scaffolds for 1 or 4 hours over 3 days (Fig. 1A). Post-loading, RNA was extracted for RNA-seq to assess global transcriptional changes. Differential expression was performed with adjusted p-value < 0.05 and absolute log₂ fold change > 1 considered significant. To assess changes in chromatin organization, tenocyte-seeded scaffolds subjected to 8% strain for 4 hours over 3 days were processed for histone extraction. Immunoblotting of H3K9ac (an epigenetic activator associated with chromatin decondensation and transcriptional activation), H3K27me3 (an epigenetic repressor associated with chromatin condensation and transcriptional suppression), and histone 3 (H3) were performed. To investigate the effects of loading frequency, RNA was extracted from scaffolds loaded at 8% strain at 1 or 2 Hz for 4 hours over 3 days. Relative fold changes in mRNA expression levels for type-I collagen (COL-I), type-III collagen (COL-III), tenascin-C (TNC), and matrix metalloproteinase-3 (MMP-3) were determined using RT-qPCR, with GAPDH as the reference gene. Statistical analyses were performed using t-test or ANOVA.

Results: RNA-seq analysis revealed significant changes in gene expression in tenocytes subjected to dynamic loading. Volcano plots (Fig. 1B) highlighted a greater number of differentially expressed genes (DEGs) with prolonged loading durations (1 hour vs. 4 hours), emphasizing the impact of sustained mechanical strain. The z-score heatmap (Fig. 1C) showed increased expression of catabolic genes, particularly in tenocytes exposed to 8% strain for 4 hours. Gene ontology (GO) analysis comparing control conditions to 8% strain for 4 hours identified a downregulation in key biological processes, including cellular morphogenesis, cell-matrix adhesion, and regulation of cell growth, while RNA and protein metabolic processes were upregulated (Fig. 1D). Further analysis revealed that 8% strain loading for 4 hours led to a decrease in H3K9ac expression and an increase in H3K27me3 expression (Fig. 2A, B), suggesting that excessive repetitive mechanical loading induces a repressive chromatin state. Additionally, RT-qPCR analysis of tenocytes subjected to different loading frequencies revealed a significant decrease in the expression of tenogenic markers (COL-I, COL-III, TNC) and an increase in the catabolic marker MMP-3 at a loading frequency of 2 Hz compared to 1 Hz (Fig. 3A). This finding indicates that higher frequency mechanical overloading exacerbates catabolic processes while downregulating anabolic gene expression, potentially accelerating tendon degeneration.

Discussion: This study emphasizes the impact of repetitive high-intensity mechanical loading on tenocytes, revealing a complex interplay between transcriptomic and epigenetic changes that drive tendon degeneration. The results clearly demonstrate that both the intensity and duration of mechanical strain significantly influence gene expression in tenocytes, with greater strain and prolonged exposure leading to more pronounced changes. Under excessive mechanical loading conditions (e.g., 8% strain for 4 hours), there was a notable upregulation of genes associated with stress responses, inflammation, and ECM remodeling. Simultaneously, this condition induced a repressive chromatin state, evidenced by a decrease in H3K9ac and an increase in H3K27me3. These epigenetic shifts suggest a mechanistic link between mechanical strain and gene regulation, highlighting the role of chromatin modifications in tenocyte adaptation to overloading. Moreover, the modulation of genes involved in apoptotic and survival pathways reflects an adaptive response to sustained mechanical stress, further supporting that tenocytes under these conditions resemble an overloaded, degenerative tendon state. The findings collectively indicate that prolonged high-intensity mechanical loading induces a coordinated transcriptomic and epigenetic response, characterized by upregulated stress and inflammatory pathways, ECM remodeling, and a repressive chromatin state. These changes likely contribute to tendon degeneration, indicating loading conditions with higher strain and extended durations function as valuable models for studying tendinopathy and developing therapeutic interventions. Ongoing studies will further explore the correlation between mechanical stress-induced histone modifications and gene expression changes by profiling accessible chromatin using ATAC-seq and examining the epigenetic landscape through ChIP-seq.

Significance: This study enhances our understanding of the molecular and epigenetic responses of tenocytes to mechanical stress, revealing how mechanical forces, specific histone modifications, and gene expression profiles interact to drive pathological changes in tendon cells. By identifying this mechanism linked to overuse conditions, this research lays the groundwork for developing more effective therapeutic and preventative strategies for tendinopathy. Targeting these pathways could lead to novel interventions that not only treat but also prevent the progression of tendon degeneration in clinical settings.

References: [1] Glazebrook+ 2008, *J Orthop Res*; [2] Maeda+ 2010, *Connect Tissue Res*; [3] Freedman+ 2018, *Sci Rep*; [4] Galloway+ 2013, *JBJS*; [5] Jaenisch+ 2003, *Nat Genet*.

Acknowledgements: This work was supported by NIH (K01 AR077087, P50 AR080581, R01 HL163168).

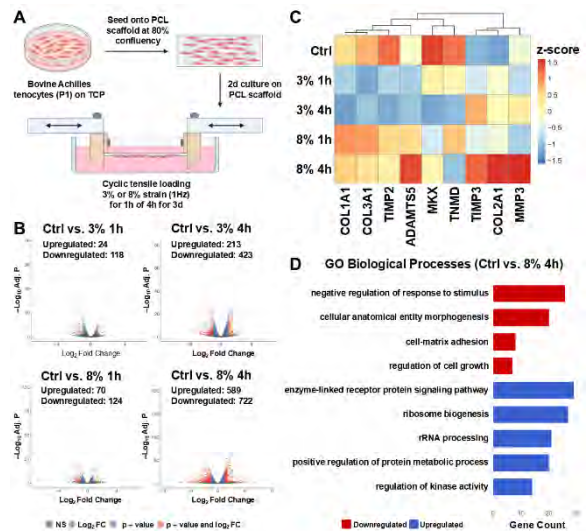


Figure 1. A: Schematic of the experimental design, **B:** Z-score heatmap of selected tenogenic genes subjected to dynamic loading at 3% or 8% strain for 1 or 4 hours, **C:** Volcano plots showing DEGs, **D:** Gene ontology analysis comparing control vs. 8% strain for 4 hours (n=3 biological replicates).

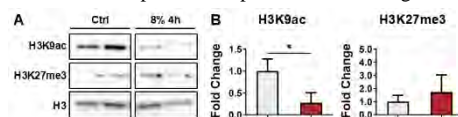


Figure 2. A: Immunoblot of histone markers extracted from tenocytes subjected to dynamic loading at 8% strain for 4 hours at 1 Hz and **(B)** quantification (normalized to H3, *p<0.05, n=4, mean + SD).

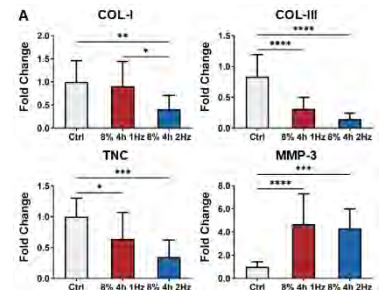


Figure 3. A: Anabolic and catabolic gene expression in tenocytes subjected to dynamic loading at 8% strain for 4 hours at frequencies of 1 or 2 Hz (normalized to GAPDH, *p<0.05, **p<0.01, ***p<0.001, ****p<0.0001, n=4, mean + SD).

Wearable Sensors Measure Wear Time and Step Count in Immobilizing Boots for Achilles Tendon Rupture

Stanton Godshall, Michelle P. Kwon, Daniel Farber, Anthony Ndu, Casey Jo Humbyrd, Josh R. Baxter, Lorraine AT Boakye
University of Pennsylvania, Philadelphia, PA
stanton.godshall@pennmedicine.upenn.edu

DISCLOSURES: Stanton Godshall (N), Michelle P. Kwon (N), Casey Jo Humbyrd (7B,8,9), Daniel Farber (3B,4,5,9), Anthony Ndu (N), Lorraine AT Boakye (8), Josh R. Baxter (N)

INTRODUCTION: Over the past 30 years, Achilles tendon ruptures have increased 10-fold [1]. Achilles tendon ruptures are common injuries that lead to functional deficits in two out of three patients. Functional deficits are a major clinical problem in this patient population. Nearly two-thirds of patients suffer at least a 15% decrease in heel-raise height 1-year after injury [2]. Safely reintroducing tendon loading to support tendon healing remains a controversial issue. Prolonged unloading was the standard of care until the early 2000's when clinical studies found that chronically underloading the tendon leads to worse outcomes and more re-ruptures [3]. The clinical standard of care for Achilles tendon ruptures shifted to using an immobilizing boot to progressively reintroduce loading over ~10 weeks [4]. However, clinical practice has relied on generalized guidelines to progress patients into unprotected weightbearing. We propose a new patient management paradigm to monitor wear time and step count in the real world to support clinicians and researchers in developing patient-specific rehabilitation strategies. For this reason, we used wearable sensors to monitor wear time and step count in patients recovering from a surgically repaired Achilles tendon. We performed this study to demonstrate the feasibility of measuring wear time and step count in immobilizing boots for Achilles tendon rupture patients and to lay the foundation of a longitudinal study to improve rehabilitation protocols. We hypothesized that 1) immobilizing boot wear time is lower than the prescribed amount and 2) step count in the immobilizing boot increases with time.

METHODS: We recruited 12 patients (1 female, age 31.7+/-11.3, BMI 27.7+/-5.3) who underwent surgical repair of an Achilles tendon rupture after obtaining written informed consent in this IRB-approved study. We fixed a commercially available wearable sensor (AX6, Axivity) to the boot during the two- and six-week post-operative clinical visit. We chose this wearable sensor because it continuously measures and logs accelerometer data at 50 Hz for ~35 days without charging or user input. We estimated wear time with an algorithm proposed and utilized in a variety of IMU applications, namely GGIR [5]. We estimated step count with a simple peak-finding algorithm that we developed with validation data we collected in-lab. Linear mixed models were used to test our hypotheses. We used patients as group identifiers and evaluated intraclass correlations to assess variability between patients.

RESULTS: Patient wear time decreased over time and was less than estimated prescribed wear times by 3.1 hours ($p < 0.05$) (Figure 1). Patient step count increased over time ($R^2 = 0.51$, $p < 0.001$) but patients demonstrated varied amounts of increased daily steps – ranging from 500 – 6000 daily steps. (Figure 2). Both groups demonstrated large amounts of patient variability, with intraclass correlations (ICC) of 0.37 for wear time and 0.33 for step count.

DISCUSSION: Our study confirmed our primary hypothesis that a wearable sensor fixed to an immobilizing boot worn by Achilles tendon rupture patients provides unique insight into the behavior of patients in the real world. We found that wear time decreases over time and is consistently below prescribed amounts, confirming our hypothesis. Additionally, we found that step counts increase with time in most patients. However, patient variability was large ($ICC = 0.33$) indicating the presence of behavioral subgroups. Our findings suggest that generalized rehabilitation instructions lead to highly variable wear time and step counts, which may explain patient outcome disparities. This proof-of-concept study focused on developing the tools to monitor rupture patients in real-world environments. Our ongoing work is applying this wearable sensor paradigm in a cohort of patients with Achilles tendon ruptures to identify the link between real-world wear time and physical activity and healing outcomes. We expect that our novel wearable paradigm for immobilizing boots will provide new opportunities to explain differences in healing outcomes in patients receiving care for Achilles tendon ruptures.

SIGNIFICANCE/CLINICAL RELEVANCE: This experiment is a necessary step towards developing precision rehabilitative care for patients with Achilles tendon ruptures. We expect that by linking real-world patient wear time and physical activity to tendon healing and symptoms, we will establish evidence-based behavioral profiles that improve patient outcomes by supporting clinical decision making. Additionally, these data provide important practical rehabilitative information that can inform preclinical models and serve as clinically relevant outcome measurements for longitudinal clinical research.

REFERENCES: [1] Lantto+, *Scand J Med Sci Sports*, 2015; [2] Brorsson+, *Am J Sports Med*, 2017; [3] McCormack+, *BJSM*, 2015; [4] Willits+, *J Bone Jt Surg*, 2010; [5] Rowlands+, *JMPB*, 2019.

ACKNOWLEDGEMENTS: This research was supported by NIH/NIAMS P50AR080581, the University of Pennsylvania Thomas B. McCabe and Jeannette E. Laws Fund, and the American Orthopaedic Foot & Ankle Society Established Research Grant.

IMAGES AND TABLES:

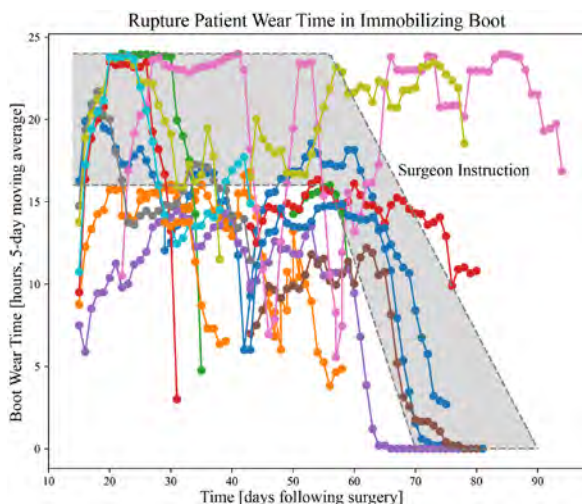


Figure 1. Daily wear time for Achilles tendon rupture patients. Each line represents one rupture patient. The gray shaded region represents a general recommendation for boot wear time.

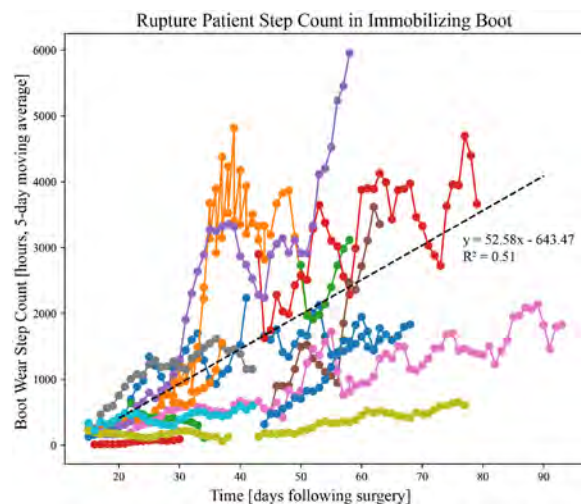


Figure 2. Daily step counts for Achilles tendon rupture patients. Each line represents one rupture patient.

Trans-Signaling by Soluble CD14 Sensitizes Chondrocytes to Lipopolysaccharide Stimuli, Increasing Chondrocyte Inflammatory Responses

Anna E. Rapp¹, Baofeng Hu¹, Carla R. Scanzello^{1,2}

¹Division of Rheumatology, Department of Medicine, University of Pennsylvania, Philadelphia, PA, USA; ²Translational Musculoskeletal Research Center, Corporal Michael J. Crescenz VA Medical Center, Philadelphia, PA, USA
anna.rapp@pennmedicine.upenn.edu

The understanding of osteoarthritis (OA) has evolved significantly over the past decade. Recently attention is being drawn to the role of pattern-recognition receptor (PRR) signaling in chondrocytes. In OA, chondrocytes face a pro-inflammatory environment, influenced by various soluble factors within the synovial fluid, which includes both known and potential PRR ligands. Studies have identified elevated concentrations of lipopolysaccharide (LPS) and its soluble co-receptor CD14 (sCD14) within the synovial fluid of OA patients, correlating with disease severity. The interaction of (s)CD14 with LPS facilitates binding of LPS to its receptor TLR4, thereby sensitizing certain cell types and allowing them to respond to lower ligand concentrations. However, if sCD14 has a similar trans-activating effect on chondrocytes has never been tested. In this study, we aimed to investigate the responsiveness of chondrocytes to TLR4 stimulation by LPS, and test whether sCD14 amplifies their response, as previously observed in fibroblasts.

We exposed human chondrocyte-like cells (cell line C28/I2, Merck Millipore) to varying concentrations of LPS (1 ng to 1 µg/ml; Ultrapure LPS, InvivoGen), both with and without the addition of recombinant soluble hCD14 (2 µg/ml; R&D Systems). A control group with no LPS was included. We evaluated the activation of the NFκB signaling pathway through western blot analysis after 30 and 60 min of incubation and assessed the expression of pro-inflammatory and catabolic genes via RT-qPCR after 24 hours. Statistical analysis was performed using 2-way ANOVA followed by Dunnet's post-hoc test.

We observed both a concentration and time-dependent effect of LPS ± CD14 stimulation on chondrocytes. When stimulated with LPS, we observed a significant up-regulation of NFκB activation only after 60 min when cells were exposed to 100 and 1,000 ng/ml. However, when we added CD14, NFκB was significantly induced after 30 min in presence of 1,000 ng/ml LPS and activation was significantly enhanced by sCD14 addition after 60 min incubation (Fig. 1B) Gene expression analysis revealed a significant up-regulation of IL-8 starting from 10 ng/ml LPS, with further significant elevation upon addition of sCD14. Similar effects were observed for MMP13 expression in the presence of both 10 and 100 ng/ml LPS combined with CD14. IP-10 expression was significantly enhanced by sCD14 when cells were stimulated with 100 ng/ml LPS.

In conclusion, our findings demonstrate a robust pro-inflammatory response of chondrocytes to LPS stimulation, which is potentiated by the addition of sCD14. sCD14 had a sensitizing effect, resulting in augmented and earlier activation of chondrocytes to LPS, as evidenced by NFκB activation and increased expression IL-8, IP-10 and MMP13. Notably, IP-10 expression suggests the activation of TRIF-dependent TLR-signaling in chondrocytes, a novel finding in this context that will be explored in future studies. Overall, our study sheds light on the previously unexplored role of CD14 trans-signaling in OA pathology, with direct implications for chondrocyte function in the inflammatory milieu of the osteoarthritic joint.

Tracing muscle mesenchymal progenitors in fracture healing

Qi He¹, Jiawei Lu¹, Michael Duffy¹, Jaimo Ahn², Nathaniel A Dymant¹, Joel Boerckel¹, Ling Qin¹

¹Department of Orthopaedic Surgery, ¹University of Pennsylvania, Philadelphia, Pennsylvania; ²University of Michigan, Ann Arbor, Michigan, USA

In clinical practice, compromised fracture healing often occurs at sites with less soft tissue especially muscle coverage, and muscle flaps are frequently used to assist skeletal healing when there is severe tissue loss. Recent animal studies using muscle graft transplants showed that fibro-adipogenic progenitors (FAPs), a population of muscle interstitial mesenchymal cells, migrate to the fracture site and contribute to chondrocytes and osteoblasts in callus. However, it is unclear whether this observation is physiologically relevant. Examination of muscle scRNA-seq datasets revealed that FAPs express Prg4. Next, we generated Prg4-CreER Rosa-tdTomato (Prg4ER/Td) mice to trace the fate of FAPs. Mice at 2 months of age received Tamoxifen for 5 days and a closed transverse fracture or a drill-hole injury on their right tibiae 2 weeks later. In un-injured legs, Td specifically labeled FAPs at 24.0±1.3% (n=3 mice, flow cytometry) or 20.6±1.9% (n=3 mice, CFU-F assay), but it did not label any cells in bone marrow or in periosteum. RNA FISH validated Prg4 expression in muscle Td+ cells only. During fracture, muscle surrounding the injured site was damaged as well. At day 3 post fracture, we observed a sharp increase of Td+ cells in muscle next to the fracture site (5.9-fold, n=5 mice/group) and inside the fracture hematoma. Meanwhile, thickened periosteum did not contain any Td+ cells, suggesting that periosteal mesenchymal progenitors are responsible for the periosteum activation. Td labeled many Col2+ chondrocytes, Osterix+ osteoblasts, and osteocytes at day 7, 14, and 28, respectively. Interestingly, those Td+ cells were mostly located in the outer part of callus, which is next to muscle. On the contrary, cells in the inner part of callus, which is next to the cortical bone, were Td-. Flow cytometry confirmed that 8.9±0.4% of mesenchymal cells in day 14 callus were Td+ (n=5 mice). At day 56 when bones were almost healed, many Td+ cells were detected in the periosteum and cortical bone at the prior fracture site. Bone cells distal to the injury site remained as Td-. These tracing results clearly show that muscle FAPs move to bone surface and become bone cells during injury. In these mice, a second fracture at the same site activated periosteal Td+ cells and promoted them to become chondrocytes and osteoblasts in the inner part of callus. Importantly, ablation of Prg4+ cells before fracture using Prg4-CreER Td DTA mice significantly reduced bone volume fraction by 38.4% (n=5 mice/group) in the callus at day 21 post fracture. In the drill-hole model, which has less muscle injury than fracture, Td+ cells were mostly observed in the fibrosis tissue next to the healing site but not inside the defect site nor in bone marrow. Taken together, our data demonstrate the critical role of muscle mesenchymal progenitors in endochondral bone repair and a novel trans-differentiation mechanism from muscle cells to bone cells.

A Novel Porous Microcarrier for Extended Release of mRNA-Lipid Nanoparticles for Musculoskeletal Tissue Repair

Auhin K. Maparu^{1,2}, Keerthana Iyer^{1,2}, Zain Siddiqui¹, Karthikeyan Rajagopal^{1,2}, Jacob Kim¹, Robert L. Mauck^{1,2}, Michael J. Mitchell¹, Lachlan J. Smith^{1,2}

¹University of Pennsylvania, Philadelphia, PA, ²Corporal Michael J. Crescenz VA Medical Center, Philadelphia, PA
 auhin.maparu@penmedicine.upenn.edu

Disclosures: Auhin K. Maparu (N), Keerthana Iyer (N), Zain Siddiqui (N), Karthikeyan Rajagopal (N), Jacob Kim (N), Robert L. Mauck (8-JOR Spine; Mechanotherapeutics, 4Web Medical), Michael J. Mitchell (N), Lachlan J. Smith (8-JOR Spine, Connective Tissue Research; 9-ORS Spine Section, National MPS Society).

INTRODUCTION: Non-viral gene therapy is emerging as a safe and versatile strategy for repair and regeneration of musculoskeletal tissues such as articular cartilage and intervertebral disc [1], and lipid nanoparticles (LNPs) are a promising nanomaterial for delivering RNA-based therapeutics [2]. In recent work, we identified mRNA-LNP formulations capable of transfecting a range of skeletal cell types, including chondrocytes, with very high efficiency [3,4]. Challenges of local administration of mRNA-LNPs include transient expression limited to a few days and rapid clearance from the delivery site. In order to attain significant therapeutic benefits, multiple doses of mRNA-LNPs would likely be required, which is burdensome for patients and may cause inflammation at the site of injection. Therefore, the objective of this study was to develop a novel carrier for extended release of mRNA-LNPs to articular cartilage and intervertebral disc. We hypothesized that co-incubation of mRNA-LNPs with poly(lactic-co-glycolic acid) (PLGA) based porous microcarriers (PMCs) would enable loading of mRNA-LNPs within the pores of PMCs via electrostatic and hydrophobic interactions (Fig. 1A) and that the mRNA-LNPs would then exhibit extended release from PMCs via porous diffusion followed by degradation of PLGA over time (Fig. 1B).

METHODS: *Fabrication and Characterization of Microcarriers:* PLGA-based PMCs were fabricated using a modification of previously reported methods [5]. Pluronic F127 was used as a porogen. PMC size and porosity were determined using scanning electron microscopy (SEM). To visualize PMCs under confocal microscopy, Nile red (NR) was incorporated during fabrication. *Fabrication of mRNA-LNPs:* Green fluorescent protein (GFP) mRNA was encapsulated within LNPs, as previously reported [6]. LNP formulations containing 10% or 40% DOTAP (a permanently cationic lipid) producing LNPs that were overall anionic and cationic, respectively, were employed. Surface charge was measured using a Zetasizer. For visualization of mRNA-LNP loading under confocal microscopy, mRNA-LNPs were labeled with an infrared dye, DiR. *Loading and Release of mRNA-LNPs:* Freeze-dried PMCs were incubated with an mRNA-LNP suspension in PBS on a gentle shaker. After 24 h, the resulting suspension was filtered using a syringe filter and mRNA concentration was measured using the RiboGreen assay. Encapsulation efficiency of the PMCs was calculated as $(X-Y)/X \times 100$ where X and Y are the mRNA contents in the filtrate at the initial and final stage of incubation, respectively. Finally, release of mRNA-LNPs into PBS at time points up to 21 days was examined. All loading and release experiments were performed in triplicate. Statistical differences in mRNA-LNP loading and release over time were established using two-way ANOVA and one-way ANOVA with Tukey's test, respectively.

RESULTS: *Characterization of PMC Architecture:* SEM analysis of the unloaded PMCs (Fig. 2A) revealed formation of PMCs of average size of $30.35 \pm 4.54 \mu\text{m}$ and pore size of $1.26 \pm 0.76 \mu\text{m}$ (average of 10 images). Confocal imaging of PMCs loaded with fluorescent dye NR also revealed the porous architecture (Fig. 2B). In particular, the interconnectivity of the pores was clearly visible, maximizing permeation of LNPs even to the innermost section of the PMCs. *Loading and Release of mRNA-LNPs from PMCs:* Unloaded PMCs did not exhibit near infra-red fluorescence (Fig. 2C); however, when were incubated with DiR-labeled mRNA-LNPs, fluorescence was detected (Fig. 2D), confirming successful loading. The zeta potential values of PMCs, anionic LNPs and cationic LNPs are shown in the inset of Fig. 3A. As shown in Fig. 3A, almost 100% encapsulation efficiency was achieved within 24 h of incubation, with slightly faster loading observed for cationic LNPs (n = 3). Preliminary release kinetics demonstrated a linear release of anionic mRNA-LNPs beginning at day 3 and continuing until at least day 21 (n = 3, Fig. 3B).

DISCUSSION: In this study, we successfully developed a novel PLGA-based microcarrier for extended release of mRNA-LNPs in musculoskeletal tissues. Potential applications include targeting both catabolic and anabolic pathways to regenerate tissues such as cartilage and intervertebral disc. PLGA was chosen due to its excellent biocompatibility and biodegradability, which can be controlled by changing the proportion of lactic/glycolic acid [7], while porosity can be controlled by tuning the amount of porogen. As PMCs were slightly anionic in nature, conjugation with anionic LNPs was likely mediated by hydrophobic interactions, as both LNPs and PMCs were hydrophobic. Cationic LNPs adsorbed more quickly into PMC pores, likely due to additional electrostatic interactions, resulting in faster encapsulation. Ongoing studies will confirm bioactivity of released mRNA-LNPs on disc and cartilage cells *in vitro* and *in vivo*.

SIGNIFICANCE/CLINICAL RELEVANCE: The present study demonstrates a novel, robust, scalable and highly translatable technology for extended release of mRNA-LNPs for treatment of musculoskeletal disorders such as intervertebral disc degeneration and osteoarthritis.

REFERENCES: [1] Gantenbein+, *Front. Bioeng. Biotechnol.*, 2020; [2] Kenjo+, *Nat. Commun.*, 2021; [3] Rajagopal+, *ORS*, 2023; [4] Xue+, *JACS*, 2022; [5] Kim+, *Biomaterials*, 2011; [6] El-Mayta+, *J. Vis. Exp.*, 2023; [7] Mohanraj+, *Adv. Funct. Mater.*, 2019.

ACKNOWLEDGEMENTS: Funding support from the NIH (R01 AR077435) and the Department of Veterans Affairs (I01 RX001321).

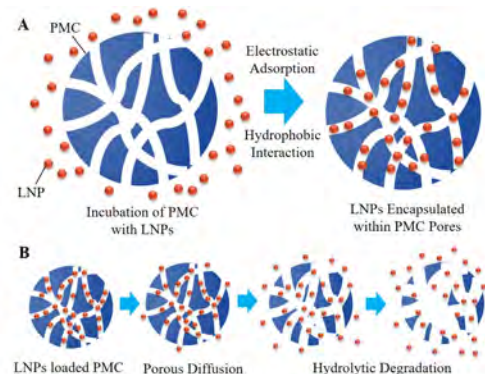


Fig. 1: (A) Schematic illustrating the principles and processes of loading LNPs within PMC pores. (B) Mechanism of extended release of LNPs from PMCs via porous diffusion and followed by hydrolytic degradation. The LNPs are representing bare LNPs, dye labeled LNPs and mRNA-LNPs.

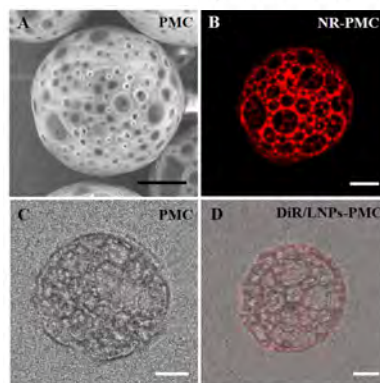


Fig. 2: (A) SEM image of the fabricated PMCs, depicting their morphology and porous nature. Confocal images of (B) NR loaded PMCs, (C) unloaded PMC and (D) PMC loaded with DiR dye labeled LNPs. Scale bar: 10 μm .

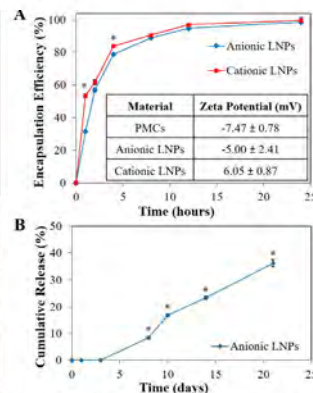


Fig. 3: Plots for (A) encapsulation efficiency of the PMCs (*p < 0.05 for anionic vs cationic) and (B) cumulative release of mRNA-LNPs from PMCs over time (*p < 0.05 for subsequent time points).

Targeting an *Fgfr3* enhancer as a potential therapeutic tool for achondroplasia

Marco Angelozzi, Arnaud N. Molin, Anirudha Karvande, Angela Fernandez-Iglesias, Abdul Haseeb, Samantha Whipple*, and Véronique Lefebvre

Department of Surgery, Division of Orthopaedics, Children's Hospital of Philadelphia, PA, USA

**Presenting author*

Achondroplasia (ACH), the most common form of skeletal dysplasia, is characterized by disproportionate short stature with spine and craniofacial malformations. It is caused by heterozygous variants in *FGFR3* that over-activate the gene-encoded fibroblast growth factor receptor 3 and thereby negatively regulate the growth of endochondral bones. Treatments currently exist for ACH, but surgical ones only improve specific defects and can be associated with severe complications, while pharmacological ones have limited effects and unknown long-term consequences. Thus, new therapeutic strategies must be developed. Our work aims to reach this goal by developing genetic approaches. Using publicly available datasets for histone modifications and SOX9 genomic occupancy, we have identified several putative cis-regulatory elements (CREs) 5' of *Fgfr3* that are highly conserved among the human and other vertebrate genomes. *In vitro* reporter assays in chondrocytic cells suggest that the CRE located 29 kb 5' of *Fgfr3* (-29E) is the most potent enhancer. New mouse lines demonstrate that this CRE has considerable activity *in vivo*. Indeed, it is sufficient to activate a *Hsp68* minimal promoter-*lacZ* transgene specifically in chondrocytes, and most strongly in growth plate chondrocytes (GPCs). Its deletion in otherwise wild-type mice shows that it is necessary for high expression of *Fgfr3* in endochondral skeletal elements. *In situ* analysis shows that it is most needed in columnar and prehypertrophic GPCs, where wild-type *Fgfr3* is most actively expressed. To test the effect of -29E deletion on ACH, we excised this enhancer in a murine model carrying the mouse equivalent of the most common *FGFR3* variant causing ACH in humans. These mice faithfully reproduce the main skeletal features of the human condition, but die around weaning age, possibly from hydrocephalus. When -29E is deleted in the allele carrying the *Fgfr3* pathogenic variant, mice reach adulthood and their skeletal growth is greatly restored (e.g., 87% instead of 73% of femur length, and 76% instead of 56% of vertebral length). Additionally, spinal stenosis and craniofacial malformations are substantially improved. Altogether, these results expand the knowledge of *Fgfr3* transcriptional control and pave the way to the development of novel therapeutic approaches for ACH based on cartilage-specific gene regulatory elements.

Identifying Key Molecular Factors in Chondrocyte Dedifferentiation through Single-Nuclei Multiome Sequencing

Ellen Y. Zhang¹, Sang Hyun Lee², Yuna Heo¹, Melike Lakadamyali¹, Robert L. Mauck¹, Inkyung Jung², and Su Chin Heo¹
¹University of Pennsylvania, Philadelphia, PA, ²Korea Advanced Institute of Science & Technology (KAIST), Daejeon, KR
 yzhang98@seas.upenn.edu

Disclosures: Zhang (N), Lee (N), Heo (N), Lakadamyali (N), Mauck (5-4WEB Medical, 8-JOR Spine), Jung (N), and Heo (5-4WEB medical).

Introduction: Repairing articular cartilage poses a significant challenge due to the limited intrinsic healing capacity of the tissue. Autologous chondrocyte implantation (ACI) is a promising surgical intervention for treating cartilage defects [1]. However, a major limitation of ACI is the dedifferentiation of chondrocytes during *in vitro* expansion, leading to the loss of their phenotype. This dedifferentiation process involves the downregulation of key canonical markers essential for maintaining the cartilage phenotype, thereby reducing the therapeutic efficacy of ACI [2]. Understanding the mechanisms underlying this phenotype loss is crucial for developing strategies to preserve chondrocyte identity, ultimately enhancing the therapeutic potential of ACI for cartilage repair. To address this challenge, we employed single-nuclei multiome sequencing (snMultiome-Seq) to investigate gene expression and chromatin accessibility changes during dedifferentiation of primary human chondrocytes. By elucidating these molecular changes, our findings aim to optimize cell-based cartilage regeneration therapies.

Methods: Human articular chondrocytes from four donors (A: 46-year-old male; B: 55-year-old male; C: 52-year-old male; D: 42-year-old-male, provided by LifeLink Foundation) were isolated and expanded on tissue culture plastic up to passage six (P0 to P6). Bulk RNA sequencing (bulk RNA-Seq) was first conducted to assess transcriptional changes during dedifferentiation, with data analyzed using DESeq2 and clusterProfiler R packages. To investigate chromatin organization and regulatory element accessibility, single-nuclei ATAC sequencing (snATAC-Seq) and single-nuclei RNA sequencing (snRNA-Seq) were performed on P0, P3, and P6 chondrocytes. Data processing included quality control with Seurat, peak calling with MACS2, and integration of RNA and ATAC data using a weighted nearest neighbor approach. Pseudotime trajectories were inferred with Monocle3, and motif enrichment analysis was performed with the JASPAR2020 database.

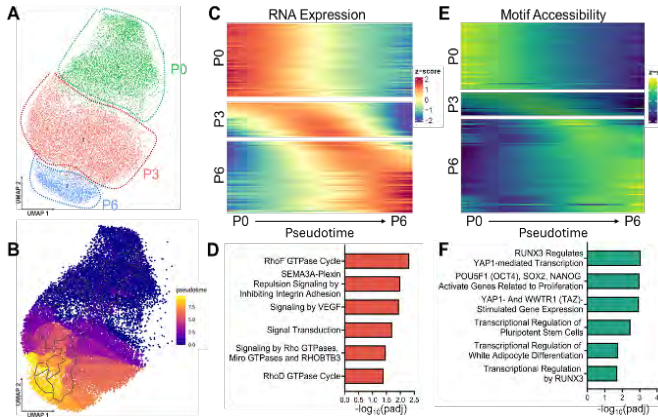


Figure 2. A: Clustering of chondrocyte populations by passage number using integrated snMultiome-Seq data. B: Pseudotime analysis of the integrated dataset showing progression of chondrocytes. C: Top differentially expressed genes along pseudotime. D: Pathway enrichment analysis of differentially expressed genes in the P3 cluster. E: Top differentially accessible motifs along pseudotime. F: Pathway enrichment analysis of differentially accessible motifs in the P3 cluster.

imaging, we demonstrated that chondrocyte chromatin becomes less condensed with dedifferentiation [3], suggesting significant alterations in the epigenetic landscape during *in vitro* expansion. In this study, bulk RNA-Seq data further confirmed a shift away from the specialized chondrogenic phenotype. To understand how chromatin reorganization contributes to the loss of chondrogenic phenotype, we employed snMultiome-Seq, revealing key genes and regulators involved in the transition from a chondrocyte-like to a dedifferentiated state. Notably, transcription factors such as TEAD2, which interact with YAP1 in mechanotransduction, and CEBPA, a well-known enhancer binding protein, emerged as critical regulators in this process, suggesting that mechanotransduction pathways and as a consequence alteration of regulatory elements, are likely crucial drivers of chondrocyte dedifferentiation. The enrichment of pathways related to Rho GTPase signaling further underscores the importance of cytoskeletal reorganization in this process [4, 5]. This indicates that chondrocytes may be adapting to new mechanical environments during *in vitro* expansion, creating a feedback loop where changes in the cytoskeleton and chromatin accessibility reinforce each other, driving the progression towards a dedifferentiated phenotype. The complex interplay of the eight identified regulators may play a crucial role in the dedifferentiation process and represent potential targets to prevent phenotype loss, thereby enhancing the efficacy of ACI. In summary, our study reveals that chondrocyte dedifferentiation is characterized by genome-wide transcriptional misregulation and chromatin reorganization, highlighting the crucial roles of mechanotransduction and cytoskeletal regulation in maintaining the chondrocyte phenotype. Targeting these pathways could offer new strategies to prevent dedifferentiation and preserve the therapeutic efficacy of chondrocyte-based interventions. Future studies will focus on the specific roles of transcription factors including TEAD2 and YAP1 in the dedifferentiation process and will investigate how modulating Rho GTPase signaling affects chondrocyte phenotype and function.

Significance: This study identifies key molecular drivers during chondrocyte dedifferentiation. By targeting these pathways, we can develop strategies to preserve chondrocyte identity during *in vitro* expansion, potentially leading to more effective and durable cartilage repair. This research could significantly enhance ACI outcomes, improving joint function and quality of life for patients with cartilage injuries and degenerative joint diseases.

References: [1] Roberts+, *Arthritis Res Ther* 2003; [2] Cote+, *Nat Commun* 2016; [3] Zhang+, *ORS* 2023; [4] Hallstrom+, *Mol Biol Cell* 2023; [5] Woods+, *J. Biol. Chem* 2005. **Acknowledgement:** This work is supported by NIH R01 AR079224 and NSF CMMI 1548571.

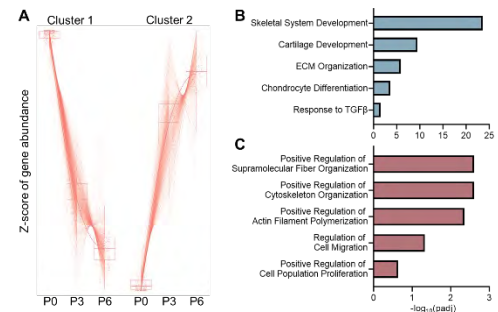


Figure 1. A: LRT demonstrating significant changes in gene expression during chondrocyte dedifferentiation. B: Top gene ontology terms associated with the 548 genes continuously downregulated in Cluster 1. C: Top gene ontology terms related to the 400 genes continuously upregulated in Cluster 2.

Results: The Likelihood Ratio Test (LRT) from bulk RNA-Seq data demonstrated significant changes in gene expression during chondrocyte dedifferentiation from P0 to P6 (Fig. 1A). Cluster 1 comprised 548 continuously downregulated genes associated with extracellular matrix (ECM) remodeling, cartilage development and chondrocyte differentiation (Fig. 1B). Conversely, Cluster 2 consisted of 400 genes that were continuously upregulated, linked to cytoskeleton organization and dynamics (Fig. 1C). Integration of snRNA-Seq and snATAC-Seq data identified three distinct chondrocyte clusters based on passage number (Fig. 2A). Pseudotime analysis demonstrated a progression from a chondrocyte-like state (P0) towards a dedifferentiated state (P6), with a transitional phase at P3 (Fig. 2B). Analysis of the top differentially expressed genes and differentially accessible DNA binding motifs along this pseudotime identified key transitional genes and upstream regulators (Fig. 2C, E). Pathway enrichment analysis in the P3 cluster (Fig. 2D, F) highlighted the involvement of YAP1-mediated transcription and Rho GTPase signaling in cytoskeletal reorganization and alterations in cellular tension. Among the enriched motifs, we narrowed down the putative candidates based on the correlation between gene expression dynamics and motif enrichments. Eight motifs including ATF4, ZIC4, TEAD2, TCFL5, CEBPA, FOXJ3, CEBPG, and EBF2 are closely linked with both expression changes and chromatin accessibility shifts (Fig. 3).

Discussion: This study provides critical insights into the molecular mechanisms underlying chondrocyte dedifferentiation, a key challenge in cartilage repair strategies with ACI. Previously, using super-resolution imaging, we demonstrated that chondrocyte chromatin becomes less condensed with dedifferentiation [3], suggesting significant alterations in the epigenetic landscape during *in vitro* expansion. In this study, bulk RNA-Seq data further confirmed a shift away from the specialized chondrogenic phenotype. To understand how chromatin reorganization contributes to the loss of chondrogenic phenotype, we employed snMultiome-Seq, revealing key genes and regulators involved in the transition from a chondrocyte-like to a dedifferentiated state. Notably, transcription factors such as TEAD2, which interact with YAP1 in mechanotransduction, and CEBPA, a well-known enhancer binding protein, emerged as critical regulators in this process, suggesting that mechanotransduction pathways and as a consequence alteration of regulatory elements, are likely crucial drivers of chondrocyte dedifferentiation. The enrichment of pathways related to Rho GTPase signaling further underscores the importance of cytoskeletal reorganization in this process [4, 5]. This indicates that chondrocytes may be adapting to new mechanical environments during *in vitro* expansion, creating a feedback loop where changes in the cytoskeleton and chromatin accessibility reinforce each other, driving the progression towards a dedifferentiated phenotype. The complex interplay of the eight identified regulators may play a crucial role in the dedifferentiation process and represent potential targets to prevent phenotype loss, thereby enhancing the efficacy of ACI. In summary, our study reveals that chondrocyte dedifferentiation is characterized by genome-wide transcriptional misregulation and chromatin reorganization, highlighting the crucial roles of mechanotransduction and cytoskeletal regulation in maintaining the chondrocyte phenotype. Targeting these pathways could offer new strategies to prevent dedifferentiation and preserve the therapeutic efficacy of chondrocyte-based interventions. Future studies will focus on the specific roles of transcription factors including TEAD2 and YAP1 in the dedifferentiation process and will investigate how modulating Rho GTPase signaling affects chondrocyte phenotype and function.

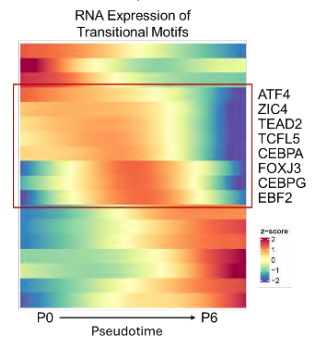


Figure 3: Correlation analysis between gene expression and chromatin accessibility data, highlighting key motifs linked with changes in both parameters.

Utilizing VNIR Spectroscopy to Assess Bone Graft Maturation: A Novel Approach for Optimizing Implant Timing in Alveolar Ridge Restoration

When a tooth is lost the supporting bone begins to resorb, creating a deficiency that often requires a bone graft prior to the placement of a dental implant. A bone graft is placed in the area of bone resorption and secured with a collagen membrane. Over time, the graft is gradually replaced by new, native bone. However, assessing the level of graft maturation is challenging due to variability in patient healing and difficulties in quantifying bone quality through traditional radiographic imaging. Recent interest has led to the use of visible near infrared (VNIR) spectroscopy as a non-invasive method to evaluate graft maturation based on compositional changes. The aim of the current study was to evaluate whether VNIR spectroscopy could effectively distinguish between different models representing stages of bone graft maturation. Methods: Four distinct tissue models were prepared with varying ratios of Straumann Xenograft grafting material and porcine bone (all were soaked in porcine blood to mimic the natural healing environment) and placed in a circular bone graft holder covered with a collagen membrane and porcine gingiva (cut to the thickness of the average human gingival tissue, 1.04mm). The models represented the stages of graft maturation: early stage (75% Xenograft/25% porcine bone), middle stage (50% Xenograft/50% porcine bone), almost mature (25% Xenograft/75% porcine bone), and fully mature (15% Xenograft/85% porcine bone). An ASD Labspec 4 VNIR spectrometer with a fiber optic probe was used to collect spectral data from the models. The data were processed by smoothing and normalization, followed by a second derivative filter and a Principal Component Analysis (PCA) was performed to analyze the data. Results: The spectral data from the models representing different maturation stages showed clear qualitative differences, primarily based on differences in water and protein content. PCA analysis showed that a fully healed site could be differentiated from earlier stages. These results suggest that VNIR spectroscopy holds promise for quantitatively assessing graft maturation and determining the appropriate time for implant placement. Further research with additional models and specific healing timepoints will enhance the understanding of VNIR's capability in monitoring bone graft progression.

Investigating the Effect of Motor Neurons and Endothelial Cells on Skeletal Muscle Maturation and Regeneration

Authors

S. DAS ^[1,2], M.C. HILMAN ^[2,3], F.A. LAIMO ^{[1],[2]}, F. YANG ^[4], F. MOURKIOTI ^[5], W. YANG ^[4],
D. K. CULLEN ^{[1],[2],[3]}

^[1] Center for Brain Injury & Repair, Department of Neurosurgery, Perelman School of Medicine, University of Pennsylvania, Philadelphia, PA, USA

^[2] Center for Neurotrauma, Neurodegeneration & Restoration, Corporal Michael J. Crescenz Veterans Affairs Medical Center, Philadelphia, PA, USA

^[3] Department of Bioengineering, School of Engineering and Applied Science, University of Pennsylvania, Philadelphia, PA, USA

^[4] Department of Medicine, Institute for Regenerative Medicine, University of Pennsylvania Perelman School of Medicine, Philadelphia, Pennsylvania

^[5] Department of Cell and Developmental Biology, Perelman School of Medicine, University of Pennsylvania, Philadelphia, PA.

Disclosures

D.K.Cullen & S.Das: U.S. Patent App. PCT/US2019/060585 titled “Engineering of Innervated Tissue and Modulation of Peripheral Organ Activity”.

Support

Financial support was provided by the U.S. Department of Defense through the Medical Research and Materiel Command (W81XWH-19-1-0867) and Dept of Health, Commonwealth of Pennsylvania, Health Research Formula Grant, 2021.

Abstract

Skeletal muscle is an excitable, dynamic tissue that is highly dependent on innervation and vascularization for maturation, functional regulation and nutrient supply. Neural and vascular implications on skeletal muscle have been studied independently but their combined effect on myocyte maturation has yet to be explored. In this study, we describe a novel myoneurovascular triculture system comprising human iPSC derived skeletal myocytes (MYO) and motor neurons (MN) with primary human endothelial cells (EC) plated in a specific sequence and maintained in an optimized triculture media. In vitro studies, showcase that neuromuscular cocultures (MYO+MN) exhibited significantly greater myocyte fusion and myofiber length than myovascular cocultures (MYO+EC) or myocytes alone (MYO). Genetic studies indicate upregulation of slow type I myofiber related gene (*TNNT1*), developmental myosin isoforms (*MYH3*, *MYH8*) and insulin regulated glucose transporter gene (*GLUT-4*) in MYO+MN coculture. Motor neurons were observed to upregulate expression of key neuromuscular genes like *RAPSYN*, *DOK-7* and *LRP-4* in MYO+MN coculture whereas endothelial cells exhibited low levels of *LRP-4* in MYO+EC coculture. Endothelial and motor neurons synergistically improved levels of neuromuscular gene *MUSK*, as well as *GLUT-4* in MYO+MN+EC triculture. This myoneurovascular triculture was cultured on aligned nanofiber sheets to develop vascularized innervated tissue engineered muscle which were implanted in a rat model of volumetric muscle loss (VML). Immunohistochemistry and confocal microscopy revealed survival of implanted myocytes and motor neurons to at least 4 weeks post-implantation following VML. We further observed interaction between implanted motor neurons and endothelial cells with host neural and vascular cells along with formation of neuromuscular junctions and proliferation of muscle satellite cells near the injury area. Current studies are focused on further analyses of histological and electrophysiological data to investigate the efficacy of these human myoneurovascular constructs in augmenting functional recovery in rodent models of VML.

Bone-selective Ultrashort Echo Time MRI for Pediatric Patients with Craniofacial Abnormalities

Nada Kamona¹, Jinggang J. Ng², Yohan Kim², Brian-Tinh D. Vu¹, Brandon C. Jones¹, Hyunyeol Lee^{1,4}, Holly Cordray², Connor S. Wagner², Chamith S. Rajapakse^{1,4}, Scott P. Bartlett², Felix W. Wehrli¹

¹Department of Radiology, Perelman School of Medicine, University of Pennsylvania; ²Division of Plastic, Reconstructive, and Oral Surgery, Children's Hospital of Philadelphia; ³School of Electronics Engineering, Kyungpook National University, Daegu, South Korea;

⁴Department of Orthopaedic Surgery, University of Pennsylvania.

Introduction: Head CT is the clinical standard for pre-operative and post-operative assessment of pediatric patients. However, ionizing radiation risk remains a concern for children with craniofacial abnormalities. High-resolution MRI can be an ionization-radiation-free alternative to CT. We developed a dual-radiofrequency, dual-echo, three-dimensional ultrashort echo time (DURANDE) sequence¹, which exploits the sensitivity of bone proton magnetization to both T₂ and RF pulse duration to further suppress soft-tissues and increase bone contrast. In this study, we quantitatively evaluated the proposed MRI technique against clinical-standard CT and another common bone-selective MRI sequence in a cohort of pediatric patients.

Methods: Pediatric patients indicated for clinical CT were recruited (n=6, 3 females, age range 8 to 16 years), with a variety of medical conditions, including craniosynostosis, jaw asymmetry, and glabellar mass. Patients were imaged at 3T with a 20-channel head/neck coil using two MRI sequences. DURANDE is a custom sequence with TR/TE1/TE2 = 7/0.06/2.36 ms, RF1/RF2 = 0.04/0.52 ms, flip angle = 12°, FOV = 280x280x280 mm, matrix size = 256x256x256, and scan time = 6 minutes. ZTE-PETRA (zero echo time) sequence with TR/TE = 2.85/0.07 ms, flip angle = 2°, FOV = 280 mm³, matrix size = 256³, and scan time = 5 minutes. For DURANDE, bone-specific images were generated by echo subtraction of the short- and long T₂ images [$Image_{bone} = (Image_{echo1} - Image_{echo2}) / (Image_{echo1} + Image_{echo2})$]. For ZTE-PETRA², bias-field correction was applied using the nonparametric N4ITK method and bright-bone images were derived via logarithmic inversion. From the 3D skull renderings, six craniometric measurements were manually derived. The agreement in craniometrics between MRI and CT was assessed using Lin's concordance correlation coefficient (CCC), and the similarity of the binary bone masks was evaluated using the dice similarity coefficient (DSC).

Results: Example bone slices for one pediatric patient comparing MRI to CT along with corresponding 3D skull rendering are shown in **Figure 1**. DSC had an overall average of 0.75±0.18, 0.70±0.19, and 0.77±0.15 for DURANDE versus CT, ZTE-PETRA versus CT, and DURANDE versus ZTE-PETRA, respectively. Comparing DURANDE to CT, the average percent difference in six craniometrics was less than 2% and the agreement based on Lin's CCC ranged from 0.90 to 0.99 (**Table 1**).

Discussion and Conclusions: Two MRI sequences were validated against clinical CT in pediatric patients with craniofacial abnormalities by assessing the similarities among their skull segmentations and geometric accuracy. Based on DSC, there is overall good skull overlap between MRI and CT; however, it decreases near the orbits and nasal concha where there are thinner bone structures and more bone-air interfaces. Additionally, compared to adults, children have thinner bones and are generally less compliant, the latter resulted in motion artifacts in a few patients during both DURANDE and ZTE-PETRA. Compared to ZTE-PETRA, DURANDE had greater bone-contrast in the facial regions and higher segmentation overlap with CT based on the DSC. Thus, DURANDE had higher agreement with CT for the interzygomatic distance and orbital heights. Moreover, DURANDE had smaller absolute percent differences in craniometrics when compared to CT (<2%), while ZTE-PETRA had greater differences (<5%). In summary, there was good agreement between CT and the proposed DURANDE MRI sequence in a small cohort of pediatric patients, demonstrating the clinical feasibility of the technique for craniofacial imaging in children.

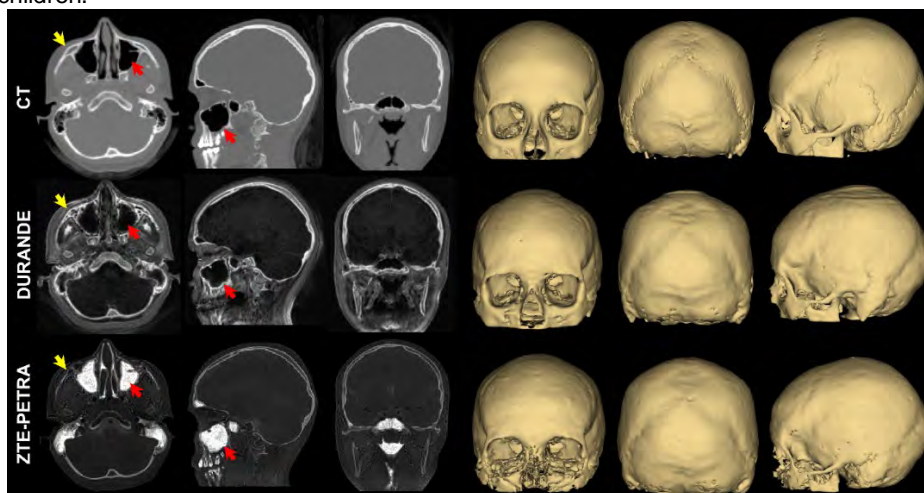


Figure 1: CT images compared against the bone-selective images from two MRI sequences for a female pediatric patient diagnosed with jaw asymmetry. Air appears with background intensity in DURANDE and white in ZTE-PETRA (red arrows). DURANDE clearly resolves thin facial bone structures, unlike ZTE-PETRA (yellow arrows).

Table 1: Agreement in craniometric measurements based on Lin's concordance correlation coefficient (n=6). All craniometric values were determined from the 3D renderings using the ruler tool in *3D Slicer*.

Craniometric Distance	Lin's Concordance Correlation Coefficient (r [95% Confidence Interval])		
	CT vs DURANDE	CT vs ZTE-PETRA	DURANDE vs ZTE-PETRA
Interzygomatic Distance	0.90 [0.55, 0.98]	0.85 [0.46, 0.96]	0.97 [0.83, 1.00]
Right Orbit Height	0.98 [0.88, 1.00]	0.67 [0.05, 0.91]	0.61 [0.04, 0.88]
Left Orbit Height	0.97 [0.86, 0.99]	0.38 [-0.22, 0.77]	0.32 [-0.46, 0.82]
Cranial Width	0.95 [0.75, 0.99]	0.95 [0.77, 0.99]	0.99 [0.97, 1.00]
Cranial Length	0.99 [0.96, 1.00]	1.00 [0.98, 1.00]	1.00 [0.98, 1.00]
Cranial Height	0.90 [0.47, 0.98]	0.94 [0.76, 0.99]	0.84 [0.40, 0.96]

Using Deep Learning for Gunshot Wound Bullet Fragment Detection in Emergency Medicine

Yi-An Hsieh¹, Rashad Madi², Winnie Xu², Min-Keun Song², Enrie Gan², Yuanyuan Chen³, Elena Taratuta², Jeremy Cannon⁴, Kristen Chreiman⁴, Hannah Rosenblatt², Rasleen Grewal², Christiana Cottrell², Olivia Rosen⁵, Autumn Tyler⁶, Digonto Chatterjee¹, Brandon Yan⁷, Chamith S. Rajapakse²

¹Department of Bioengineering, School of Engineering and Applied Sciences, University of Pennsylvania, Philadelphia, PA, ²Departments of Radiology and Orthopaedic Surgery, Perelman School of Medicine, University of Pennsylvania, Philadelphia, PA, ³Boston University, Boston, MA,

⁴Department of Surgery, Division of Trauma, Surgical Critical Care and Emergency Surgery, Perelman School of Medicine, University of Pennsylvania, Philadelphia, PA, ⁵Utica University, Utica, NY, ⁶Department of Healthcare Management and Policy, Wharton School, University of Pennsylvania, Philadelphia, PA, ⁷Department of Computer and Information Sciences, School of Engineering and Applied Sciences, University of Pennsylvania, Philadelphia, PA

yi-an.hsieh@pennmedicine.upenn.edu

INTRODUCTION: Gun violence is a public health issue in the United States, with over 48,000 deaths per year from related injuries. For patients with gunshot wounds (GSW), computed tomography (CT) scans are crucial for identifying injuries sustained from ballistic trauma, including solid organ injuries, acute hemorrhage, penetrating fractures, and retained bullet fragments. However, a rapid assessment of multiple GSWs in emergency settings is clinically difficult and risks treatment delays and complications. This work aims to build and assess the capabilities of machine learning pipelines to identify bullet fragments in CT scans quickly, accurately, and precisely to facilitate trajectory determination and injury identification for orthopaedic surgical planning.

METHODS: Leveraging CT scout view images and manual annotations from 1335 patients treated for GSW injuries at Penn Medicine, an urban Level 1 trauma center, from 2019 to 2022, three pipelines built upon pre-existing architectures were trained for bullet detection and segmentation (Figure 1). Pipeline 1 employed a Mask R-CNN model trained on bullet fragment annotations to detect and segment bullet fragments. Pipeline 2 employed a Mask R-CNN model trained on high-density annotations to detect high-density ROIs then classify and segment bullet fragments. Pipeline 3 used a Faster R-CNN model to detect high-density ROIs, two ResNet50 models to classify images as coronal or sagittal and determine if they contain the patient's head, three ResNet50 models to classify ROIs as bullet fragments, and a FCN model for segmentation. All models were trained from scratch with no pretrained weights using 80% of the dataset and evaluated with the remaining 20% of the dataset. Non-maximum suppression with intersection over union thresholds ranging across 0 to 0.5 was applied on model predictions of the locations of bullet fragments to obtain the final set of predictions used to evaluate the pipelines.

RESULTS: Pipeline 3 identified the most bullet fragments at 89-91% prediction intersection of bullet annotations across varying non-maximum suppression intersection over union thresholds (76-79% for pipeline 1, 62-66% for pipeline 2), yielded 88-91% accuracy in ROI classification (63%-71% for pipeline 1, 48-59% for pipeline 2), and also provided the greatest overlap of predicted masks and annotations with a Dice coefficient of 0.488 (0.336 for pipeline 1, 0.247 for pipeline 2). Intermediate models in pipeline 3 classified images as coronal vs sagittal with 98.8% accuracy and containing the head or not with 99.3% accuracy. Notably, while pipelines 1 and 2 both utilize the same base architecture, it is clear from these metrics that they result in different performance from the inclusion of a high-density non-bullet ROI class. Additionally, the outperformance of pipeline 3 over 1 and 2 highlights the indispensability of tailored machine learning models within larger pipelines for precise bullet fragment detection and segmentation.

DISCUSSION: Exploration into specific image categories where Mask R-CNN exhibits varying performance may offer insights for optimizing model efficacy and generalizability. Further fine-tuning could enhance bullet fragment detection, potentially matching the performance of radiologists and facilitating the calculation of additional metrics, such as bullet movement over time relative to major arteries, to improve time-sensitive clinical decision-making and expedite treatment in emergency settings.

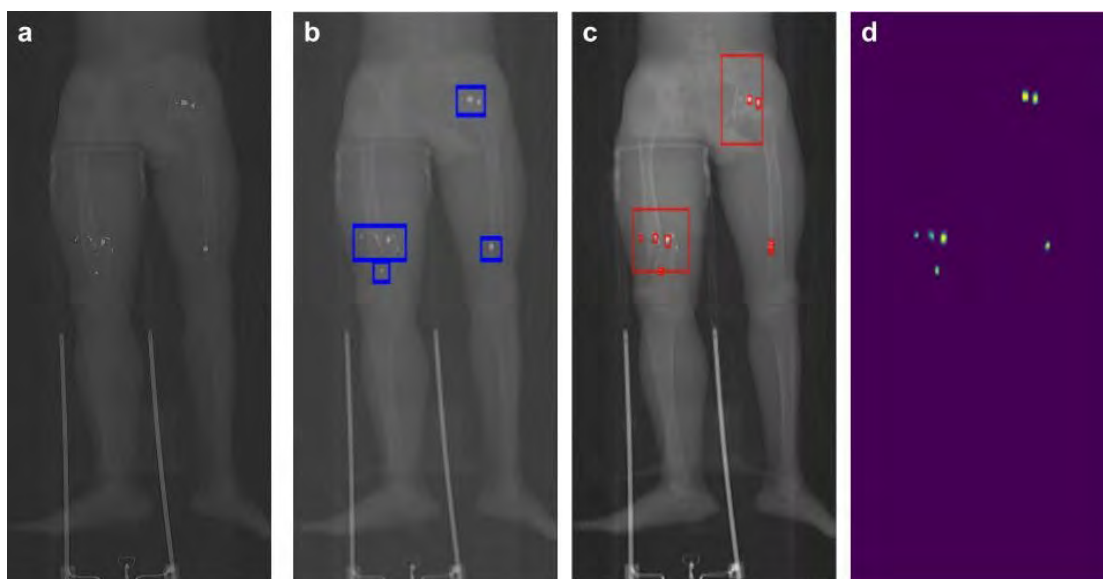


Figure 1. Bullet fragment detection and segmentation. a) The CT scout view image on the left is the original image. b) In the normalized image in the left center, the blue boxes are the ground truth manual annotation. c) In the preprocessed image in the right center, the red boxes are the bounding boxes predicted by the model. d) The segmentation mask contains bullet fragments predicted by the model.

Missense variants weakening a SOX9 phosphodegron linked to odontogenesis defects, scoliosis and other skeletal features

Abdul Haseeb,^{1,8} Anirudha Karvande,^{1,8} Imane Ettaki,^{2,3,8,*} Ghita Amalou,² Asmae Saih,³ Imane AitRaise², Salsabil Hamdi,² Lahcen Wakrim,² Abdelhamid Barakat,² Hassan Fella³, Mustapha El Alloussi,^{4,*} Véronique Lefebvre^{1,*}

¹Division of Orthopaedics, Children's Hospital of Philadelphia, Philadelphia, PA

²Institut Pasteur du Maroc, Casablanca, Morocco

³Hassan II University of Casablanca, Casablanca, Morocco

⁴International University of Rabat, Sala-Al Jadida, Morocco

⁸These authors contributed equally

SOX9 encodes an SRY-related transcription factor that critically controls chondrogenesis and sex determination among other processes. Loss-of-function variants cause campomelic dysplasia and Pierre Robin Sequence, whereas both gain- and loss-of-function variants cause disorders of sex development. SOX9 has also been linked to scoliosis and many types of cancers, but variants remain undetermined. While SOX9 is highly expressed in tooth progenitor cells, its odontogenic roles remain elusive and tooth defects have not been reported in human conditions. We here performed whole-exome sequencing for nine unrelated children who presented with tooth eruption delay and no known syndromes, and identified a seven-year-old girl heterozygous for a SOX9 p.Thr239Pro variant and a ten-year-old boy heterozygous for SOX9 p.Thr239Pro and p.Thr240Pro variants presumably located in the same allele. The variants were *de novo* and rare in control populations. The girl had yet to erupt many primary teeth, and the boy, who also had delayed primary dentition, had mesiodens blocking eruption of his permanent central upper incisors. He also had severe scoliosis and mild craniofacial and appendicular skeletal abnormalities. p.Thr239 and p.Thr240 are located in a Cdc4/FBXW7-targeted phosphodegron (CPD) motif that is fully conserved in SOX9 vertebrate orthologs and in SOX8 and SOX10 paralogs, but whose importance *in vivo* is yet unknown. Structural modeling by AlphaFold3 predicted a weaker interaction of the FBXW7's WD40 domain with the SOX9 CPD motif containing the p.Thr240Pro or p.Thr239Pro/p.Thr240Pro variants than with the motif in its wildtype or p.Thr239Pro variant form. Accordingly, functional assays in cultured cells showed that the p.Thr240Pro and p.Thr239Pro/p.Thr240Pro variants largely blocked FBXW7-induced SOX9 degradation, whereas the p.Thr239Pro variant only mildly reduced it, and these effects proportionally increased SOX9-dependent reporter transactivation. Altogether, these findings concur that SOX9 has key roles in odontogenesis and that gain-of-function variants may cause pronounced defects in this process and skeletogenesis, including scoliosis.

Investigating Sex-Based Differences in a Rat Model of Orthopedic Infection

Arianna J. Moniodes¹ Anna C. Sonchen¹ Carly J. Smith¹, Amanda Watkins², Thomas P. Schaer², Theresa A. Freeman¹

¹Department of Orthopedic Surgery, Thomas Jefferson University, Philadelphia, PA

²University of Pennsylvania, School of Veterinary Medicine, Kennett Square, PA

Theresa.Freeman@jefferson.edu

Introduction: Post-surgical orthopedic infection is a complication of prosthetic joint implant procedures (1). Recent years have seen a growing recognition of the disparities between the sexes, although the etiology of these differences remains largely unstudied (2). In general, females tend to exhibit a stronger immune response to infection than males (3), while males usually demonstrate more efficient bone healing than females (2). There are numerous elements that may underlie these disparities, such as genetics, sex hormones, cellular and molecular mechanisms, immune composition, lifestyle, and behavior (2). The objective of this project is to investigate sex-based differences in cytokine expression and bone remodeling in a rat model of orthopedic infection.

Methods: *Animals and Surgical Procedure:* Index Surgery Day- Under anesthesia, male and female Sprague-Dawley rats underwent craniolateral incision between the vastus lateralis and biceps femoris to expose the right femur. At the proximal and distal ends of the femur, a 1.7 mm titanium screw was drilled into place, passing through the entire width of the femur. An empty center hole was also created in the anterior aspect of the femur to expose the medullary cavity. A collagen sponge inoculated with 250 μ L of *Staphylococcus aureus* ATCC 25923 at 1×10^6 CFU (infected) or saline (uninfected) was positioned over the screws and the empty hole, and the craniolateral incision was closed. 7 days after surgery, animals were humanely sacrificed. *RT-qPCR:* RNA was isolated from the right biceps femoris muscle, made into cDNA, and qPCR was performed to determine expression levels of immunomodulatory cytokines IL-1 β , IL-6, NOS2, IL-17, SOCS3, IL-10 and TGF- β . Fold change values were calculated using the $2^{-\Delta\Delta C_T}$ method (4). *Microbial Analysis:* Serial dilutions of the fluid from the vastus lateralis were transferred to Petri films, incubated at 37 C for 24 hours, and counted to determine log CFU/mL. *Bone remodeling calculations:* Rat femurs were scanned on Bruker Micro-CT SkyScan 1275. Scans were reconstructed using NRecon software and cropped using DataViewer. Bone volume to total volume (BV/TV) ratios were calculated for the drill hole in the center of the femur in CTAn software.

Results: All infected rats showed significant increases in IL-1 β expression, which correlated with higher CFU counts. Significant increases in the proinflammatory cytokines IL-6, NOS2, and IL-17 were observed only in females when comparing infected to uninfected rats by sex. When infected males were directly compared to infected females, NOS2 and IL-17 were significantly increased in females. Interestingly, in uninfected males versus females, the anti-inflammatory cytokine IL-10 was significantly higher in males. As inflammation is often associated with increased bone remodeling, we measured BV/TV ratios in holes drilled through the center of the femur in infected rats (n = 3 males, n = 3 females). Surprisingly, no significant difference in BV/TV between infected male and female rats was observed.

Discussion: The experimental findings from this study reflect current literature showing that females exhibit a more robust immune response to infection than males. Additionally, the correlation of IL-1 β expression to CFU count supports the idea that bacterial load impacts magnitude of inflammation. That BV/TV ratios were not significantly different may be due to the small sample size of Micro-CT scanned rat femurs. This project presents an avenue for further research investigating whether sex-related cytokine expression could account for differences in bone remodeling between males and females. IL-6 and IL-17 have been implicated as promoters of osteoclastogenesis, indicating that an increased bone resorption may be present in females with infection. On the other hand, immunosuppressor IL-10 has been shown to inhibit osteoclastogenesis, which may inhibit bone resorption in males. The roles of cytokines NOS2, SOCS3, and TGF- β in bone remodeling remain elusive or understudied (5). Additional samples are required to more fully understand these processes.

Significance/Clinical Relevance: Males experience treatment failure for prosthetic joint infections more than females (6); however, the effect of sex differences in inflammatory cytokines and the immune response in general are understudied. As loss of bone can impact implant fixation, understanding sex differences in bone remodeling with infection is important to tailor treatment appropriately in a healthcare setting. Thus, this is an area that merits further study.

Acknowledgements: This work was supported by NIH grant R01AR076941 (Freeman) from NIAMS. Special thanks to Amber J. Slaweski, Ryan E. Tomlinson, and Autumn Melvage for their help with data analysis.

References:

1. L uthje FL, Jensen LK, Jensen HE, Skovgaard K. The inflammatory response to bone infection - a review based on animal models and human patients. *APMIS*. 2020 Apr;128(4):275–86.
2. Ortona E, Pagano MT, Capossela L, Malorni W. The role of sex differences in bone health and healing. *Biology (Basel)*. 2023 Jul 12;12(7).
3. Dias SP, Brouwer MC, van de Beek D. Sex and gender differences in bacterial infections. *Infect Immun*. 2022 Oct 20;90(10):e0028322.
4. Livak KJ, Schmittgen TD. Analysis of relative gene expression data using real-time quantitative PCR and the $2^{-\Delta\Delta C(T)}$ Method. *Methods*. 2001 Dec;25(4):402–8.
5. Zhou P, Zheng T, Zhao B. Cytokine-mediated immunomodulation of osteoclastogenesis. *Bone*. 2022 Nov;164:116540.
6. The Impact of Sex on the Outcomes of Prosthetic Joint Infection Treatment with Debridement, Antibiotic [Internet]. [cited 2024 Nov 5]. Available from: <https://documentcloud.adobe.com/boxintegration/index.html?state=%7B%22fileIds%22%3A%5B%221246981347015%22%5D%7D>

Mechanical Priming of Fibrochondrocyte-Derived Extracellular Vesicles to Enhance Meniscus Regeneration

Catherine Cheung¹, Zizhao Li¹, Yoonho Roh¹, Jina Ko¹, Su Chin Heo¹

¹University of Pennsylvania, Philadelphia, PA

catwxy@seas.upenn.edu

DISCLOSURES: Catherine Cheung (N), Zizhao Li (N), Yoonho Roh (N), Jina Ko (N), Su Chin Heo (5; 4WEB Inc.)

INTRODUCTION: The menisci provide joint cushioning, shock absorption, and proprioception, among other essential loadbearing functions of the knee. However, aberrant loading can lead to meniscus tears, resulting in disrupted functionality, knee pain, and joint instability [1]. Unfortunately, the meniscus has a poor innate healing capacity, and altered joint mechanics post-injury contribute to the development of osteoarthritis (OA) in nearly two-thirds of meniscus tear patients [2]. Current clinical and surgical treatments often fail to restore tissue function and prevent OA, underscoring the need for innovative therapies to enhance endogenous meniscus repair. Extracellular vesicles (EVs), nanoscale membrane-bound mediators of paracrine signaling, have emerged as potential therapeutic agents [4]. However, the impact of mechanical cues on EV biogenesis and secretion by meniscus fibrochondrocytes (MFCs), and the effects of these “mechanically primed” EVs on neighboring cells remain largely unexplored. To address this gap, we investigate a novel method of priming EVs through cyclic tensile loading of MFC-laden scaffolds. We further aim to determine whether these mechanically primed EVs promote a regenerative response in recipient progenitor cells (i.e., mesenchymal stem cells, MSCs). We hypothesize that controlled, physiologic levels of mechanical loading of MFCs will stimulate greater production and secretion of EVs, and that these mechanically primed EVs will trigger a pro-regenerative response from recipient MSCs, thereby advancing meniscus repair strategies.

METHODS: Outer zone MFCs and bone marrow-derived MSCs were isolated from juvenile (~3-month-old) bovine knee joints [3]. Aligned nanofibrous polycaprolactone (PCL) scaffolds were fabricated by electrospinning and subsequently seeded with MFCs as previously described [3]. The scaffolds were pre-cultured for 2 days in basal medium (BM) before undergoing dynamic tensile loading in a custom bioreactor (Fig. 1A) [5]. Scaffolds were subjected to 3% strain at 1 Hz frequency in media containing exosome-depleted FBS (Exo-D BM). EVs were isolated from four different technical replicate samples and pooled into one for subsequent analysis (Fig. 1A). To assess EV yield, scaffolds were either loaded for 3 hours (L) or left free swelling (NL) in Exo-D BM. To evaluate the effect of cellular contractility on EV yield, Y27632 (10 μM) was applied to cell-seeded scaffolds for 1 hour prior to dynamic loading in Exo-D BM to inhibit the RhoA/ROCK pathway. Additionally, GW4869 (20 μM) was applied to cells 24 hours before dynamic loading to inhibit the ESCRT-independent EV biogenesis pathway. For multiple-day loading experiments, scaffolds were loaded for 1 hour, removed from the bioreactor, and allowed to remain in free-swelling conditions in the same media between loading sessions. Post-loading, scaffolds were processed for MFC mRNA isolation, and cell culture media was subjected to differential ultracentrifugation for EV isolation [6]. Particle concentrations and size distributions were determined by nanoparticle tracking analysis (NTA). Surface tetraspanins CD9, CD63, and CD81 were detected by super-resolution microscopy using the EV Profiler Kit 2 (ONI). MSCs treated with donor-matched EVs (Fig. 2B) were assessed for cell viability using the CCK-8 assay. RT-qPCR was performed to determine expression levels of type I collagen (Col1), aggrecan (ACAN), and housekeeping gene GAPDH in both loaded MFCs and recipient MSCs. Fold change was calculated by the delta-delta-CT method. Statistical analyses were performed using Student's t-test and one-way ANOVA.

RESULTS: Dynamic mechanical loading for 3 hours significantly increased EV yield compared to free-swelling controls (Fig. 1B, $p < 0.001$, $n = 7$ biological replicates). Super-resolution microscopy revealed nanoscale clusters of EV-positive tetraspanins CD9, CD63, and CD81, confirming the collected particles as EVs (Fig. 1C). NTA distributions demonstrate consistent particle size distribution between mechanically primed and control EVs (Fig. 1D). These findings suggest dynamic loading is effective in increasing EV yield, which is a key challenge in EV therapeutics. Inhibition of the RhoA/ROCK pathway with Y27632 did not significantly impact the increased EV yield associated with dynamic loading (Fig. 1E, $p > 0.05$, $n = 3$ biological replicates), indicating that cellular contractility is not a major contributor to the loading-induced higher yield. Treatment with GW4869, an ESCRT-independent EV biogenesis inhibitor, reduced overall EV yield (data not shown), but this effect was mitigated by 3 hours of dynamic loading (Fig. 1F), suggesting that loading may rather enhance an ESCRT-dependent biogenesis pathway. MFCs subjected to 1 hour of dynamic loading for 1 day (1dL) or 3 days (3dL) exhibited increased aggrecan expression (Fig. 2A, $p < 0.0001$, $n = 8$ from 2 biological donors). Correspondingly, MSCs treated with EVs secreted by these cells also exhibited a significant increase in aggrecan expression (Fig. 2C, $p < 0.0001$, $n = 8$ from 2 biological donors), suggesting that EVs influence MSC differentiation. Notably, culturing MSCs with these EVs did not affect MSC viability or proliferation (Fig. 2D, $n = 3$), indicating the biocompatibility of EVs.

DISCUSSION: This study demonstrates that dynamic loading effectively stimulates EV biogenesis, leading to a significant increase in EV production from loaded MFCs. This enhanced EV yield offers a promising approach to address one of the key challenges in EV therapeutics. The observed similarity in gene expression profiles in recipient cells treated with EVs from dynamically loaded cells further suggests that mechanical priming may influence EV content to promote regenerative responses. However, this study has limitations, including the small number of biological donors and the exclusive focus on cyclic tensile loading. Ongoing studies aim to further characterize mechanically primed EVs through proteomic and small RNA-seq analyses, and to identify the mechanosensitive pathway(s) by which dynamic loading enhances EV production. These insights are critical for optimizing EV-based therapies and advancing their clinical applications in meniscus regeneration and other areas of musculoskeletal repair.

SIGNIFICANCE: This study highlights the potential of using MFC-derived EVs to stimulate meniscus regeneration and introduces a method to enhance EV yield, improving their therapeutic potency. These advancements offer promising approaches for scaling EV-based therapies to clinical applications, potentially leading to more effective treatments for meniscus injury.

REFERENCES: [1] Fox+ 2015, Clin. Anat., [2] Riera+ 2011, Arthritis Res. Ther., [3] Baker+ 2007 Biomaterials, [4] Magdy+ 2020, Appl. Sci. 10, [5] Heo+ 2016, eLife., [6] Théry+ 2006, Curr. Protoc. Cell Biol.

ACKNOWLEDGEMENTS: This work was supported by the NIH (K01 AR077087) and NSF (CMMI-1548571).

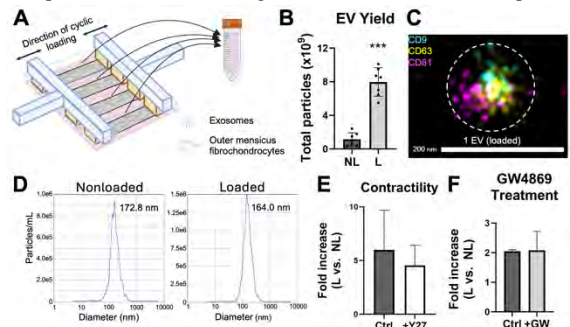


Fig. 1: (A) Schematic of the bioreactor setup and EV collection process: EVs were isolated from four different technical replicate samples and pooled into one for subsequent analysis. (B) Comparison of EV yield with loading ($n = 7$ biological replicates, $***: p < 0.001$ vs. non-loaded controls). (C) Super-resolution microscopy confirming EV identity through detection of colocalized CD9, CD63, and CD81. (D) Representative NTA distributions showing particle size of loaded vs. non-loaded EVs. (E) Comparison of fold increase in EV yield with and without Y27632 treatment or (F) with and without GW4869 treatment ($n = 2$ biological replicates).

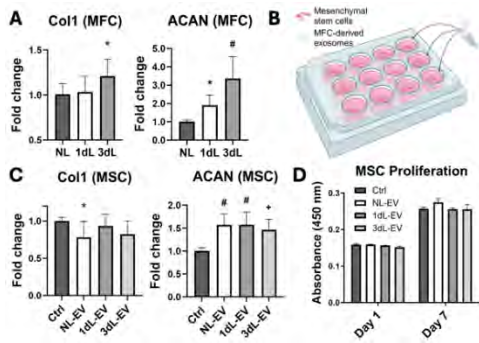


Fig. 2: (A) RT-qPCR analysis of MFC gene expression ($n = 8$ from 2 donors; $*$: $p < 0.05$ vs. non-loaded, $\#$: $p < 0.0001$ vs. non-loaded). (B) Schematic of MSC treatment with EVs. (C) RT-qPCR analysis of gene expression in recipient MSCs after 7-day EV treatment ($n = 8$ from 2 donors; $*$: $p < 0.05$ vs. control, $+$: $p < 0.001$ vs. control, $\#$: $p < 0.0001$ vs. control). (D) MSC proliferation assessed by CCK-8 assay ($n = 3$).

Investigating Hypoxia in Achilles Tendinopathy Through Oxygen Saturation Measurement

Maggs Capalbo, Dr. Spencer Szczesny

Introduction

Tendinopathy affects 6% of the whole population during their lifetime¹. Tendinopathy is the diagnosis for swelling, pain, and/or impaired function of a tendon². While AT is influenced by many risk factors (e.g. sex, body mass index, age), one of the most critical risk factors is overuse³. Overuse, defined as repetitive or extreme mechanical loads, causes disorganized collagen, abnormal cellularity, and apoptosis in tendons⁴. Cells respond through a degenerative state, leading to the breakdown of collagen fibers via proteinases, the secretion of inflammatory cytokines, and the production of atypical matrix components, such as cartilage or bone tissue⁵. While the Achilles tendon's response to fatigue loading is well-known, the drivers causing the tendon degenerative cellular response activated by overuse/fatigue-loading is unexplained.

Hypoxia, or low oxygen levels, has been suggested as a driver of tendinopathy. Hypoxia-inducible factor 1 α (HIF-1 α), a regulator of cellular responses to hypoxia, has been found in several tendinopathy studies. When comparing healthy flexor and rotator cuff tendons to their diseased counterparts, HIF-1 α is upregulated in tendinopathic tissue^{6,7}. Additionally, inhibiting HIF-1 α appears to increase the severity of Achilles tendinopathy in a rat model⁸. However, the presence of HIF-1 α alone does not confirm hypoxia of a diseased Achilles tendon because hypoxia does not lead to the production of HIF-1 α , only its accumulation⁹. The objective of this study is to identify the presence of hypoxia within tendinopathic human tendons.

Methods

Healthy subjects were recruited from the Penn State Biomedical Engineering department (n=8). A red laser tissue blood oxygenation monitor (BOM-L1TRSF, Omega Wave, Tokyo, Japan) was used to measure oxygen saturation of subjects' Achilles tendons. Blood oxygen saturation of the tendon was determined by the monitor by dividing oxyhemoglobin by total hemoglobin and multiplying by 100. Subjects were asked to lie prone. Adhesives were placed on the posterior side of each leg 30 mm proximal to the calcaneus. The probe (SF-DS, Omega Wave) was stuck to the adhesive of the right leg and the laser was turned on. The probe was given 3 minutes to stabilize before a 2-minute recorded measurement. The laser was turned off, and the probe was removed. A new adhesive was placed on the right leg, and after 5 minutes, the stabilization and measurement process was repeated. The measurements were repeated on the left leg.

Paired t-tests were performed to determine whether a significance difference is present between left and right leg as well as 0-minute and 5-minute measurements. Significance was set to $p < 0.05$.

Results

Four measurements were gathered per person: right leg 0-minute, left leg 0-minute, right leg 5-minute, and left leg 5-minute. These measurements were averaged into 5 values:

right leg, left leg, 0-minute, 5-minute, and overall average.

Among the 8 subjects, the average oxygen saturation is $62.4\% \pm 2.7\%$ (Fig. 1). The average difference between the left and right leg is $1.5\% \pm 5.9\%$ (Fig. 2B), but there is no significant difference between the averages of each leg (Fig. 2A). Additionally, the difference between the 0-minute and 5-minute readings is $0.24\% \pm 2.3\%$ (Fig. 3B), but there is no significant difference between the averages of the time points (Fig. 3A).

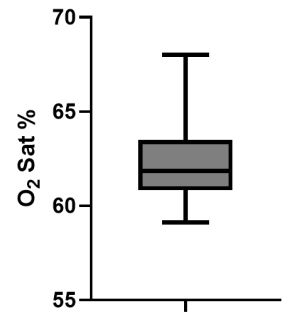


Fig. 1: Average oxygen saturation of each individual shown in group distribution. Bars represent the min and max values. Box represents 25th to 75th quartiles.

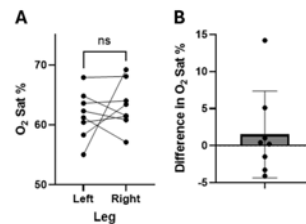


Fig. 2: Representations of comparing oxygen saturation of the left and right leg. (A) A paired analysis of oxygen saturation of the two legs. (B) A distribution representing the mean and standard deviation of the difference between legs (right minus left).

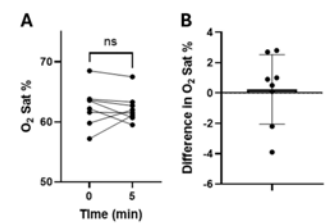


Fig. 3: Representations of comparing oxygen saturation at the 0- and 5-min points. (A) A paired analysis of oxygen saturation at the two times. (B) A distribution representing the mean and standard deviation of the difference between time points (0 minus 5).

Discussion

This study confirmed our usage of the red laser tissue blood oxygenation monitor. We determined the average blood oxygenation for healthy subjects is $62.4\% \pm 2.7\%$. This matches previous research resulting in an overall average oxygen saturation of $60.7\% \pm 3.9\%$ ^{10,11}. In terms of oxygen level, our measurement means the human Achilles tendon is about 3.9% O₂¹² as opposed to the atmospheric level (21%). As this is a preliminary study, we used this data to conduct a reverse power analysis to determine our necessary effect size for a significant result with 80% power and a sample size of 12. If we choose to use a paired analysis between legs, we would need a difference similar to that we gathered. If we analyze between time points, we can maintain significance with a mean difference as low as 0.45.

References

1. Chen et al. *J. Sport Health Sci.* (2024).
2. Kozlovskaja et al. *Sports Med.* (2017).
3. Herod & Veres. *J. Orthop. Res.* (2018).
4. Kaux et al. *J. Sports Sci & Med* (2011).
5. Li & Hua. *BioMed Res. Int.* (2016).
6. McBeath et al. *Aging Cell* (2019).
7. Moschini et al. *ORS Conference.* (2023).
8. Jiao et al. *Int. Immunopharmacol.* (2022).
9. HIF-1 signaling pathway - Homo sapiens (human). *Kegg.* (2024).
10. Kubo et al. *Eur. J. Appl. Physiol.* (2008).
11. Kubo et al. *Eur. J. Appl. Physiol.* (2009).
12. Gray & Steadman. *J. Physiol.* (1964).

Optimizing Fracture Prediction: Deep Learning for Opportunistic MR Imaging of Osteoporosis

Albi Domi¹, David Barreto¹, Enrie Gan¹, Lihini Ranaweera¹, Austin Vu¹, Jianna Kim¹, Vachan Patel¹, Frank Pham¹, Amber Lan¹, Thamarie Pinnaduwaige¹, Makayla Clark¹, Nilan Nandish¹, Elaina Truong¹, Angelina Diaz¹, Harry Shi¹, Sarem Khan¹, Eva Gonzalez-Whitehouse¹, Ethan Che¹, Hannah Rosenblatt¹, Sarah Bargamian¹, Gregory Chang¹, David Casper¹, Chamith Rajapakse¹
¹University of Pennsylvania Perelman School of Medicine, Philadelphia, PA

INTRODUCTION: As the US population ages, spinal degeneration poses a growing challenge. Surgeries like decompression and spinal fusion carry risks, especially with factors like poor bone quality, increasing patient complications. Advanced surgical planning tools and predictive models are crucial. We utilized a 3D U-Net model to predict spinal fracture risk due to osteoporotic degeneration, streamlining manual segmentation and enhancing post-operative outcomes analysis. Our study aimed to develop a non-invasive method for predicting spine fractures by automating the lumbar vertebrae segmentation in MR scans using a 3D U-Net model, followed by a discriminatory analysis between spine health measures derived between patients experiencing spine incidence fractures and no-fracture reference group.

METHODS: This research utilized retrospectively collected spine MR images from 732 patients (ages 28 to 93). Spine and hip DXA scores from 614 of these patients were collected and 104 patients experienced at least 1 fracture post-scan and post-DXA (0.72 +/- 2.65 years after). The cohort predominantly comprised females (92.3%), chosen due to higher prevalence of osteoporosis in women. These scans, using T1-weighted spin-echo sequences, were sourced from the Hospital of the University of Pennsylvania with Institutional Review Board approval. Digital Imaging and Communications in Medicine (DICOM) series were manually segmented by trained annotators using ITK-SNAP. Each 2D slice in a single case underwent independent manual segmentation, with individual vertebrae being uniquely labeled for semantic segmentation. These segmented images underwent augmentations and padding as model training inputs. A 3D U-Net model was trained for 100 epochs on an NVIDIA V100 GPU. The loss function was a combination of the Tversky loss (with parameter $\alpha=0.3$) and the Categorical Cross Entropy. The segmented predictions were overlaid onto the scan volume to generate vertebral volumes. ANOVA analysis was performed on fractures with vertebral mean intensities and separately with DXA values.

RESULTS: Incidence spine fracture patients had significantly higher intensity mean vertebral values across all lumbar vertebrae ($p < 0.0001$). Interestingly, DXA values were not able to predict fractures, except for hip T-score ($p < 0.0001$). The trained model obtained an average Dice Score of 0.88 across all vertebrae (L5-T11) and a score of 0.89 for lumbar vertebrae (Fig. 1).

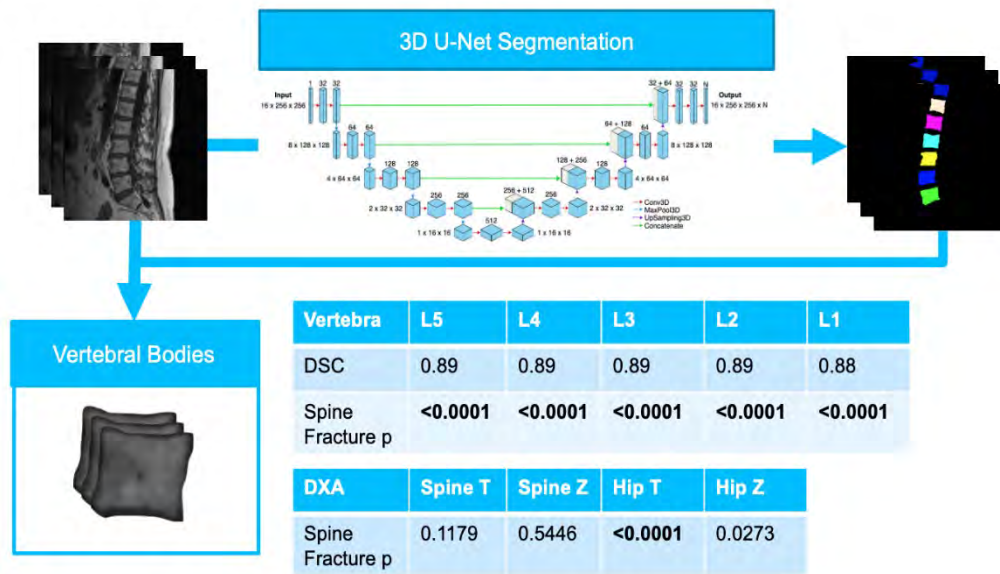


Fig. 1) Workflow of extracting vertebral body intensities using the 3D U-Net. Model performance for each lumbar vertebra is shown in the upper table. The p values are shown to compare performance of lumbar intensities to DXA scores in predicting spine incidence fractures.

DISCUSSION: This 3D U-Net efficiently segments lumbar vertebrae in MR scans, which is vital for analyzing fractures with complex anatomical structures. Fracture patients exhibited high intensity values due to soft tissue inside vertebral regions, which appears bright in MR scans. The correlation between fractures and mean vertebral intensity surpassed that of fractures and DXA, suggesting that MR scans are a superior predictor of spine fractures.

SIGNIFICANCE: Our research focuses on the intersection of machine learning, biological analysis, and artificial intelligence. The 3D U-Net model is a reliable tool for spinal analysis, offering promising results in vertebral segmentation and fracture prediction. This model has the potential to enhance accuracy and reduce the time required for pre-operative spine assessments.

ACKNOWLEDGEMENTS: This work was supported by National Institutes of Health grants R01 AR068382 and R01 AR076392.

Evaluating the relationships between lesion size and location, muscle activation, and motor and cognitive impairment in stroke subjects.

Reem Azar, M.S.1,2, Dr. Michelle J Johnson, PhD1,2,3,4

1. University of Pennsylvania, 2. Bioengineering Department, 3. Perelman School of Medicine, 4. Department of Physical Medicine and Rehabilitation

Introduction:

Stroke is one of the most common causes of death and disability in America and in other countries around the world; on average, about 53 billion of dollars is spent every year to treat patients¹. Stroke causes brain damage in the form of a lesion, which can be dissected into lesion size and location. Studies show that 77% of stroke survivors have upper limb motor deficits, and these deficits impede on stroke survivor's quality of life and function². Stroke rehabilitation traditionally relies on "impairment-level treatments" based solely on their motor and cognitive performances, with an emphasis on motor performance³. After stroke, the neuronal damage can affect normal muscle activity in the affected limb. Electromyography (EMG), specifically surface EMG (sEMG), provides information about muscular activation, which can provide information on the biopotentials of affected muscles⁴. Even in subjects that have functional limbs, there is evidence that co-activation of agonist and antagonist muscles is not appropriate and leads to abnormal limb movements⁵. Furthermore, the literature supports that cognitive impairments may mask motor performance, which may lead to incorrect therapeutic intervention when relying on behavior alone⁶⁻⁸. Additionally, there is a relationship between brain structure and resulting function. Muscle activation and lesion metrics are left out of therapeutic decisions in traditional therapy, however, relying on behavior alone may lead to incorrect intervention techniques. Given that cognitive impairments may mask motor high motor performance, a subject may incorrectly categorize a patient's impairment level and possibly, therapeutic strategy. Thus, relying on behavior alone to assess function assumes a simplistic and unrealistic view of the brain. Robotic-assisted therapy is an emerging treatment for stroke patients, and feedback from these robots allows for a quicker and more personalized treatment plan. This study's goal is to collect lesion metrics from retrospective scans, acquire muscle activation through sEMG, and assess stroke subject impairment through robotic evaluation. We hypothesize that there is a relationship between lesion location and subject behavior. We also hypothesize that there is a relationship between muscle activation and lesion location.

Materials and Methods:

Subjects that had diagnosis of stroke were consented into the study. All subjects underwent robotic assessments with the Haptic Theradrive, a 1 degree of freedom (DOF) robot equipped with a crank arm that allows for movement of shoulder, elbow, and wrist. To measure motor and cognitive impairment with the robot, three assessments were used: Trajectory Tracking (motor), N-Back (cognitive), and Spatial Span (motor and cognitive). Muscle activation during robot activity were acquired using sEMG from the subject's impaired arm via two four-channel sensors (Trigno Quattro, Delsys, Inc., Natick, MA, USA), for a total of eight channels. The sEMG targeted muscles from the shoulder, elbow, wrist, and hand, covering flexion, abduction and extension to varying degrees. To collect lesion metrics, CT scans were acquired retrospectively from patient charts. ITK-SNAP, an interactive tool developed for medical imaging segmentation, was used to create the lesion masks. The Statistical Parametric Mapping (SPM Version 12) Clinical Anatomy toolbox in MATLAB is used to register individual CT scans to a uniform space. After normalizing the images to a uniform space, ITK snap was used to compute lesion volume. To accomplish the goal of capturing whole brain regions of interest and subcortical brain regions, the Automated Anatomical Labeling Atlas 3 (AAL 3) was used. Region of interest volume involvement was acquired by using the layer tool in ITK Snap.

Results and Discussion:

Lesion metrics were harnessed from the radiological images of eleven subjects (57 ± 10 years old; male: 82.0%) manually. All subjects were 18 years or older, clinically diagnosed with stroke, had a CT scan, and able to voluntary move their upper extremity. All subjects were able to complete the robotic assessments with sEMGs equipped. Ten subjects had unilateral lesions, while one subject had bilateral lesions, however, the bilateral lesion was unable to be identified. Seven of the identified lesions were characterized on the left brain, meanwhile two subjects displayed lesions on the right side of the brain. Interestingly, two subjects did not have identifiable lesions. The lesions spanned the entire brain, covering cortical, subcortical, and brain stem areas.

Conclusion: These preliminary results suggest that we can harness lesion metrics from acute CT scans, a contested topic in the literature. These results also suggest possible relationships between structure and function; however, a larger sample size is needed. Future analyses will be focused on understanding the connection between lesion location and muscle function (sEMG) and behavior (robotic assessments).

Acknowledgements

This work was made possible through the core services and support from the NIH-funded T32 grant (Training in Musculoskeletal Research), NIH-funded parent and diversity supplement grants R42 HD104325, University of Pennsylvania Fontaine Society, and the Departments of Bioengineering and Physical Medicine and Rehabilitation. Dr Michelle Johnson, who is the PI on the R42 grant has a patent that uses devices inspired by the device being evaluated through this research. The PI is a co-founder of Recupero Robotics LLC.

**Plasma Activated Liquid Enhances the Bactericidal Activity of Vancomycin Against *Staphylococcus Aureus*.
Autumn Melvage¹, Carly Smith¹, Noreen Hickok¹, Theresa A. Freeman¹**

¹ Department of Orthopedic Surgery, Thomas Jefferson University, Philadelphia, PA

Theresa.Freeman@jefferson.edu

Introduction: Orthopedic infections are commonly caused by *Staphylococcal aureus* (ATCC 25923; *S. aureus*) which resides in biofilms. Biofilm structures protect bacteria from direct killing by antibiotics and immune cells. Cold atmospheric plasma (ionized gas consisting of charged particles, UV radiation, electric currents, and ROS) treatment of liquid (PAL) gives the liquid antimicrobial properties. These properties of PAL make it a promising approach for disrupting biofilms and enhancing the treatment of conventional therapies, which have limitations. In this *in vitro* study, we investigate the bactericidal ability of PAL against *S. aureus* alone and in combination with the antibiotic, vancomycin (Vanc), which is commonly used for treatment of orthopedic infection.

Methods: *In vitro* biofilm production and PAL treatment 96 well plate biofilm: Standardized *S. aureus* biofilms were grown on a 96-well plate and incubated in TSB for 24 hrs., then rinsed and air-dry before treatment with either PAL, TSB, or Saline (positive controls). ***In vitro* biofilm production on polycaprolactone (PCL) discs to test PAL treatment:** Standardized *S. aureus* biofilms were grown on PCL discs in TSB for 24 hrs. Discs were then moved to a new well containing either PAL, PAL/Vanc, Saline, or Saline/Vanc for 30 min., then incubated overnight in TSB or TSB/Vanc, respectively. Serial dilutions were performed and plated onto Petri films, incubated overnight, and the colony-forming units (CFU) were assessed. **Liquid Kirby-Bauer Test:** Sterile wells were created in an agar plate, then it was streaked with *S. aureus*, PAL, PAL/Vanc, Saline or Saline/Vanc were placed in the wells and incubated overnight. The next day, the zone of inhibition was measured.

Results: PAL Treatment Bacterial Killing: For biofilm in 96-wells plated, PAL treatment significantly reduced bacterial colonies (1.144 logCFU/mL (p<0.0001)) and saline (0.2694 logCFU/mL (p= 0.0009)) compared to the TSB controls. **Determination of Vancomycin conc.:** A conc. of 50ug/ml Vanc was chosen after it showed the highest reduction of bacterial colonies compared to untreated controls (1.003 logCFU/mL (p= <0.0001)). **Combination Treatment:** Reduction in PCL disc biofilm CFU counts in response to the treatments indicated are shown in Table 1. (sig. **** = p≤ .0001; * = p≤.1). PAL/Vanc treated discs had the most bacterial reduction, followed by PAL. Saline/Vanc and Vanc also significantly decreased biofilm growth. Saline (pH 2) treatment was not significantly different from untreated controls. **Zone of inhibition:** PAL/Vanc and Vanc had clear zones of inhibition with a slight difference in average diameter, while PAL had a small, specked zone of inhibition.

Treatment	NoTrx	Saline	PAL	Vanc.	Saline/Vanc	PAL/Vanc
Mean CFU	8.672	8.006	6.376	7.747	7.414	4.926
Mean Diff.	0	- 0.6722 (ns)	- 2.302 ****	- 0.9314 **	- 1.264 ****	- 3.752 ****

Discussion: The results indicate that PAL/Vanc has significant bactericidal effects on *S. aureus* biofilms. Although vancomycin is effective alone, the effect of vancomycin was less than that of PAL/Vanc combination treatments. In the zone of inhibition assay, Vanc and the combined PAL/Vanc treatment showed only slight differences in diameter. Taken together, these findings suggest that PAL, especially when used in combination with vancomycin, offers a promising strategy for treating *S. aureus* biofilms in orthopedic infections.

Significance/Clinical Relevance: Plasma Activated Liquid (PAL) in combination with antibiotics presents an innovative treatment option for combating *Staphylococcus aureus* biofilms in orthopedic infections.

ACKNOWLEDGEMENTS: This work was supported by NIH grant R01AR076941 (Freeman) from NIAMS. Thank you to Alannah Bratten and Arianna Moniodes for their aid in collecting results. Special thanks to Asia Winslow and Rachel Evans from the Hickok lab for helping with bacterial protocols.

Bacterial Phenotype: Effects of Media Representative of Peri-Operative Joint Environment
Asia Winslow¹, Rachel S. Evans¹, Caroline Purtill¹, Selin Isguven¹, Thomas P. Schaer², Noreen J. Hickok¹

¹ Department of Orthopedic Surgery, Thomas Jefferson University, Philadelphia, PA

² University of Pennsylvania School of Veterinary Medicine, Kennett Square, PA

Noreen.Hickok@jefferson.edu

Introduction: Periprosthetic joint infections (PJI) are an infrequent and devastating complication of total joint arthroplasty, with *Staphylococcus aureus* (*S. aureus*) the most frequent pathogen. PJIs are difficult to treat, and our *in vitro* studies suggest that the joint environment may be a major cause of this difficulty. Acknowledging that the post-operative environment evolves from a bloody wound through serosanguineous fluid to synovial fluid over the course of weeks, we asked the effects of these environments on *S. aureus* properties. Using model and retrieved physiological fluids, we investigate *S. aureus* bacterial phenotypes, biofilm formation, and antibiotic tolerance as a function of fluids representing the evolving post-surgical joint environment. These changes in response will allow better targeting of both times and ways to treat PJI.

Methods: *In vitro* biofilm formation and vancomycin treatment on Ti rods: Bacterial properties were compared between trypticase soy broth (TSB) and multiple different physiological fluids such as human serum, 50% human serum with glucose (to model wound fluid), and pseudo-synovial fluid. A biofilm of *S. aureus* was formed by incubating 10⁸ CFU/mL bacteria with a Ti rod for 24 hours. Biofilm-coated rods were incubated in fresh media containing antibiotics for 6 or 24 hours, and adherent bacteria recovered by resuspension with trypsin treatment. Resuspended bacteria were diluted, plated, and counted using 3M PetriFilms. ***In vitro* bacterial quorum sensing and virulence factors gene expression:** *Accessory gene regulatory (agr)* regulation was determined using a MRSA P3lux reporter line, where the time course of expression was measured. In parallel, bacterial numbers were determined by turbidity (*A*₆₀₀). P3 activity and growth were determined for the different conditions. In addition to P3lux reporter line, PSM-alpha, PSM-beta, and P2lux reporter lines were measured in different medias as well.

Results: Bacterial adhesion depended on media where adhesion was greatest in TSB and least in synovial fluid. Using vancomycin (VAN) concentrations, biofilms formed in TSB for 24 hours showed a small dose dependent decrease with an ~ 10X (1 log, (p≤0.0001) at 100ug/mL; however, in HS, there were little to no change in CFU counts independent of dosage. However, when the treatment was extended to 24h, HS also showed a dose dependence, with >1 log decrease at 100 ug/mL. (p≤0.0001). Because biofilms grown in the different media show different structures, we asked if biofilm bacteria responded to antibiotics based on the formation or the subsequent bathing media. Biofilm (24 hours) antibacterial responses to treatment with VAN (24 hours, 0, 2, or 10 ug/mL) in HS, TSB, and 50% HS/PBS/glucose suggested that the formation medium dominated the response as all three media gave similar reductions in bacterial counts. When measuring the luciferase activity of multiple MRSA USA300 strains that reflect Agr activity, peak luciferase activity in TSB, HS, SynF, and pSynF were drastically different, despite ultimately ending with the same number of bacteria. Together these results implied suppressed virulence factor expression in the HS- and SynF-based media.

Discussion: PJIs are an infrequent but costly and detrimental complication of joint replacement. From these results, we determined if different media altered numbers of bacteria adherent to model implants, modified bacterial antibiotic response to the same vancomycin concentration, and modulated virulence factor production. The environment in which the biofilm formed affected biofilm bacterial number as well as antibiotic sensitivity, even after bacteria were bathed in a new fluid. In HS more time is required for the antibiotics to result in a significant amount of bacterial killing. Virulence factors/toxins under control of the *agr* locus include the phenol soluble modulins (reflected in the P3 values reported) which activate the immune system and determine biofilm mass, hemolysins, and others that determine matrix adherence, nutrition, and other properties. In all model physiological fluids, virulence factor expression was significantly depressed compared to that measured in TSB, and in fact, for P3 were at levels for most of the measurements that fell within the background range. However, the bacteria remained viable in those conditions.

Significance/Clinical Relevance: Infections in the joint are difficult to treat and we suggest that the bacterial properties that we describe form a critical part of that difficulty. The response of the bacteria to the environmental changes associated with the operation suggests that time of treatment may be critical.

ACKNOWLEDGEMENTS: This work was supported by NIH AR082038 and NIH grant R01AR076941. Special thanks to Neil Zhao, Autumn Melvage, and Carly Smith for protocols and technical assistance.

YAP and TAZ mediate a transcriptional feedback loop to maintain tensional homeostasis in tenocytes

Elizabeth Seidl¹, Manav Surti², Nathaniel Dymant¹, Joel D. Boerckel^{1,2}
University of Pennsylvania¹, Center for Engineering Mechanobiology (CEMB)²

INTRODUCTION: Tenocytes exhibit tensional homeostasis, by which tension of the extracellular matrix regulates cytoskeletal tension and mechanotransductive gene expression to maintain cell and matrix equilibrium [1]. Tenocytes sense mechanical changes in the collagenous matrix and transduce these signals to gene expression through mechanotransduction. However, when the tissue is unloaded, either locally by microdamage or by full rupture, a loss of mechanotransductive signals triggers matrix metalloproteinase (MMP) expression and the collagen matrix becomes degraded and disorganized [1]. Recently, we showed that the transcriptional regulators Yes-Associated Protein (YAP) and Transcriptional co-activator of MMP [1]. However, the mechanisms by which the tenocytes maintain homeostasis of their cell-intrinsic cytoskeletal tension in dynamic mechanical environments is poorly understood. Cytoskeletal tension is generated by RhoA GTPase-mediated activation of myosin motors, and can be regulated by RhoA-inactivating GAP (ARHGAP) proteins [3]. Here, we show that YAP and TAZ mediate a mechanotransductive feedback loop through transcriptional regulation of the ARHGAP, DLC1. Further, we here report the generation of an inducible, tenocyte-conditional knockout mouse model for the study of tensional homeostasis *in vivo*.

METHODS: *In vitro:* Human tendon fibroblasts from adult donor patellar and Achilles tendons were obtained commercially and cultured in sterile conditions. Cells were transfected with either SMARTpool ON-TARGETplus siRNA for *YAP1* and *WWTR1* (which encodes TAZ) or non-targeting control siRNA. Transfection was performed using Lipofectamine RNAiMAX. 48 hours after transfection, cells were lysed and purified using Qiagen RNeasy Mini Kit. RNA was converted to cDNA with Applied Biosystems' High-Capacity cDNA Reverse Transcription Kit. Gene expression was evaluated using quantitative real-time PCR and Applied Biosystems' SYBR Green PCR Master mix on a QuantStudio 6 Pro machine. Fold change values were obtained through the delta delta Ct method and compared by unpaired, two-tailed t-tests ($\alpha = 0.05$). Additionally, cells were transfected with the siRNA listed above were fixed in 4% Paraformaldehyde, blocked and permeabilized with 5% goat serum and 0.3% Triton X-100. The cells were then stained with conjugated Cell Signaling YAP/TAZ Rabbit mAb (Alexa Fluor 647) antibody. After staining overnight, the cells underwent washes and staining with (Alexa Fluor 488) Phalloidin and Hoechst. The cells were imaged on a fluorescent microscope and fluorescence was quantified in CellProfiler software.

In vivo: A novel inducible YAP/TAZ Knockout mouse model was generated using a mouse model that utilizes the tamoxifen-inducible Cre-ER(T) protein controlled by the pro alpha 2(1) collagen gene [4]. This mouse was crossed with a mouse with both alleles floxed for YAP and TAZ. Progeny were crossed to generate homozygous floxed alleles for both YAP and TAZ with tamoxifen-inducible recombination in Col1a2-expressing cells. After 4 intraperitoneal Tamoxifen injections dissolved in corn oil at 100 mg/kg dosage approximately 24 hours apart, both a Cre- and Cre + mouse's patellar and Achilles and plantaris were harvested for gene analysis. The tissues were grinded with a motorized pestle in QIAzol Lysis Reagent and RNA was isolated utilizing the Zymo Direct-zol RNA MicroPrep kit.

RESULTS: *In vitro:* siRNA targeting *YAP1* and *WWTR1* significantly downregulated *YAP* and *TAZ* mRNA expression (Fig. 1 A,B) and significantly reduced both YAP and TAZ protein levels, as measured by immunofluorescent staining. YAP/TAZ depletion also reduced expression of downstream targets of YAP/TAZ-TEAD transcription, *CYR61* and *CTGF* (Fig. 1 C,D). Consistent with our prior findings [2], YAP/TAZ depletion upregulated both MMP3 and MMP14 (Fig. 2 A,B). Notably, YAP/TAZ depletion significantly downregulated expression of *DLC1* (*ARHGAP7*) (Fig. 2 C).

In vivo: We created a new mouse model to study the roles of YAP/TAZ signaling in tenocytes *in vivo*. Preliminary studies indicate ~35-80% efficient tamoxifen-inducible deletion of YAP and TAZ in both patellar tendon and Achilles tendon and plantaris (N = 1). In ongoing work, we will use this novel mouse model to understand the roles of YAP/TAZ mechanotransduction in tenocyte tensional homeostasis *in vivo*.

DISCUSSION: Together, these data suggest a novel framework for understanding tenocyte tensional homeostasis and its disruption by overuse injury. Specifically, we present a model whereby damage-induced loss of matrix tension inactivates YAP/TAZ-mediated mechanotransduction, resulting in two outcomes: disinhibition of MMP expression that initiates matrix remodeling and loss of ARHGAP7/DLC1 expression that maintains homeostasis of the actin cytoskeleton [4]. Thus, matrix detensioning may induce both matrix disorganization and cell-autonomous actomyosin over-activation, together contributing to long term scarring and tendon fibrosis. With our new tenocyte-conditional YAP/TAZ knockout mice in hand, we aim to elucidate the role of YAP/TAZ mechanosignaling in tenocyte tensional homeostasis *in vivo*.

SIGNIFICANCE: Understanding the mechanisms that maintain tensional homeostasis in tenocytes may reveal new therapeutic approaches to prevent tendinopathy and promote tendon healing.

REFERENCES: [1] Lavagnino & Arnoczki *J Orthop Res.* 2005, [2] Jones+ *JPNAS.* 2023 [3] Hooglugt+ *J Cell Sci.* 2024 [4] Zheng+ *Am J Pathol.* 2002 [5] Mason+ *JCB.* 2019

ACKNOWLEDGEMENTS: Work Supported by Grant NIH/NIAMS P50AR080581 from the National Institute of Arthritis and Musculoskeletal and Skin Diseases of the NIH and PCMD grant P30 AR069619

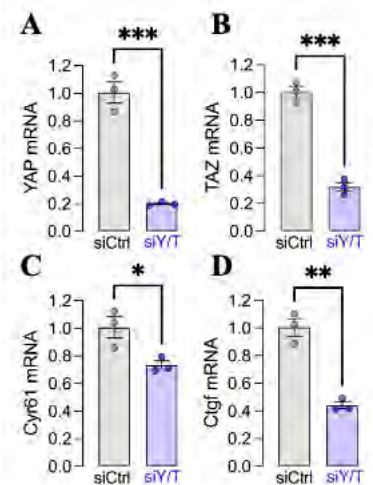


Figure 1. Human tendon fibroblasts transfected with siRNA targeting *Yap* and *Taz* (*Wwtr*) show significantly decreased gene expression of *YAP*, *TAZ* (A,B) and downstream *YAP/TAZ* target genes (C,D) * = $p < 0.05$.

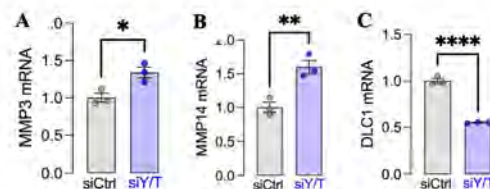


Figure 2. Human tendon fibroblasts transfected with siRNA targeting *Yap* and *Taz* (*Wwtr*) show significantly increased gene expression of MMPs (A,B) and ARHGAP7 (*DLC1*) (C) * = $p < 0.05$.

Figure 2. Human tendon fibroblasts transfected with siRNA targeting *Yap* and *Taz* (*Wwtr*) show significantly increased gene expression of MMPs (A,B) and ARHGAP7 (*DLC1*) (C) * = $p < 0.05$.

Title: Master roles for RUNX2 and RUNX3 in growth plate chondrocytes

Authors: Daniel Halloran, Marco Angelozzi, Abdul Haseeb, Chantal Voskamp, Samantha Whipple and Véronique Lefebvre

Division of Orthopaedic Surgery, Children's Hospital of Philadelphia, PA

Category: Other Research

Abstract:

Cartilage growth plates (GPs) are pivotal developmental templates for all endochondral bones. Their resident chondrocytes (GPCs) undergo a multi-step program of maturation that involves drastic changes in proliferation and differentiation status. This sequential maturation occurs spatially in specific tissue zones referred to as resting, columnar, pre-hypertrophic, hypertrophic, and terminal. It involves many types of regulatory genes and, accordingly, genetic variants affecting GPC activities have been shown to cause several hundreds of distinct human chondrodysplasias. However, deep knowledge gaps persist in our understanding of the molecular networks wherein these genes participate to specify the GPC activities in wild-type and disease conditions. The Runt-related transcription factor RUNX2 has been well demonstrated to be a master regulator of osteoblast lineage commitment and differentiation since haploinsufficiency of its gene was shown to cause cleidocranial dysplasia in humans, and since mice lacking *Runx2* were shown to form cartilage primordia and GPs, but no intramembranous and endochondral bone tissues. RUNX2 was shown two decades ago to act largely redundantly with RUNX3 in the chondrocyte lineage to ensure GPC maturation from prehypertrophy onwards. Indeed, mouse fetuses with global deletion of both *Runx2* and *Runx3* featured cartilage primordia, but failed to form GPs. To date, however, the mechanisms whereby RUNX2/RUNX3 control GP formation remain incompletely deciphered. The current project aims to fill this knowledge gap. Since *Runx2* and *Runx3* are co-expressed in columnar GPCs, but only *Runx2* remains expressed at subsequent cell maturation stages, we hypothesized the two redundant factors likely control key genes in columnar cells. Mice in which *Runx2* and *Runx3* were inactivated with *Prx1Cre* from the limb bud skeletogenic mesenchyme stage were born, as previously shown with global mutants, with very short limbs, as cartilage primordia were unable to form GPs. Unexpectedly, we saw that these primordia developed postnatally massive amounts of hypertrophic cells, which were eventually replaced by marrow cavities. Likewise, when we inactivated *Runx2* and *Runx3* in postnatal chondrocytes using *Acan^{CreER}*, mouse growth was stunted as GPCs halted proliferation and massively underwent hypertrophy. To decipher the molecular activities of RUNX2/RUNX3 in GPCs, we are performing single-cell profiling of transcriptomes and accessible chromatin regions in GPCs of control and mutant mice, and we are also characterizing the genome-wide occupancy of the transcription factors in GPCs of control mice. Preliminary data analyses, along with *in vitro* reporter assays, reveal that RUNX2/RUNX3 directly and indirectly control a wider spectrum of genes than previously estimated and that these genes regulate many aspects of GP cell activities and spatial and temporal organization. In conclusion, our work reinforces evidence that RUNX2 and RUNX3 are master regulators of GPCs from specification to terminal maturation, and thereby decisively determine skeletal growth and patterning. We anticipate that our work will help explain the molecular underpinnings of many forms of chondrodysplasias and could provide molecular tools and targets to design direly-needed strategies to efficiently treat these skeletal disorders.

High-Density Surface Electromyography to Monitor Neuromuscular Activity Across Joints Affected by Common Musculoskeletal Pathologies

Maggie M. Wagner^{1*}, Flavia Vitale¹, and Josh R. Baxter²

¹Department of Bioengineering, University of Pennsylvania, Philadelphia, PA, US

²Department of Orthopaedic Surgery, University of Pennsylvania, PA, US

*Email: magwag@seas.upenn.edu

Introduction: Muscle neuromechanics govern the complex network of motor units that control everyday movements. These complex control mechanisms are often compromised following injury, immobilization, and treatment – complicating return to sport and activity [1]. Researchers and clinicians use traditional surface electromyography (sEMG) to quantify muscle neuromechanics during functional tasks. However, sEMG only provides a localized approximation of muscle activity. Our group is addressing this unmet clinical need by designing and fabricating customizable high-density surface electromyography (HDsEMG) using a carbon-based nanomaterial, $\text{Ti}_3\text{C}_2\text{T}_x$ MXene – which we call “MXtrodes.” Our earlier validation work found that MXtrodes have comparable or better electrical properties to traditional metal electrodes, including a higher signal-to-noise ratio without conductive gels [2]. In this study, we implement MXtrodes across two muscle groups affected by common musculoskeletal injuries: 1) the plantar flexors that are impacted by Achilles tendon pathology and 2) the shoulder muscles that are impacted by rotator cuff injuries. We integrated MXtrodes into our custom-developed data acquisition tool that uses a wireless EMG processor to facilitate unimpeded movement from subjects.

Methods: We fabricated sets of four MXtrodes, consisting of two 20-electrode and two 12-electrode arrays, for a total of 64 electrodes per set (Fig. 1A). We fabricated these MXtrodes by saturating a laser-patterned absorbent substrate with conductive MXene ink and then insulated the resultant electrodes in a silicone polymer. We studied the plantar flexors and shoulder muscles to demonstrate MXtrode utility across two commonly studied joints. Plantar flexors. We measured bilateral plantar flexor function using pairs of 20-electrode arrays on each gastrocnemius and pairs of 12-electrode arrays on each soleus in two healthy controls. These subjects performed maximum voluntary isometric contractions on a dynamometer (Biodex, System 4) and a series of heel raises with their toes pointed inward, outward, and neutral. Shoulder. We measured bilateral infraspinatus function using 20-electrode arrays and deltoid function using 12-electrode arrays in one healthy control and three individuals with rotator cuff pathology. These subjects completed a series of functional exercises, including loaded and unloaded reaching exercises. We recorded their muscle activation using a wireless EMG processor (Ripple Neuomed, Explorer Summit) that permitted free movement and synchronized recordings from the dynamometer and MXtrodes using our custom data acquisition tool. We filtered the collected EMG data using a 20-450 Hz bandpass 4th order Butterworth filter, calculated the root-mean-square potential for each electrode, and visualized the HDsEMG signals using color heat maps (Fig. 1B).

Results and Discussion: Plantar flexor and shoulder muscle activation differed depending on activity. Plantar flexors. We found that gastrocnemius muscle activity increased during neutral heel raises, which involves an extended knee that increases gastrocnemius engagement. Shoulder. We found that infraspinatus muscle activity decreased and shifted towards the trapezius in participants with shoulder cuff pathology. These findings demonstrate the utility of HDsEMG because detecting regional changes in muscle activity is less likely with a single EMG sensor or a low-density electrode grid. Our HDsEMG system incorporates high-density electrode arrays that we custom design and fabricate based on the muscle, a wireless data logging system to facilitate unencumbered movement, and a custom-written data acquisition interface that provides real-time access to HDsEMG signals and other lab equipment, including dynamometers and constant current stimulators, to control experimental conditions. Our ongoing work is identifying activation patterns during rehabilitation exercises to develop personalized strategies to rehabilitate specific muscles in orthopaedic populations. By controlling for changes in muscle activation through HDsEMG during rehabilitation, we expect to mitigate suboptimal outcomes associated with altered muscle neuromechanics.

Significance: Through our MXtrode data acquisition platform, we aim to identify patterns of muscle activity during rehabilitative exercises and changes in muscle activation throughout healing from musculoskeletal pathologies. By better understanding the underlying mechanisms that affect patients’ functional outcomes, we could better inform and guide rehabilitation and potentially improve their functional outcomes following rehabilitation.

Acknowledgements: Supported by NIH (R01AR081062, P50AR080581) and NSF Graduate Research Fellowship (DGE-2236662)

References: [1] J. T. Hopkins and C. D. Ingersoll, *J. Sport Rehabil.*, 9(2):135, 2000; [2] R. Garg et al., *Small Methods*, 2201318, 2022

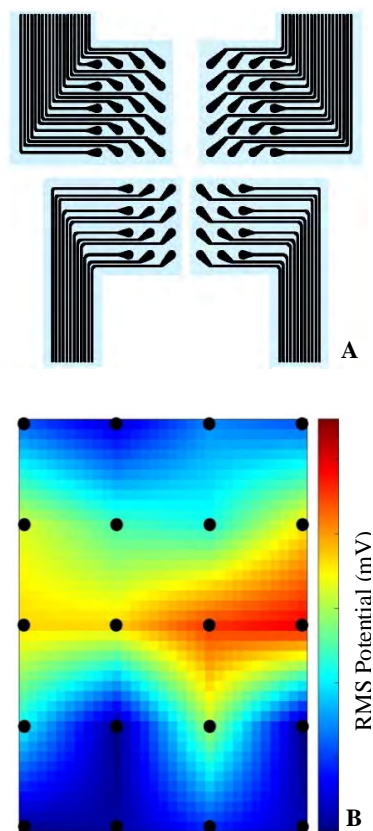


Figure 1. HDsEMG array design (A) and example muscle activation heat map (B). Each black dot on the heat map represents an electrode, with the recorded potential interpolated between the dots.

ASK1 inhibition with Selonsertib results in decreased chondrogenic differentiation dependent on age and/or sex

Eirene Choi¹, Alzbeta Chabronova², Mandy Peffers², John Collins¹ and Theresa A Freeman¹.

¹Department of Orthopedic Surgery, Thomas Jefferson University, Philadelphia, PA, United States.

²Department of Musculoskeletal and Ageing Science, University of Liverpool, Liverpool, United Kingdom.

Introduction: Apoptosis Signal-Regulating Kinase 1 (ASK1) is a mitogen-activated triple protein kinase that is activated by various stress stimuli including reactive oxygen species and pro-inflammatory cytokines. Our previously published studies have highlighted the role of ASK1 in chondro- and osteogenesis, osteoarthritis, and cartilage regeneration. ASK1 loss or inhibition studies in the literature have shown a reduction of apoptotic and pro-inflammatory signaling pathways. Given the profound effect of ASK1 inhibition or loss on cartilage regeneration, we asked if similar pathways were transcriptionally regulated during chondrogenic differentiation in an *in vitro* micromass cartilage model.

Methods: Human bone marrow-derived mesenchymal stem cells (HBMSCs) from younger male (n=5), older male (n=4), and younger female (n=4) and older female (n=4) donors were cultured to undergo chondrogenic differentiation with TGF β -3 in micromasses. To test the effect of ASK1 inhibition, micromasses were treated with no TGF β -3, TGF β -3 (control), TGF β -3 with selonsertib (6 days), a small molecule ASK1 inhibitor. On day 10 all micromasses were harvested for RNA isolation and qPCR for markers of early and late chondrogenic differentiation, COL2A1, ACAN and SOX9 (early) and MMP13 and COL10A1 as late markers of chondrocyte hypertrophy. Differential gene expression and pathway analysis were conducted using R package DEseq2 (v1.44.0) and pathway analysis with fgsea (v1.30.0). STRING (v12.0) was utilized to conduct functional enrichment analysis.

Results: qPCR showed the addition of TGF β -3 successfully increased chondrogenic gene expression in the micromasses. Selonsertib treatment in addition to TGF β -3, resulted in reduced expression of chondrogenic differentiation and hypertrophy gene markers for all samples compared to control. Analysis of the micromass RNAseq data by the STRING protein-protein interaction network confirmed selonsertib treatment resulted in a network of downregulated genes associated with chondrogenesis, including COL2A1 and ACAN. To determine if sex or age-based differences existed between the groups, further analysis of the RNAseq data by PCA showed PC1 vs PC2 clustering based on TGF β -3 treatment, which also segregated by age. PC3 and PC4 showed segregation of the clusters by sex. Additionally, only 8 genes were differentially expressed in the older donors in response to selonsertib treatment versus 699 in younger donors. To understand how pathways differed by age and sex, Gene Set Enrichment Analysis (GSEA) using the HALLMARK gene sets was performed. Selonsertib treatment significantly positively enriched the INFLAMMATORY_RESPONSE (IR), TNFA_SIGNALING_VIA_NFKB (TNF) and EPITHELIAL_MESENCHYMAL_TRANSITION (EMT) gene sets in all groups except older males in which EMT was unchanged, and TNF and IR had the opposite (negative) enrichment. In fact, there was only 1 other pathways in older males that was significantly affected by selonsertib treatment, the MYC_TARGETS_V2 was positively enriched. Additional research is necessary to decipher the functional significance and mechanisms responsible for these differences.

Conclusion and Discussion: This study demonstrates that ASK1 inhibition is generally associated with the slowing of chondrocyte differentiation, possibly maintaining more of a stem-like or articular cartilage phenotype, due to repression of hypertrophy. Interestingly, there were differences based on age and sex with less/differentially effectiveness between groups which may explain variations in clinical trial results for this drug.

Diversification of synovial joint progenitors into articular cartilage and ligament cells: scRNAseq and computational analyses

Saunders, C., Mundy, C., Catheline, S.E., Ramesh, S., Song, C., Long, F., Koyama, E. and Pacifici, M.

Division of Orthopaedic Surgery, The Children's Hospital of Philadelphia, Philadelphia, PA 19104

Introduction/Rationale: Synovial joints are composed of different tissues, but the developmental biology of these tissues remains largely unclear. Joint development starts with emergence of a mesenchymal tissue -called the interzone - at each prescribed anatomical joint site. We and others previously demonstrated that the interzone cells serve as unique progenitors, diversify over time and give rise to most joint tissues, including articular cartilage and ligaments. However, the mechanisms driving such process of cell lineage diversification remain unknown. In this study, we resorted to single cell RNAseq (scRNAseq) to gain molecular insights into the transcriptome of incipient interzone cells and changes over time, focusing on transcriptional and protein signaling pathways possibly involved in chondrocyte differentiation versus ligament and meniscal cell development. We used computational tools including Monocle 3 to gain insights into developmental trajectories and relationships between progenitor and differentiated cells.

Materials and Methods: The prospective knee region was isolated from E13.5, E14.5 and E16.5 mouse embryos by microsurgical procedures and converted into single cell suspensions by enzymatic treatment. These time points were selected as they represent the initial formation of the compacted interzone at E13.5, the early morphogenic changes at E14.5 and the emergence of incipient chondrocytes and ligament cells by E16.5, the latter being the time point when a synovial cavity is also apparent. The isolated cells (at least 10,000/sample) were processed for scRNA-seq by our centralized facilities. Monocle 3 was used to analyze scRNA-seq data, reconstruct cellular trajectories, map pseudotime, and generate heatmaps of selected genes, thereby elucidating developmental pathways followed by the interzone cells.

Results: We first analyzed the E13.5 and E14.5 scRNA-seq datasets and constructed cellular and pseudotime trajectories delineating the differentiation progression of interzone cells into various joint tissues. Newly emerged interzone cells are uniquely characterized by expression of the TGF β superfamily member *Gdf5*. Indeed, the datasets displayed a large cluster of *Gdf5*-expressing interzone cells that exhibited a distinct branching point over pseudotime, one directed toward chondrogenic differentiation and the other directed toward meniscal and ligament cell development. Heatmap analyses revealed that the chondrogenic lineage was characterized by expression of such key chondroprogenitor markers as *Sox5* and *Sox9*, continuing with expression of early chondrocyte markers such as *Aggrecan (Acan)* and *type II collagen (Col-II)*. This analysis revealed also cells expressing *Prg4* and *Fgf18* that may represent future superficial zone articular cells. In comparison, the meniscus/ligament cell lineage was characterized by expression of *Scleraxis (Scx)*, *Forkhead Box C1 (FoxC1)*, *Decorin*, and *Tenomodulin*, highlighting a specialized pathway for meniscus and ligament development.

Next, we analyzed the datasets at E16.5, paying particular attention to the emergence of permanent articular chondrocytes at that stage. Heatmap analyses revealed unique gene expression profiles among chondrocytes destined toward a permanent articular phenotype versus transient metaphyseal chondrocytes. The presumptive permanent chondrocyte population exhibited significant enrichment in genes such as *Gdf5*, *Prg4*, *Pthlp*, and *Erg*, a transcription factor belonging to the ETS family. In contrast, there was minimal expression of *Matrilin-1(Matn1)* and *UCMA*. Conversely, the transient chondrocyte population displayed an expression profile characterized by elevated levels of *Matn1*, *UCMA*, *Acan*, and *Col-II* expression while being largely devoid of *Gdf5* and *Prg4* expression.

Conclusions: Our scRNAseq and computational analyses provide novel insights into how interzone joint progenitor cells diversify over time and produce distinct tissues. The data reveal that the interzone cells begin to branch into separate cell lineages as early as E13.5/E14.5, time points when the cells are morphologically identical when viewed microscopically. Such early commitment process may reflect the very distinct nature of different joint tissues and a need to commit progenitors early to such distinct fates. Incipient permanent articular chondrocytes become apparent by E16.5 following the establishment of a branching point at earlier stages.

Clinical Significance: Studies such as the present one may provide potential therapeutic strategies for joint diseases including osteoarthritis, suggesting ways to steer stem/progenitor cells into different cell lineages to repair different tissues during degenerative joint conditions.

YOUR FEEDBACK IS IMPORTANT!

Please take a minute to complete the survey to help with future Symposiums

https://upenn.co1.qualtrics.com/jfe/form/SV_5at9EDmwvnE7wEu



QR Code to Survey